Summer 8-15-2017

Aluminosilicate Dissolution and Silicate Carbonation during Geologic CO2 Sequestration

Yujia Min
Washington University in St. Louis

Recommended Citation

WASHINGTON UNIVERSITY IN ST. LOUIS

School of Engineering & Applied Science

Department of Energy, Environmental & Chemical Engineering

Dissertation Examination Committee:
Young-Shin Jun, Chair
Richard Axelbaum
Alexander Bradley
John Fortner
Daniel Giammar
Sophia Hayes

Aluminosilicate Dissolution and Silicate Carbonation during Geologic CO_2 Sequestration
by
Yujia Min

A dissertation presented to
The Graduate School
of Washington University in
partial fulfillment of the
requirements for the degree
of Doctor of Philosophy

August 2017
St. Louis, Missouri

Table of Contents

List of Figures

Acknowledgments

I would like to express my sincere gratitude to my advisor Dr. Young-Shin Jun for her support and advice. I am especially thankful for her patience during my journey from a graduate student into an independent researcher.

I would like to thank Dr. Richard Axelbaum, Dr. Alexander Bradley, Dr. John Fortner, Dr. Daniel Giammar, and Dr. Sophia Hayes for kindly giving the time to serve on my thesis committee, and providing their valuable suggestions. I would also like to express my appreciation to my collaborators, Dr. James D. Kubicki at University of Texas at El Paso for conducting computational modeling, and Dr. Marco Voltolini and Dr. Timothy Kneafsey at Lawrence Berkeley National Laboratory, for their valuable insights on the imaging of samples. I would also like to give my thanks to Prof. James Ballard and Prof. Sandra Matteucci for helping me to improve my writing.

I would also like to acknowledge my colleagues in the Environmental Nanochemistry Laboratory. I sincerely thank Dr. Yi Yang, who served as a mentor when I started to work in the lab. I am also very grateful to Dr. Yandi Hu, Dr. Jessica Ray, Dr. Chelsea Neil, Dr. Qingyun Li, Doyoon Kim, Haesung Jung, Lijie Zhang, Xuanhao Wu, Zhenwei Gao, and Yaguang Zhu. Special thanks are extended to Dr. Zezhen Pan, Dr. Di Liu, and other colleagues and friends in the department of Energy, Environmental & Chemical Engineering for making my PhD life colorful and enjoyable.

Last, but most important, I wish to express my deepest gratitude and appreciation to my parents, my brother, and my sister for their encouraging words and endless love during my journey.

Yujia Min

Washington University in St. Louis

August 2017

ABSTRACT OF THE DISSERTATION

Aluminosilicate Dissolution and Silicate Carbonation during Geologic CO_2 Sequestration

by

Yujia Min

Doctor of Philosophy in Energy, Environmental & Chemical Engineering

Washington University in St. Louis, 2017

Professor Young-Shin Jun, Chair

Geologic CO_2 sequestration (GCS) is considered a promising method to reduce anthropogenic CO_2 emission. Assessing the supercritical CO_2 (scCO_2)–gas or liquid phase water (g, l)–mineral interactions is critical to evaluating the viability of GCS processes. This work contributes to our understanding of geochemical reactions at CO_2–water (g, l)–mineral interfaces, by investigating the dissolution of aluminosilicates in CO_2-acidified water (l). Plagioclase and biotite were chosen as model minerals in reservoir rock and caprock, respectively. To elucidate the effects of brine chemistry, first, the influences of cations in brine including Na, Ca, and K, have been investigated. In addition to the cations, the effects of abundant anions including sulfate and oxalate were also examined. Besides the reactions in aqueous phase, we also examine the carbonation of silicates in water (g)-bearing supercritical CO_2 (scCO_2) under conditions relevant to GCS. For the metal carbonation, in particular, the effects of particle sizes, water, temperature, and pressure on the carbonation of wollastonite were systematically examined.

For understanding the cations effects in brine, the impacts of Na concentrations up to 4 M on the dissolution of plagioclase and biotite were examined. High concentrations of Na significantly inhibited plagioclase dissolution by competing adsorption with proton and

suppressing proton-promoted dissolution. Ca has a similar effect to Na, and their effects did not suppress each other when Na and Ca co-existed. For biotite, the inhibition effects of Na coupled with an enhancing effect due to ion exchange reaction between Na and interlayer K, which cracked the basal surfaces of biotite. The K in aqueous phase significantly inhibited the dissolution. If the biotite is equilibrated with NaCl solutions initially, the biotite dissolved faster than the original biotite and the dissolution was inhibited by Na and K in brine. The outcomes improve our current knowledge of silicates dissolution to the high salinity conditions in subsurface environments.

In addition to cations, the role of anions in geochemical reactions in subsurfaces are important. This study investigated the anion effects by studying sulfate and oxalate. Sulfate formed monodentate surface complexes with the Al sites on plagioclase surface and enhanced the dissolution. Oxalate was also found to enhance the plagioclase dissolution. Co-existing oxalate and sulfate suppressed the effects of sulfate on plagioclase dissolution. This information provides useful insights for understanding the roles of sulfate and organic compounds on the CO_2–water–mineral interactions during $scCO_2$ enhanced oil recovery. The results also aid in formulating a scientific guideline of the proper amount of SO_2 co-injection with CO_2.

Water in GCS sites can exist in water-bearing $scCO_2$ in addition to the aqueous phase in brine. Thus, it is important to understand the effects of water-bearing $scCO_2$ on the carbonation of silicates. To address the gap between the nano- and micro-sized particles used in the laboratory to the large grains in field sites, we utilized wollastonite and investigated the effects of particle sizes on the wollastonite carbonation in water-bearing $scCO_2$. The thickness of the reacted layer on the particle surfaces was found to be constant for different sized particles. The amorphous silica layer formed act as a diffusion barrier for water-bearing $scCO_2$. In addition, the reaction extent was higher with more water, lower temperature, and higher pressure. Further, higher water saturation

percentage and lower temperature can lead to the formation of more permeable amorphous silica layers.

This thesis included the investigations of both liquid phase and vapor phase water that contacted with scCO$_2$, and the effects of cations and anions on both formation and caprock minerals. The findings from this work improve our knowledge of the geochemical reactions at CO$_2$–water–mineral interfaces, which will help us design a safer GCS operation and assess the impacts of GCS on the environmental safety and quality.

Chapter 1: Introduction

1.1 Background

1.1.1 Geologic CO₂ Sequestration

Geologic CO_2 sequestration (GCS) is a promising strategy to alleviate the adverse impacts of global climate change.[1-6] GCS operations can decrease the CO_2 emissions from large point sources like power plants by capture, injecting, and sequestrating CO_2 in geologic formations. The potential storage sites include deep saline aquifers, depleted oil and gas reservoirs, and basalt formations.[5] Among these candidates, the deep saline aquifer option has been estimated to have the largest storage capacity.[3-5, 7]

The reservoir rocks in GCS sites need to be porous to provide space for CO_2 storage, and also has to be permeable to allow transport of CO_2 in the pores.[8] To efficiently use these storage spaces, CO_2 is usually stored in the supercritical phase, which has higher density than CO_2 in the gas phase.[9] Thus, the temperature and pressure in the GCS sites should be at least higher than 31 ℃ and 73 atm, which is the critical point of CO_2. The temperature and pressure in GCS sites could vary with the depth of the reservoir. The relationship can be roughly estimated based on T (℃) = 15 + 33d (depth in kilometer) and P (atm) = 1 + 100d.[9] Globally, conditions of GCS sites range from 31 to 110 ℃ and from 73 to 592 atm.[10] Injected CO_2 would tend to migrate upward due to buoyance, because the density of supercritical CO_2 ($scCO_2$) is smaller than the density of brine under most of the GCS conditions.[11] To prevent the leakage of CO_2 to atmosphere, the storage sites require an impermeable caprock layer above the reservoir rock. The caprock hindered the upward migration of CO_2, which results in structural or stratigraphic trapping. CO_2 is also trapped

as bubbles in the pores of reservoir rock, which is known as residual trapping. Solubility trapping happens when CO_2 dissolves in brine. The dissolved CO_2 can further react with cations in brine and trapped in carbonate minerals, which is named mineral trapping.[5]

1.1.2 Dissolution and Precipitation at CO_2–Water–Rock Interfaces

The economic efficiency and environmental safety of GCS processes can be affected by the interactions among CO_2, brine, and rocks.[12] At the CO_2–water–rock interfaces, the injection of CO_2 would cause dissolution of minerals in storage and may result in precipitation of secondary minerals.[13] The wettability, pore structures, permeability of pre-existing rock, and the pH and compositions of brine could be changed.[6] These changes can affect the seal of CO_2, the capacity of storage, the injectivity of wells, and the transport of CO_2.[14]

Silicates and aluminosilicates are abundant minerals in sandstone, shale, and basalts, which are found often in GCS sites and other subsurface operation sites.[15] Considering the abundance and reactivity of silicates and aluminosilicates, their dissolution and subsequent precipitation can be important for understanding and predicting the capacity of storage and the seal of CO_2. In addition, these reactions also provide a driving force for the mineral trapping of CO_2. Therefore, this dissertation investigated the reaction of several representative silicates and aluminosilicates: Plagioclase is chosen as a model of minerals in reservoir rock and biotite is used as a model of minerals in caprock.

Plagioclase is the Na-Ca series feldspar. Feldspar is the most abundant mineral group and makes up 60% of the earth's crust. Plagioclase is one of the main components of sandstone,[10, 16, 17] and the main components of basalt.[13, 18, 19] Dissolution of plagioclase would affect the porosity of sandstone, and thus the capacity of storage. Plagioclase dissolution increases the pH and release

Ca. The brine pH affects the solubility of CO_2 in brine, and dissolution and precipitation of various minerals. Release of Ca from the dissolution of pre-existing minerals provides cations for the formation of $CaCO_3$, which contributes to the mineral trapping and could change surface properties, porosity, and permeability of rocks.

Biotite is the Mg and Fe-containing mica. Mica is a typical sheet silicate and is abundant in the caprock. Dissolution of biotite could change the vertical permeability of caprock, and thus affect the structural trapping. Biotite dissolution can lead to the mobilization of small sheet particles from the silicate sheets.[20] Release of Fe from biotite dissolution can lead to precipitation of Fe-(hydr)oxides.[20]

In addition to the dissolution and precipitation in the aqueous phase, this work also investigated the reactions in absence of liquid phase water. In subsurface environments, there can be contacting areas between CO_2 and caprock without the presence of brine.[21] In addition, the higher diffusivity and lower capillary entry pressure of $scCO_2$ allows it to diffuse in rocks easier than brine and enter the small pores that brine cannot enter. While CO_2 without dissolved water does not show significant reactivity,[22-27] water dissolved in CO_2 has higher reactivity than water in the aqueous phase.[21, 28, 29] Thus, water-bearing supercritical CO_2–mineral reactions are at least as important as reactions in aqueous phase.[21]

To investigate silicates reacting with water-bearing $scCO_2$, Wollastonite ($CaSiO_3$) was chosen as a model due to its simple compositions and high reactivity.[27, 30] Wollastonite has a similar structure with pyroxene, which is one of the main components of basalt.[18, 19] It could also be a representative of Ca-bearing and chain structural silicates. Wollastonite carbonation also traps CO_2 in carbonate. The carbonate and amorphous silica formed during the reaction cover the surface

3

of wollastonite, which can lead to changes in wettability. In addition, because the densities of the carbonate and amorphous silica are different from the density of wollastonite, when dissolution of wollastonite and secondary mineral precipitation occurs, it can cause volume change, and thus it is relevant to fracture opening or healing.

1.1.3 Co-sequestration of CO_2 and SO_2

A special situation considered in this work is the co-sequestration of CO_2 and SO_2. In carbon capture and sequestration (CCS), the cost of separating CO_2 and gas impurities and compressing the resultants have been estimated to account for 75% of the total cost of the process.[31] Sulfur dioxide is one of the main gas impurities, especially in emissions from hydrocarbon combustion.[31] Lowering the cost of acid gas separation by allowing a certain amount of impurities like SO_2 can, therefore, dramatically lower the overall cost. However, allowing too much SO_2 may cause unexpected impacts on the environmental safety of GCS operations. Therefore, scientific guidelines for the co-injected SO_2 are needed, and they require a better understanding of the potential effects of SO_2 co-injection on GCS operations.

1.1.4 Enhanced Oil Recovery

The cost of GCS can be further reduced when GCS is combined with enhanced oil recovery.[5] CO_2 is used to displace the oil, and improve the oil production. After oil extraction, CO_2 can be stored in the oil reservoir. The efficiency of EOR are strongly affected by wettability and porosity.[32] Therefore, the dissolution of silicates and aluminosilicates and precipitation of carbonates could affect not only the performance of GCS, but also the recovery of oil. Compared with the saline aquifer, the oil reservoir is more abundant with organic compounds. In addition, $scCO_2$ is a better solvent for organic compounds, compared with water.[33] The injection of CO_2

could extract large amounts of organic compounds, and increase their concentrations in brine. A recent report from the Frio formation suggested that 34 days after the termination of scCO$_2$ injection, the concentrations of several organic compounds increased by a factor of 100.[34] It is critical to understand the impact of organic compounds on the geochemical reactions at CO$_2$–water–rock interfaces.
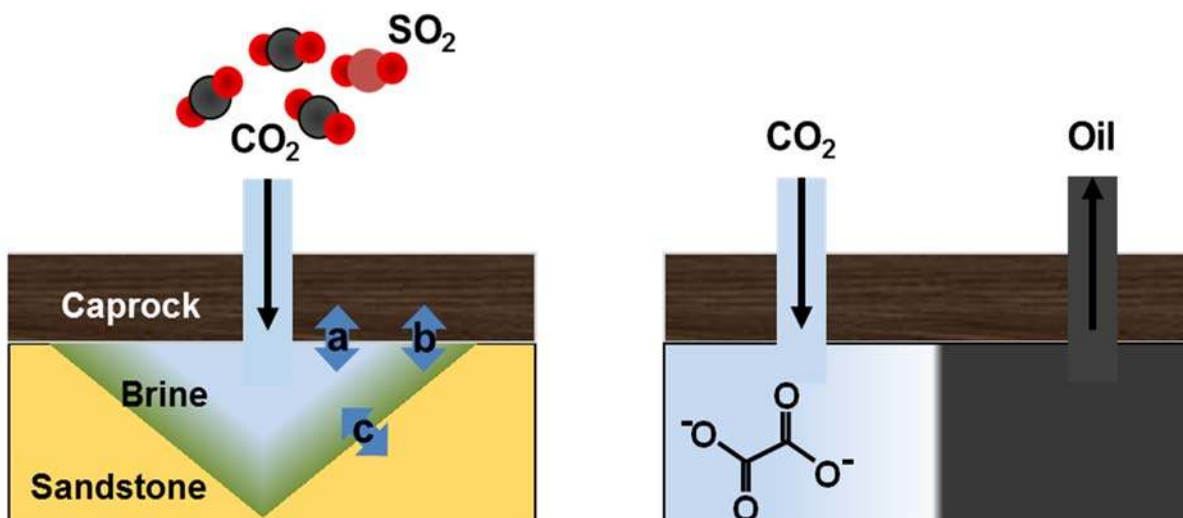
Figure 1.1. Schematic diagram of the system considered in this work. Left side is a diagram depicting CO$_2$-SO$_2$ co-sequestration in saline aquifer. a. Silicate carbonation in water-bearing scCO$_2$; b. Caprock dissolution in CO$_2$-acidified brine; c. Sandstone dissolution in CO$_2$-acidified brine. Right side is a schematic diagram of enhanced oil recovery. The reservoir is more abundant with organic compounds.

1.2 Research Objectives

1.2.1 Limitations of Previous Studies

Our current understanding of geochemical reactions at CO$_2$–water–rock interfaces is far from enough to predict their chemical impacts on GCS processes. Previous studies have investigated the reaction of rock from selected field site under simulated GCS conditions.[35, 36] However, because the mineral compositions vary between different reservoirs. Those results have very limited applicability to other field sites. In addition, because the rock contains many different

minerals, it is hard to deconvolute the role of each mineral species. Consequently, these studies of multi-mineral systems cannot contribute to a database of geochemical reactions at the CO_2–water–rock interfaces. Due to the lack of accurate database, the geochemical modeling suffers from large uncertainties in predicting the pathways and the kinetics of reactions experimentally observed.[37] For these reasons, the approach of current studies is to study the reaction of single silicate and aluminosilicate under simulated GCS conditions.

For the dissolution of aluminosilicate in brine (with liquid phase water), the effects of cations are not well understood. Previously, the dissolution of aluminosilicates has been extensively studied because the weathering of aluminosilicates is an important geochemical process.[38-40] In those studies, the dissolution rate is usually modelled as a function of pH, temperature, and ΔG.[39] One of the limitations of these previous studies is that they focused on the surface environment conditions. A major difference between the surface environment conditions and the GCS conditions is the high salinity in the brine in subsurface environments. A previous study has shown that Na can significantly affect dissolution of plagioclase.[41] However, the concentration applied in previous study is limited to < 0.1 M.[41] In contrast, the Na concentrations can vary between 0.01–3 M in formation brine.[42] Thus, a knowledge gap exists since we do not know the effect of high concentration Na on dissolution of plagioclase. In addition, Ca is also abundant in formation brine with 0–1 M concentrations reported.[42] However, information on the Ca effects on plagioclase dissolution and how Ca would impact the Na effects when coexisting is limited.

The cations effects on biotite dissolution also remain unclear. Previous studies showed that 1 M Na can enhance dissolution compared to DI water.[20] However, effects of other Na concentrations still remained unclear. Furthermore, Na was found to affect biotite dissolution

6

through ion-exchange with K.[20] The ion-exchange is also affected by K. Information on the K effect on biotite dissolution is also very limited. Another situation that has not been considered in previous studies is that the biotite in geologic formations may contact with formation brine and reach equilibrium with the Na in brine before CO_2 injection. The potential difference between the Na-equilibrated biotite and original K-biotite causes uncertainties in predicting the biotite dissolution in GCS sites.

Besides cations effects, more information about anions effects on geochemical reactions with minerals at GCS sites is needed. Previous studies on the SO_2 co-sequestration have predicted a decrease of pH and a formation of sulfate anions due to the dissolution and oxidation of SO_2.[43-46] While the reduction of pH was discussed,[47, 48] interestingly, the effects of sulfate anion were ignored. Sulfate is also naturally abundant in formation brine with concentrations up to 0.05 M reported. Its concentration can further increase with SO_2 co-injection.[43-46] Considering the significant effects of sulfate on the dissolution of Al- and Fe-(hydr)oxides reported in previous studies under surface environmental conditions (i.e., ambient pressure and temperature),[49-52] it is critical to understand the sulfate effects on plagioclase dissolution. In addition, previous studies found that carboxylic acid ligands such as oxalate can enhance the dissolution of plagioclase by surface complexation.[53] However, the potential competence between oxalate and co-existing anions like sulfate has not been considered.

Compared to the mineral dissolution in CO_2-acidified liquid phase water, fewer studies examined the carbonation of silicates in water-bearing $scCO_2$. Previous studies used different size particles.[30, 54-62] Without knowing the effects of particle sizes, the results obtained in previous studies are not comparable. More importantly, previous studies used nano- or micro-sized particles.[30, 54-62] It is uncertain whether the findings can be applicable to different sized mineral

grains in field sites. Further, there is a lack of systematical investigation of different parameters including temperature, pressure, and water saturation conditions. Moreover, the minerals in field sites can experience varying conditions, because the temperature, pressure, and water saturation would change during and after CO_2 injection. To address this knowledge gap, this study sought to understand the historic effects of samples reacted in one condition to another different condition on their net mineral dissolution.

1.2.2 Specific Objectives

The overall objective of this study was to improve our understanding of CO_2–water–rock interactions. Specifically, Objective 1 was to elucidate the impact of cations (e.g., Na, Ca, and K) in brine on the dissolution of plagioclase and biotite. Objective 2 was to investigate the influence of anions (i.e. sulfate and oxalate) in brine on the dissolution of plagioclase. In addition to effects of ions in brine, in Objective 3, water-bearing $scCO_2$ systems were tested to study the carbonation of silicates. In the water-bearing $scCO_2$ systems, we focused on improving our understanding of the role of particle sizes, water, temperature, and pressure on the carbonation of wollastonite.

Objective 1: Elucidate effects of cations on plagioclase and biotite dissolution under GCS conditions.

Hypothesis 1.1: Na inhibits dissolution of plagioclase by competing with proton adsorption on mineral surfaces. Ca competes with Na when co-existed.

Hypothesis 1.2: Na enhances dissolution of biotite by ion-exchange with interlayer K. Aqueous phase K suppress the Na-K ion-exchange and inhibit the biotite dissolution.

Objective 2: Investigate effects of anions on plagioclase dissolution and subsequent secondary precipitation under GCS conditions.

Hypothesis 2: Sulfate and oxalate can enhance plagioclase dissolution by surface complexation with Al on surface and inhibit secondary precipitation by aqueous complexation with Al^{3+} and decrease the saturation ratio of Al-containing mineral. Oxalate will suppress the effect of sulfate when co-existed.

Objective 3: Examine effects of particle sizes, water saturation conditions, temperature, and pressure on wollastonite carbonation in water-bearing $scCO_2$ under GCS conditions.

Hypothesis 3: Reaction extent of wollastonite in water-bearing $scCO_2$ is controlled by the kinetics of the hydrolysis of wollastonite and will be higher with smaller particle size, more water, and higher temperature and pressure.

1.3 Dissertation Overview

In pursuit of the three objectives above, three tasks were completed. **Task 1** corresponds to **Objective 1**, examining the impacts of high concentration Na and other cations including Ca and K on the dissolution of plagioclase and biotite. The outcomes extend the findings in previous studies on silicates weathering in surface environment to the high salinity conditions in formation brine. **Task 2** addressed **Objective 2** and elucidates the role of sulfate anions and oxalate on the plagioclase dissolution. The findings improve our knowledge on the CO_2–water–rock interactions during CO_2–SO_2 co-sequestration and EOR. **Task 3** corresponds to **Objective 3** and systematically investigated the effects of particle sizes, water, temperature, and pressure and their alteration history of experimental conditions on the wollastonite carbonation in water-bearing $scCO_2$. The

results link the findings in previous studies to the field sites and provide fundamental information on silicate carbonation for CO_2 storage and utilization as metal carbonate formation.

Task 1 is addressed in **Chapter 2 and 3**. The dissolution rates of plagioclase and biotite powders were measured using batch reactor at 35–90 $^{\circ}$C and 100 bar, conditions relevant to GCS. Na concentrations of 0–4 M have been used to represent the high Na concentrations in formation brine. For plagioclase dissolution, Ca concentrations from 0–1 M was used. For biotite dissolution, K concentrations from 0–10 mM was applied. Na-biotite were prepared by extracting interlayer K from biotite powders using NaCl solutions. In addition to the powder samples, biotite flake samples were used to allow surface characterization using atomic force microscopy (AFM). The secondary precipitations were characterized using transmission electron microscopy (TEM).

Task 2 is addressed in **Chapter 4**. Effects of 0.05 M sulfate anion on plagioclase dissolution were investigated at 90 $^{\circ}$C and 100 bar. The surface complexation between sulfate and plagioclase surfaces was measured using attenuated total reflection-Fourier transformed infrared spectroscopy (ATR-FTIR). The results were compared to the prediction based on density functional theory (DFT) calculations. The secondary precipitations were characterized using scanning electron microscopy (SEM) and TEM. In addition, the effects of 10 mM oxalate on plagioclase dissolution were investigated at 90 $^{\circ}$C and 100 bar. The co-existing oxalate and sulfate were also examined.

Task 3 is addressed in **Chapter 5 and 6**. To investigate the particle size effect, the carbonation of five different size wollastonite particles at 60 $^{\circ}$C and 100 bar have been quantified. Experiments at 35–93 $^{\circ}$C, 25–125 bar, and $0–14 \times S_w$ water saturation (S_w represents the amount of water needed for 100% saturation in $scCO_2$), have been conducted using selected particle size. To

examine the role of varying conditions, sample initially reacted at 35 °C was resubmitted to the reaction at 60 °C, and the sample initially reacted at 60 °C further reacted at 35 °C. Similar to the varying temperatures, varying pressure and water saturation were also investigated using 50 and 100 bar, and 100% and $45 \times S_w$ water saturation.
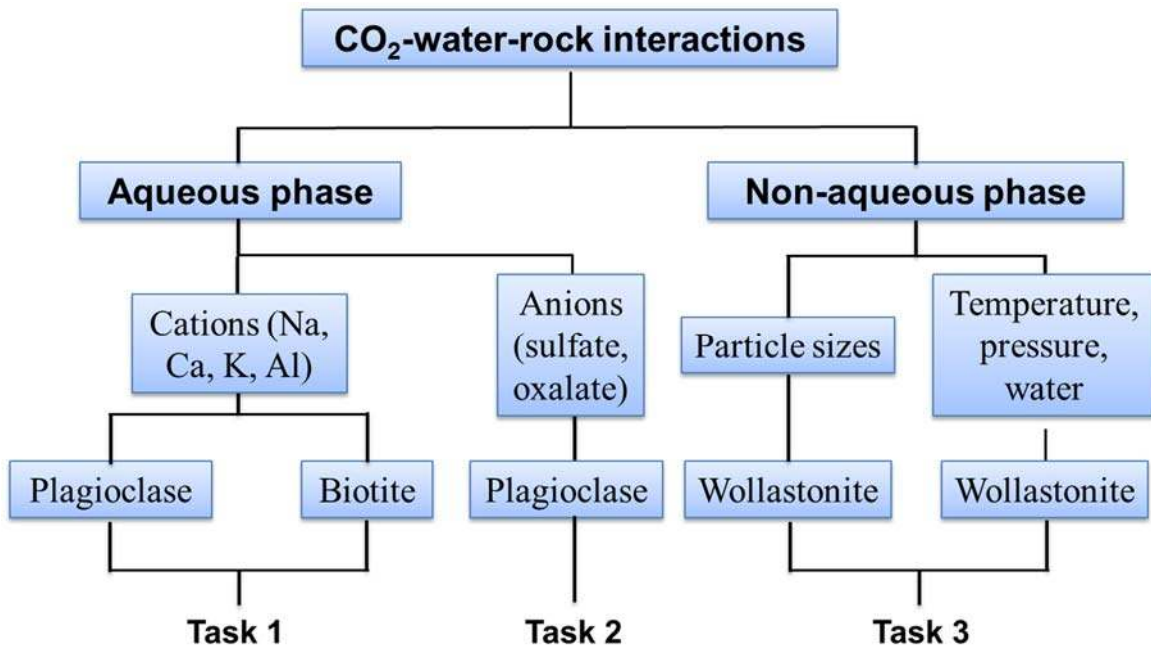
Figure 1.2. Summary of Tasks in this dissertation.

Finally, in **Chapter 7**, the main conclusions and implications of the current studies are summarized and future directions are suggested.

Chapter 2: Anorthite Dissolution under Conditions Relevant to Subsurface CO_2 Injection: Effects of Na^+, Ca^{2+}, and Al^{3+}

Abstract

Supercritical CO_2 is injected into subsurface environments during geologic CO_2 sequestration and CO_2-enhanced oil recovery. In these processes, the CO_2-induced dissolution of formation rocks, which contain plagioclase, can affect the safety and efficiency of the subsurface operation. In subsurface brines, Na^+ and Ca^{2+} are naturally abundant, and Al^{3+} concentration increases due to acidification by injected CO_2. However, our current understanding of cation effects on plagioclase dissolution does not provide sufficiently accurate prediction of plagioclase dissolution at such high salinities. This study investigated the effects of up to 4 M Na^+, 1 M Ca^{2+}, and 200 μM Al^{3+} on anorthite (as a representative mineral of Ca-containing plagioclase) dissolution under conditions closely relevant to subsurface CO_2 injection. For the first time, we elucidated the inhibition effects of Al^{3+} on anorthite dissolution in far-from-equilibrium systems, and found that the Al^{3+} effects were enhanced at elevated temperature. Interestingly, Na^+ inhibited anorthite dissolution as well, and the effects of Na^+ were 50% stronger at 35 °C than at 60 °C. Ca^{2+} had similar effects to those of Na^+, and the Ca^{2+} effects did not suppress Na^+ effects when they coexisted. These findings can contribute to better predicting plagioclase dissolution in geologic formations and will also be helpful in improving designs for subsurface CO_2 injection.

2.1 Introduction

Several energy-related engineering processes inject CO_2 into subsurface environments. For example, geologic CO_2 sequestration (GCS) is a promising method to mitigate global climate change. In GCS, CO_2 is captured from point sources, such as large power plants, then pressurized and injected into geologic formations, including deep saline aquifers and depleted oil and gas reservoirs.[5] As a more economically viable option, CO_2–enhanced oil recovery (EOR) injects CO_2 into oil reservoirs to improve oil production.[3]

These subsurface engineering processes can be affected by the CO_2-induced dissolution of minerals, such as plagioclase, in field sites.[14] Plagioclase forms 39% of the Earth's crust and occurs in sandstone and basalts, which are potential formations for CO_2 storage.[10, 13] For instance, the reported fractions of plagioclase are 19.8% and 12.3% in the Frio and Sleipner CO_2 injection sites, respectively.[63, 64] The chemical formula for plagioclase is $Na_{1-x}Ca_xAl_{1+x}Si_{3-x}O_8$, where x is anorthite content. Anorthite is the plagioclase member with x > 0.9. While Na-rich members of plagioclase, such as albite, occur in sedimentary rocks, Ca-rich members of plagioclase, such as anorthite, are more abundant in basic igneous rock, and are important in Ca release during various geochemical processes.[65] Simultaneously releasing cations, their dissolution can increase pH, leading to secondary mineral precipitation and promoting mineral trapping of CO_2.[66] More importantly, in even less time than required for CO_2 mineral trapping, dissolution of plagioclase and subsequent secondary mineral precipitation can occur and change the wettability and porosity of reservoir rocks,[67] in turn affecting the transport of CO_2, oil, and gas. Therefore, the dissolution of plagioclase is important in understanding the safety and efficiency of CO_2 injection in subsurface environments.

High concentrations of cations in naturally existing brine in formations (e.g., reported maximum concentrations of 3.4 M Na^+ and 1.2 M Ca^{2+})[42] can affect the dissolution of plagioclase. In our previous studies of mica dissolution under conditions relevant to GCS, we observed that Na^+ and Ca^{2+} can significantly enhance the dissolution of phlogopite and biotite.[29, 68] Furthermore, with the injection of CO_2, the brine pH in formations can decrease to as low as 3–5,[15] which can sustain higher concentrations of Al^{3+}(aq) than neutral pH. More specifically, according to our thermodynamic calculations using Geochemist's Workbench (GWB, Release 8.0, RockWare, Inc.), at 25 °C and pH 3 and 6, the maximum concentrations of aqueous Al^{3+} without precipitation are 0.23 molal and 1.26 nano-molal, respectively.

However, information about the effects of cations on plagioclase dissolution available in recent literature is not sufficient to accurately predict the situations in geologic formations. Stillings and Brantley reported that dissolution of plagioclase was significantly inhibited by Na^+ at 25 °C and pH = 3,[69] because Na^+ adsorption competed with proton adsorption on the surface of plagioclase, and thus inhibited the proton-promoted dissolution. They predicted that other cations can have similar effects.[41] Thus, it can be expected that Ca^{2+} inhibits the dissolution of anorthite in the same way as Na^+, because Ca^{2+} adsorption on the mineral surface is preferred over Na^+ adsorption.[70] In contrast, Oelkers and Schott reported that dissolution of anorthite was not significantly affected by Ca^{2+} at 45–95 °C and pH 2.4–3.2.[71] Moreover, the Na^+ and Ca^{2+} concentrations used in these previous studies were limited to < 0.1 M.[41, 69, 71-73] However, high ionic strengths will affect the activity of cations and the Gibbs free energy (ΔG) of plagioclase dissolution, suppress the electric double layer, and change water structures on mineral surfaces.[74-76] With these potential uncertainties, it is unclear whether results obtained in previous studies can be extended to high ionic strength ranges.

Another complication concerning the effects of Na^+ and Ca^{2+} on plagioclase dissolution is the co-existence of Na^+ and Ca^{2+}. A previous study on quartz dissolution found that Ca^{2+} dominated the overall effect when it co-existed with Na^+.[77] However, to the best of our knowledge, no similar study can be found for plagioclase. Therefore, an improved understanding of the effects of co-existing Na^+ and Ca^{2+} on the dissolution of plagioclase is needed to predict the dissolution rates in complex brine chemistries.

An additional uncertainty lies in the effects of Al^{3+} and ΔG on anorthite dissolution. Al^{3+} is a product of plagioclase dissolution and can affect the ΔG of the dissolution. Oelkers and Schott found the dissolution rate of anorthite is not affected by Al^{3+} in a ΔG range from -115 to -65 kJ/mol at 45–95 °C and pH 2.4–3.2.[71] This finding is different from the decreasing dissolution rate with $\Delta G > -200$ kJ/mol at 50 °C and pH 2.7–3.0 observed by Sorai and Sasaki.[78] Such different observations lead to difficulties in understanding and predicting the effects of Al^{3+} and ΔG on anorthite dissolution.

The goal of this study is, therefore, to elucidate the effects of Al^{3+} and ΔG, and the effects of high concentrations of Na^+ and Ca^{2+} and their co-existence on anorthite dissolution. We investigated the effects of 0–200 μM Al^{3+}, 0–4 M Na^+, and 0–1 M Ca^{2+} on the dissolution of anorthite at conditions closely relevant to subsurface CO_2 injection scenarios. The results can contribute to advancing our knowledge of plagioclase dissolution in many subsurface engineering operations where high salinity is present.

2.2　Experimental Section

2.2.1　Minerals and chemicals

Natural anorthite samples (Miyake Island, Izu Archipelago, Tokyo Prefecture, Japan) were purchased in cm size pieces coated with lava. The specimens were crushed to mm size pieces. Pieces without coating were picked out manually, cleaned by sonication in water, dried in nitrogen, then ground and sieved. Particles with sizes between 53 to 106 microns were used. Based on X-ray fluorescence, the chemical formula was determined to be $Na_{0.04}Ca_{0.95}Al_{1.94}Si_{2.06}O_8$ (Table 2-S1). The specimens were characterized by high resolution X-ray diffraction (HR-XRD) in our previous studies.[79] According to BET measurement (AX1C-MP-LP, Quantachrome Instruments), the specific surface area was 0.1707 m^2/g.

All chemicals used in this study were at least ACS grade, and all the solutions were prepared using ultra purified water (Barnstead, resistivity > 18.2 MΩ•cm). Na^+ and Ca^{2+} were added as NaCl (BDH) and $CaCl_2$ (BDH) solutions. Al^{3+} and Si were added as $AlCl_3$ (Alfa Aesar) solution and sodium silicate solution (Sigma-Aldrich). Trace metal HCl (BDH) was used to adjust the pH.

2.2.2　Dissolution experiments under simulated GCS conditions

Dissolution experiments were conducted in a 300 mL Hastelloy C-276 vessel (Parr Instruments, Moline, IL), used in our previous studies.[80] A pH probe (Corr Instrument, TX) that can function under 1–136 atm and 20–120 °C was used to monitor *in situ* pH. For most experiments, duplicate experiments were conducted for up to 80 hours. Descriptions of the high pressure and temperature reactor system and the pH probe calibration and measurement are available in S1 and S2 of the Supporting Information.

The conditions (35–90 °C and 100 atm CO_2) used in this study are within the range of conditions in subsurface CO_2 injection sites (31–110 °C, 73.8–600 atm).[10] For example, 37 °C and 100 atm were observed at the Sleipner site,[64] 65 °C and 150 atm in the Frio formation,[34] and 63 °C and 140 atm at the Weyburn field site.[81] The experimental conditions are also comparable with the 30–130 °C and 90 atm used in a recent laboratory study by Carroll and Knauss on water–plagioclase interactions.[82] Carroll and Knauss also suggested that elevated CO_2 pressure affects plagioclase dissolution indirectly by changing pH.[82] Thus, we can focus on the effects of cations by using the same pH and same pressure for different concentrations of cations. For chosen sets, while all other conditions were maintained, we tested temperature effects. The concentrations of Na^+, Ca^{2+}, and Al^{3+} used in the current study were 0–4 M, 0–1 M, and 0–200 μM, respectively, while we kept the experimental pressure the same (i.e., 100 atm CO_2).

To make sure the pH conditions were the same, HCl was added to the solutions. The measured pH was tuned to 3.10 and 2.94 for the Na^+ and Ca^{2+} experiments, respectively. These pH values are the *in situ* pH values of 1 M NaCl and 1 M $CaCl_2$ without added HCl at 35 °C and 100 atm CO_2. We chose these pHs for the following reasons: First, a pH of 3 is more related to the early period of CO_2 injection, which starts the mineral dissolution process, or to sites close to injection wells, while the pH in field sites would be buffered to 4.5 to 5.5 after a long time. Second, to thoroughly investigate the effects of cations on dissolution, we need a system without precipitation, which is difficult to achieve for pH > 4, because Al precipitation forms very easy. Third, pH ~3 is the *in situ* pH of CO_2 acidified brine without any additional salts. To increase pH to 4.5 to 5.5, we would need to add base solutions, which would introduce extra cations. It would be difficult to deconvolute the effects of the cations we want to study and the extra cations used to tune the pH. We expect that a similar mechanism of cation effects would happen for both the pH

18

~3 used in the current study and other acidic pH conditions. Within 80 hours, no significant change (± 0.02) in pH was observed at the highest solid to liquid ratio applied in this study. For Al experiments, pH was tuned to same value, 2.97, for the same reason as above, and this will also prevent any precipitation.

To obtain proper solid/liquid ratios (mass to volume ratio) to investigate Na^+ and Ca^{2+} effects, solid/liquid ratios from 0.005 to 0.05 g/L were tested. For all conditions used in this study, the tested solid/liquid ratios were low enough that no secondary precipitation formed.[80] While we did not attempt to simulate the solid/liquid ratios at field sites, by using such low solid/liquid ratios, we could focus on cations effects on the dissolution without influence from secondary precipitation.

For each sample, 1–2 mL solution was collected and immediately acidified with 20 μL of 67–70% nitric acid (BDH). Samples were analyzed using an inductively coupled plasma-optical emission spectrometer (ICP-OES) (Perkin Elmer, Optima 7300DV). The concentrations of Si, Al, and Ca are shown in Table 2-S3. In this study, overall, steady-state congruent dissolution of anorthite was obtained. Detailed information about the determination of the dissolution rate is available in S3 of Supporting Information. The activities of aqueous species, ΔG, and pH were calculated using the THERMO.com.v8.r6+ database in Geochemist's Workbench (GWB, Release 8.0, RockWare, Inc.), which uses the B-dot equation for the calculation of activity coefficients of aqueous species with ionic strengths up to 3 M. The solubility of CO_2 was calculated according to a published model by Duan and Sun, which can be applied to up to 4.5 molal NaCl and $CaCl_2$.[83] More details about ΔG calculations are also available in the Supporting Information (S4).

2.3   Results and Discussion

In the following sections, to determine suitable solid/liquid ratios to investigate cation effects, we first investigated the effects of solid/liquid ratios on anorthite dissolution rate. Then, to explain the observed effects of the solid/liquid ratio, we investigated the effects of Al^{3+} and ΔG on dissolution. By doing so, we found that the Al^{3+} effect, rather than ΔG effect, was more responsible for the solid/liquid ratio effect. Finally, with an optimized solid/liquid ratio that minimized the effects of Al^{3+}, we examined the effects of Na^+ and Ca^{2+}.
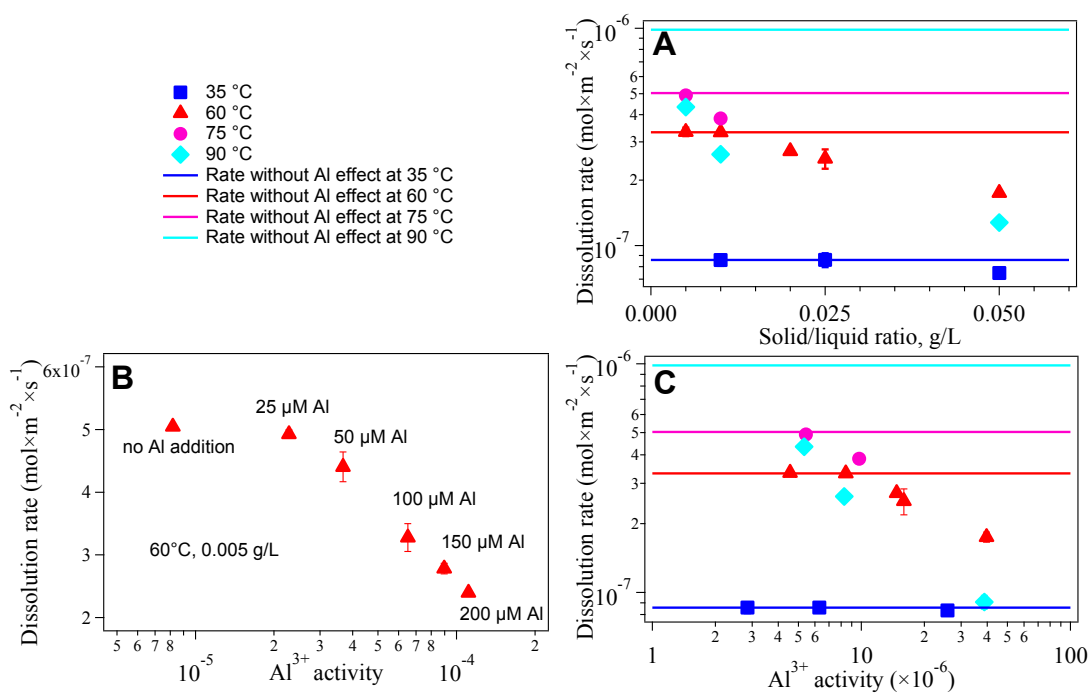
Figure 2.1. (A) The Si-based dissolution rate of anorthite at different solid/liquid ratios at 35, 60, 75, and 90 °C and 100 atm CO_2. The error bars show the results of duplicate experiments. At 35 °C, the dissolution rate is not significantly affected by the solid/liquid ratio within 0.005 to 0.05 g/L. At 60 °C, 0.005 and 0.01 g/L do not show significant differences in dissolution rate, while the dissolution rate decreases beyond 0.01 g/L. At 75 and 90 °C, the dissolution rate decreases significantly with a larger solid/liquid ratio. The horizontal lines are the dissolution rates at different temperatures without the Al^{3+} effect, calculated by applying the activation energy determined in this study. **(B)** The Si-based dissolution rate of anorthite at different concentrations of Al^{3+} at 60 °C, 100 atm CO_2, and a solid/liquid ratio of 0.005g/L. The rate is almost not affected by < 25 μM Al^{3+}. Beyond 25 μM Al^{3+}, the log rate gradually becomes linearly decreasing with log Al^{3+} activity. **(C)** The Si-based dissolution rate of anorthite at different Al^{3+} activities corresponding to the solid/liquid ratios in (A).

20

2.3.1 Inhibited anorthite dissolution at high solid/liquid ratios

To identify the optimum solid/liquid ratio for investigating cation effects, we measured the Si-based dissolution rates at different temperatures, using solid/liquid ratios from 0.005 to 0.05 g/L (Figure 2.1). At 35 $^{\circ}$C, the dissolution rate was not significantly affected by the solid/liquid ratios that we used. At 60 $^{\circ}$C, 0.005 and 0.01 g/L showed similar dissolution rates. But as the solid/liquid ratio was further increased, the dissolution rate gradually decreased. At 75 $^{\circ}$C, the dissolution rate at a solid/liquid ratio of 0.01 g/L was 22% lower than that at 0.005 g/L. At 90 $^{\circ}$C, the effects of the solid/liquid ratio became even more significant: the dissolution rate at a solid/liquid ratio of 0.01 g/L was 39% lower than that at 0.005 g/L, and the dissolution rate became even lower than those at 60 and 75 $^{\circ}$C. These trends can be explained by different solid/liquid ratios leading to different concentrations of Al^{3+} and different ΔG.

2.3.2 Inhibited anorthite dissolution by Al^{3+}

To explain the effect of solid/liquid ratios on anorthite dissolution rates, we investigated the effects of Al^{3+} on anorthite dissolution by adding up to 200 μM Al^{3+}. This concentration is the maximum Al^{3+} concentration that does not lead to precipitation at pH 3 and 60 $^{\circ}$C, based on the prediction of GWB. The smallest fixed solid/liquid ratio (0.005 g/L) was used. The dissolution rate of anorthite decreased with increasing Al^{3+} activity (Figure 2.1B). Within our batch reactor, the Al^{3+} concentrations changed by Al release from anorthite. The Al^{3+} activities were calculated based on the average concentrations before and after reaction, which can better reflect the actual Al^{3+} concentrations in our batch system during the sampling period. The changes in Al^{3+} concentrations were within 12.5 μM. We also found that Al^{3+} concentrations < 25 μM did not have significant effects on anorthite dissolution, while inhibition effects were evident with > 25 μM Al^{3+} (Figure 2.1B). This observation is different from the absence of Al^{3+} effect on anorthite at

21

45–95 °C observed by Oelkers and Schott.[71] In this study, we found that 200 μM Al^{3+} decreased the dissolution rate by approximately 50% compared with no Al^{3+} addition (Figure 2.1B). Such a difference in dissolution rate is within the error range in Oelkers and Schott's work. Another potential reason for the different observations between Oelkers and Schott's work and ours is the different pH used. The pH in Oelkers and Schott's work was 2.5 to 2.6, which is lower than the value of 2.97 used in our work. With 237–295% more abundant protons, we expect correspondingly more Al^{3+} is needed to achieve the same extent of inhibition effect. As a result, the Al^{3+} effect may have been even weaker in Oelkers and Schott's study, and thus hidden in the error range. Another possible explanation is the different anorthite species used. We used specimens with 94% anorthite content ($Na_{1-x}Ca_xAl_{1+x}Si_{3-x}O_8$, x = 0.94), while 96% anorthite (Hokkaido, Japan) was used in Oelkers and Schott's study. A slight change in anorthite content within 90% and 100% can lead to significant changes in the kinetics of dissolution.[84] It is possible that the Al^{3+} effect was weaker in Oelkers and Schott's study due to a slightly higher anorthite content.

Understanding Al^{3+} effects on anorthite dissolution provides valuable insight on the dissolution mechanism of the plagioclase series. Recent studies found that Al^{3+} can significantly inhibit the dissolution of plagioclase.[85, 86] Chen and Brantley explained the effects of Al^{3+} on plagioclase dissolution by competing adsorption with protons.[85] In contrast, Oelkers and Schott explained the Al^{3+} effects on most plagioclase dissolution, except anorthite, by the back reaction of Al^{3+}.[86] The dissolution rate was thought to be controlled by precursors consisting of the Si structure left in plagioclase by the dissolution of Al sites, and the dissolution of Al sites in plagioclase was considered as being reversible. So high concentrations of Al^{3+} would enhance the back reaction, decrease the surface concentrations of precursors, and in turn decrease the

22

dissolution rates. Later, Oelkers and Schott observed the absence of Al^{3+} inhibition effects on anorthite and explained that the concomitant dissolution of Si with Al was responsible.[71] In anorthite, the Al/Si ratio is nearly 1:1. All of the four neighbor cations of almost every Si are Al. Thus, after Al sites are dissolved, all four chemical bonds connected to the Si sites are broken. The Si sites are concomitantly dissolved, with no precursors left. Oelkers and Schott concluded that the dissolution rate of anorthite is controlled by the dissolution of Al sites, rather than by the precursor, as in the case of other plagioclases with smaller Al/Si ratios.[87] However, specimens with 100% anorthite content are quite rare in natural environments. For many real anorthite samples, the Al/Si ratio is not exactly 1:1.[71, 78] Not all the Si sites dissolve concomitantly with Al sites. There is still Si structure left, which is similar to the precursor in other plagioclases. Thus, a recent modeling study has reported that these small amounts of Si precursor must be considered to predict anorthite dissolution rate.[84] In other words, although the role of Si sites in anorthite dissolution is relatively small compared with other plagioclases, anorthite dissolution is not solely determined by Al sites. This suggests that the dissolution mechanism of anorthite is not fundamentally different from other plagioclases, and that Al^{3+} inhibition effects are applicable to the whole plagioclase series. In addition, it is necessary to point out that the different bond strengths of Al and Si sites do not mean their overall release rates would be incongruent. The dissolution of Si precursor is the rate-controlling step, which limits the progress of plagioclase–water interfaces and, therefore, controls the contact between Al sites and water. Thus, congruent dissolution would be reached. Furthermore, based on our experimental data (Figure 2.1C), the Al^{3+} effects can explain the observed effects of solid/liquid ratios. At higher solid/liquid ratios, the Al^{3+} concentration is higher, and thus has stronger inhibition effects.

Constant dissolution rates at ΔG < -107 kJ/mol. However, Al^{3+} effects may not be the only explanation for the observed trend of anorthite dissolution rates as a function of the solid/liquid ratio. The effects of solid/liquid ratios may also result in changes in ΔG. Al^{3+} is one of the products of anorthite dissolution, and the addition of Al^{3+} can also change the ΔG of the dissolution reaction. Sorai and Sasaki reported ΔG can affect the anorthite dissolution rate even when ΔG is as small as -200 kJ/mol at 50 °C and pH 2.7–3.0.[78] If a similar situation was present in our system, the effects of Al^{3+} and the solid/liquid ratio that we observed could be attributed to the ΔG effect.
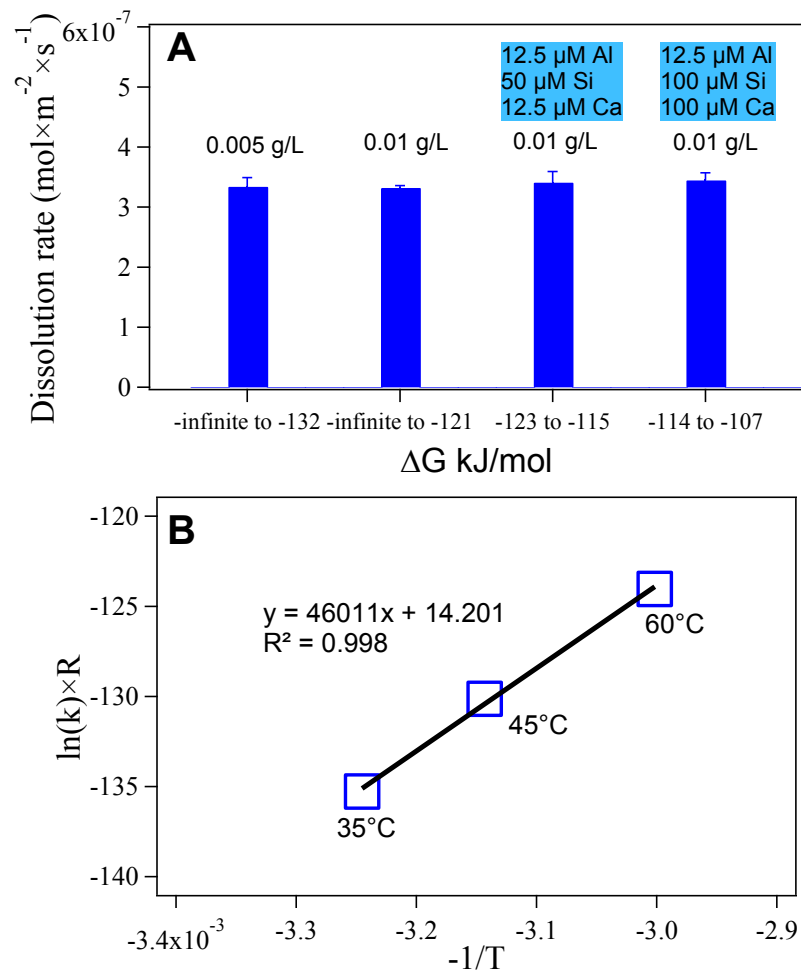
Figure 2.2. (A) The Si-based dissolution rate of anorthite at different ΔG at 60 $^{\circ}$C and 100 atm CO_2. The ranges from -infinite to -131.7 kJ/mol and from -infinite to -121.3 kJ/mol are the ΔG at the beginning and the end of experiments with 0.005 and 0.01 g/L solid to liquid ratios, respectively. The -123.2 to -115.1 kJ/mol data was achieved by the addition of 12.5 μM Al^{3+}, 50 μM $SiO_2(aq)$, and 12.5 μM Ca^{2+}. The -114.1 to -107.2 kJ/mol data was achieved by the addition of 12.5 μM Al^{3+}, 100 μM Si, and 100 μM Ca^{2+}. The similar dissolution rates at different ΔG mean that the rate is not affected by $\Delta G < -107$ kJ/mol at 60 $^{\circ}$C. **(B)** The apparent activation energy of anorthite dissolution at pH 3.1. The calculation is based on dissolution rates determined within 40 hours at 35, 45, and 60 $^{\circ}$C. The E_a is determined to be 46 kJ/mol.

To study the effects of ΔG on anorthite dissolution, the dissolution products of anorthite, Al^{3+}, Ca^{2+}, and $SiO_2(aq)$, were added to our system to make different ΔG. According to the Al^{3+} effects we measured, the addition of < 25 μM Al^{3+} will not significantly decrease the dissolution rate at 60 $^{\circ}$C. When we added 12.5 μM Al^{3+} + 50 μM $SiO_2(aq)$ + 12.5 μM Ca^{2+}, the initial ΔG was -123.2 kJ/mol; for 12.5 μM Al^{3+} + 100 μM $SiO_2(aq)$ + 100 μM Ca^{2+}, the initial ΔG was -114.1

kJ/mol. At the end of the experiments, the ΔG were -115.1 and -107.2 kJ/mol, respectively. The dissolution rates are the same for these two ΔG ranges, and also the same as the rates measured using solid/liquid ratios of 0.005 and 0.01 g/L without any additional cations (Figure 2.2A). For these two solid/liquid ratios, the ΔG started with - infinite and ended with -131.7 and -121.3 kJ/mol, respectively. Our results suggest that the dissolution rate of anorthite is not affected when $\Delta G < -107.2$ kJ/mol at 60 ${}^{\circ}$C and pH 3 (Figure 2.2A).

Our observations of no significant ΔG effect are different from the ΔG effect observed at 50 ${}^{\circ}$C and pH 2.7–3.0 in a recent study by Sorai and Sasaki.[78] Unfortunately, the specific concentrations of Al^{3+}, Ca^{2+}, and SiO_2(aq) used in their study are not available. While it is hard to make direct comparisons, potentially the decrease of dissolution rate at different ΔG observed in their study could be actually due to the different Al^{3+} concentrations. Another possible reason for the different observations is that the dissolution rate determined by surface characterization in their paper is very specific to the {001} crystal surface, unlike the rate measured by analyzing cation concentrations, which provides average values from dissolution of anorthite powder samples.

Based on the discussion above, we conclude that the effects of the solid/liquid ratio we observed at different temperatures are attributed to different Al^{3+}, rather than different ΔG. The injection of CO_2 will acidify the formation brine and cause dissolution of Al-containing minerals. The potential increase in Al^{3+} concentration could have significant effects on mineral dissolution. Hence, the information obtained in this study can help evaluate the impact of Al^{3+} on anorthite dissolution at CO_2 injection sites. In addition, the ΔG effect findings can help predict anorthite dissolution at field sites with a certain ΔG range.

Apparent activation energy of anorthite dissolution. As mentioned previously, the effects of Al^{3+} were not significant at 35 °C for solid/liquid ratios of 0.005, 0.01, and 0.05 g/L. At 60 °C, solid/liquid ratios of 0.005 and 0.01 g/L showed similar dissolution rates. Therefore, we assume that the effects of Al^{3+} are also not significant at an intermediate temperature, 45 °C, for solid/liquid ratios of 0.005 and 0.01 g/L. With the dissolution rates measured at these temperatures, we obtained the activation energy of anorthite dissolution without significant influence from Al^{3+} (Figure 2.2B). The 46.0 ± 2.2 kJ/mol obtained in this work is higher than the 18.4 kJ/mol measured in Oelkers and Schott's paper.[71] Most silicate dissolution reactions have activation energies ranging from 40 to 80 kJ/mol. Diffusion-controlled reactions have activation energies < 20 kJ/mol, and kinetic-controlled reactions have activation energies > 20 kJ/mol.[88] Plagioclase dissolution in a far-from-equilibrium system is controlled by surface reactions, so the activation energy we obtained is reasonable. The new apparent activation energy obtained can be useful in predicting the dissolution rates of anorthite at different depths, and thus different temperatures at field sites.

With the activation energy we obtained, we calculated the dissolution rate without effects of Al^{3+} at 75 and 90 °C (Figure 2.1; more details about activation energy calculation are available in Supporting Information S5). Combined with the dissolution rate we measured, it is obvious that the inhibition effects of Al^{3+} are more significant at higher temperatures. Unfortunately, we cannot provide quantitative information, because it is difficult to achieve the low solid/liquid ratio necessary for investigating Al^{3+} effects at > 60 °C. However, the rapid enhancement of the Al^{3+} inhibition effect at elevated temperatures indicates that Al^{3+} effects are particularly important for understanding plagioclase dissolution in high temperature energy-related subsurfaces.

2.3.3 Inhibited anorthite dissolution by Na^+
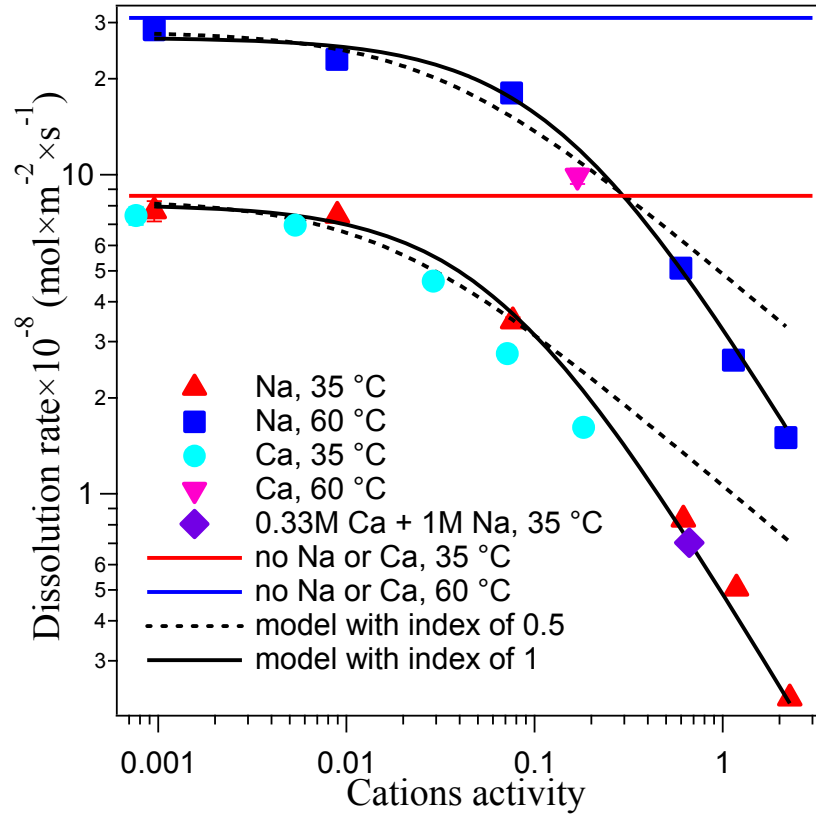
Cations and temperature	$k \times 10^6$	K_H	K_M	*n*	R^2
Na, 35 ºC	5.16	20.57	16.37	1[*]	0.9930
Na, 60 ºC	10.34	35.22	7.76	1[*]	0.9780
Ca, 35 ºC	5.45	18.42	23.78	1[*]	0.9950

[*]value fixed

Figure 2.3. The Si-based dissolution rates of anorthite at different concentrations of Na^+ and Ca^{2+} at 35 and 60 ºC and 100 atm CO_2 for 40 hr experimental time. The dissolution rates decrease significantly with increasing Na^+ activity. The Na^+ effects at 35 ºC are stronger than the Na^+ effects at 60 ºC. The effects of Ca^{2+} are very similar to the effects of Na^+. Ca^{2+} did not suppress the effects of co-existing Na^+. These effects are better predicted with the competing adsorption model with an index of *n* = 1 than by a recent model with an index of 0.5. The table shows the parameters of the fittings.

Based on our experimental results (Figure 2.1), the Al^{3+} effect on dissolution is not significant at low temperature. Thus at 35 and 60 ºC, we can minimize the influence of Al^{3+}, and focus on Na^+ and Ca^{2+} effects. By further minimizing the Al^{3+} effect by using a low solid/liquid

ratio (Table 2-S2), we tested the effect of Na^+ on the dissolution rate of anorthite at 35 and 60 ºC (Figure 2.3). NaCl concentrations of 0.001, 0.01, 0.1, 1, 2, and 4 M were used. The dissolution rates decreased significantly with increasing Na^+ activity, especially for Na^+ concentrations > 0.1 M NaCl. At 35 ºC, the dissolution rates without any added Na^+ were 2.45 times faster than the rates with 0.1 M Na^+, and were 35.8 times faster than the rates with 4 M Na^+. At 60 ºC, the dissolution rates without any added Na^+ were 1.89 times faster than the rates with 0.1 M Na^+, and were 24.6 times faster than the rates with 4 M Na^+. Apparently Na^+ effects at concentrations > 0.1 M NaCl are important in predicting the dissolution rates of plagioclase in CO_2 injection sites with high salinity. These results also showed that the effects of Na^+ become less significant with increasing temperature. This trend is different from the increasing effects of Al^{3+} with temperature. We postulate that this difference results from adsorption competition between cations and protons. Recent studies found that adsorption of alkali cations on oxides is mainly outer-sphere, and adsorption of transition metal cations and proton is inner-sphere.[41, 77] The formation of inner-sphere complexes needs to extensively disrupt the hydration sphere of cations, which usually has positive net enthalpy and entropy changes. The formation of outer-sphere complexes involves less disruption of hydration spheres, and has negative net enthalpy and entropy changes.[89] Thus, it is likely that the adsorption of Na^+ may be less sensitive to temperature, while the adsorption of protons is more temperature-sensitive. Hence, Na^+ inhibition effects became weaker at higher temperature. In contrast, Al^{3+} effects are more significant with increasing temperature, which suggests the adsorption of Al^{3+} increases more than the adsorption of protons at higher temperature, or that Al back reactions are favored at higher temperature. These suggested trends are consistent with a previous study that found a stronger adsorption of Al^{3+} than protons on plagioclase at higher temperature.[85] The different trends of Na^+ and Al^{3+} effects with temperature

observed in this study provide new information for predicting the impact of Na^+ and Al^{3+} on plagioclase dissolution at different reservoir depths and at sites with different temperatures.

To test the applicability of a recent feldspar dissolution model based on < 0.1 M NaCl data to the high concentration conditions, we fitted our results with a competing adsorption-based dissolution model described in Brantley and Stillings' paper, which suggested $n = 0.5$.[41] The fitting was conducted using the curve fitting toolbox in Matlab, which used least square non-linear fitting. The n values were fixed at 0.5 and 1. The values of k, K_H, and K_M were obtained from the fitting process.

$$rate = k(\frac{K_H a_H}{1+K_H a_H + K_M a_M})^n \tag{2.1}$$

where k is the rate coefficient, K_H and K_M are the adsorption constants for proton and cations, and a_H and a_M are the activities of proton and cation (M). This model is based on competing Langmuir adsorption between protons and M. $K_H a_H$ represents the proton adsorbed sites, and $K_M a_M$ represents the cation adsorbed sites. The 1 in the bracket of the equation represents sites with no adsorption. So the term in bracket is the fraction of proton adsorbed sites, which is responsible for plagioclase dissolution in acidic conditions.[41]

The fitting results of dissolution rates using this model are shown by the dotted line in Figure 2.3. The fitting using $n = 0.5$ is good at concentrations < 0.1 M NaCl. However, at higher concentrations, the fitting is less satisfactory (R^2 = 0.9603 and 0.9487 for 35 and 60 °C, respectively). The fitting is better with $n = 1$, shown by the solid line in Figure 2.3 (R^2 = 0.9930 and 0.9780 for 35 and 60 °C, respectively). The k, K_H, and K_M obtained using $n = 1$ are shown in the inset table in Figure 2.3. Due to the limited number of data points, rather than providing a correlation analysis among the parameters k, K_H, and K_M, the values obtained were applied only to

describe the trend of cation effects on plagioclase dissolution observed in this study. We noticed that Equation (2.1) with $n = 1$ is the same as the competing adsorption-based mineral dissolution model suggested in a recent paper by Ganor and Lasaga, which described the general inhibition mechanism of inhibitors, including cations, on mineral dissolution.[90] This model with $n = 1$ was also mentioned in Brantley and Stillings' paper.[41] They suggested that the index n should be 1 if only the sites at plagioclase–water interfaces contribute to the dissolution. Otherwise, the index n should be 0.5 if sites throughout the hydration layer on the plagioclase surface contribute to the dissolution, and if diffusion across the hydration layer plays a role. In our study, the fitting results are best when the index n is 1, indicating that the dissolution is surface reaction-controlled, with no significant diffusion-limited process included. In other words, the dissolution of anorthite in our experimental system should be limited to plagioclase–water interfaces, and not all the sites throughout the hydration layer contribute to the dissolution.

In Brantley and Stillings' study,[41] the index of 0.5 was suggested since the index of 0.5 can also conveniently be used to explain the pH dependence of plagioclase dissolution. Because the $K_{H}a_{H}$ term is usually small, the index of n is coincidently equal to the pH dependency if $K_{M}a_{M}$ is constant. However, to explain the overall plagioclase dissolution, we found that the index n in the equation (2.1) should be treated separately from the pH dependence of plagioclase dissolution. Furthermore, the 0.5 pH dependence is applicable only to plagioclase with anorthite content < 0.76. It is reported that pH dependence increases with anorthite content.[38] When the anorthite content increases to 0.76, pH dependence is 0.75.[91] When the anorthite content increases to nearly 1, the pH dependence of anorthite is 1.5, based on Oelkers and Schott.[71] In the current work, we estimated the pH dependence of anorthite to be 1.14, based on dissolution rates measured at 2.94 and 3.10 without any additional cations. The 1.14 obtained here is consistent with 1.12–1.14 at pH

= 2–5, 25–70 °C, as determined by several recent publications.[92-94] To describe the pH dependence

of plagioclase dissolution, we recently reported the pH dependence of plagioclase dissolution by

relating it to the anorthite content and the ordering state of the plagioclase crystal.[84, 91, 95] Because

equation (2.1) did not include these factors (e.g., anorthite content and crystal ordering), it can

properly describe only cations effects, not pH dependency. Therefore, we suggest that an index of

1 should be applied in equation (2.1) when one describes the Na^+ effect on anorthite dissolution in

high ionic strength systems. Furthermore, we propose that because the dissolution mechanism of

anorthite is not fundamentally different from other plagioclases, other plagioclases can also use

the index of 1 to predict the Na^+ effect on their dissolutions.

2.3.4 Inhibited anorthite dissolution by Ca^{2+} and its co-existence with Na^+

To investigate Ca^{2+} effects on anorthite dissolution, we first measured the dissolution rate

of anorthite with the addition of 0.001, 0.01, 0.1, 0.33, and 1 M $CaCl_2$, at 35 °C without significant

influence of Al^{3+} (Figure 2.3). The results suggested that the effects of Ca^{2+} on anorthite were very

similar to the effects of Na^+. Then, we found that the effects of 1 M $CaCl_2$ at 60 °C were also

similar to the effects of Na^+ at the same activity and temperature. Note that Ca is naturally abundant

in anorthite. The Ca^{2+} could have additional effects besides competing with proton adsorption.

High concentrations of Ca^{2+} may cause back reaction, just like the Al^{3+} back reaction suggested

by Oelkers and Schott.[87] In addition, high concentrations of Ca^{2+} can inhibit the diffusion of

dissolved Ca^{2+} through the hydration layer to the aqueous phase, due to the smaller concentration

gradient. However, the similar effects of Ca^{2+} and Na^+ observed in our study indicated that the

influences of back reaction and inhibited diffusion of Ca^{2+} on anorthite dissolution were not

significant. This is reasonable for two reasons: Ion exchange between Ca^{2+} and protons can be

thermodynamically favored, as supported by observations in previous studies that Ca^{2+} dissolves

rapidly due to exchange reactions with protons.[87] Hence, the back reaction of Ca^{2+} incorporation is not significant although the Ca^{2+} concentration is high. Furthermore, because diffusion across the hydration layer does not affect the dissolution of anorthite in our experimental systems, the potential inhibition of Ca^{2+} diffusion in the hydration layer does not affect the dissolution rate.

The finding that Ca^{2+} and Na^+ have similar effects on plagioclase dissolution helps us understand the impact of Ca^{2+} on anorthite dissolution in subsurface CO_2 injection sites, because formation brines are often contain up to 1.2 M Ca^{2+}.[42] The concentration of Ca^{2+} can further increase due to calcium carbonate or dolomite dissolution after CO_2 injection. Thus, this information can also be beneficial in understanding calcium-abundant formations, such as carbonate oil reservoirs.[96]

Furthermore, comparing the effects of Ca^{2+} and Na^+ on anorthite dissolution enables us to check the applicability of several mechanisms suggested in previous studies. First, the similar effects of Ca^{2+} and Na^+ suggest that the free water mechanism is not applicable to plagioclase dissolution.[97] Finneran and Morse suggested that the different inhibition effects of Na^+ and K^+ on calcite dissolution are due to less free water.[97] In the aqueous phase, cations are hydrated. The effective numbers of water molecules for the hydration of Na^+, K^+, and Ca^{2+} are about 3.9, 1.7, and 12, respectively.[98, 99] Previously, the stronger effect of Na^+ than K^+ on calcite dissolution was explained by the larger amount of water attracted to cations and thus the smaller amount of free water left. According to this mechanism, Ca^{2+} should have a much stronger inhibition effect on mineral dissolution than Na^+. However, for the plagioclase studied here, the similar effects of Na^+ and Ca^{2+} at same activity indicate the inhibition effects of Na^+ and Ca^{2+} are not due to decreasing amounts of free water.

Second, similar to the free water mechanism, high ionic strengths could also affect the mineral dissolution by decreasing the activity of water. A certain amount of water is reactant in the plagioclase dissolution reaction. The dissolution rate should depend on the activity of the water. However, the inhibition effect of 1 M $CaCl_2$ is much weaker than that of 1 M NaCl, while the activity of water is much smaller at 1 M $CaCl_2$. We infer that the water activity effect is not the main reason for the inhibition effect observed in this study.

A third potential mechanism is related to water structure on the surface. A recent study related the inhibition effect of high ionic strengths on dolomite dissolution to the breaking of water–water interactions.[76] The rate-limiting step of plagioclase dissolution should be the detachment of metal cations from the crystal structure,[87] rather than the breaking of H-bonds in the aqueous phase. Ruiz-Agudo et al. also explained the inhibition effects of ionic strength on the dissolution of dolomite and calcite by changes in interfacial energy and in water structure on dolomite and calcite surfaces.[74, 75] Considering the higher ionic strength and weaker Ca^{2+} effect compared with same concentration of Na^+, these mechanisms may not be the main reason for the Na^+ and Ca^{2+} inhibition of anorthite dissolution found in our study.

In sum, we concluded that the main mechanism of the Na^+ and Ca^{2+} effects observed in the current work is competing adsorption with protons, rather than changing the ionic strength. However, there is a caveat that at a high ionic strength, the suppressed electric double layer on the mineral surface can inhibit the adsorption of cations as well.

After investigating the Ca^{2+} effect, we studied the co-existence of Na^+ and Ca^{2+}. Dove et al. investigated the effects of Na^+ and Ca^{2+} on quartz dissolution.[77] They found that Na^+ and Ca^{2+} enhanced quartz dissolution, and that the effects of Na^+ were stronger than the effects of Ca^{2+}.

Still, when Na^+ and Ca^{2+} co-existed, even though the concentration of Na^+ was three times higher than Ca^{2+}, the overall effects were dominated by Ca^{2+}. This observation was explained by the stronger adsorption of Ca^{2+} on mineral surfaces. To test the effects of co-existing Na^+ and Ca^{2+} on anorthite dissolution, we chose 1 M NaCl and 0.33 M $CaCl_2$, because their ionic strength are similar. The concentration of Ca^{2+} is usually lower than Na^+ in field sites,[42] and 0.33 M is high enough to show any possible competing effect with 1 M Na^+. It is very clear in Figure 2.3 that 0.33 M Ca^{2+} did not dominate over the effect of 1 M Na^+. Because the Ca^{2+} effect is very similar to the Na^+ effect, the overall effect can be predicted by simply adding their activities. The activity coefficient of Ca^{2+} can be much smaller than that of Na^+ at high ionic strengths. As a result, for plagioclase, Na^+ effects can be dominant, which is different from the situation of quartz. Because Na^+ and Ca^{2+} are the most abundant cations in field sites, this finding is important in predicting plagioclase dissolution during CO_2 injection.

2.4 Environmental Implications: Subsurface CO_2 Injection

GCS is an important environmental engineering process which is closely linked to environmental sustainability as well as environmental quality. CO_2–water–rock interactions play a significant role in assessing the viability of GCS,[13] and are critical to site selection, risk assessment, and public acceptance.[100] Among CO_2–water–rock interactions, mineral dissolution is a key process. For example, due to an insufficient understanding of silicate dissolution and precipitation kinetics, the rate and extent of CO_2 mineralization are uncertain.[37] Recent studies on natural CO_2 reservoirs and on interactions between core samples from field sites and simulated brines have reported the importance of the dissolution of minerals, including plagioclase, and the subsequent formation of precipitates, including carbonate and clay minerals.[36, 101] These reactions can enhance mineral trapping of CO_2 and change the wettability of mineral surfaces, which is

crucial for residual trapping. Furthermore, based on a previous study, 22–81% of the total pore volume of sandstones had radii less than 100 nm.[102] Hence, if plagioclase dissolution and subsequent secondary precipitation happen at pore throats, they can change the porosity of reservoir rocks and the permeability of geological formations. These changes could affect the transport of CO_2, oil, and gas. Therefore, a better understanding of mineral–fluid interactions is vital in predicting the performance of subsurface CO_2 injection processes.

However, reservoir rocks contain multiple kinds of minerals. Considering the heterogeneous nature of the mineralogies in various field sites, the results obtained in a multi-mineral system can be applicable only to specific sites under specific conditions. For a multi-mineral system, it is difficult to attribute the increased concentrations of metal cations to each single kind of mineral. Single mineral experiments, as shown in this study, can aid in filling this knowledge gap. Recent modeling work predicted the dissolution rates of many minerals as a function of temperature, pH, and ΔG,[103, 104] but few models considered the role of cations critically. The results obtain in this study showed that subsurface-abundant cations can inhibit proton-promoted dissolution. With high concentrations up to 4 M in formation brines, the effects can be comparable to the effects of temperature, pH, and ΔG. Thus these findings contribute to building an accurate database of mineral dissolution kinetics as inputs for geochemical modeling. As with plagioclase, the dissolution of most aluminosilicates in acidic conditions involves proton-promoted dissolution of Al–O–Si linkages.[79, 95, 105] Hence our findings may provide valuable insights for other minerals, such as potassium feldspar and clay minerals. Cations effects can be an important aspect to be consider for multi-mineral systems in the future.

Furthermore, the effect of CO_2 on plagioclase dissolution is mainly an indirect effect through the low pH condition, so cation effects are not limited to CO_2-related processes. Our

findings can provide broader implications for understanding of other energy-related subsurface engineering processes (e.g., energy production/extraction, subsurface storage of energy, and subsurface waste disposal and environmental remediation) where plagioclase dissolution in high salinity brine is involved. In addition, the release of heavy metals and other contaminants from formation rocks, such as aluminosilicate, could be strongly affected by cations. Thus, an improved understanding of cation effects on aluminosilicate is important for evaluating environmental impacts. Furthermore, the weathering of plagioclase in the environment is crucial for the global carbon cycle.[106, 107] Previous studies have discussed why dissolution rates observed in the field are much slower than rates measured in the laboratory.[38] These differences in dissolution rate can also be partially explained by cation effects.

Acknowledgments

Supporting Information for Chapter 2

Contents: Experimental details

        Two figures

        Three tables

S2.1. High pressure and high temperature experimental setup

Anorthite dissolution experiments were conducted in a 300 mL vessel (Parr Instruments, IL), made of Hastelloy C-276. The temperature was controlled by a temperature controller working together with thermocouple and cooling loop. The cooling loop provided an efficient way to decrease the temperature, so that the temperature control could be more stable. The pressure in the vessel was maintained by a syringe pump (Teledyen Isco Inc.), connected to a gas cylinder. The solution in the vessel was mixed by a magnetic stirrer. Samples were collected by a dip tube mounted with a 2.2 µm filter, both made of Hastelloy C-276. During sampling, the gas inlet valve (7 in Figure 2-S1) was closed, and the liquid outlet valve (8 in Figure 2-S1) was opened. Approximately 1 mL solution was driven out through the dip tube, then the liquid outlet valve was closed and the gas inlet valve was opened. The pressure loss during sampling was recovered in several seconds. The reactor also equipped an *in situ* pH probe to monitor the pH during reaction. A more detailed description of the pH probe is available below. A diagram of the reactor setup is shown in Figure 2-S1.
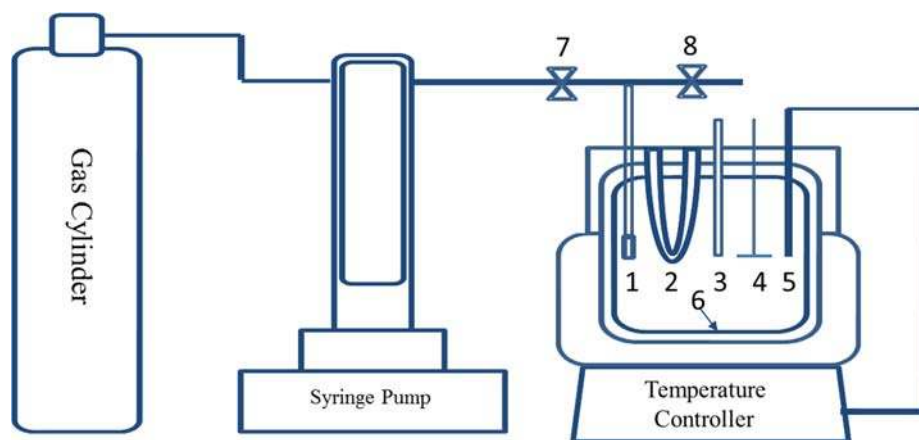
Figure 2-S1. Experimental setup. 1, *In situ* sampling tube; 2, Cooling loop; 3, pH probe; 4, Stirrer; 5, Thermocouple; 6, Teflon liner; 7, gas inlet valve; 8, liquid outlet valve. This schematic diagram was adopted from our previous publication.[80] Reprinted from Min, Y.; Kubicki, J. D.; Jun, Y.-S. Plagioclase Dissolution during CO_2–SO_2 Cosequestration: Effects of Sulfate. *Environ. Sci. Technol.* **2015,** *49* (3), 1946-1954. Copyright © 2014 American Chemical Society.

S2.2. *In situ* pH probe calibration and measurements (adapted from our recent publication,[80] with permission from Copyright © 2014 American Chemical Society)

In situ pH values in the reaction system were measured using a pH probe (Corr Instruments, TX) that can function under 1–136 atm and 20–120 ºC. The tubing of the electrode was made of HC alloy C-276. The probe showed mV values, which could be converted to pH using calibration curves. Standard solutions were made using NaCl, $CaCl_2$, and HCl. The pH values of standard solutions were calculated by Geochemist's Workbench (GWB, Release 8.0, RockWare, Inc.). A linear relationship was found between the calculated pH of the standard solution and the mV values measured. Applying the calibration curve measured under different conditions, the *in situ* pH was calculated based on mV values measured. In 80 hours, no significant change (± 0.02) in pH was observed with the highest solid-to-liquid ratio applied in this study. The error between replicates of the pH measurement was ± 0.01.

S2.3. Steady-state dissolution of plagioclase

In this study, steady-state congruent dissolution of anorthite was obtained. We monitored the metal cations' concentrations, and found their concentrations increased linearly with reaction time (An example is available in Figure 2-S2). In other words, a zero-order reaction was observed. The zero-order steady-state dissolution is due to the low solid/liquid ratio applied in this work. Based on the prediction of Geochemist's Workbench Standard 8.0 and our previous study using the same conditions,[80] no secondary precipitation would form at the highest solid/liquid ratio used in this study. Therefore, the cation release rate was equal to the dissolution rate, and the dissolution rate was not significantly affected by the small changes in pH. The dissolution rates of Ca, Al, and Si were about 0.5:1:1, which is the stoichiometric ratio of anorthite (Figure 2-S2). Congruent dissolution of anorthite has been observed in recent studies.[71, 80] Usually, for plagioclase dissolution, the Si rate is used to represent the mineral dissolution rate, because Si suffers less from complex reactions in the aqueous phase, and its dissolution represents the breakdown of the framework in the crystal structure of plagioclase. So in this study, we always used the Si-based dissolution rate. The dissolution rates can be calculated using the Si slope (concentration vs. time) divided by the BET surface area, solid/liquid ratio, and stoichiometric ratio of Si in anorthite. Duplicate experiments were conducted for up to 80 hours for most experimental conditions.
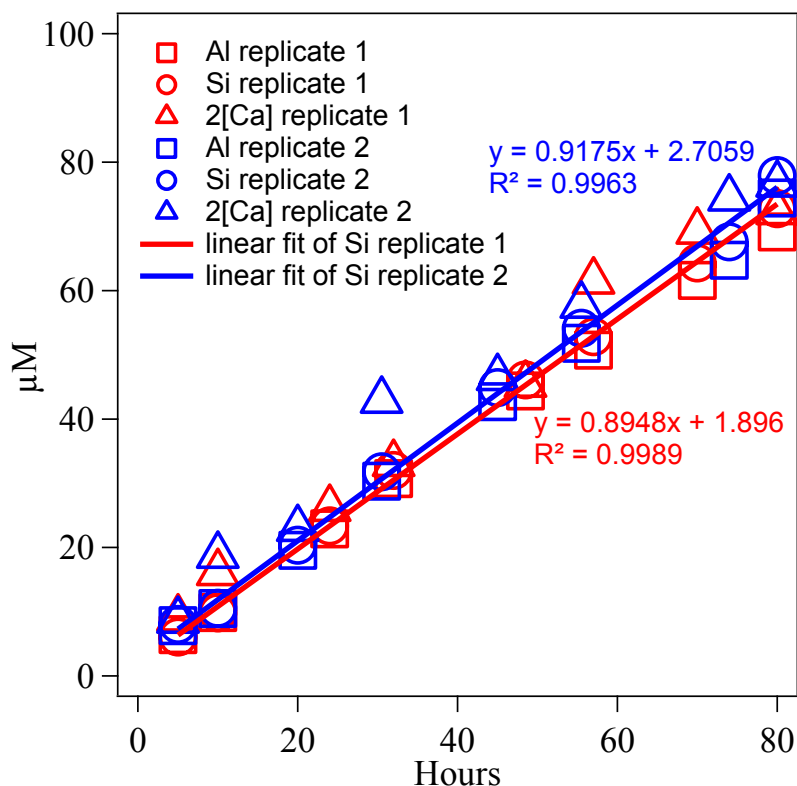
Figure 2-S2. Steady-state congruent dissolution of anorthite was observed in this study. The concentrations of Al, Si, and Ca are measured during anorthite dissolution at 35 °C and 100 atm CO_2. The data shows very good linearity within 5 to 80 hours, which indicates steady-state dissolution of anorthite. The Ca concentration multiplied by a factor of 2 shows very similar values to Al and Si, which means the dissolution of anorthite is congruent.

S2.4. ΔG calculations in Geochemist's Workbench Standard 8.0

The GWB calculates the ΔG of anorthite dissolution based on the following equations:

$$Anorthite + 8H^+ = Ca^{2+} + 2Al^{3+} + 2SiO_2(aq) + 4H_2O \qquad \text{(2-S1)}$$
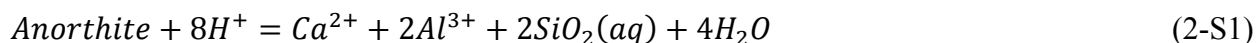
$$\Delta G = RTln(\frac{a_{H_2O}^4 a_{Ca^{2+}} a_{Al^{3+}}^2 a_{SiO_2(aq)}^2}{K a_{H+}^8}) \qquad \text{(2-S2)}$$

$$logK = 31.21 - 0.1978T + 0.0004466T^2 - 5.704 \times 10^{-7}T^3 + 9.918 \times 10^{-11}T^4 \qquad \text{(2-S3)}$$

41

For example, at T= 35 °C (i.e., 308K), pH = 3.10, when $a_{Ca}{}^{2+}$ = 2.5×10^{-5} and $a_{Al}{}^{3+}$ = $a_{SiO2(aq)}$ = 5×10^{-5}, ΔG will be -128.6 kJ/mol.

S2.5. Activation energy calculations

The apparent activation energy is calculated based on this equation:

$$E_a = R\left(\frac{\partial \ln(r)}{\partial\left(\frac{1}{T}\right)}\right) \tag{2-S4}$$

where r is the rate of dissolution, and R is 8.134 J × mol^{-1} × K^{-1}. So the activation energy is the slope obtained by plotting $\ln(r) \times R$ with 1/T. The rate at other temperatures can be predicted based on the plot.

Table 2-S1. X-ray fluorescence (XRF) analysis of anorthite used in this study (in weight %).[80] (adapted from our recent publication,[80] with permission from Copyright © 2014 American Chemical Society)

	Anorthite		Number of ions on the basis of 8 O
SiO_2	44.09	Si	2.042
CaO	19.07	Ca	0.946
Al_2O_3	35.13	Al	1.917
TiO_2	0.00	Ti	0.000
Fe_2O_3	0.57	Fe	0.020
MnO	0.00	Mn	0.000
MgO	0.64	Mg	0.044
Na_2O	0.43	Na	0.039
K_2O	0.01	K	0.010
P_2O_5	0.00	P	0.000
Loss on ignition	0.06		

The Mg and Fe may originate from the lava coating of the anorthite specimens. We broke the specimen into mm size pieces and manually picked out pieces without observable coating. As we did not observe significant impurities in XRD, we do not expect these small amount impurities affected the dissolution rate.

Table 2-S2. Dissolution rates of anorthite obtained using Si slope (µM vs hours) divided by the BET surface area, solid/liquid ratio, and stoichiometric ratio. (Rate in $mol \times m^{-2} \times s^{-1}$).

Experiments	No.	$T/^oC$	pH	Added cations				Solid/liquid (g/L)	Slope	Rate
				Na/M	Ca/M	Al/µM	Si/µM			
Solid/liquid ratio	1	35	3.10					0.01	0.1905	7.73E-08
	2	35	3.10					0.01	0.2108	8.58E-08
	3	35	3.10					0.025	0.4737	7.71E-08
	4	35	3.10					0.025	0.5272	8.58E-08
	5	35	3.10					0.05	0.8948	7.28E-08
	6	35	3.10					0.05	0.9175	7.47E-08
	7	60	3.10	N/A	N/A	N/A	N/A	0.005	0.4103	3.34E-07
	8	60	3.10					0.005	0.3735	3.04E-07
	9	60	3.10					0.01	0.7978	3.25E-07
	10	60	3.10					0.01	0.8159	3.32E-07
	11	60	3.10					0.02	1.3382	2.72E-07
	12	60	3.10					0.025	1.2259	1.99E-07
	13	60	3.10					0.025	1.5433	2.51E-07
	14	60	3.10					0.05	2.1473	1.75E-07
	15	75	3.10					0.005	0.6035	4.91E-07
	16	75	3.10					0.01	0.9453	3.85E-07
	17	90	3.10					0.005	0.5335	4.34E-07
	18	90	3.10					0.01	0.6466	2.63E-07
Al effect	19	60	2.97			0		0.005	0.6202	5.05E-07
	20	60	2.97			0		0.005	0.6156	5.01E-07
	21	60	2.97			25		0.005	0.6056	4.93E-07

	No.									
	22	60	2.97				25	0.005	0.5894	4.80E-07
	23	60	2.97				50	0.005	0.5413	4.40E-07
	24	60	2.97				50	0.005	0.4829	3.93E-07
	25	60	2.97				100	0.005	0.4028	3.28E-07
	26	60	2.97				100	0.005	0.4572	3.72E-07
	27	60	2.97				150	0.005	0.3419	2.78E-07
	28	60	2.97				150	0.005	0.3626	2.95E-07
	29	60	2.97				200	0.005	0.2946	2.40E-07
	30	60	2.97				200	0.005	0.3041	2.47E-07
Chemical affinity	31	60	3.05		12.5E-5	12.5	50	0.01	0.9559	3.41E-07*
	32	60	2.94		12.5E-5	12.5	50	0.01	1.4247	3.78E-07*
	33	60	2.94		1E-4	12.5	100	0.01	1.2997	3.45E-07*
	34	60	2.94		1E-4	12.5	100	0.025	3.4789	3.69E-07*
45 °C	35	45	3.10					0.01	0.3918	1.59E-07
	36	45	3.10		N/A	N/A	N/A	0.01	0.4349	1.77E-07
Na effect	37	35	3.10	0.001				0.01	0.1903	7.74E-08
	38	35	3.10	0.001				0.05	0.8204	6.68E-08
	39	35	3.10	0.01				0.01	0.186	7.57E-08
	40	35	3.10	0.1				0.01	0.0912	3.71E-08
	41	35	3.10	0.1				0.01	0.086	3.50E-08
	42	35	3.10	1				0.25	0.5894	9.59E-09
	43	35	3.10	1				0.05	0.1203	9.79E-09
	44	35	3.10	2				0.25	0.3664	5.96E-09
	45	35	3.10	2	N/A	N/A	N/A	0.25	0.356	5.79E-09

	No.									
	46	35	3.10	4				1	0.623	2.53E-09
	47	35	3.10	4				0.5	0.309	2.51E-09
	48	60	3.10	0				0.01	0.818	3.33E-07
	49	60	3.10	0				0.01	0.8159	3.32E-07
	50	60	3.10	0.001				0.01	0.652	2.65E-07
	51	60	2.94	0.001				0.025	2.4567	2.61E-07*
	52	60	3.10	0.01				0.01	0.5306	2.16E-07
	53	60	3.10	0.1				0.01	0.4341	1.77E-07
	54	60	3.10	0.1				0.01	0.4321	1.76E-07
	55	60	3.10	1				0.01	0.1277	5.20E-08
	56	60	2.94	1				0.025	0.517	5.48E-08*
	57	60	3.10	2				0.25	1.5971	2.60E-08
	58	60	3.10	2				0.25	1.7607	2.87E-08
	59	60	3.10	4				0.25	0.832	1.35E-08
	60	60	3.10	4				0.25	0.8847	1.44E-08
Ca effect	61	35	2.94		0			0.025	0.7265	7.71E-08*
	62	35	2.94		0			0.025	0.7209	7.65E-08*
	63	35	2.94		0.001			0.025	0.702	7.45E-08*
	64	35	2.94		0.001			0.025	0.793	8.41E-08*
	65	35	2.94	N/A	0.01			0.025	0.6554	6.95E-08*
	66	35	2.94		0.01			0.025	0.6702	7.11E-08*
	67	35	2.94		0.1			0.05	0.8752	4.64E-08*
	68	35	2.94		0.1			0.05	0.7968	4.23E-08*
	69	35	2.94		0.33			0.05	0.5191	2.75E-08*

	No.									
	70	35	2.94		0.33			0.05	0.4818	2.56E-08[*]
	71	35	2.94		1			0.25	1.5238	1.62E-08[*]
	72	35	3.10		1			0.25	1.1066	1.79E-08
	73	60	3.13		1			0.05	1.1309	9.90E-08[*]
	74	60	3.13		1			0.05	1.2565	1.10E-07[*]
Na + Ca	75	35	2.94	1	0.33			0.5	1.3253	7.03E-09[*]
	76	35	2.94	1	0.33			0.5	1.253	6.65E-09[*]

* rate is normalized to pH 3.10

Table 2-S3. Concentrations of Si, Al, and Ca measured at different elapsed times. The experiment No. corresponds to **Table 2-S2**. For some experiments, Ca cannot be measured, because the high concentrations of Ca in some samples affected the ICP-OES. For this reason, some experiments measured only Si, or Al and Si.

No.	Hours	Si /μM	Al /μM	Ca /μM	No.	Hours	Si /μM	Al /μM	Ca /μM
1	5	1.21	1.29	0.901	2	5	3.16	2.14	N/A
	10	1.98	1.98	1.61		10	4.14	3.05	
	24	4.75	4.65	2.64		22.5	7.02	5.87	
	32	6.55	6.28	3.37		33	8.97	7.68	
3	5	2.93	3.68	1.72	4	5	2.33	3.70	2.48
	10	5.86	5.63	3.00		10	5.12	6.58	4.55
	23	12.0	11.8	6.26		25	12.9	13.4	8.15
	31.5	15.7	16.2	8.01		32	16.6	17.3	9.76
5	5	6.07	6.45	4.51	6	5	8.04	7.82	4.32
	10	9.83	9.86	8.03		10	10.5	10.5	9.39
	24	23.4	22.9	13.0		20	20.4	19.6	11.5
	32	32.0	30.7	16.5		30.5	31.8	30.3	21.4
	48.5	46.1	44.4	22.7		45	44.9	42.7	23.2
	57	52.8	50.7	30.7		55.5	54.1	51.8	28.9
	70	64.3	61.6	34.6		74	67.6	64.7	37.2
	80	72.8	69.1	36.1		80	77.9	74.4	38.3
7	5	2.91	2.55	N/A	8	5	1.51	3.19	2.09
	10	4.76	4.08			10	3.43	3.25	1.86
	20	8.17	7.33			23	7.89	7.88	5.80
	31	13.7	12.6			31	11.4	11.1	6.12
9	6	2.68	3.78	8.24	10	5	4.62	3.80	N/A
	10	5.57	6.00	5.77		10	7.22	7.12	
	23	15.0	13.7	9.72		22	17.7	17.1	

	33	24.5	19.7	16.7		33	27.0	24.2	
11	6.5	9.93	9.17	6.10	**12**	5	7.09	6.06	9.16
	10	14.3	13.0	8.07		10	13.3	11.4	13.6
	23	33.0	29.5	18.5		22	27.7	24.6	19.4
	32.5	44.2	40.0	25.0		32	40.3	38.1	29.2
13	5	8.91	8.50	7.25	**14**	5	17.7	16.1	10.9
	10	17.2	15.7	11.1		10	31.7	29.6	19.1
	22.5	36.8	32.0	20.1		21	55.0	51.9	28.9
	33	52.1	44.8	30.7		30	78.0	72.6	39.3
						45.25	107.6	100.4	52.6
						55	125.1	116.2	62.6
15	4	2.54	2.59	4.56	**16**	5	6.20	5.62	
	10	5.83	5.21	6.20		10	11.6	9.84	N/A
	21	12.2	10.0	9.96		21	22.0	18.4	
	31	18.8	15.5	13.1		32	31.9	26.9	
17	4.5	2.90	2.82	2.25	**18**	5	1.92	5.25	6.75
	10	6.19	5.31	4.00		10	7.91	9.26	11.8
	22.5	12.3	10.7	10.1		22	14.3	16.6	22.4
	33	18.3	14.9	9.64		31	22.0	22.3	26.6
19	5.5	8.94	5.26		**20**	6	5.23	4.43	
	10.5	13.0	8.77			11	7.95	7.45	N/A
	21	19.3	14.6			21	13.8	12.3	
	31	25.1	19.5	N/A		31	20.6	18.5	
21	5	5.76	28.0		**22**	21.5	13.6		
	13	10.8	32.8			30	19.0		N/A
	23	17.3	38.5			45	28.1		
	33	22.6	42.6			55	33.4		
23	5	4.31			**24**	5	3.33	54.24	3.76
	10	7.25				10	5.34	56.77	6.09
	22.5	14.7				20	10.6	60.9	7.60
	32.5	19.0				30	15.2	66.5	11.8
25	4.5	3.33			**26**	6	2.36		
	9.5	6.28				10	4.43		
	23	12.7				23	10.3		
	33	20.1		N/A		33	14.6		
27	5	3.21			**28**	5	3.90		
	11	4.77				10	6.52		
	22	9.14				23.5	11.2		N/A
	32	12.2				34.5	14.9		
29	5.5	2.6			**30**	5	3.36		
	10.5	4.74				10	5.36		
	22.5	7.86				22	8.84		
	32.5	10.8				35	12.5		
31	5	57.6	13.5	17.7	**32**	5	57.6	20.2	
	10	62.7	17.1	18.7		10	64.7	26.1	N/A
	20	73.3	22.0	23.0		20	78.0	39.1	
	30	81.2	32.1	26.3		30	93.4	53.5	

Group				
33	5.25	110.2	13.9	108.9
	10	114.9	17.6	112.2
	23.5	130.5	27.9	117.1
	33.5	147.3	38.6	120.4
35	5	2.61	N/A	
	10	4.80		
	24	10.5		
	31	12.7		
37	5	0.210	1.34	
	10	0.885	2.52	
	22.5	3.28	4.80	
	32.5	5.04	6.60	
39	5	2.31	3.39	
	10	3.43	3.51	
	23	6.28	5.63	
	33	8.28	7.81	N/A
41	5	0.637	0.801	
	10	0.886	1.28	
	22.5	2.06	2.20	
	32	2.74	3.10	
43	10	2.52	N/A	
	20	3.68		
	30	5.25		
	45	6.86		
	55	7.87		
45	10	5.40	6.08	14.7
	20	8.32	9.97	14.3
	30	11.7	14.3	18.3
	45.5	17.4	21.4	21.1
	55	21.0	27.2	25.0
47	5	2.69	2.28	1.96
	10	4.89	4.08	3.28
	23	8.65	7.63	6.10
	32	11.6	10.1	6.36
	47	15.4	13.8	7.10
	57	19.1	17.2	9.76
49	5	2.79	4.48	3.42
	10	7.10	7.97	5.90
	24	16.9	17.2	11.4

Group				
34	5	118.0	29.0	
	10	133.6	43.6	
	20	168.6	76.3	
	37.5	220.7	126.9	
	47	261.3	164.5	
	57	301.9	202.8	
36	5	4.58	N/A	
	10	6.96		
	24	13.2		
	31	15.8		
38	10	11.0	9.66	
	21	18.1	17.6	
	29.5	25.5	25.1	
	45.5	38.3	38.0	
	55	45.5	45.6	N/A
40	5	1.54	1.04	
	10.5	2.02	1.47	
	21.5	3.00	2.23	
	32	4.00	3.06	
42	10	9.85		
	21	16.7		
	30	20.9		
	46	30.1	N/A	
	55	36.8		
	70	45.1		
	81.5	51.9		
44	5	6.92	5.09	
	10	8.93	7.23	
	20.5	12.0	10.1	
	30	15.3	13.4	N/A
	45.5	22.2	19.7	
	55	24.9	22.9	
46	5	10.7		
	10	17.8		
	21.5	22.2	N/A	
	30	29.3		
	45	37.9		
	55	43.1		
48	5	4.46	4.69	2.79
	10	8.17	10.5	5.57
	21.5	16.5	18.8	9.88
	32	26.8	31.1	14.9
50	5	3.28	4.75	N/A
	10	7.19	7.91	
	22.5	13.5	14.0	

32	25.6	25.3	15.3		**30**	20.4	20.7	
51 5	15.5	12.6	N/A	**52** 5	1.93	4.29	2.70	
10	27.4	23.5		10	4.48	7.71	4.14	
22	56.0	50.8		20	9.85	13.9	6.87	
34	83.8	77.1		32	16.2	21.4	10.2	
48	118.6	111.7						
56.5	143.6	133.5						
53 6	4.11	4.49	3.23	**54** 5	4.33	4.98	2.49	
11	6.81	5.99	4.12	10	6.74	7.24	3.62	
23	12.0	12.1	6.60	22.5	11.9	12.4	6.22	
33	16.0	15.5	7.91	31	15.7	16.5	8.25	
55 5	0.737	2.86	N/A	**56** 5	3.24	2.86	N/A	
10	1.53	5.31		10	6.09	5.31		
24	3.39	12.6		23	12.7	12.6		
33	4.31	16.3		33	18.1	16.3		
				47	25.1	22.1		
				57	30.2	26.7		
57 5	14.1	11.9	N/A	**58** 5	9.16	9.11		
10	23.1	18.9		10	18.0	19.35		
20	47.0	34.4		22.5	37.9	43.1		
30	62.4	46.4		34.5	60.5	67.7		
45.25	82.9	66.8		47	80.2	90.2		
55	93.5	76.6		57.5	102.5	117.6		
59 5	6.85	N/A		**60** 5	4.24	4.78	3.04	
10	11.5			10	8.47	8.47	5.81	
20	19.6			23.5	20.4	18.5	12.1	
30	27.8			33	27.5	25.7	16.6	
61 6	4.74	5.30		**62** 5	4.70	5.01	3.61	
11	8.20	9.45		10	7.93	8.12	5.70	
23	16.8	17.0		21.5	15.1	15.0	9.50	
33	24.4	24.8		31	23.1	22.5	13.7	
63 5	6.32	5.84		**64** 6	5.74	6.58	3.79	
10	9.79	10.1		10	10.4	10.6	5.73	
21.5	18.5	19.0		22	20.3	18.7	10.3	
30	23.6	24.2		30	25.4	23.4	11.9	
65 5	3.94	4.47	N/A	**66** 5	3.44	3.66	N/A	
10	8.87	9.05		10	6.88	6.67		
23	16.2	18.0		26	16.7	15.4		
33	23.0	27.5		35	23.0	20.9		
				47	31.2	28.7		
				58.5	39.3	35.7		
67 5	6.46	4.84		**68** 5	6.72	N/A		
15	13.7	14.6		11	11.5			
24	21.8	26.2		22	20.7			
33.5	31.4	39.9		36	32.0			
				49	41.6			
				58	49.2			
69 5	4.41	3.60		**70** 5	2.93	2.63	2.66	

	11	8.79	6.86		10	5.80	4.99	4.43
	23	14.5	12.5		22	11.6	9.50	7.14
	31	18.2	15.1		32	16.2	13.1	8.66
71	7	15.3	17.4	**72**	6.5	10.8	10.3	
	13	30.6	30.7		11.5	17.5	15.4	
	23	39.8	41.3		23.5	31.9	29.0	
	33	55.0	58.3		33.5	44.3	40.0	
73	5	4.78	4.90	**74**	5	9.56	12.0	
	10	10.5	9.00		10	13.3	19.2	
	22	25.2	20.5		22.5	30.9	33.0	N/A
	33	36.1	30.1		32	41.1	46.5	
75	5	13.0	12.9	**76**	5	8.46	7.90	
	10	20.4	19.6		10	13.2	12.3	
	23	36.6	35.2		22	28.3	26.2	
	32	49.3	47.4		34	39.8	37.8	
					48	55.7	51.8	

Chapter 3: Effects of Na⁺ and K⁺ Exchange in Interlayers on Biotite Dissolution under Geologic CO₂ Sequestration Conditions

Abstract

The performance of geologic CO_2 sequestration (GCS) is affected by CO_2-induced dissolution of the caprock in geologic formations. The dissolution of biotite, a model mica mineral that can exist in the caprock, is strongly affected by Na^+ and K^+ in formation brine. However, it is unclear how the effects of Na^+ and K^+ on the dissolution of biotite depend on these cation concentrations. This study investigated the dissolution of biotite with 0–4 M Na^+ and 0–10 mM K^+ at 95 °C and 100 bar CO_2. Na^+ replaced K^+ in the biotite interlayer and enhanced the biotite dissolution at < 0.5 M concentration. In > 0.5 M range, however, the enhancing effect of Na^+ was mitigated by an inhibition effect caused by competing sorption between Na^+ and proton. With a Na^+ concentration of 0.5 M, co-existing K^+ significantly inhibited the biotite dissolution, with high sensitivity at even lower K^+ concentrations, such as 0.1–0.5 mM. In addition, for the first time, we reported the dissolution of Na-treated biotite, which mimics the biotite naturally equilibrated with Na^+-abundant brine. Na-treated biotite dissolved faster than natural K-containing biotite and during dissolution, it transformed to vermiculite. Aqueous Na^+ inhibited the dissolution of Na-treated biotite by suppressing the release of interlayer Na^+, and aqueous K^+ inhibited the dissolution by replacing the interlayer Na^+. These findings contribute to better understanding of biotite dissolution in the presence of potassium-containing clay swelling inhibitor and different salinities at GCS sites.

3.1 Introduction

In Chapter 2, we investigated the dissolution of plagioclase, which is a model of the minerals in sandstone. In this chapter, biotite, a kind of mica, is chosen to represent the minerals in caprock. Mica is a common aluminosilicate group abundant in many GCS sites. For example, the weight fraction of mica in the caprock is 30% at the Sleipner site,[9] and 10–30% at the Venture site.[10] The interactions among CO_2, brine, and mica can affect the integrity of caprock and the potential for CO_2 leakage. During mica dissolution, small particles can peel off from the surface of mica, and secondary mineral phases like illite can precipitate as nanoparticles.[11, 12] These small particles can plug pore throats and decrease the permeability of formations. Surface roughness can be changed during biotite dissolution and affect the wettability of biotite surface, which eventually affect the transport of CO_2.[13] In addition, the interactions between micas and Na^+ and K^+ in the brine can affect the frictional strength of faults, which change the mechanical integrity of geologic formation.[14]

Although the caprock in field sites contains multiple minerals, studies using single mineral can help delineate the role of each mineral component in the dissolution of caprock and contribute to an accurate database of mineral dissolution kinetics. In this study, we chose biotite $(K(Mg,Fe)_3AlSi_3O_{10}(OH,F)_2)$ as a representative of the mica group minerals. Biotite is more reactive than other micas, such as muscovite. Thus, it can better show the dissolution of mica in laboratory studies on a scale of several days. The crystal structure of biotite is formed by aluminosilicate layers, and each layer contains two tetrahedral sheets occupied by Al and Si and an octahedral sheet occupied by Mg and Fe. Interlayer K^+ cations weakly bound these 2:1 layers together. The surfaces along the layers are called basal surfaces, and the surfaces perpendicular to

the layers are called edge surfaces. The dissolution of edge surfaces is 30–300 times faster than that of basal surfaces.[15]

Recent studies on the dissolution of biotite and other micas under GCS conditions found that the Na^+ in the brine can ion-exchange with the interlayer K^+.[12, 16, 17] The Na^+-K^+ exchange caused swelling of the interlayer spaces, and built up stress, leading to the formation of cracks on the basal surfaces. The dissolution rates of biotite were significantly enhanced by 1 M NaCl compared to deionized water, which was explained by the formation of cracks.[11, 18, 19] However, this information is not enough to accurately predict the dissolution of biotite in GCS sites, because the concentration of Na^+ in the brine in geologic formations varies from 0.01 to 3 M.[20] To predict how dissolution rates depend on Na^+ concentrations, we need to extend recent findings to field sites containing various Na^+ concentrations, beyond simply water and 1 M NaCl.

Na^+-K^+ ion-exchanges are affected not only by Na^+ concentration, but also by K^+ concentration. K^+ can be released from biotite during dissolution, and can also naturally exist in formation brine, with 0.08–170 mM concentrations reported.[20] However, the information in the literature on the effects of K^+ on biotite dissolution is limited and contradictory. Gilkes and Young found that adding K^+ inhibited the dissolution of biotite in 0.1 M HCl.[21] However, Malmstrom and Banwart reported that the dissolution rates of biotite were similar in 0.5 M Na^+ and 0.05–0.5 M K^+ solutions.[22] Further study on the K^+ effects on biotite dissolution is required to elucidate these complicated observations.

In addition, in field sites, a certain portion of biotite in the caprock can be naturally in contact with the formation brine. Considering the high Na^+ concentrations in formation brine, a certain portion of K^+ in the biotite (K-biotite) can be replaced by Na^+ (called Na-biotite). Although some previous studies investigated the Na^+-K^+ exchange reactions in biotite, their findings focused

54

only on structure changes.[23-25] The influence of ion-exchange on the dissolution is unclear. Little information on the dissolution of Na-exchanged biotite is available in the literature. With extensive exchange reactions taking place before dissolution, the dissolution of Na- biotite can be significantly different from that of the original K-biotite, and can play an important role in mineral dissolution and transport in GCS sites.

Therefore, the objective of this study is to investigate the effects of 0–4 M Na^+ and 0–10 mM K^+ on the dissolution of original biotite and biotite treated with NaCl (Na-biotite) at conditions closely relevant to GCS. The outcomes provide new information on how cation effects on dissolution depend on the cations' concentrations, and how they couple with interlayer ion-exchange reactions. The results can contribute to understanding the dissolution of biotite and other micas in subsurface environments containing various concentrations of Na^+ and K^+.

3.2   Experimental Methods

3.2.1 Minerals sample preparation and chemicals

Biotite specimens from Bancroft, Ontario, Canada were obtained from Ward's Natural Science, NY. Based on XRF analysis (Siemens SRS-300), the chemical formula was $K_{0.91}Na_{0.08}Ca_{0.005}(Mg_{0.57}Mn_{0.02}Fe_{0.37}Ti_{0.04})_3(Al_{1.00}Si_{3.00})O_{10}(F_{0.51}(OH)_{0.49})_2$. Biotite flakes with 0.5 cm × 0.5 cm basal surfaces and 0.32 ± 0.01 mm thickness were washed with ethanol, acetone, and isopropanol to remove organic matter, and rinsed with deionized water (>18.0 MΩ·cm). In addition to flakes, powder samples were prepared by grinding and sieving to obtain 53–106 μm particles. The powder samples were also washed with the same method as the flake samples to remove organic matter, and were rinsed with water for 8 times to remove most attached tiny particles.

To mimic biotite that is naturally equilibrated with brine in field sites, 0.1 g biotite powder was mixed with 40 mL 0.5 M NaCl solution at 95 ºC and atmospheric pressure. Because the brine pH was neutral, no significant dissolution of biotite powder was expected during treatment. After every 2 hours, the powder and the solution were separated by centrifugation. An inductively coupled plasma-optical emission spectrometer (ICP-OES) (Perkin Elmer, Optima 7300DV) was used to detect cations in the solutions. The powder was mixed with fresh NaCl solution until no K^+ was detected in the solution. Mg, Fe, Al, and Si were not detectable. This sample is referred to as "Na-biotite." The Na-biotite powder was collected by centrifugation, washed thoroughly with DI water, and dried in nitrogen. To observe the morphology and elemental composition changes, the Na-biotite powder was analyzed using scanning electron microscopy (SEM, JEOL 7001LVF FE-SEM), coupled with energy dispersive X-ray spectrometry (EDS). To examine the swelling of the interlayer space caused by Na^+-K^+ exchange, the Na-biotite powder was analyzed using X-ray diffraction (XRD). The specific surface area of the Na-biotite powder was measured using the BET method (Nova 2000e, Quantachrome Instruments). To quantify the amount of Na^+ newly incorporated into the biotite, a reverse extraction using 10 mM KCl solution was conducted at 95 ºC and atmospheric pressure. The solutions were replaced with fresh KCl solutions every 2 hours until no Na^+ was detected in the solution. The accumulated Na^+ concentration detected in the solutions was used to quantify the amount of interlayer Na^+ in the Na-biotite powder.

All solutions used in this study were prepared using ultra-purified deionized water (>18.0 MΩ·cm) and ACS grade NaCl and KCl (BDH). The pH was adjusted using HCl (BDH).

3.2.2 Dissolution experiments under simulated GCS conditions

Biotite dissolution experiments were conducted using a high temperature and high pressure reaction system modified from our previous work.[26-30] Each biotite flake or 0.01 g biotite powder

56

was reacted with 4 mL solution in a PTFE tube. PTFE tubes with biotite samples were put in a reaction vessel (Parr Instruments, IL). CO_2 was injected into the vessel using a high pressure syringe pump (500D, Teledyne Isco.). A schematic diagram of the setup is available in Figure S1 in the Supporting Information. The PTFE tubes were capped and small holes in the wall of the tubes allowed CO_2 to enter and dissolve in the solutions. The pressure was controlled at 100 bar. Notably, 95 °C is a relatively higher temperature than typical field site conditions (37 °C and 100 bar at the Sleipner site,[31] 65 °C and 150 bar in the Frio formation,[32] and 63 °C and 140 bar at the Weyburn field site.[33]). However, the relatively high temperature allowed us to accelerate the reaction kinetics. Even so, these conditions are within the ranges reported for GCS sites: 31–110 °C and 74–600 bar.[34]

The *in situ* pH of the solutions in the reactor was calculated using the THERMO.com.v8.r6+ database in Geochemist's Workbench (GWB, Release 8.0, RockWare, Inc.). The B-dot equation was used for the calculation of the activity coefficients of aqueous species with ionic strengths up to 3 M. The solubility of CO_2 in brine containing up to 4 M NaCl was calculated according to a model by Duan and Sun.[35] The calculated pH was also verified using a *in situ* pH probe (Corr Instruments.), which could be used at 20–120 °C and 1–136 atm. Details on the *in situ* pH measurement are available in S1 in the Supporting Information. The *in situ* pH of 1 M NaCl solution at 95 °C and 100 bar CO_2 was measured to be 3.20 ± 0.02. To prevent any pH effect and to focus on the effects of cations, the pH of all solutions were pre-tuned to selected values so that after CO_2 was injected into the reactor, the initial *in situ* pH of all solutions were 3.20 ± 0.02. We chose this pH because it is related to the starting period of CO_2 injection at the given experimental pressure and temperature. In addition, pH 3.2 can also mimic locations close to the injection well. On the other hand, in field sites, the pH can increase to 4.5 to 5 due to mineral dissolution after a

long time. However, tuning the pH to 4.5 to 5 would have introduced extra cations into the systems, making it difficult to deconvolute the extra cations used to tune pH from the cations we want to study. In addition, a high pH system would cause more extensive precipitation in our batch system, while this study mainly focused on dissolution of biotite.

The experiments lasted for 3, 24, 48, and 72 hours. After reaction, the vessel was cooled and depressurized over 30 mins. The solutions in the PTFE tubes were filtered using 0.22 µm PTFE filters, acidified using 40 µL concentrated nitric acid, and analyzed using ICP-OES. The solid samples were rinsed with DI water and dried in nitrogen. The basal surfaces of reacted flakes were analyzed using contact mode atomic force microscopy (AFM, Nanoscope, Veeco). The mineral phase changes of reacted powders were analyzed using XRD. To identify the phase of precipitates further, high resolution transmission electron microscopy (HRTEM, JEOL JEM-2100F field emission) with electron diffraction was utilized. For the HRTEM sample preparation, the reacted powders were sonicated in ethanol to detach the precipitates on the surface. A drop of the ethanol was placed on Cu grid for imaging.

3.3 Results and Discussion

3.3.1 Dissolution of biotite flakes
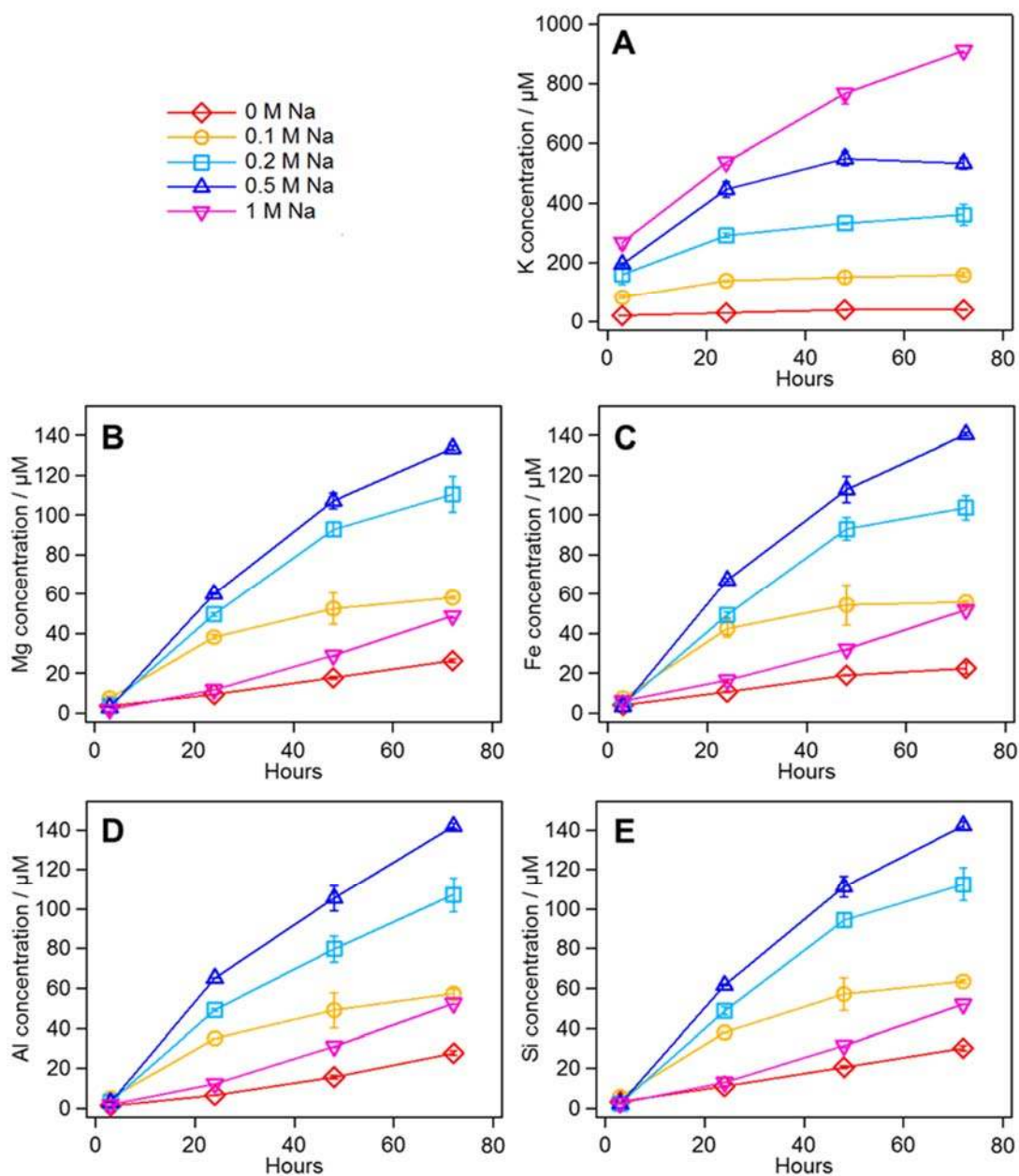
Figure 3.1. The concentrations of **(A)** K, **(B)** Mg, **(C)** Fe, **(D)** Al, and **(E)** Si, released from biotite flakes after 3 to 72 h reaction with 0 to 1 M NaCl. All concentrations were normalized to the stoichiometric ratios. The K concentrations were higher in presence of higher concentration NaCl. For Mg, Fe, Al, and Si, the concentrations were similar and increased with NaCl concentrations from 0 to 0.5 M. However, the concentrations were significantly low in presence of 1 M NaCl.

To study the Na^+ and K^+ effects, dissolution of biotite at 95 ºC and 100 bar CO_2 was demonstrated using flake samples. Figure 1 shows the concentrations of elements released during biotite flake dissolution at different Na concentrations. The concentrations of Mg, Fe, Al, and Si were found to be similar after being normalized by their stoichiometric ratios of elemental components based on XRF analyses. Their concentrations generally increased linearly within 3 to 72 h. In contrast, the concentration of K^+ was much higher than other elements. The release of K^+ was rapid in the first 3 hours, and then gradually slowed down. Our observation is consistent with findings in the literature that K^+ dissolution is faster than that of other elements, because the chemical bonding between K^+ and the silica sheets of biotite is relatively weaker than the bonding of other elements within the sheets.[25] The dissolution of K^+ from biotite occurs mainly through ion-exchange reactions with proton and other cations in solutions.[12] This reaction is diffusion-controlled,[11] so the rate increases with the concentration of other cations and decreases with the concentration of K^+ in solution. In our batch system, the K^+ concentration increased due to K^+ dissolution, so that the ion-exchange reactions slowed after the first 3 hours. This explanation is also consistent with the observation that K^+ release was significantly enhanced with higher Na^+ concentrations (Figure 1A).
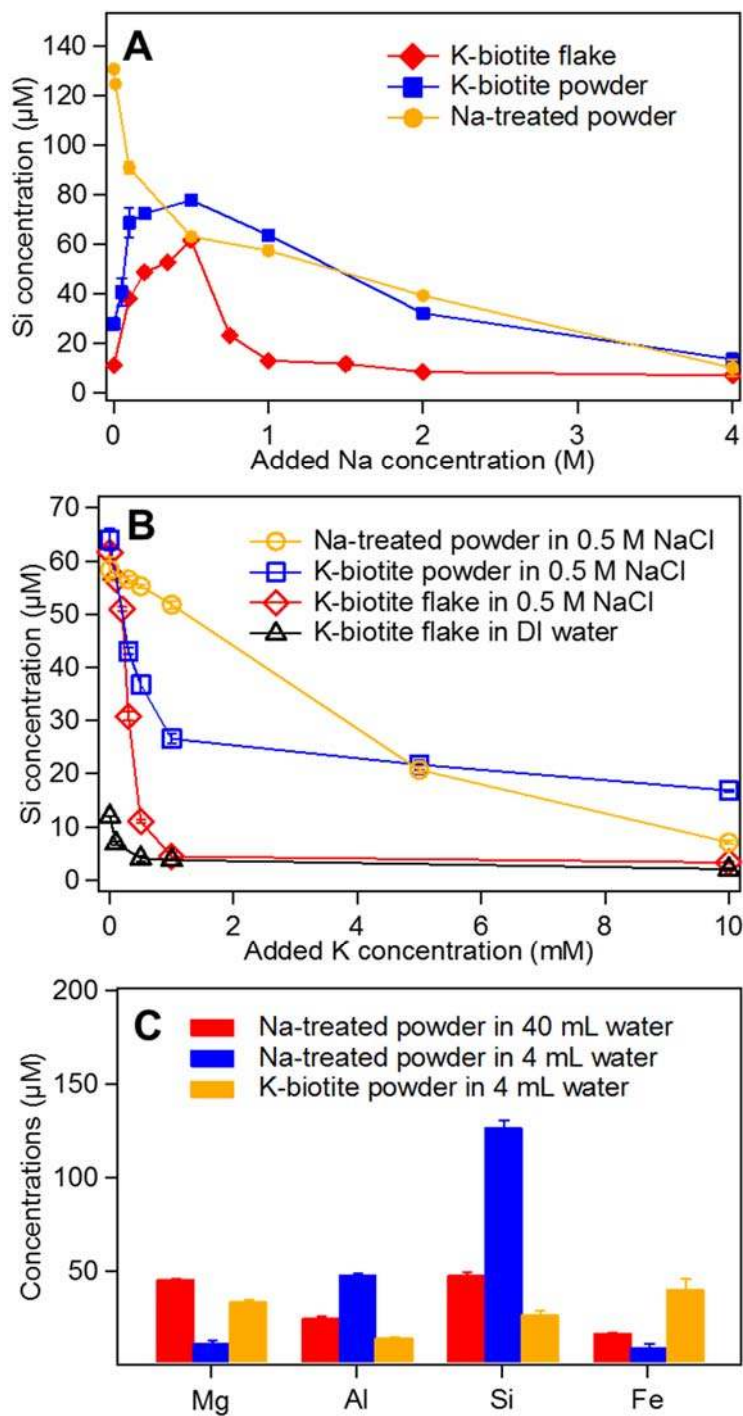
Figure 3.2. (A) The Si concentrations for biotite flakes, biotite powder, and Na-biotite powder reacted in different concentrations of NaCl for 24 hours. **(B)** The Si concentrations for biotite flakes, biotite powder, and Na-biotite powder reacted in different concentrations of KCl for 24 hours. **(C)** The Mg, Al, Si, and Fe concentrations for biotite powder reacted in 4 mL water, and Na-biotite powder in 4 and 40 mL water for 24 hours. For powder samples, concentrations were normalized based on the BET surface area.

61

Effects of Na on biotite dissolution. Figure 1 shows that the concentrations of Mg, Fe, Al, and Si do not increase for all Na^+ concentrations, and may in fact decrease. Because these elements dissolved congruently, we selected the Si concentration to represent the dissolution kinetics. As shown by the red diamond in Figure 2A, from 0 to 0.5 M Na^+, the Si concentrations measured at 24 h increased with higher Na^+ concentrations. Na^+ caused significant ion-exchange reactions with interlayer K^+ and cracked the basal surfaces, which in turn enhanced the biotite dissolution. Evidence can be found in the AFM images of the basal surfaces reacted in DI water and 0.5 M NaCl. Figure S2 shows that many cracks can be seen on the sample reacted in 0.5 M NaCl while the sample reacted in DI water was relatively intact. The formation of cracks on basal surfaces created more reactive surface areas, by creating more edge surfaces. Further, because edge surfaces are 30 to 300 times more reactive compared to basal surfaces,[15] the dissolution rates can be significantly increased.

However, interestingly, from 0.5 to 4 M Na^+, the Si concentrations gradually decreased (Figure 2A). These observations indicate that besides the enhancing effect by the cracking basal surface, Na^+ has another effect in inhibiting the dissolution. This effect can be explained by the inhibition effect of cations observed in our previous study on plagioclase ($CaAl_2Si_2O_8$) dissolution.[36] The dissolution of silicates, including plagioclase and biotite, is usually enhanced by protons. In our previous study, we found that the adsorption of protons on plagioclase surfaces competes with the adsorption of cations, such as Na^+.[36] Similarly, Na^+ should also compete with protons at the surface and the interlayer space of biotite. High concentrations of Na^+ can suppress proton sorption in biotite and inhibit proton-promoted dissolution. Thus, we suggest that the Na^+ effects on biotite dissolution are combined with an enhancing effect by Na^+–K^+ exchange and an inhibition effect by Na^+–H^+ competing sorption. Our previous study found that the Na^+ inhibition

effect on plagioclase was weak at < 0.1 M concentrations, but was particularly strong at > 0.5 M concentrations.[36] This trend is consistent with this current observation: at < 0.5 M concentrations, the inhibition effect by Na^+–H^+ competing sorption was still weak, so that the Si concentrations kept increasing with Na^+ concentrations due to enhancing effect of the Na^+–K^+ exchange. Because the Na^+–K^+ exchange is diffusion-limited, the enhancing effect became less sensitive to Na^+ concentration in a high concentration range. Conversely, the inhibition effect became stronger at high concentration ranges. Therefore, Si concentrations significantly decreased with > 0.5 M Na^+. Because the enhancing effect occurs by cracking the basal surfaces, the transition concentration point (i.e., 0.5 M in our system) should depend on the ratio between basal and edge surfaces. If the dissolution of the basal surface plays a more significant role in the overall dissolution, the transition point could move to higher Na^+ concentrations.

Effects of K on biotite dissolution. Na^+ affect biotite dissolution by Na^+–K^+ exchange, which is also affected by K^+. To investigate the effect of K^+, 10 mM KCl was added to either DI water or 0.5 M NaCl. Figure 2B shows that Si concentration released in DI water in 24 hours was approximately 5 times higher than that in 10 mM KCl (black triangles), which suggests that K^+ significantly inhibited the dissolution of biotite. With a background NaCl concentration of 0.5 M, the Si concentration without 10 mM KCl was around 20 times higher than in the solution of 0.5 M NaCl + 10 mM KCl. These results are surprising, because K^+ can have a significant inhibition effect at a concentration much smaller than the Na^+ concentration, and this effect of K^+ was not suppressed even in a much higher background concentration of Na^+.

As we mentioned above, the inhibition effects caused by competing surface adsorption between cations and protons are not significant at < 0.1 M range.[36] The strong effect of 10 mM K^+ is not likely due to competing surface adsorption with protons. Note that after several hundred μM

of K was released during dissolution, the release of K^+ slowed significantly (Figure 1A), which indicated that several hundred μM of K^+ could inhibit the Na^+–K^+ exchange reactions in our system. Therefore, K^+ concentrations as high as 10 mM can strongly suppress these ion-exchange reactions. Figure S2 shows that with 10 mM KCl, no cracks can be observed on the basal surface of biotite flakes reacted in either water or 0.5 M NaCl. We speculate that K^+ inhibits biotite dissolution by suppressing the ion-exchange. In DI water, the ion-exchange reactions were between protons and K^+. The 10 mM K^+ suppressed these H^+–K^+ reactions and limited the access of protons to the interlayer space, so that the proton-promoted dissolution of silica sheets was inhibited. In 0.5 M NaCl, not only H^+–K^+ exchange, but also the Na^+–K^+ exchange was suppressed. Consequently, with addition of 10 mM KCl, the formation of cracks in 0.5 M NaCl was completely inhibited. These observations show that the interlayer spaces in biotite have a strong preference for K^+ over Na^+, so that a small concentration of K^+ can suppress Na^+–K^+ exchange and significantly inhibit dissolution in a high background concentration of Na^+.

To provide more information on the K^+ effect, we also investigated the dissolution of biotite in other K^+ concentrations within the range of 0–10 mM with 0.5 M background NaCl. As shown by the red diamond in Figure 2B, the K^+ effect was highly sensitive to the concentrations. The Si concentrations were similar within 0–0.1 mM, rapidly decreased between 0.1–0.5 mM, and then gradually reached a plateau beyond 1 mM. In addition, K release was still faster than other elements and followed a similar trend as Si (Figure S3). The K^+ concentration range in the subsurface environments was reported to be 0.08 to 170 mM, which covers the sensitive range of 0.1–0.5 mM. These findings mean that to accurately predict biotite dissolution, we need accurate information on the K^+ concentrations in specific sites. These observations also indicate a critical Na^+/K^+ range where changes in the Na^+/K^+ ratio have a strong influence on the Na^+–K^+ exchange

64

reaction. At 95 °C and pH 3.2, the critical range is approximately 1000–5000. When the Na^+/K^+ ratio is too large or too small compared to the critical range, the inhibition effect of K is not significant or is maximized.

3.3.2 Dissolution of biotite powder

While biotite flakes mimic the biotite in caprocks, biotite powder samples can simulate mobilized biotite particles detached from the caprock. We initially thought that the powder would dissolve much faster than the flake, because of its larger surface area and more edge surfaces exposed to brine. Interestingly, Figure 2A shows that the Si concentrations released from the powder sample were not much higher than those from the flake sample. We suggest that the reactive surface area during the dissolution process is different from the BET or geometric surface area. Most of the reactive surface area during dissolution of biotite may be created by the release of K^+ from the interlayer spaces, which is followed by dissolution reactions in interlayer spaces. The reactive surface area would depend on the extent of ion-exchange reactions of K^+ with protons and Na^+ in solutions. With same amount of protons and Na^+ in the solutions, the extent of ion-exchange reactions would be similar for flakes and powders. Thus, the dissolution rates of flakes and powders would be similar, as we found.

In addition, the Na-enhancing effect on the powder sample was weaker than for the flakes. As shown in Figure 2A, for biotite powder, the maximum Si concentration was approximately 3 times higher than the Si concentration in DI water, compared to the 5 times higher concentration for flakes. The smaller influence of Na^+ on the dissolution of powder can be explained by two reasons: First, Na^+ enhanced biotite dissolution by cracking the basal surfaces, while the powder samples contain more edge surfaces than flake samples. Because of the faster dissolution of edge surfaces, the role of basal surfaces in the dissolution of powder was relatively small. Thus, the

influence of Na^+ was weak. Second, because the particles were small, swelling caused by Na^+–K^+ exchange may lead to exfoliation of biotite sheets rather than formation of cracks. The exfoliation would only create more basal surfaces, which are less reactive than the edge surfaces created by cracking.

Besides the Na^+ enhancing effect, the inhibition effect of K^+ was also weaker for powder, as shown in Figure 2B. With more edge surfaces, powder samples have larger surface area for ion-exchange than flakes. The ion-exchange reactions were easier so that inhibition by K^+ was smaller. Another reason is that K^+ inhibited the dissolution of biotite in NaCl by suppressing the Na^+-enhancing effect. Because Na^+-enhancing effect was found to be weak for the powder samples, the role of K^+ became less important. The weak enhancing effect of Na and weak inhibition effect of K on powder samples can help explain the similar dissolution rate in Na and K solutions reported in a recent study by Malmstrom and Banwart.[22] These findings show that the shape and size of biotite in geologic formations need to be considered when predicting their dissolution. Because the kinetics of ion-exchange change with the size of the biotite specimens, the effects of Na^+ and K^+ were different for flakes and powder samples.

3.3.3 Dissolution of biotite powder pretreated with NaCl solution
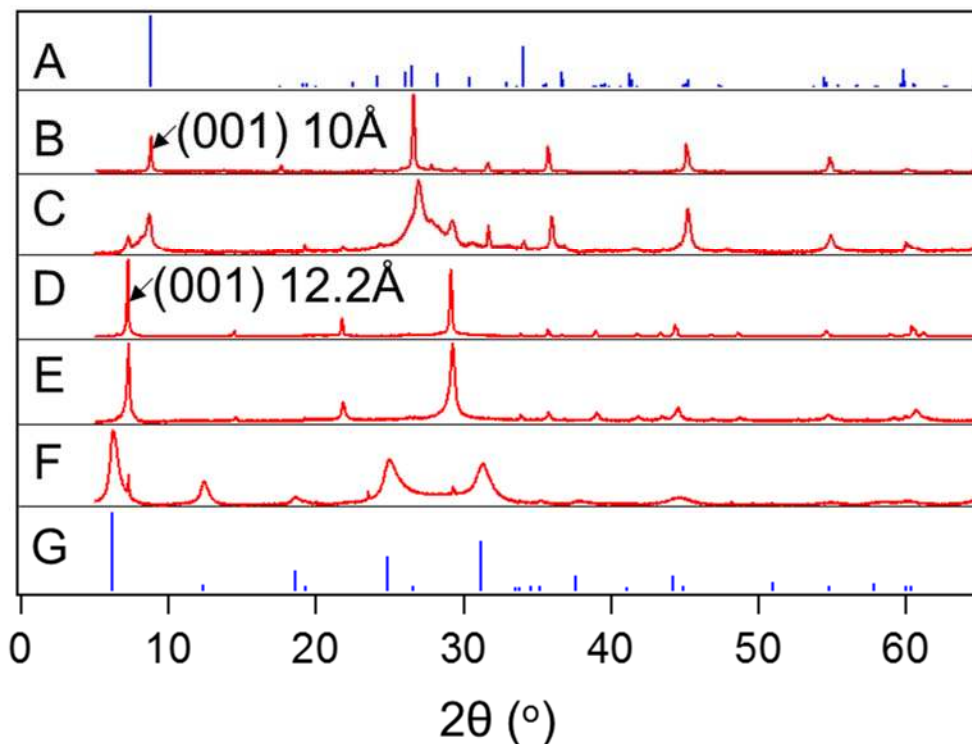
Figure 3.3. XRD patterns of **(A)** biotite PDF card #01-80-1106 **(B)** original biotite sample, **(C)** Na biotite sample reacted with 0.5 M NaCl + 10 mM KCl for 24 h, **(D**) pretreated Na biotite sample, **(E)** Na biotite sample reacted with 0.5 M NaCl for 24 h, **(F)** Na biotite sample reacted with water for 24 h, and **(G)** vermiculite PDF card #00-060-0341. The y axis is the intensity of peaks, which have been normalized to the intensity of the highest peak of each pattern. Compared to the K biotite, pretreatment with NaCl caused left shift of (001) peaks from 10 to 12.2 Å, which indicates that ion exchange of K by Na caused the expansion of interlayer spaces. Na biotite maintained its structure after reaction with 0.5 M NaCl, transformed to vermiculite after reaction with water, and recovered the biotite structure after reaction with 0.5 M NaCl + 10 mM KCl.

Besides biotite flakes and powder samples, we also investigated the dissolution of Na-biotite. To understand the dissolution of biotite naturally equilibrated with formation brine, we pretreated biotite with NaCl solutions to replace the interlayer K^+ with Na^+. The (001) peak shifted from 10 Å to 12.2 Å after treatment (Figure 3B and 3D). This swelling of the interlayer space was consistent with the observations in literature.[22] From the EDS analysis, K was not detected after treatment, while Na was detected (Figure S4). By reversing the Na^+–K^+ exchange using KCl

solutions, the amount of Na^+ in 0.01g Na-biotite was found to be 0.36 mg, which means 71 % of the interlayer cations was Na^+ (Details in S2 in the Supporting Information). This observation is consistent with the observation in a recent study that the charge deficiency of silica sheets in biotite decreases during NaCl treatment, thus the number of interlayer cations needed to compensate for the charge deficiency also decreases.[24] SEM images show that the pretreatment using the NaCl solution did not significantly change the morphology of the biotite particles (Figure S4). However, the specific surface area measured by BET increased from 0.94 ± 0.01 to 2.68 ± 0.01 m^2/g, which may result from the exfoliation of biotite particles.

The dissolution of Na-biotite in DI water was significantly different from the original K-biotite. The *in situ* pH of original K-biotite reacted for 1 hour was 3.20 (Table S1). In contrast, the *in situ* pH of Na-biotite reacted for 1 hour increased to 3.96. Such a quick increase of pH is likely due to the rapid release of Na, because 0.23 mg of Na was detected after 1 h reaction, which means most of the Na in Na-biotite had been released. In addition, after 24 h reaction, no Na can be detected in the EDX analysis (Figure S4). The high pH is likely to decrease the dissolution rate of Na-biotite. The dissolution rate of biotite was found to be a function of $(H^+)^{0.58}$,[37] which means the dissolution rate at pH 3.96 would be 2.7 times lower than that at pH 3.20. However, much larger Si concentrations for Na-biotite have been observed (Figure 2A and 2C), even after normalization by BET surface area. This observation indicates that the intrinsic dissolution rate of Na-biotite biotite is much faster than that of the original K-biotite. The extensive Na^+–K^+ exchange during pretreatment may create many defects in the crystal structure of biotite, enhancing dissolution.
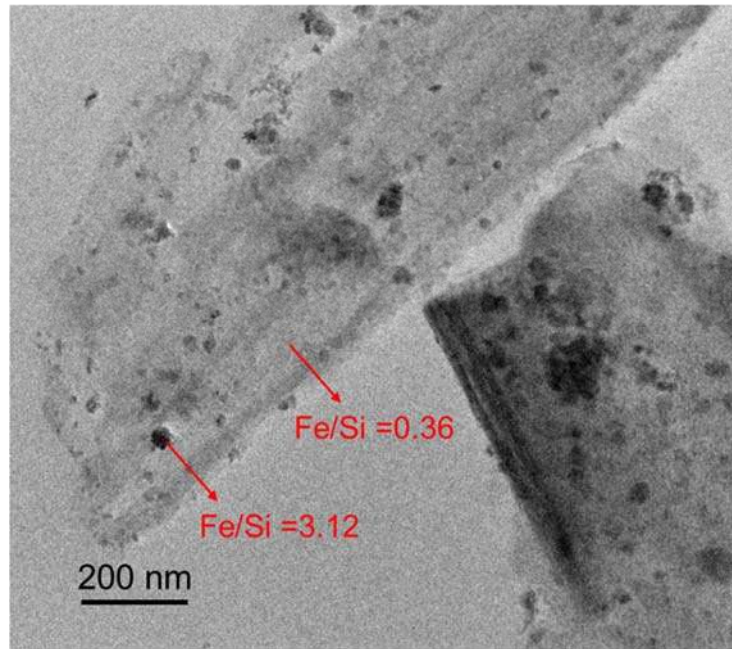
Measured d-spacing	hematite	Crystal plane	maghemite	Crystal plane
3.69	3.68552	102	3.73066	210
2.53	2.51900	110	2.51521	113
2.21	2.20838	113	2.22949	321
1.86	1.84276	204	1.82037	421
1.73	1.69662	116	1.70280	224
1.47	1.45435	300	1.47467	440

Figure 3.4. TEM image of small particles detached from Na-biotite powder reacted for 24 h in water. Nanoparticles rich in Fe was observed. The electron diffraction pattern showed the d-spacing (Å) matched with hematite and maghemite.

Furthermore, the high pH caused by Na release led to the formation of secondary precipitations. Figure 2C shows that for Na-biotite, dissolution was not congruent, and the concentrations of Mg, Al, and Fe were significantly lower than Si. In our previous studies on mica dissolution under GCS conditions, secondary precipitation containing Al, including kaolinite, gibbsite, and boehmite, were observed.[17] In this work, by TEM analysis, we observed some nm size particles rich in Fe on the biotite surfaces (Figure 4). By matching the d-spacings determined by electron diffraction, the particles could be hematite or maghemite. Because the formation of

69

hematite needs a long time of aging, the precipitation in our system is more likely to be the metastable phase maghemite. These precipitations can explain the low Al and Fe concentrations observed. A unique observation of the Na-biotite is the low concentration of Mg. Mg may precipitate as Mg-substituted Al and Fe hydroxides. In addition, we suggest that Mg can precipitate as vermiculite ($Mg_{0.7}(Mg, Fe, Al)_6(Si, Al)_8O_{20}(OH)_4 \cdot 8H_2O$). Figure 3F shows that the Na-biotite after 24 h reaction in water transformed into vermiculite, which has a similar structure to biotite. The main difference is that the interlayer cations in vermiculite are hydrated cations like Mg^{2+} instead of K^+. It is likely that the removal of K^+ in biotite and rapid release of Na^+ facilitate the formation of vermiculite. Further evidence of these precipitations can be found in additional experiments which used 40 mL water instead of 4 mL. As larger volumes of water were used, the concentration of released Na would be smaller and the pH would be lower. Thus, smaller amount of precipitations formed and we detected larger Mg and Fe concentrations, as shown in Figure 2C.

In contrast to the enhancing effect on original K-biotite, Na^+ inhibited the dissolution of Na-biotite, based on the Si concentrations in Figure 2A. The absence of the Na^+ enhancing effect is because there is no interlayer K^+ and thus no cracking of basal surfaces caused by the Na^+–K^+ exchange. The inhibition effect is probably because the high Na^+ concentrations in solutions can suppress the release of interlayer Na^+ from Na-biotite: the *in situ* pH after 1 h reaction in 0.5 M NaCl was 3.35 for 0.5 M NaCl, compared to 3.96 for DI water (Table S1). In addition, after 24 h reaction in 0.5 M NaCl, the XRD patterns of Na-biotite have broader peaks but the same locations (Figure 3D and 3E), which means the formation of vermiculite was inhibited.

Figure 2B shows that the inhibition effect of K^+ on the dissolution of Na-biotite was weaker than on the dissolution of original K-biotite. The Si concentrations decreased with higher concentrations of K^+ within 1–10 mM. The inhibition was not significant with < 1 mM K^+. There

70

was no critical concentration range, compared to the 0.1–0.5 mM range for original K-biotite. For K-biotite, K^+ inhibits dissolution by suppressing the release of interlayer K^+. For Na-biotite, the interlayer K^+ is replaced by Na^+, and so, K^+ did not show an inhibition effect at low concentrations. Figure 3C shows that after reaction with 10 mM KCl, the Na-biotite recovered the structure of the original K-biotite. As mentioned above, K^+ is strongly preferred over Na^+ as interlayer cation for biotite. K^+ concentrations as high as 10 mM can replace the interlayer Na^+ in Na-biotite, even in 0.5 M NaCl. Because the dissolution of the original K-biotite is slower than Na-biotite, such a high concentration of K^+ can inhibit the dissolution. These findings show that the cations effects on the dissolution of Na-biotite are very different from those on the original K-biotite, providing insights into the dissolution of biotite equilibrated with formation brine.

3.4 Environmental Implications

Silicate dissolution rates in GCS sites are usually modelled as a function of pH, temperature, and ΔG. Our previous study pointed out that, considering the high Na concentrations in geologic formations, the Na inhibition effect can be as important as the effect of the pH and temperature.[36] The findings in this work further showed that for silicate with the potential of significant ion-exchange reactions, the overall effects of Na can be more complicated. To accurately predict the silicate dissolution kinetics in GCS sites, the cations concentrations in specific sites need to be examined.

In addition, the ion-exchange between interlayer cations and cations in formation brine can also lead to different dissolutions of biotite. This information contributes to understanding the dissolution of biotite and other micas and the subsequent secondary precipitation. These reactions

can change the permeability of the caprock in GCS sites, which has to be considered when evaluating the environmental safety and economic efficiency of GCS operations.

Similarly, the results of this study can provide insights for other energy-related geoengineering processes injecting CO_2 into the subsurface environment, including CO_2 enhanced oil recovery and hydraulic fracturing. For example, this study can help understand the interactions between Na^+ and mica, which were found to cause permeability damage in oil fields.[38] In addition, the fracturing fluid often contains Na^+ and K^+ as swelling inhibitors, with 500–2000 ppm concentrations reported.[39] The drilling fluid used in well drilling also contains 3 to 20 wt% KCl as a swelling inhibitor.[40] This fluid can mix into the formation brine, which eventually affects the dissolution of minerals like biotite. Our results show that these chemical additives can have significant impacts on the dissolution of minerals in subsurface environments.

Besides subsurface environments, similar Na^+ and K^+ effects can potentially be found during the dissolution of biotite in surface environments. For example, the Na^+ and K^+ in soil solutions may affect the weathering of biotite in soil environments in a similar way. Biotite weathering is an important step in the formation of soil,[41] which in turn shapes landscapes, withdraws atmospheric CO_2, affects watershed chemistry, and controls the supply of soil nutrients.[42] Furthermore, the findings also provide hints for the dissolution of sheet silicates other than micas. For example, clays such as montmorillonite, which are also abundant in caprocks and other subsurface environments, also have a strong capability for ion exchange and swelling. Thus, similar effects of cations reported in this work may be applicable to other clay minerals.

Acknowledgments

Supporting Information for Chapter 3

Contents: Experimental details

Four figures

Three tables
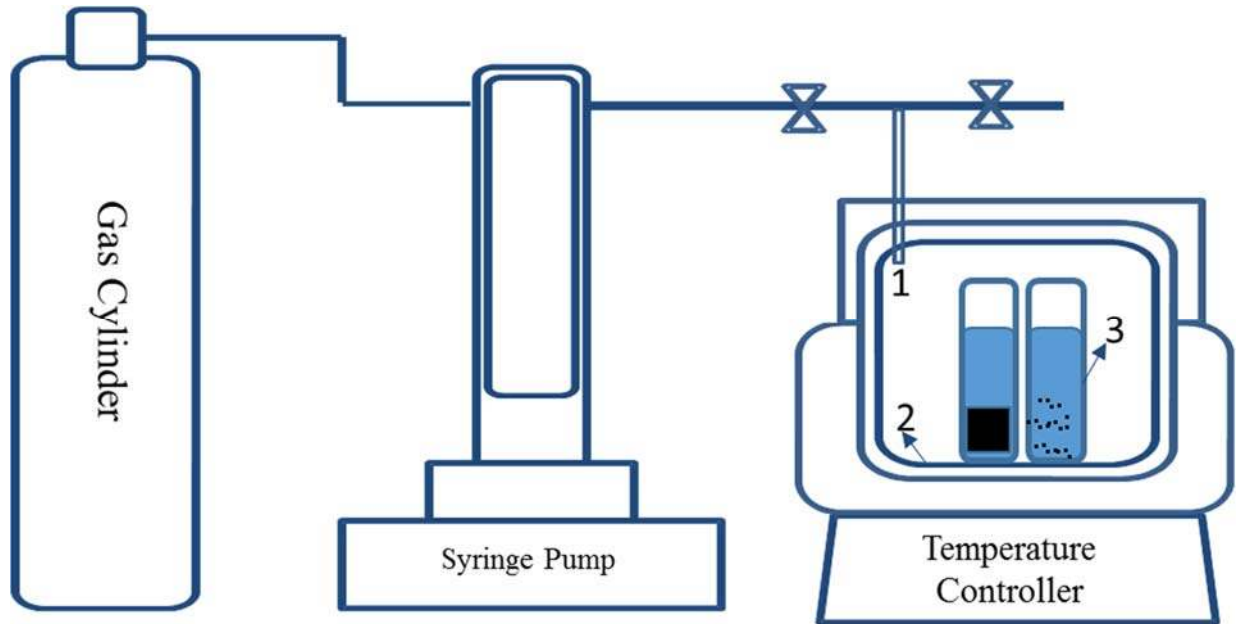
Figure 3-S1. Experimental setup. 1, Gas inlet and outlet; 2, PTFE liner; 3, PTFE tubes containing solutions and biotite flakes or powder samples. Pressure gauge and thermocouple are installed, but not shown.

S3.1. *In situ* pH probe calibration and measurements (adapted from our recent publication,[80] with permission from Copyright © 2014 American Chemical Society)

In situ pH values in the reaction system were measured using a pH probe (Corr Instruments, TX) that can function under 1–136 atm and 20–120 ºC. The tubing of the electrode was made of HC alloy C-276. The probe showed mV values, which could be converted to pH using calibration curves. Standard solutions were made using NaCl and HCl. The pH values of standard solutions were calculated by Geochemist's Workbench (GWB, Release 8.0, RockWare, Inc.). A linear relationship was found between the pH values of the standard solutions and the voltage measured in mV. Applying the calibration curve measured under different conditions, the *in situ* pH was calculated based on mV values measured. The error between replicates of the pH measurement was ± 0.01. For flake samples, our previous study found that changes were within ±0.1 for 72 hours.[20] The in situ pH for powder samples were measured using 0.5 g powder and 200 mL solutions. The results are shown in table:

Table 3-S1. In situ pH of solutions containing powder samples

In situ pH from 1h to 24h	in water	in 0.5 M NaCl
K biotite	2.96 to 3.11	3.15 to 3.29
Na biotite	3.96 to 4.00	3.35 to 3.61

S3.2. Reverse extraction of Na from Na-treated biotite powders

To quantify the amount of Na in Na-treated biotite powders, 1 mg of Na-treated biotite powders was used to mix with 5 mL 10 mM KCl solution at 95 °C and atmospheric pressure. The solution was replaced with fresh 10 mM KCl solution every 2 hours. The solutions were filtered with 0.22 μm PTFE filter, diluted 10 times, and measured using ICP-MS. Results are shown below:

Table 3-S2. Na concentration during reverse extraction

Times of Extraction	Na (μM)
1	22.9
2	6.46
3	1.65
4	0.70
5	0.12
6	0.00
total	31.83

Based on these concentrations, the amount of Na in 1 g of Na-treated biotite powder was 36 mg. The molecular weight is 457, based on XRF results. Thus, the stoichiometric number of Na in Na-treated biotite powder is 0.71.
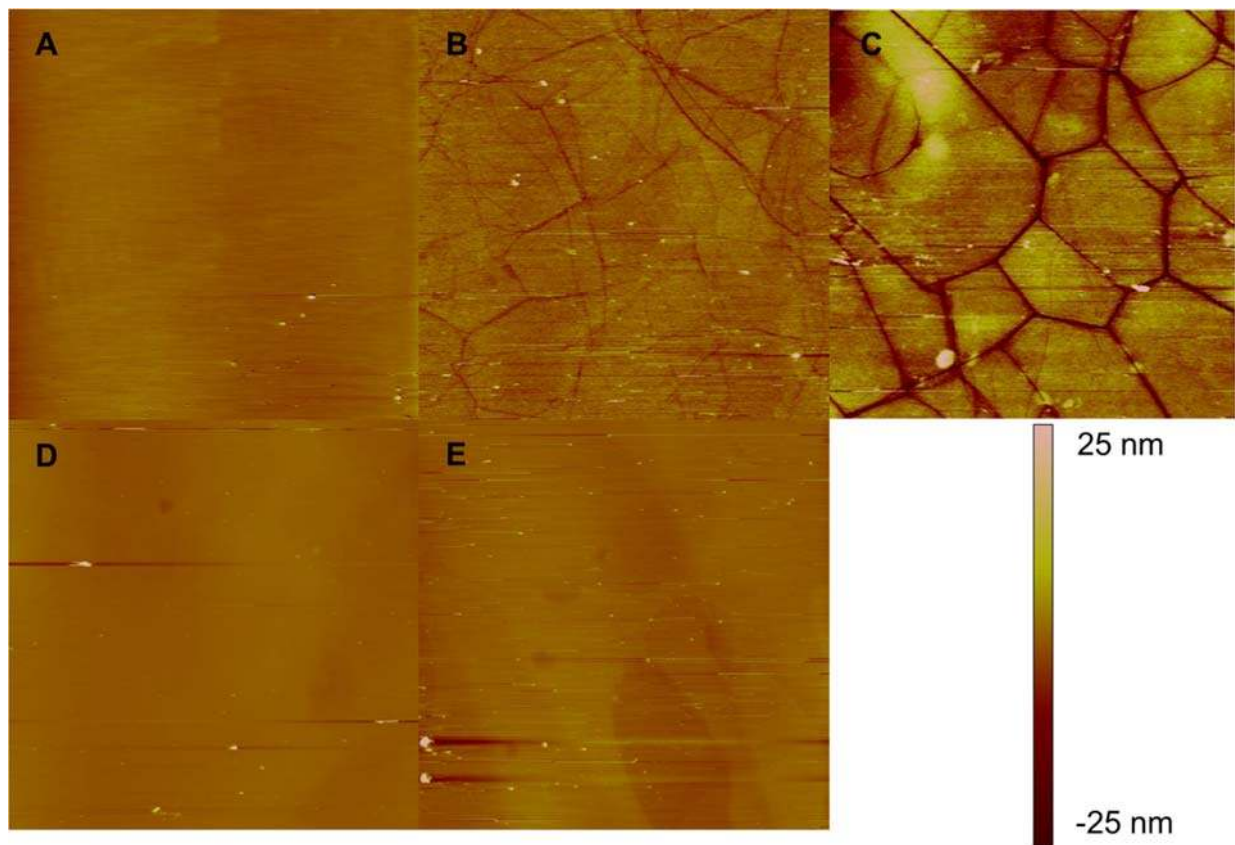
Figure 3-S2. Contacting mode AFM images (50×50 μm) of basal surfaces for **(A)** biotite sample reacted with water, **(B)** biotite sample reacted with 0.5 M NaCl, **(C)** biotite sample reacted with 1 M NaCl, **(D)** biotite sample reacted with 10 mM KCl, and **(E)** biotite sample reacted with 0.5 M NaCl +10 mM KCl, for 72 hours. The height scale is 50 nm. The surface was fractured after reaction in 0.5 M NaCl, while the surface was intact in other conditions.
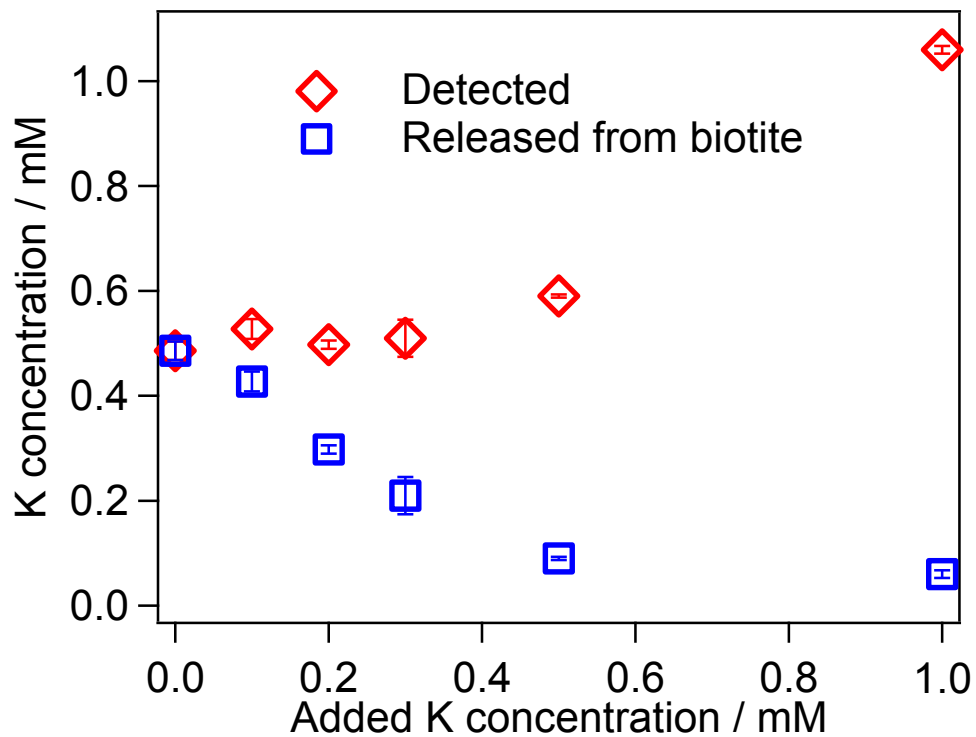
Figure 3-S3. The K concentration during biotite flake dissolution in 0.5 M NaCl for 24 h with different additional K concentration. The K released from biotite was calculated by subtracting added K from detected concentrations.
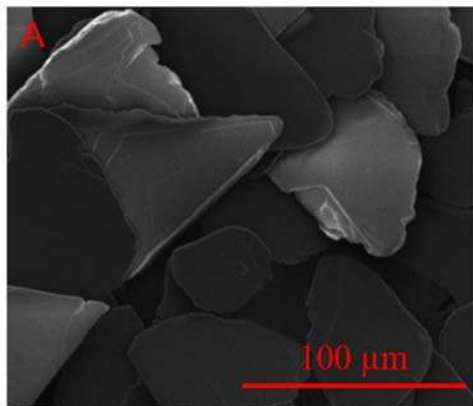
Elements	Atom%
O	65.81
Na	0.21
Mg	7.43
Al	4.84
Si	15.52
K	5.16
Fe	1.03
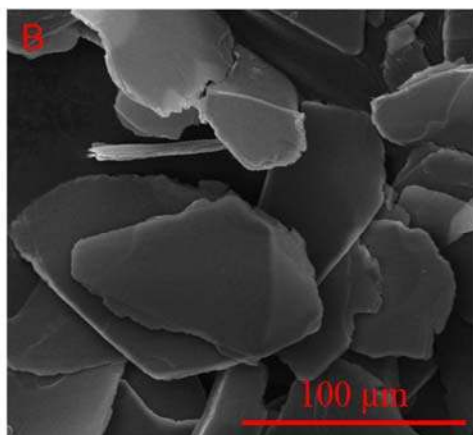
Elements	Atom%
O	61.43
Na	3.91
Mg	8.01
Al	5.67
Si	19.39
K	0.15
Fe	1.44
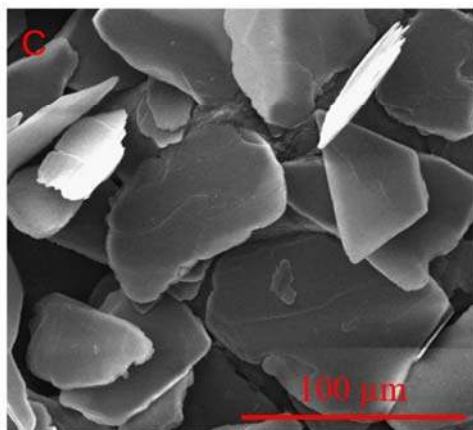
Elements	Atom%
O	66.65
Na	0.29
Mg	8.56
Al	5.60
Si	17.67
K	0.20
Fe	1.03

Figure 3-S4. SEM images and EDX results of **(A)** K-biotite powder, **(B)** Na-treated powder, and **(C)** Na-treated powder reacted with water. All particles maintained flake shape. The Na-treated powder contains Na rather than K, showing that Na treatment was properly conducted. After reaction with water, little amount of Na and K was detected.

Table 3-S3. X-ray fluorescence (XRF) analysis (Siemens SRS-300) of biotite used in this study (in weight %).

	Biotite		Number of ions on the basis of 10 O
SiO_2	39.0	Si	3.00
CaO	0.10	Ca	0.005
Al_2O_3	11.1	Al	1.00
TiO_2	2.19	Ti	0.12
FeO	17.5	Fe	1.11
MnO	0.84	Mn	0.06
MgO	13.9	Mg	1.71
Na_2O	0.60	Na	0.08
K_2O	9.40	K	0.91
Others	5.37		

Chapter 4: Plagioclase Dissolution during CO₂-SO₂ Co-sequestration: Effects of Sulfate

Abstract

Geologic CO_2 sequestration (GCS) is one of the most promising methods to mitigate the adverse impact of global climate change. The performance of GCS can be affected by mineral dissolution and precipitation induced by injected CO_2. Co-sequestration with acidic gas such as SO_2 can reduce the high cost of GCS, but it will increase the sulfate's concentration in GCS sites, where sulfate can potentially affect plagioclase dissolution/precipitation. This work investigated the effects of 0.05 M sulfate on plagioclase (anorthite) dissolution and subsequent mineral precipitation at 90°C, 100 atm CO_2, and 1 M NaCl, conditions relevant to GCS sites. The adsorption of sulfate on anorthite, a Ca-rich plagioclase, was examined using attenuated total reflectance Fourier-transform infrared (ATR-FTIR) spectroscopy and then simulated using density functional theory (DFT) calculations. We found that the dissolution rate of anorthite was enhanced by a factor of 1.36 by the formation of inner-sphere monodentate complexes between sulfate and the aluminum sites on anorthite surfaces. However, this effect was almost completely suppressed in the presence of 0.01 M oxalate, an organic ligand which can exist in GCS sites. Interestingly, sulfate also inhibited the formation of secondary mineral precipitation through the formation of aluminum–sulfate complexes in the aqueous phase. This work, for the first time, reported the surface complexation between sulfate and plagioclase which can occur in GCS sites. The results

provide new insights for obtaining scientific guidelines for the proper amount of SO_2 co-injection, and finally for evaluating the economic efficiency and environmental safety of GCS operations.

4.1 Introduction

Chapter 2 and Chapter 3 discussed cation effects on the dissolution of aluminosilicate. In this chapter, anion effects are studied, with consideration of SO_2 co-injection and enhanced oil recovery. Co-sequestration of SO_2 during GCS can alleviate the cost of separating SO_2 in flue gas from coal-fired power plants and reduce the amount released to the atmosphere.[44, 46, 48, 128, 129] However, the high chemical reactivity of co-injected SO_2 with CO_2 can trigger potential dissolution of pre-existing reservoir rocks and secondary mineral precipitation, resulting in changes in the porosity and permeability of the reservoirs. These changes can further impact the stability of porous formations and caprock integrity.[44, 48, 128] Therefore, the feasibility of SO_2 co-injection can be affected by its compatibility with the mineralogy of storage sites.[128]

Recent studies found that co-injected SO_2 can form sulfuric acid in the presence of oxidants.[43-46, 130, 131] A previous report by Xu et al. predicted a pH as low as 0, and a sulfate concentration as high as 0.8 M in brine (1 M NaCl) with 3.6 wt% SO_2 co-injection.[46] While recent studies have debated the extent of pH reduction in reservoirs,[47, 48] discussions on the effects of sulfate have been limited to only the formation of sulfate minerals.[132, 133] However, it is necessary to recognize the effects of sulfate on mineral dissolution under GCS conditions. For example, the dissolution rate of gibbsite was enhanced ten times by 5 mM sulfate at pH 2 and 5°C over that without sulfate.[51] A better understanding of the effects of sulfate on mineral dissolution under conditions relevant to GCS is critical to establish allowable amounts of SO_2 co-injection. Furthermore, sulfate is also one of the most naturally abundant anions in GCS sites. A maximum

sulfate concentration of 1000 mg/L (i.e., 0.01 M) in oil field brine has been reported.[42] Thus, even without SO_2 co-sequestration, sulfate exists in significant amounts which can strongly affect mineral dissolution during GCS. However, experimental studies simulating GCS conditions and focusing on the role of sulfate on mineral dissolution are sparse.

In GCS sites, plagioclases often exist in formation rocks as well as caprocks.[13] In this study, plagioclase was chosen as representative of rocks in GCS sites, because it is one of the main components of sandstones and basalts.[10, 13] Moreover, Ca-rich members of plagioclase, such as anorthite, play an important role in calcium release in geochemical processes, and calcium is important for mineral trapping of injected CO_2 during GCS.[65, 66] To the best of our knowledge, there has been no experimental work on the effects of sulfate on plagioclase dissolution under conditions relevant to GCS sites.

Furthermore, predicting the effects of sulfate on plagioclase dissolution is not straightforward. It is expected that sulfate will form aqueous phase complexes with metal cations, such as Al,[134] and increase the apparent solubility of plagioclase and secondary precipitates. These effects will enhance the dissolution of plagioclase. However, the potential effects of sulfate surface adsorption cannot be ignored. Previous studies reported inhibition effects of sulfate on the dissolution of Fe (III) (hydr)oxides, and predicted that sulfate would have similar inhibition effects on aluminosilicates.[135, 136] On the contrary, several studies reported that sulfate can enhance the dissolution of gibbsite,[49-52] and predicted that potential enhancing effects of sulfate may be found on other aluminum containing minerals.[51] Thus the prediction by previous studies using iron hydroxides differed from the prediction by previous studies related to gibbsite, because the effects of adsorption depend on the type of surface complexation.

84

In general, the inhibition effects of sulfate were attributed to the formation of binuclear bidentate surface complexes between sulfate and metal on mineral surfaces.[135, 136] Because the binuclear surface complexes formed by divalent ligands are uncharged, they do not enhance surface protonation.[135] In addition, the simultaneous detachment of two metal centers from the surface needs to overcome a high activation energy.[136] As a consequence, the mineral dissolution can be inhibited. In contrast, the formation of a mononuclear complex will lead to enhancing effects by causing nucleophilic interactions with metal ions and facilitating surface protonation.[135, 137] However, information about the type of sulfate adsorption on the plagioclase surface is lacking. As a consequence, the prediction of sulfate effects on plagioclase dissolution is challenging.

Another potential effect of sulfate on plagioclase dissolution is competing adsorption with carboxylic acids. The dissolution of plagioclase can be strongly affected by carboxylic acid ligands, including oxalate.[53] Carboxylic acids are abundant in oil and gas reservoirs,[42] which are potential sites for GCS and enhanced oil recovery (EOR). A concentration of as much as 5.6 mM oxalate in subsurface water has been reported.[42] Sulfate adsorption is known to compete with low molecular weight carboxylic acids adsorption in soil environments.[138] Hence, sulfate could affect plagioclase dissolution in GCS sites by competing adsorption with carboxylic acids. However, the effects of sulfate co-existing with carboxylic ligands on plagioclase dissolution have not been systematically investigated yet.

This study, for the first time, investigated the type of sulfate adsorption on plagioclases, using attenuated total reflectance Fourier transform infrared (ATR-FTIR) spectroscopy, and it elucidated the effects of sulfate surface adsorption on plagioclase dissolution under GCS conditions. Furthermore, we studied the influence of oxalate on the surface adsorption of sulfate and adsorption's effects on plagioclase dissolution. This new information can be helpful when

predicting plagioclase dissolution with high concentrations of sulfate. The plagioclase dissolution can cause significant changes in the permeability of rocks, if it takes place at pore throats of reservoir rocks. Therefore, the outcomes can be useful in accurately evaluating the subsequent wettability, porosity, and permeability changes, and in predicting the transport of CO_2. Ultimately, this study contributes to our understanding of the role of sulfate in GCS sites and in predicting the impact of SO_2 co-injection with CO_2.

4.2 Experimental Methods

4.2.1 Minerals and chemicals

All chemicals used in this study were at least ACS grade. All the solutions were prepared using ultra purified water (Barnstead, resistivity > 18.2 MΩ•cm). Anorthite samples (Miyake Island, Izu Archipelago, Tokyo Prefecture, Japan) were thoroughly characterized using high resolution X-ray diffraction (HR-XRD) in our previous study.[79, 95, 105] The specimen was coated with a thin layer of clay. To remove the clay coating, the specimen was crushed to mm size, and the specimen pieces without coating were picked out manually. Selected specimen pieces were ultra-sonicated in ultra-purified water for 15 min and then dried in nitrogen. Finally, specimen pieces were ground, and sieved without further treatment. Particles with sizes between 53 to 106 microns were used. Using X-ray fluorescence (Table 4-S1) and the BET method (AX1C-MP-LP, Quantachrome Instruments), the chemical formula and specific surface area were determined to be $Na_{0.04}Ca_{0.95}Al_{1.94}Si_{2.06}O_8$ and 0.1707 m^2/g.

4.2.2 Dissolution experiments at simulated GCS conditions

Dissolution experiments were conducted in a 300 mL high pressure and high temperature reactor (Parr Instruments, Moline, IL) used in our previous studies.[79, 95, 105, 120, 139] A schematic

86

diagram of the reaction system setup is available in the Supporting Information (Figure 4-S1). The conditions (90°C, 100 atm CO_2, and 1 M NaCl) are within the range of conditions observed in GCS sites (31–110°C, 73.8–600 atm, and 0.01–2 M NaCl).[10] For example, the typical conditions are 65°C and 150 atm in the Frio formation,[34] and 63°C and 140 atm in the Weyburn field site.[81] These conditions are also comparable with the 30–130°C and 90 atm values used in a recent laboratory study about water–plagioclase interactions without sulfate under GCS conditions.[82] A sulfate concentration of 0.05 M was used to simulate the sulfate concentration during SO_2 co-injection. The SO_2 in CO_2 emissions from most power plants in the US is between 0.5 and 1 vol%.[128] According to Crandell et al.,[47] the co-injection of 1 vol% SO_2 would result in an equilibrium sulfate concentration of 0.1 M. Considering that sulfate concentration is also affected by the heterogeneity of specific field sites' mineralogies, especially the carbonate minerals in injection sites, 0.05 M sulfate in the current work is a conservatively appropriate starting concentration to investigate the effect of sulfate on plagioclase dissolution. An oxalate concentration of 10 mM was used to simulate the carboxylic acid ligands' concentration in GCS sites. In addition, oxalate can represent ligands with similar structures, such as malonate, with a concentration of 24.9 mM reported.[42] This oxalate concentration is close to the 5.6 mM reported in natural conditions, although a little bit higher than the maximum concentration. Furthermore, higher organic concentrations can occur after CO_2 injection due to the superb solvent capability of $scCO_2$ for organic compounds.[33] A recent study also reported that the concentration of organic compounds was increased by a factor of 100 after CO_2 injection.[34]

To investigate the effects of sulfate on plagioclase dissolution in a far-from-equilibrium system, a low solid/liquid ratio of 0.05 g/L was used. Then, to study the effects of sulfate on secondary mineral precipitation, a high solid/liquid ratio of 0.25 g/L was applied. Although the

solid to liquid ratio can be different from real field site situations, the knowledge obtained here can help us elucidate the mechanisms of sulfate–plagioclase interactions.

A sampling tube equipped with a 2.2 μm HC alloy-276 filter prevented solid loss during *in situ* sampling. A Teflon® liner was installed in the reactor to avoid contamination. The solution was stirred using a magnetic stirrer at 600 rpm. For each sample, 1–2 mL of solution was collected and immediately acidified with 20 μL 67–70% nitric acid (BDH). All solution samples were analyzed with an inductively coupled plasma-optical emission spectrometer (ICP-OES) (Perkin Elmer, Optima 7300DV). The solubility of CO_2 was calculated according to a published model by Duan and Sun.[83] The THERMO database in Geochemist's Workbench (GWB, Release 8.0, RockWare, Inc.) was used, which uses the B-dot equation for the calculation of activity coefficients of aqueous species. *In situ* pH values in the reaction system were obtained using a special pH probe (Corr Instrument, TX) that can function under 1–136 atm and 20–120 °C. In 80 hours, no significant change (± 0.02) in pH was observed at the highest solid to liquid ratio applied in this study. The error between replicates of pH measurement was ± 0.01. The pH of the experimental system without the addition of sulfate was measured to be 3.10. Considering the effects of SO_2 and pre-existing highly soluble minerals, such as carbonate and feldspar,[14] the choice of pH 3.1 can be a starting point to achieve a better understanding of the effect of sulfate on plagioclase dissolution. The method of pH probe calibration is described in the Supporting Information and in our previous study using similar conditions.[110]

4.2.3 Fourier transform infrared (FTIR) spectroscopy analyses and dynamic light scattering measurements

To investigate which types of surface complexes are formed between sulfate and mineral surfaces, FTIR analyses are often applied.[140, 141] Attenuated total reflectance (ATR)-FTIR, which

allows measurement without drying the sample, is usually used to avoid unintended changes of surface complexes by drying.[142, 143] The ATR-FTIR spectra were collected using a Thermo Scientific, Nicolet Nexus 470 spectrometer and a horizontal Ge ATR crystal (Pike Technologies). To magnify the specific surface area, anorthite was ground using a high energy ball mill (SPEX SamplePrep) with an alumina ceramic vial. The ground powder was suspended in ultra-purified water and centrifuged at 5000 rpm for 10 min. The volume mean size of particles in the supernatant was 520 nm, measured by dynamic light scattering (Malvern, Zetasizer, nano series) immediately after ultrasonication. The measurement was done within 3 min. The preparation of anorthite deposition was similar to previous studies.[141-143] Briefly, the supernatant was evenly spread on the Ge crystal and allowed to dry in nitrogen gas. We did not expect any changes in composition during drying due to the slow reaction kinetics of feldspar.[71] The dried deposit was rinsed with ultra-purified water to remove loosely attached particles, so that the deposit that remained was stable and the background of the spectra would not be altered during changing solutions. Before each measurement, the film was coated with a different solution.

The solutions, also used in dissolution experiments, were (a) 1 M NaCl, (b) 0.89 M NaCl + 0.05 M Na_2SO_4, (c) 0.98 M NaCl + 0.01 M $Na_2C_2O_4$, and (d) 0.88 M NaCl + 0.01 M $Na_2C_2O_4$ + 0.05 M Na_2SO_4. All solution ionic strengths are maintained as 1 M. The pH of the solutions was tuned to 3.1, which is same as the *in situ* pH under 90°C, 100 atm CO_2, and 1 M NaCl, using trace metal hydrochloride acid (J.T.Baker). The pH after measurements remained at 3.1. An average of 400 scans with a resolution of 2 cm^{-1} was used. The spectrum with solution (a) was used as background and was automatically subtracted when collecting other spectra. Spectra were deconvoluted using the Omnic 8.2. Gaussian function, which performs better than Voigt and Lorentizians, was used to simulate the peaks. To show the effects of sulfate adsorption on the zeta-

potential (similar to surface potential) of anorthite particles, the ground particles were well mixed

with the solutions described above and injected into the zeta cell (DTS1060C, Malvern Instruments)

after ultrasonication. Zeta-potentials were measured immediately using DLS.

4.2.4 DFT calculations

Calculated Frequency	Intensity	Mode
981	462	S–O– (Al)
997	568	Al–O– (Si)
1074	244	S–O– (symm)
1115	417	S–O– (symm), S–O–(Al), S–O–H
1140	327	S–O– (asymm), S–O–H
1212	302	S–O– (asymm), S–O–H
1268	154	S–O–H, Si–O–H
1451	157	S–O–H, Si–O–H
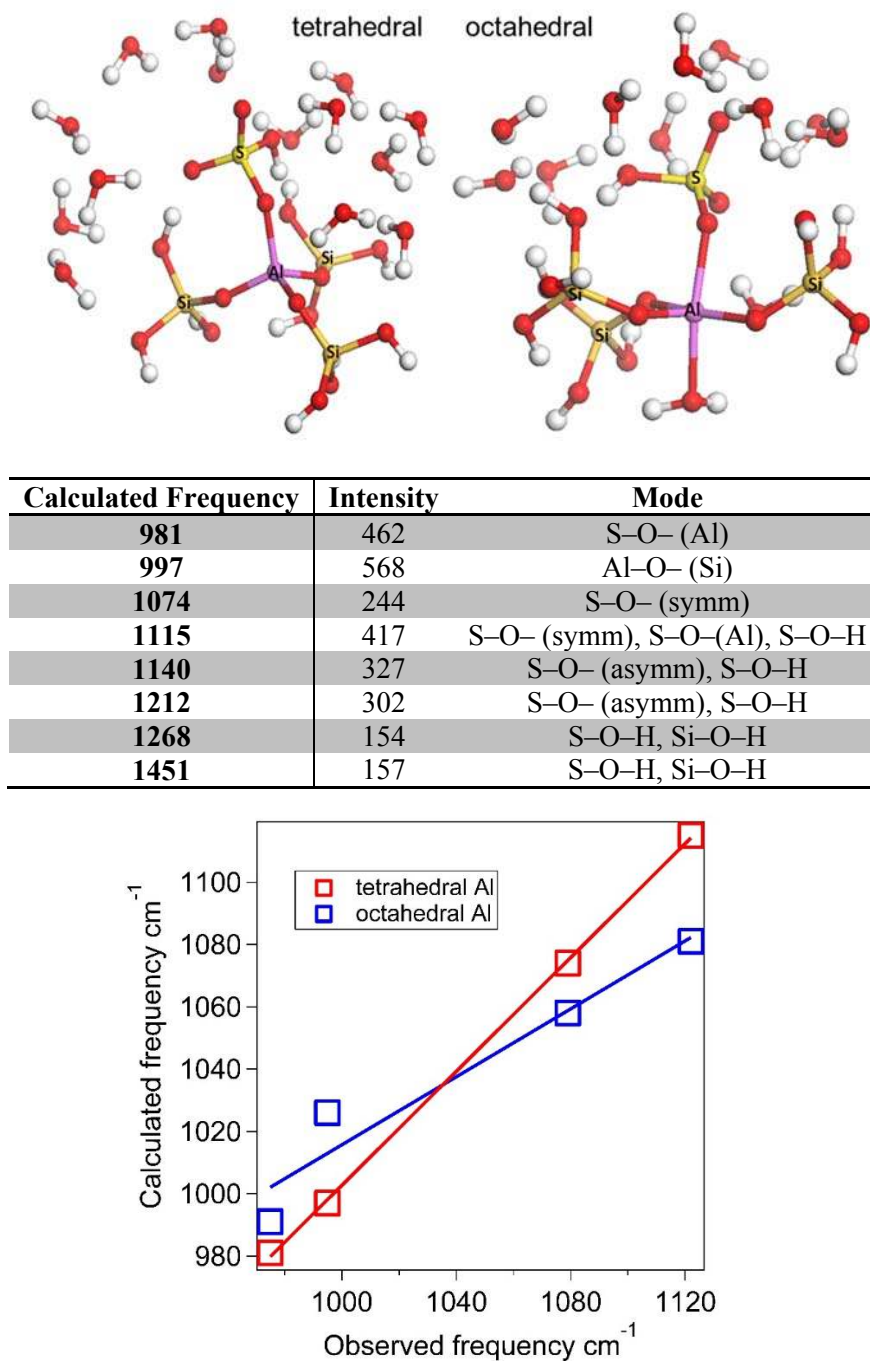
Figure 4.1. (Top) $(Si(OH)_3)_3Al\text{-}HSO_4^-$ and $(Si(OH)_3)_3(OH_2)_2Al\text{-}HSO_4^-$ surface models. (Middle) Calculated frequencies of $Q^3\text{-}^{[4]}Al\text{-}HSO_4^-\cdot13(H_2O)$. (Bottom) Correlation between observed and calculated frequencies. Lines are linear fittings of frequencies. Peaks at 981, 997, 1074, 1115, 1140, 1212, 1268, and 1451 cm^{-1} were predicted, corresponding to symmetric and asymmetric S–O stretching vibrations and S–O–H vibrations. The tetrahedral model ($R^2 = 0.999$, slope = 0.91, intercept = 88 cm^{-1}) showed a better correlation with ATR-FTIR observations than the octahedral model ($R^2 = 0.989$, slope = 0.84, intercept = 183 cm^{-1}). Peaks in high frequencies were not observed.

DFT calculations were performed using the program Gaussian 09.[144] The B3LYP exchange-correlation function,[145, 146] was used along with the 6-31G(d) basis set.[147] Surface models of the tetrahedral Al, $(Si(OH)_3)_3Al$, and octahedral Al, $(Si(OH)_3)_3(OH_2)_2Al$, were derived from Criscenti et al..[148] Models of the HSO_4^- surface complexes were constructed manually, using the Visualizer module of Materials Studio (Accelerys Inc., San Diego, CA). To account for solvation effects (i.e., H-bonding) on the vibrational frequencies of the HSO_4^-, 10 and 13 H_2O molecules were added to the $(Si(OH)_3)_3Al-HSO_4^-$ and $(Si(OH)_3)_3(OH_2)_2Al-HSO_4^-$ surface models, respectively (Figure 4.1). Atoms were allowed to freely relax during energy minimizations without constraint or imposition of symmetry. Analytical frequencies were calculated and scaled by 0.9614,[149] to account for anharmonicity and computational error.[150]

4.2.5 Secondary mineral phase identification

After the reaction at 90°C and 100 atm CO_2, solid samples were collected, rinsed with ultrapure deionized water and ethanol, and dried in nitrogen. Scanning electron microscopy and energy-dispersive x-ray spectroscopy (SEM-EDX, Nova NanoSEM 230) were used to observe the morphology and the elemental compositions of precipitates. Samples were coated with AuPd to increase their conductivity, and 10.00 kV was the electron accelerating voltage. The working distance was 5−6 mm. High resolution transmission electron microscopy (HR-TEM, JEOL JEM-2100F field emission) was also used to identify the *ex situ* phase of the secondary minerals. Solid samples after reactions at 90°C and 100 atm CO_2 were sonicated in ethanol for 10 min to detach precipitates. A drop of suspension was placed on a Formar/carbon coated-Cu grid, dried, and stored under nitrogen gas. By matching the d-spacings in electron diffraction patterns of samples, potential phases of secondary minerals were identified. There are, however, caveats that some

small quantity of secondary mineral phases or poorly crystalline phases cannot be detected by this identification procedure, and the *ex situ* phase can be different from the *in situ* phase.

4.3   Results and Discussion

4.2.1 Effects of sulfate on plagioclase dissolution
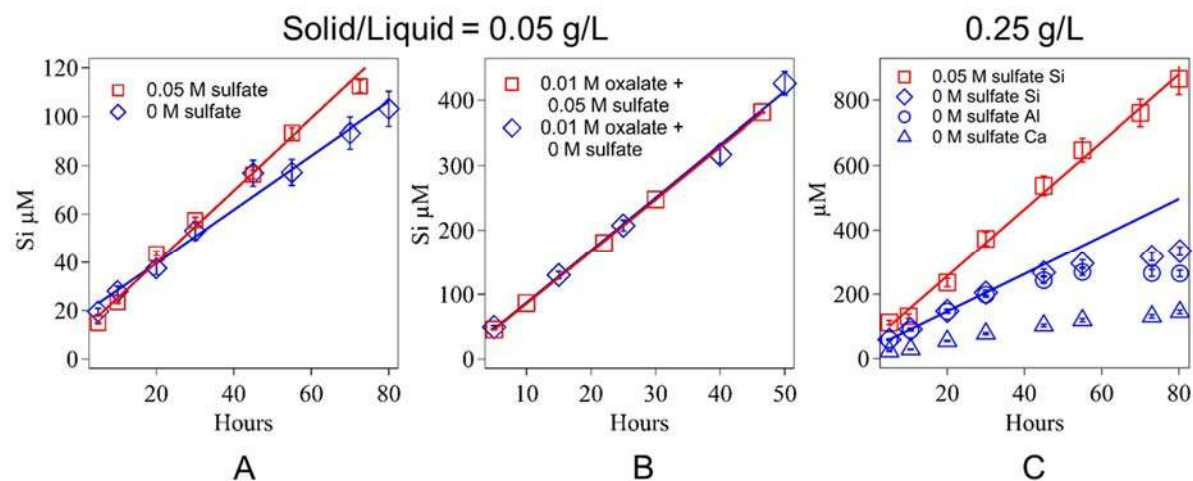
Figure 4.2. Dissolved ion concentrations at 90°C, 100 atm CO_2, and in 1 M NaCl. *In situ* pH values were all controlled at 3.1. Error bars are the ±% difference between dissolution rates of duplicate experiments. At a solid-to-liquid ratio of 0.05 g/L, the addition of 0.05 M sulfate enhances dissolution. With the addition of 0.01 M oxalate, sulfate does not show any effect. At a solid-to-liquid ratio of 0.25 g/L, similar enhancing effects were observed in the first 30 hours. The blue line shows the linear fitting of Si data in first 30 hours. Beyond 30 hours, without sulfate, the dissolution rate slows down. In contrast, with sulfate, the slope does not change within 80 hours. The observation is attributed to the formation of aqueous phase Al–sulfate complexes, which inhibit secondary precipitation and enhance apparent dissolution. Rates and concentrations of other elements are available in Table 4-S2 and 4-S3.

Within 80 hours, the Si concentrations increased with time according to zeroth order kinetics (Figure 4.2). The dissolution rates based on Si, Ca, and Al are available in the Supporting Information (Table 4-S2). The dissolution of Ca, Al, and Si were congruent, except at the high solid- -to-liquid ratio (0.25 g/L), in which secondary precipitation formed. For other experiments, good linearity was maintained from 5 to 80 hours, indicating that the dissolution rates reached steady-state. The slope was used to calculate the dissolution rates. The rate of anorthite dissolution (based on the Si release rate of 1.82×10^{-7} mol·m^{-2}·s^{-1}, divided by the stoichiometric ratio of Si,

2.06) without sulfate ions was 8.86×10^{-8} mol·m^{-2}·s^{-1}, which is comparable with a previous study

by Oelkers et al. under 45–95 ºC and pH 2.4–3.2.[71] On the other hand, 0.05 M sulfate was found

to have a 36% enhancement on the dissolution rate of anorthite.

This enhancing effect supports the prediction of previous studies using gibbsite.[51] However,

the extents of enhancements are different. Bloom and Erich reported 50 times faster dissolution of

gibbsite in the presence of sulfate than of nitrate at 25 or 40ºC.[151] Packter and Dhillon found 15–

30 times faster dissolution in the presence of sulfate than that in perchloric acid solution at 20 to

65ºC.[50] However, as pointed out in Ridley et al.'s study,[51] these studies did not maintain the same

pH and ionic strength. In our systems, *in situ* pH and ionic strength were maintained at 3.1 and

1 M ionic strength. Ridley et al. reported 10 times faster dissolution in the presence of sulfate than

in the presence of chloride at 5ºC at pH 2 and 0.1 m ionic strength, and these effects were related

to aqueous complexation between sulfate and Al^{3+}(aq).[51] In contrast, in our experimental system,

reactions were far-from-equilibrium. According to thermodynamic calculations using GWB, the

chemical affinity was greater than 98.9 kJ/mol for all the experiments in this study. In this regime

($\Delta G/RT < -4.6$), the dissolution rate is not a function of the saturation ratio of the system. This is

because the thermodynamic term in the dissolution rate equation, expressed by $\{1-\exp(\Delta G/RT)\}^n$,

is almost equal to 1 in our experimental system, where n is a positive constant given by empirical

data fitting.[88, 152] Therefore, aqueous complexation cannot explain our observations. Dietzel and

Bohme observed similar effects of sulfate on gibbsite, but they explained the effects using surface

adsorption.[49] We hypothesized that the enhancing effect we observed was also owing to sulfate

adsorption on mineral surfaces. In previous studies, the formation of binuclear bidentate surface

complexes between sulfate and iron hydroxides was used to explain the inhibition effects.[135, 136]

However, binuclear complexes are not expected on plagioclase because there are no Al sites close

to each other, due to the Al avoidance principle.[153] On the other hand, monodentate surface complexes can enhance dissolution by increasing the pH of zero net proton charge (pHpznpc, the condition when the surface concentration of adsorbed proton is equal to surface concentration of adsorbed OH$^-$), facilitating surface protonation.[137] Thus it enhances proton promoted dissolution, which is the dominant dissolution mechanism of plagioclase at pH 3.[38] Therefore, the formation of monodentate complexes between sulfate and anorthite could occur. To test this hypothesis, zeta potential analyses, ATR-FTIR experiments, and molecular simulations were conducted and are described in the following section.

4.2.2 Adsorption of sulfate on anorthite surfaces

To test the adsorption of sulfate on anorthite, we first conducted zeta potential analyses of samples. The zeta potential of the anorthite system in the presence of sulfate at pH 3.1 was found to be 0.23 mV, compared to 4.1 mV in the absence of sulfate. This difference indicates that the adsorption of sulfate decreased the surface potential of the anorthite. Owing to the specific adsorption of sulfate, the fixed surface charge became less positive. The binding of sulfate led to the release of OH$^-$ from anorthite surfaces, which increased the pHpznpc. This kind of anion adsorption increases the concentration of surface protons,[137] and can change the apparent pH dependency and facilitate dissolution.
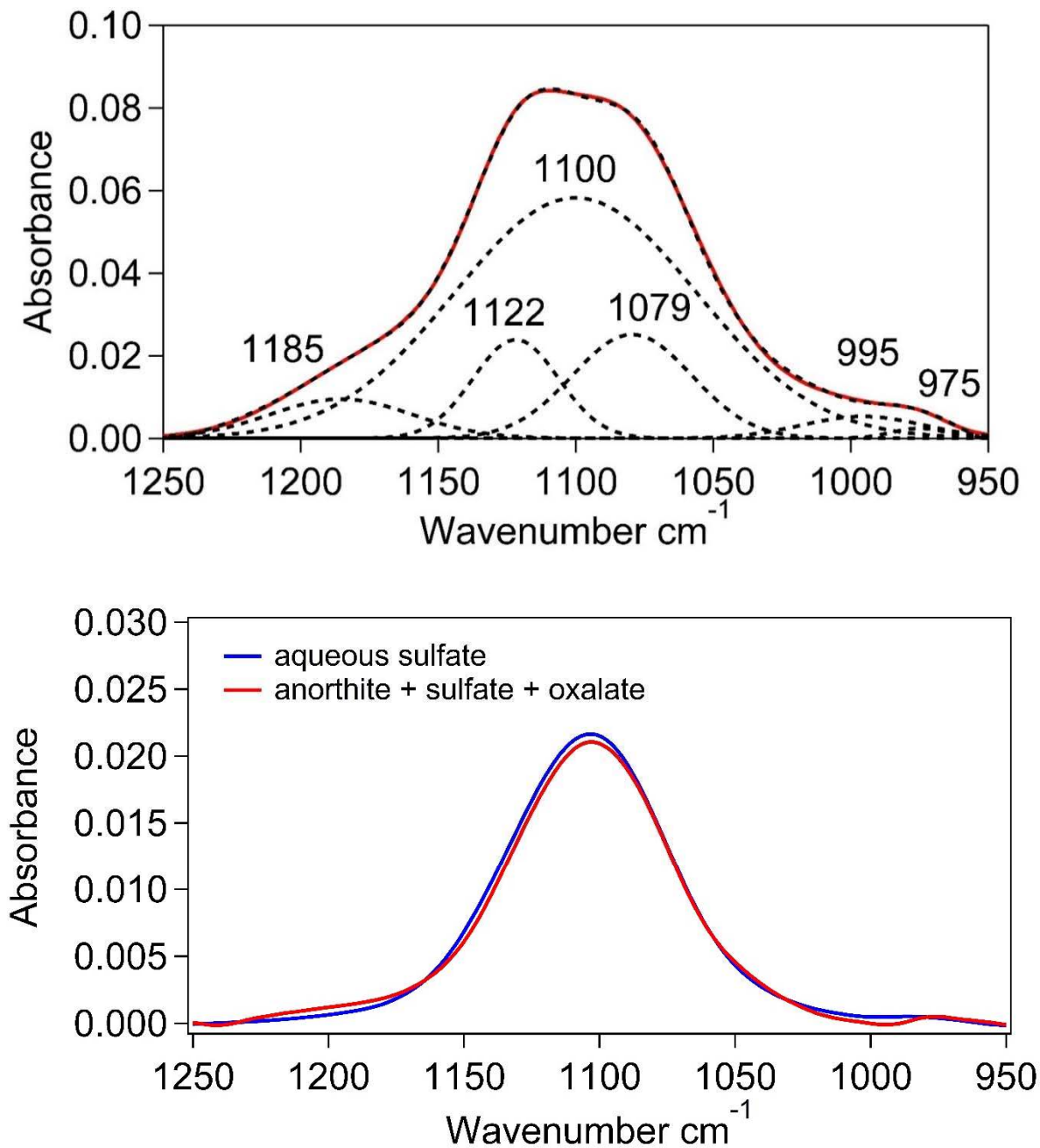
Figure 4.3. (Top) ATR-FTIR spectra of anorthite contacted with 0.89 M NaCl + 0.05 M Na$_2$SO$_4$ at pH 3.1. Spectra of anorthite contacted with 1 M NaCl was used as background. By deconvolution of peaks in the spectrum, the peak of aqueous sulfate at 1100 cm^{-1} was shown. Peaks at 975, 1079, and 1122 cm^{-1} were attributed to the monodentate surface complexes. Shoulders at 995 and 1185 cm^{-1} were attributed to the effects of Na and protons. The spectrum of anorthite is available in Supporting Information. (Bottom) The red line is the ATR-FTIR spectrum of anorthite contacting with 0.88 M NaCl + 0.05 M Na$_2$SO$_4$ + 0.01 M Na$_2$C$_2$O$_4$ at pH 3.1. The spectrum of anorthite contacting with 0.98 M NaCl + 0.01 M Na$_2$C$_2$O$_4$ was used as background. The blue line is the spectrum of a solution of 0.89 M NaCl + 0.05 M Na$_2$SO$_4$ at pH 3.1. A solution of 1 M NaCl was used as background. The red and blue lines are similar: in each only the main peak in 1100 cm^{-1} was observed, which indicates that sulfate adsorption was suppressed by oxalate.

96

The specific type of surface complexation was investigated using ATR-FTIR. According to recent studies,[141-143] two vibrations of S–O bonds are accessible: symmetric stretching and asymmetric stretching. For aqueous sulfate, symmetric stretching is not active, and only asymmetric stretching at 1100 cm^{-1} is shown. If sulfate is outer spherically adsorbed, symmetric stretching at 975 cm^{-1} will be active. If sulfate ions form monodentate complexes with metal cations on mineral surfaces, asymmetric stretching will split into two bands. For goethite or Al oxides, the two bands are located at 1070 and 1030 cm^{-1}.[141] We observed peaks at 1100 and 975 cm^{-1}, which indicated aqueous sulfate and outer spherically complexed sulfate (Figure 4.3). We also observed broadening of the 1100 cm^{-1} peak. By deconvolution, two peaks at 1079 and 1122 cm^{-1} were shown. These peaks suggest monodentate complex formation. There are also two shoulders at 995 and 1185 cm^{-1}. These peaks are comparable with 1000 and 1170 cm^{-1} shoulders observed in sulfate–goethite systems,[143] which are attributed to monodentate HSO_4^- and $NaSO_4^-$ adsorption on anorthite surfaces. This attribution is consistent with the low pH 3.1 and high concentration of Na in our solutions.

Because recent experimental studies used goethite or Al oxide instead of plagioclase,[141, 143] we conducted simulation work to confirm our ATR-FTIR observations. Simulations for monodentate and bidentate surface complexation of sulfate with Al sites on the anorthite surface were conducted. Bidentate, mononuclear surface complexes were found to be unstable, forming monodentate, mononuclear surface complexes during energy minimization. This result is consistent with the fact that we did not observe the existence of bidentate, mononuclear surface complexes from ATR-FTIR spectra. Therefore, results obtained using monodentate surface complexation models were compared with ATR-FTIR observations. The scaled calculated frequencies from the DFT calculations (981, 997, 1074, and 1115 cm^{-1}, corresponding to

symmetric and asymmetric S–O stretches) for the tetrahedral $(Si(OH)_3)_3Al–HSO_4^-$ model show a good correlation (Figure 4.1 Bottom, R^2 = 0.999, slope = 0.91, intercept = 88 cm^{-1}) with our observed frequencies (Figure 4.1C, 975, 995, 1079, and 1122 cm^{-1}), despite the fact that the high frequencies in the calculated results (1212, 1268, and 1451 cm^{-1}, corresponding to S–O–H vibrations) were not observed. In a recent study of phosphate adsorption on goethite, the high frequencies were also not observed.[154] Furthermore, the octahedral $(Si(OH)_3)_3(OH_2)_2Al–HSO_4^-$ model resulted in a poorer correlation (R^2 = 0.989, slope = 0.84, intercept = 183 cm^{-1}) of calculated versus observed frequencies. The S–O–H bending modes in this model were different from the tetrahedral model —1224 and 1406 cm^{-1}. The differences are likely due to H-bonding differences between the models, which may explain why the higher frequency modes are not observed. The models produce only one H-bonding configuration, but the samples may contain a wide variety of H-bonding configurations that tends to broaden the mode intensity.

These simulation results provide direct support for our hypothesis that sulfate formed monodentate complexes with tetrahedral Al sites (although octahedral Al sites cannot be completely ruled out without ^{27}Al NMR studies) on the anorthite surface. Based on ATR-FTIR data and DFT calculation results, we concluded that the adsorption of sulfate on anorthite is monodentate. Previous studies using gibbsite suggested that monodentate complexation by bivalent anions can enhance dissolution.[49, 137] This conclusion suggests that sulfate is likely to enhance plagioclase dissolution under atmospheric conditions. It is also consistent with the enhanced dissolution effects we observed under conditions relevant to GCS.

There is a caveat that the FTIR and DLS analysis were conducted under room temperature and atmospheric pressure. Because references about the relationship between sulfate adsorption on anorthite and temperature are generally not available, we cannot estimate the potential

differences between the high pressure and high temperature situations and our FTIR and DLS observations under atmospheric conditions. However, as the experimental observations and simulated results of adsorption are consistent with the promoted dissolution, we suggest that the mechanisms can be similar under GCS conditions.

4.2.3 Effects of sulfate on plagioclase dissolution in the presence of oxalate

Further evidence for sulfate adsorption was observed in the presence of oxalate. The adsorption of sulfate on anorthite can compete with the adsorption of oxalate, which can co-exist in GCS sites. A total oxalate concentration of 0.01 M was found to enhance the dissolution of anorthite by a factor of 7.02, compared with 1.36 by 0.05 M sulfate (Figure 4.2). With a much weaker dissolution promotion, the competing adsorption of sulfate on reactive surface sites will surely weaken the effects of oxalate. However, with coexistence of sulfate and oxalate, we observed a factor of 7.27, which is similar to the 7.02 with only oxalate. This observation indicates that sulfate does not compete with oxalate on the reactive surface sites, probably because oxalate forms bidentate mononuclear complexes and a five member ring with aluminum,[155] which would be much more stable than monodentate complexing by sulfate. This explanation may also explain the much stronger dissolution enhancement induced by oxalate than sulfate (Figure 4.2). Because sulfate is too weak to compete with oxalate, its adsorption is mitigated by a large concentration of oxalate. This reasoning is consistent with our ATR-FTIR observations that only the peak of aqueous sulfate at 1100 cm^{-1} can be detected in presence of oxalate (see Figure 4.3), which indicates that adsorption of sulfate on anorthite was suppressed by oxalate. Competing adsorption indicates that the observed enhanced dissolution effects of sulfate were due to interactions with plagioclase surfaces. Sulfate and oxalate are absorbed on the same sites, which are suspected to be

aluminum sites.[53] Therefore, the role of sulfate in plagioclase dissolution is highly dependent on the relative abundance of organic ligands in CO_2 storage sites.

4.2.4 Effects of sulfate on secondary mineral precipitation

Measured d-spacing	boehmite Ref.[156]	Crystal plane
6.12	6.11350	200
3.17	3.16541	210
3.06	3.05675	400
2.36	2.35657	410
2.33	2.34439	301
2.05	2.03783	600
1.86	1.86026, 1.85000	501, 020
1.76	1.77070	220
1.67	1.66202	511
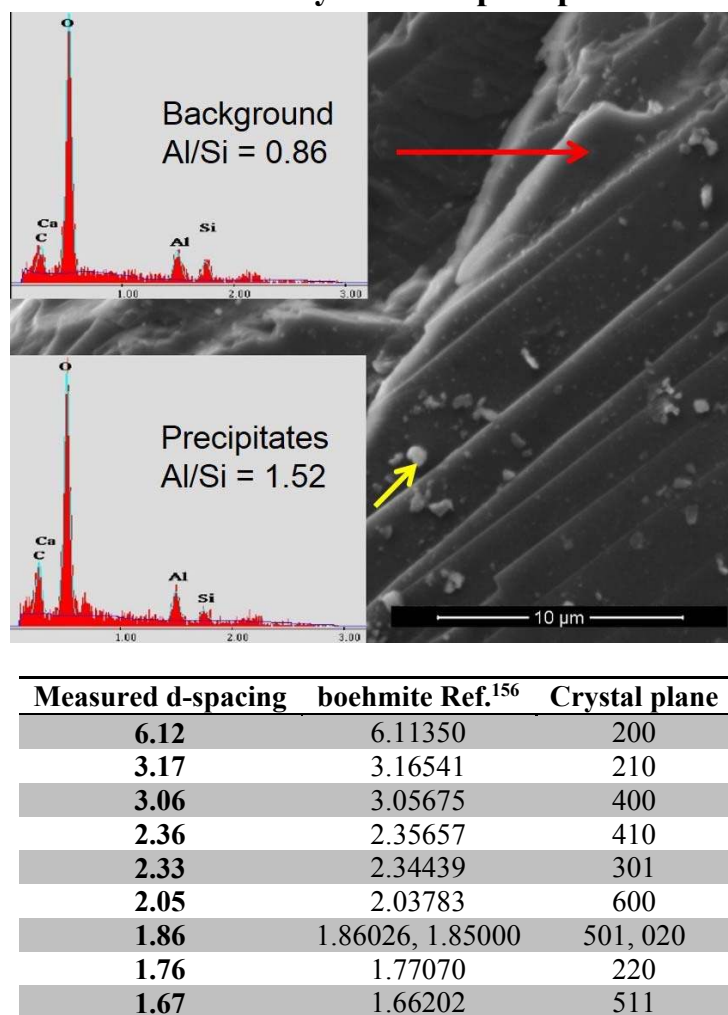
Figure 4.4. Scanning electron microscopy image of anorthite particle after 80 hours reaction in 1 M NaCl at 90ºC and 100 bar CO_2. Small particles were found on the surface of bulk particles. The energy dispersive x-ray spectroscopy analysis of the background (red arrow) and a small particle (yellow arrow) showed that the Al/Si ratios were 0.86 and 1.52 respectively. By matching the electron diffraction pattern, the small particle was identified as boehmite (γ–AlOOH). The Si signal likely results from background.

To investigate the effects of sulfate on subsequent mineral precipitation, a higher solid-to-liquid ratio of 0.25 g/L was applied, instead of the 0.05 g/L used above. For the high solid-to-liquid ratio experiments, we focused on the effect of anorthite reactions in the presence and absence of sulfate with no oxalate present. In the absence of sulfate, the net ion release rates decreased

100

significantly as the reaction time increased to 80 hours (Figure 4.2C). During the first 30 hours of reaction, the linearity of Si concentration as a function of time is generally good. The sulfate was found to increase the net Si release rate by a factor of 1.4, which is consistent with the 36% enhancement observed in low solid-to-liquid ratio conditions. Between 40 and 80 hours, the net ion release rates decreased rapidly. The significant decrease of the net ion release rates could be attributed to the formation of secondary mineral precipitates. As a high solid-to-liquid ratio was applied, the activities of aqueous metal cations could reach a higher level. Although the activity of cations is not high enough to significantly decrease the chemical affinity, they could lead to formation of secondary mineral precipitation if saturation was reached. The accumulated concentration of aluminum increased slower than the concentration of silicon (Table 4-S2), which suggests the formation of precipitation with an Al/Si ratio larger than 1. By SEM and TEM data, we identified boehmite as the precipitate phase formed on the anorthite surface (Figure 4.4). Although GWB calculations predict that boehmite is under-saturated under our conditions, the anorthite surface could act as a substrate for heterogeneous nucleation, which requires a lower free energy than homogeneous nucleation.[157] Formation of boehmite and kaolinite was suggested in different studies about CO_2–water–plagioclase interactions under GCS conditions.[65, 158-160] While kaolinite has a Al/Si ratio equal to 1, boehmite contains only aluminum, and is thought to form earlier than kaolinite.[159] In this study, no evidence for the formation of kaolinite or other precipitate phases was identified. However, the existence of an amorphous phase which cannot be identified by electron diffraction is possible. The decreased release rates of Ca and Si can also result from the surface coverage of secondary precipitation, surface adsorption, or incorporation into boehmite. A recent work on anorthite dissolution reported the incorporation of Si in boehmite.[159]

Interestingly, in the presence of sulfate, the dissolution rate did not change significantly within 80 hours, which is attributed to the absence of secondary precipitation. Sulfate could form aqueous complexes with aluminum, decrease its activity, and thus lower the apparent saturation indices of precipitates. At 90°C, 100 atm CO_2, 1 M NaCl, and 0.05 M sulfate, more than 92% of aluminum forms aluminum–sulfate complex (Figure 4-S2). No precipitation was identified in experiments with sulfate. As a result, with increasing concentration of dissolved Al cations, the aqueous complexation between Al cations and sulfate can strongly affect the apparent dissolution rate of plagioclase.

4.4 Environmental Implications

In this study, for the first time, we have reported that sulfate forms monodentate surface complexes with Al sites on anorthite surfaces at pH 3.1 and 1 M NaCl concentration. The adsorption of sulfate can facilitate the dissolution of anorthite. However, both of these effects will be suppressed in the presence of oxalate. For high solid-to-liquid ratios, the effects of sulfate on apparent plagioclase dissolution are dominated by the formation of aqueous phase complexes with Al^{3+}(aq). This new information indicates that both the concentration of sulfate and the concentration of organic ligands, such as oxalate, need to be known in order to better predict the dissolution of plagioclases. Plagioclase dissolution can result in significant changes in the permeability of rocks, particularly if it occurs in pore throats, as a previous study pointed out that most of the pore throats in sandstone have nm sizes.[102] Plagioclase dissolution and subsequent secondary precipitation could also lead to changes in wettability,[161] which is a critical factor affecting the transport of CO_2. Thus, the findings here could be helpful in predicting the transport of CO_2 and the impact of SO_2 co-sequestration. They may also be applicable to other aluminum-containing minerals and studies of other areas which involve sulfate and plagioclases, including

corrosion caused by acid rain, acid mine drainage, interaction between seawater and oceanic ridges, and reactions on ancient Mars, where sulfuric acid and plagioclases were abundant.

Acknowledgments

Supporting Information for Chapter 4

Contents: Experimental details

Three figures

Three tables

S4.1. *In situ* pH measurements

In situ pH values in the reaction system were obtained using a pH probe (Corr Instruments, TX). The glass-based probe was coupled with an Ag/AgCl reference electrode that can function under 1–136 atm and 20-120ºC. The tubing of the electrode was made of HC alloy C-276. The method of pH probe calibration was described in our previous study using similar conditions.[110] Standard solutions made by NaCl and HCl were used to make calibration curves. The pH values of standard solutions were predicted by Geochemist's Workbench (GWB, Release 8.0, RockWare, Inc.). Combined with the mV values measured by the probe, a linear function relationship was found between the pH and mV values. Based on the mV values, the pH of the solutions can be calculated. In 120 hours, no significant change ($\pm$ 0.05) in pH was observed with the highest solid-to-liquid ratio applied in this study. The error between replicates of pH measurement was between $\pm$ 0.01. The pH of the experiment without the addition of sulfate was measured to be 3.10.

Table 4-S1. X-ray fluorescence (XRF) analysis of anorthite used in this study (in weight %).

	Anorthite
SiO_2	44.09
CaO	19.07
Al_2O_3	35.13
TiO_2	0.00
Fe_2O_3	0.57
MnO	0.00
MgO	0.64
Na_2O	0.43
K_2O	0.01
P_2O_5	0.00
Loss on ignition	0.06

Table 4-S2. Dissolution rates of different elements and error range between replicates. (R in mol $\times$ m^{-2} $\times$ s^{-1})

Experiment	R_{Al} $\times$ 10^7	Error ±%	R_{Ca} $\times$ 10^7	Error ±%	R_{Si} $\times$ 10^7	Error ±%	R^2	Al/Si	Ca/Si
Solid/Liquid = 0.05 g/L in 1 M NaCl	1.80	0.8	9.65	0.1	1.82	7.0	0.9895	0.99	0.53
Solid/Liquid = 0.05 g/L in 0.89 M NaCl + 0.05 M Na$_2$SO$_4$	2.17	1.3	1.13	1.8	2.47	2.2	0.9980	0.88	0.46
Solid/Liquid = 0.05 g/L in 0.98 M NaCl + 0.01 M Na$_2$C$_2$O$_4$	12.7	5.3	5.72	5.0	12.7	4.2	0.9956	1.00	0.45
Solid/Liquid = 0.05 g/L in 0.88 M NaCl + 0.01 M Na$_2$C$_2$O$_4$ + 0.05 M Na$_2$SO$_4$	12.7	0.4	6.98	0.6	13.2	0.3	0.9999	0.96	0.53
Solid/Liquid = 0.25 g/L in 1 M NaCl	1.01	11.2	0.59	10.8	1.25	4.0	0.9399	0.81	0.47
Solid/Liquid = 0.25 g/L in 0.89 M NaCl + 0.05 M Na$_2$SO$_4$	2.79	11.5	1.45	8.4	3.20	5.6	0.9952	0.87	0.45

Table 4-S3. Concentrations of Al, Si, and Ca in aqueous samples. (Concentrations in µM)

Solid/Liquid = 0.05 g/L 1 M NaCl				Solid/Liquid = 0.05 g/L 0.89 M NaCl + 0.05 M Na_2SO_4			
Hours	Al (µM)	Si (µM)	Ca (µM)	Hours	Al (µM)	Si (µM)	Ca (µM)
5	22.85	18.29	14.00	5	14.39	14.79	6.50
10	35.13	26.16	12.92	10	22.24	23.35	9.47
20	45.63	35.01	19.26	20	40.42	43.67	20.47
30	58.77	49.61	26.85	30	53.20	57.58	25.72
45	77.41	71.86	40.37	45	72.07	76.35	33.55
55	84.08	72.17	49.88	55	85.91	93.34	39.39
70	100.54	87.16	49.71	72.5	103.33	112.40	51.95
80	106.33	96.37	52.84	79.75	119.89	131.44	60.68
Solid/Liquid = 0.05 g/L 0.98 M NaCl + 0.01 M $Na_2C_2O_4$				Solid/Liquid = 0.05 g/L 0.88 M NaCl + 0.01 M $Na_2C_2O_4$ + 0.05 M Na_2SO_4			
Hours	Al (µM)	Si (µM)	Ca (µM)	Hours	Al (µM)	Si (µM)	Ca (µM)
5	57.41	49.25	19.35	5	43.90	45.37	31.74
15	136.12	130.01	57.02	10	83.49	86.57	58.07
25	223.79	207.49	91.49	22	175.13	180.51	100.30
40	330.34	316.96	136.30	30	241.23	247.81	142.53
50	433.88	425.89	192.52	46.5	366.21	381.45	212.30
Solid/Liquid = 0.25 g/L 1 M NaCl				Solid/Liquid = 0.25 g/L 0.89 M NaCl + 0.05 M Na_2SO_4			
Hours	Al (µM)	Si (µM)	Ca (µM)	Hours	Al (µM)	Si (µM)	Ca (µM)
5	58.99	58.76	22.39	5	92.94	111.76	33.05
10.5	88.78	90.74	28.89	10	120.44	130.99	48.97
20	146.15	147.41	54.95	20	217.52	236.16	90.32
30	197.81	204.31	77.39	30	348.11	372.79	149.93
45	243.34	267.37	102.58	45	512.40	537.32	230.84
55	268.82	295.63	118.90	55	605.33	647.41	285.18
73	265.54	317.12	130.58	70	686.61	760.30	338.62
80.25	264.28	334.28	144.38	80	792.99	865.55	384.88
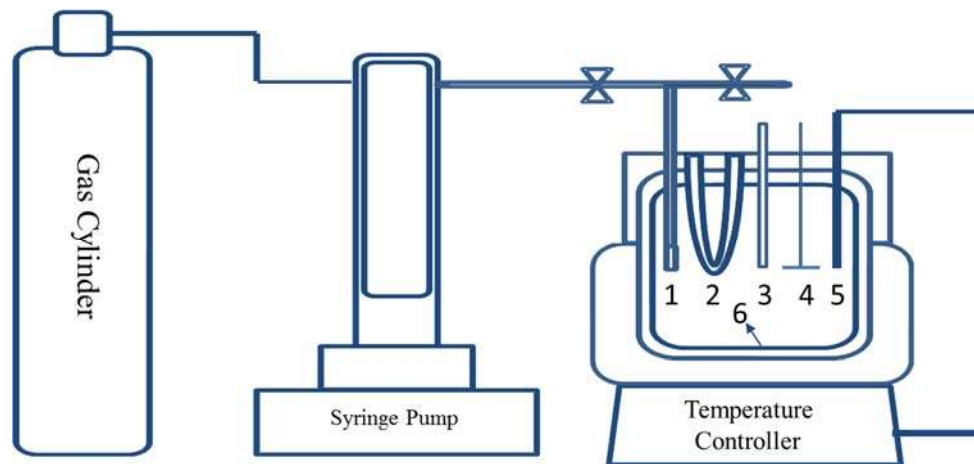
Figure 4-S1. Experimental setup. 1, *In situ* sampling tube; 2, Cooling loop; 3, pH probe; 4, Stirrer; 5, Thermocouple; 6, Teflon liner.
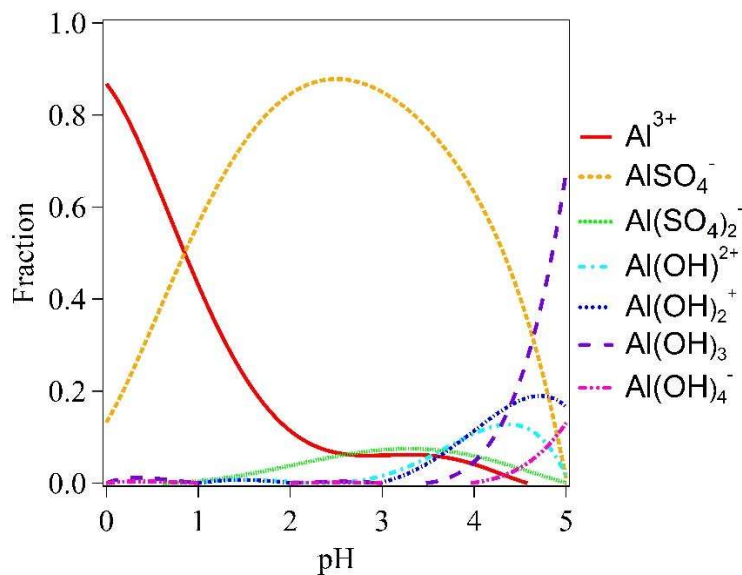
Figure 4-S2. The fraction of aluminum species at different pH ($0 < pH < 5$) in the presence of 0.05 M sulfate. All calculations were conducted using GWB at 100 bar CO_2 and 1 M NaCl, and 90°C. More than 92% of Al is complexed with sulfate at pH 3.1. This effect is not significantly changed by temperature and pressure. At 25 °C and atmospheric pressure, the fraction of Al complexed

with sulfate is 90%. Although GWB did not considered all possible species,[162] the calculation suggested that presence of sulfate can significantly decrease the activity of Al^{3+}.
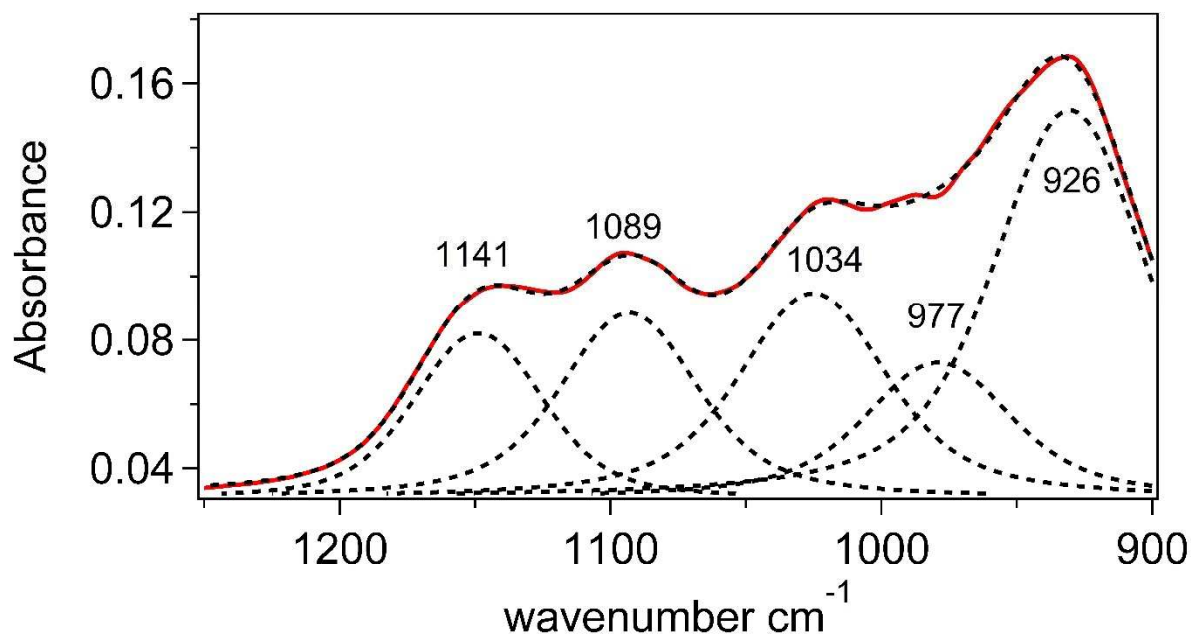
Figure 4-S3. ATR-FTIR Spectra of dry anorthite particles using a dry Ge crystal as background. All the observed peaks were assigned to asymmetric Si–O stretching vibrations.[163] The deconvolutions of spectra were conducted using the Omnic 8.2. Voigt function, which performs better than Gaussian and Lorentzian, was used to simulate the peaks.

Chapter 5: Wollastonite Carbonation in Water-bearing Supercritical CO$_2$: Effects of Particle Size

Abstract

Geologic CO$_2$ sequestration (GCS) is considered an important option for mitigating the adverse impacts of global climate change. The performance of GCS can be affected by CO$_2$ mineralization and changes in the permeability of geologic formations resulting from interactions between water-bearing supercritical CO$_2$ (scCO$_2$) and silicates in reservoir rocks. However, without understanding size effects, the findings in previous studies using nanometer or micrometer size particles cannot be applied to the bulk rock in field sites. In this study, we report the effects of particle sizes on the carbonation of wollastonite (CaSiO$_3$) at 60 ℃ and 100 bar in water-bearing scCO$_2$. After normalization by the surface area, the thickness of the reacted wollastonite layer on the particle surfaces was independent of particle sizes. After 20 hours, the reaction was not controlled by the kinetics of surface reactions, but by the diffusion of water-bearing scCO$_2$ across the product layer on wollastonite particle surfaces. Among the products of reaction, amorphous silica, rather than calcite, covered the wollastonite surface and acted as a diffusion barrier to water-bearing scCO$_2$. The product layer was not highly porous, with 10 times smaller specific surface area than the altered amorphous silica formed at the wollastonite surface in aqueous solution. These findings can help us evaluate the impact of mineral carbonation in water-bearing scCO$_2$ on GCS operations.

5.1 Introduction

In Chapters 2, 3, and 4, we investigated aqueous phase dissolution. In the following chapters, we will discuss a reaction in the non-aqueous phase, the carbonation of silicate in water-bearing CO_2. While most previous studies on $scCO_2$–water–rock chemical interactions focused on mineral dissolution and precipitation in the presence of bulk aqueous phase,[14] recent studies have revealed the following importance of interactions between $scCO_2$ and minerals in the absence of aqueous solutions.[13, 29, 100] First, because injected $scCO_2$ will displace brine, most of the contact areas between $scCO_2$ and caprocks and a certain portion of the contact areas between $scCO_2$ and formation rocks, are in the absence of bulk aqueous solution.[164] Second, $scCO_2$ has higher diffusivity, lower viscosity, and thus lower capillary entry pressure than aqueous phase fluid (i.e., CO_2-dissolved brine).[21] Therefore, $scCO_2$ can enter smaller pore throats which brine cannot enter. Third, recent studies reported that water dissolved in $scCO_2$ has higher reactivity on mineral surfaces than that of water in the aqueous phase.[21, 28, 29] Based on these considerations, the reactions of minerals with water-bearing $scCO_2$ are at least equally, if not more, important than reactions of mineral with aqueous solutions.[21, 56]

Our current understanding of water-bearing $scCO_2$–mineral interactions focuses on the carbonation of various Ca-, Mg-, or Fe-bearing minerals, including wollastonite,[30, 54, 59, 62] forsterite,[55-58, 61, 164] fayalite,[60] dolomite,[165] and phlogopite.[29] While these studies investigated the effects of the water saturation percentage of CO_2,[56, 57, 59, 61, 166] temperature,[55, 59, 60, 62] and organic ligands,[58] on carbonation reactions, we need a better understanding of the dependency of water-bearing $scCO_2$–silicates reactions on particle sizes. There are several knowledge gaps: First, previous studies mostly used micrometer or even nanometer size particles,[30, 54-62] a far cry from the bulk rock in field sites. Without understanding the effects of particle sizes, we cannot know

whether the outcomes obtained with small particles are applicable to bulk rock in field sites. Second, findings from different studies are not directly comparable due to the different particle sizes used. Thus, results from previous studies on water-bearing $scCO_2$–silicate reactions cannot be combined. Third, investigating the effects of particle sizes can reveal the mechanisms of mineral carbonation reactions. For example, a recent study of metal oxide carbonation (i.e., CaO) in dry CO_2 found that the reacted fraction is constant for different particle sizes and concluded that the reaction extent of CaO carbonation is determined by the porosity of CaO particles.[167] Similarly, investigating the effects of particle sizes on silicate carbonation in water-bearing $scCO_2$ can inform us about whether the reaction is controlled by the porosity of silicates or other limiting factors, such as the kinetics of silicate dissolution in water films. However, to the best of the authors' knowledge, there have been no studies on the effects of particle sizes on water-bearing $scCO_2$–silicate interactions.

The goal of this study is, therefore, to understand the effects of particle size on the carbonation of wollastonite in water-bearing $scCO_2$. We chose wollastonite because it has been frequently used as a representative of silicates in previous studies on silicate reaction in $scCO_2$ and in aqueous solutions.[59, 62, 168, 169] While not necessarily abundant in field sites, wollastonite has a similar structure to pyroxene, which is abundant in mafic rocks and some GCS sites.[170] More importantly, compared to other silicates, such as plagioclase, the reaction extent of wollastonite can be detectable even with relatively large particle sizes in a short time scale, which makes it highly suitable for investigating effects of particle sizes systematically and thoroughly. We hypothesize that the reaction is controlled by the kinetics of wollastonite hydrolysis, so that the reaction extent of different size particles should be similar after normalization to surface area. To test this working hypothesis, particles with five different size ranges were reacted at 60 °C and 100

112

bar, conditions closely relevant to GCS. The information provided can contribute to better understanding the water-bearing scCO$_2$–silicate reactions and scaling up findings in laboratory studies using small size mineral particles to the larger scale bulk rock formations.

5.2 Experimental Methods

5.2.1 Minerals

Natural wollastonite particles with five different size ranges were purchased from NYCO Company (Willsboro, NY). By using X-ray powder diffraction (XRPD, Bruker D8), its structure was identified to be wollastonite-1A, the most common polymorph in the natural environment.[171] The size distribution and shape for each size range were determined by laser diffraction and image analysis (Microtrac Inc.) performed by NYCO Company. Most particles were in cylindrical shape (Figure 5-S1). The spherical equivalent volumetric mean diameters were 3.8, 5.2, 11.1, 17.8, and 82.0 μm, and the respective typical aspect ratios were 3:1, 3:1, 3:1, 4:1, and 15:1. The detailed size distribution is available in the Supporting Information (Figure 5-S1). These size ranges were chosen because they can provide detectable and significantly different reaction extents. Using N$_2$ as adsorbate and 11 points on the isotherm in the BET method (AX1C-MP-LP, Quantachrome Instruments), the specific surface areas were determined to be 4.46±0.01, 3.61±0.01, 1.95±0.01, 1.45±0.01, and 0.54±0.01 m^2/g, respectively, for 3.8, 5.2, 11.1, 17.8, and 82.0 μm particles. The error ranges are based on duplicate measurements. X-ray fluorescence (Table 5-S1) showed that the Ca/Si ratio was 0.959. Thermogravimetric analysis (TGA, Q5000IR, TA Instruments) showed 0.45 % mass loss between 150–780 ºC. As shown by the XRD patterns in Figure 5-S5, the unreacted sample contains aragonite, which is estimated to be 1 wt%, based on 0.45% mass loss in TGA. No further treatment was performed after the wollastonite were obtained from the vendor.

5.2.2 Carbonation in water-bearing scCO₂ at simulated GCS conditions

Carbonation experiments were conducted in a 300 mL high pressure and high temperature reactor (Parr Instruments, Moline, IL) modified from the reactor used in our previous studies.[79, 80, 95, 105, 120] A schematic diagram of the reaction system setup is available in the Supporting Information (Figure 5-S2). The conditions (60 °C and 100 bar CO_2) are similar to typical conditions at GCS sites: 65 °C and 150 bar in the Frio formation,[34] 37 °C and 100 bar at the Sleipner site,[64] and 63 °C and 140 bar at the Weyburn field site.[81] To investigate carbonation of wollastonite in the absence of aqueous phase, wollastonite particles were placed in 10 ml Teflon tubes, while ultra-purified deionized water (Barnstead, > 18.2 MΩ·cm) was added outside the tubes. After scCO₂ was injected into the vessel, water dissolved in the scCO₂ and generated water-bearing scCO₂. Five PTFE tubes were placed in the reactor during each test. Considering the volume taken up by tubes and liners in the reactor, the volume of CO_2 during the experiment was 201 mL. The tubes were capped, but have small holes allowing contact between the wollastonite and water-bearing scCO₂. The solubility of water in CO_2 was predicted using Spycher's model.[172] At 35 and 60 °C, the mole fraction of 100% saturated water in 100 bar CO_2 is 0.41 and 0.49%, which indicates 234 and 117 μL water in the 201 mL scCO₂. The solubility of water in scCO₂ is affected by the salinity of water. As a starting point, ultra-purified water was used for simplicity. This result can serve as an important underpinning for understanding the effects of salinity on silicate carbonation in the future. Each sample contained 0.3 g particles. To check the possible influence of particle stacking inside the tubes on the reaction, results were compared with samples using 0.05 g particles. Selected samples were analyzed using XRPD. In this study, no attempt of XRPD quantitative analysis was made. Instead, the reaction extent was determined by TGA analysis. Previous studies

have shown that the results from XRPD quantitative analysis are comparable with the results from TGA analysis.[59]

5.2.3 Determination of the reaction extent

The reacted fraction of wollastonite was determined based on TGA results. After the sample was recovered from the reactor, the samples were stored at atmospheric pressure and analyzed within 24 hours. The powder sample was briefly mixed using a plastic spatula, and approximately 10 mg was used for each TGA analysis. At least duplicate samples were analyzed. Samples were heated to 900 °C with a ramp of 20 °C/min under N_2 flow (25 ml/min). Wollastonite and amorphous silica were stable below 900 °C, while calcium carbonate completely decomposed into CaO and CO_2.[59] The amount of CO_2 was measured by the mass loss between 150-780 °C during TGA (Figure 5.1B). Given the amount of CO_2, the reacted fraction of the original wollastonite was derived using this equation:

$$F = \frac{mass\ of\ reacted\ wollastonite}{mass\ of\ original\ wollastonite} = \frac{m_L \times \frac{M_{CaSiO_3}}{M_{CO_2}}}{m_o - m_L} \tag{5.1}$$

$$CaSiO_3 + CO_2 \xrightarrow{H_2O} CaCO_3 + SiO_2(am) \tag{5.2}$$

where m_L is the mass loss during TGA, which is the mass of CO_2 from $CaCO_3$ decomposition. According to equation (5.2), the mass loss is equal to the mass of CO_2 consumed during reaction with water-bearing $scCO_2$, so the mass of wollastonite consumed as reactant can be calculated using m_L and the molecular weight of CO_2 and wollastonite; m_o is the mass of the sample reacted with water-bearing $scCO_2$, which includes the mass of the original wollastonite (wollastonite before reaction with CO_2) and the mass of sorbed CO_2 on wollastonite (equal to m_L); and M is the molecular weight of different species. Given the 0.45% mass loss in unreacted

wollastonite, the detection limit of this method is estimated to be 1%. The reacted fraction of the largest particle size used (82 μm) is 7.8%, so the uncertainty of the reaction extent determined using this method is no more than 15%.

5.2.4 Calculation of the reacted thicknesses of wollastonite samples

Based on the reacted fraction, we calculated the thicknesses of the reacted layer by using a shrinking core model. The schematic diagram in Figure 5.2A shows the geometry. Before the reaction, each particle was assumed to be cylindrical in shape, with aspect ratio R and diameter D, calculated using equation (5.3) based on the spherical equivalent diameter (D_{eq}) measured by laser diffraction by the NYCO Company. During the reaction, a shell with thickness L was consumed as the reactant, and according to the model, the wollastonite particle shrank to a cylindrical shape core with diameter D-$2L$. The volume fraction of the shell is the reacted fraction of the particle. By integrating all the size intervals shown in the size distribution (Figure 5-S1), the reacted fraction of each size range was calculated. The reacted thickness L was obtained by solving equation (5.4), which equated the calculated reacted fraction and the reacted fraction determined by TGA.

$$D = D_{eq} \times \sqrt[3]{\frac{2}{3 \times R}} \tag{5.3}$$

$$F = \frac{\sum_{D_{min}}^{D_{max}}\left\{\frac{\pi \times D^2}{4} \times L \times 2 + \left[\frac{\pi \times D^2}{4} - \frac{\pi \times (D-2L)^2}{4}\right] \times (R \times D - 2 \times L)\right\}}{\sum_{D_{min}}^{D_{max}}\left\{\frac{\pi \times D^2}{4} \times R \times D\right\}} \tag{5.4}$$

In Equations 5.3 and 5.4, L is the thickness of the reacted layer, F is the reacted fraction, D_{eq} is the spherical equivalent diameter of each size range from laser diffraction results provided by NYCO Company, D is the cylindrical equivalent diameter of each size range, and R is the aspect ratio. L was obtained by solving this equation. For small particle size ranges, in which ($R \times D - 2$

116

$\times$ L) < 0, the volume measured by laser diffraction was used to replace the calculated value, because these particles are so small that the reacted fraction is 100%.

5.2.5 Determination of the amounts of structural water in reacted samples

The mass loss determined by TGA can be affected by potentially existing structural water in reacted samples, which would lead to an overestimation of the reacted fraction. To check whether large amounts of structural water existed in reacted samples, 0.3 g reacted sample (3.8 μm) were dissolved in 5 mL 1 M nitric acid (BDH), and the dissolved solutions were weighed. The Ca concentration in dissolved solutions was analyzed using ICP-OES (Figure 5-S3), which confirmed that the particles were completely dissolved in solution. The mass change was compared with the mass loss predicted based on TGA. If the mass loss is similar with the prediction, then the amount of structural water is not significant enough to affect the reacted fraction determined by TGA.

5.2.6 Amorphous silica layer formed in aqueous solution

When recent studies on wollastonite carbonation in water-bearing scCO$_2$ discussed the amorphous silica formed, references to wollastonite dissolution in the aqueous phase were cited to support their points.[30, 59] However, it is unclear whether the amorphous silica layers formed in aqueous solution and in water-bearing scCO$_2$ are comparable. To compare the amorphous silica layers formed in an aqueous solution and in water-bearing scCO$_2$, an amorphous silica layer was produced on wollastonite surface by a preferential dissolution of Ca in acidic solution. Specifically, 2 g of unreacted wollastonite (17.8 μm) were reacted in 200 mL nitric acid solution with initial pH = 1 for 1 hour. A control sample was reacted with ultra-purified water. Liquid samples were filtered using 0.22 μm PTFE filters, and analyzed using ICP-OES. Solid samples were washed with ultra-

purified water, centrifuged at 5000 rpm for 30 minutes, dried in N_2, and reacted with water-bearing scCO$_2$. The reaction extents of the pretreated sample and control sample were compared to show differences between the amorphous silica layers formed in aqueous solution and in water-bearing scCO$_2$.

5.2.7 SEM imaging

To observe the cross-section of the surface product layer, wollastonite particles were embedded into a resin (Eponate 12) and sectioned using an ultramicrotome (Leica EM UC7). The cross-sections were analyzed using scanning electron microscopy (SEM, JEOL 7001LVF FE-SEM), coupled with energy dispersive X-ray spectrometry (EDS) to obtain the elemental composition. Both SEM and EDS were operated in low vacuum mode (10 Pa), with an accelerating voltage of 10.00 kV and a probe current of 16 μA. The working distance was 10 mm.

5.3 Results and Discussion

5.3.1 carbonation of wollastonite in water-bearing scCO₂ formed calcite and amorphous silica secondary mineral phases
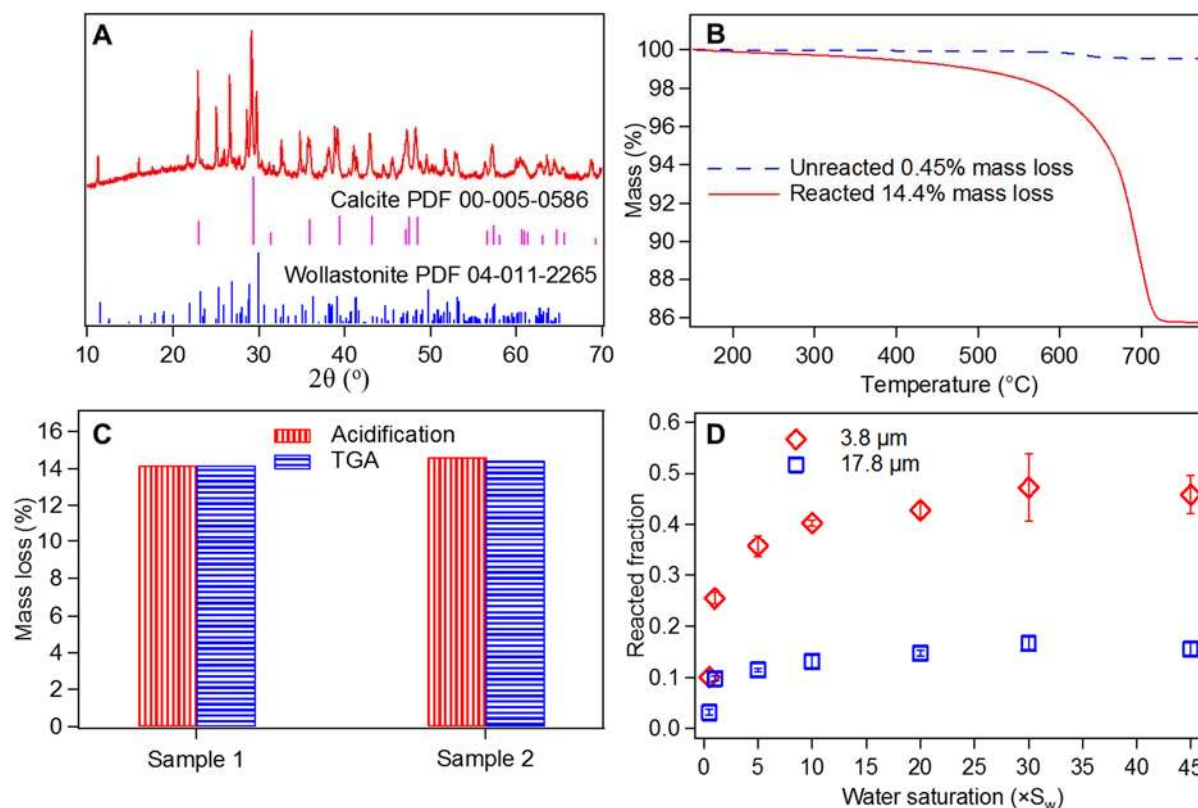
Figure 5.1. (A-B) XRPD pattern and TGA analysis of wollastonite particles reacted for 40 h with 45 times more water than needed for saturation ($45 \times S_w$), at 60 °C and 100 bar CO_2. **(C)** Mass loss of two duplicate samples of wollastonite particles reacted for 40 h at $45 \times S_w$, 60 °C, and 100 bar CO_2, during dissolution in nitric acid and TGA. **(D)** Reacted fraction of wollastonite particles with volumetric mean diameters of 3.8 and 17.8 μm, reacted for 20 h with the addition of different amounts of water. Both sizes showed no dependency on the amount of water at $45 \times S_w$.

Among the products of the reaction, calcite was the dominant crystalline phase identified by XRPD (Figure 5.1A and 5-S5-S9). This observation is consistent with previous studies,[30, 54, 59, 62] in which the carbonation of wollastonite was described as equation 5.2. The other product reported is amorphous silica, whose broad peak cannot be clearly shown in an XRPD pattern. Based on XRPD results, the amounts of aragonite and vaterite were not significant. Although the existence of amorphous calcium carbonate (ACC) is possible, it is likely that ACC transformed to

119

more stable phases during *ex situ* treatment. The difficulty in determining *in situ* phases of $CaCO_3$ does not affect the determination of reaction extent, because the formations of ACC and calcite consumed the same amount of wollastonite.

To investigate the effects of particle size on wollastonite carbonation in water-bearing $scCO_2$, we conducted experiments to ensure that the potential existence of structural water in the reaction product did not affect the accuracy of the reacted fraction determined using TGA. It is important to check because ACC or amorphous silica contain structural water, which would enhance the mass loss and, therefore, lead to an overestimation of the reacted fraction. However, the TGA curve (Figure 5.1B) is smooth between 150 and 600 °C, indicating no significant amount of structural water in the reacted samples. To further investigate the potential influence of structural water on the accuracy of determined reacted fraction, the mass loss in TGA was compared with the mass loss when the reacted sample was dissolved in nitric acid, which is affected only by CO_2 (Figure 5.1C). The mass changes were similar, which suggests that no significant amounts of structural water existed in the reaction product. Even if a small amount of structural water existed, it was not enough to affect the accuracy of the reaction fraction of wollastonite determined using equation (5.1).

Besides determining the reacted fraction, we investigated the effects of the amount of water added in our system. The model we used to calculate the solubility of water in $scCO_2$ did not consider the presence of minerals.[172] In addition, some water will adsorb on the mineral surfaces. Consequently, even though the same amount of water was added, different sizes of particles could possibly experience a different extent of water saturation. To ensure that different particle sizes were reacted under the exact same conditions, we studied the dependencies of the reacted fraction on the amount of water added to the reactor (Figure 5.1D). Our data suggested that the reacted

fraction increased with the amount of water, and is more dependent on water saturation for small particle sizes. However, for different particle sizes, plateaus were reached with 20 times more water than needed for saturation in CO_2 (For simplicity, $20 \times S_w$, where S_w represents the solubility of water in CO_2). When higher than $20 \times S_w$, the reacted fractions of different size particles do not have a strong dependency on water saturation. Therefore, to elucidate the effects of particle sizes, $45 \times S_w$ was chosen as the main condition used.
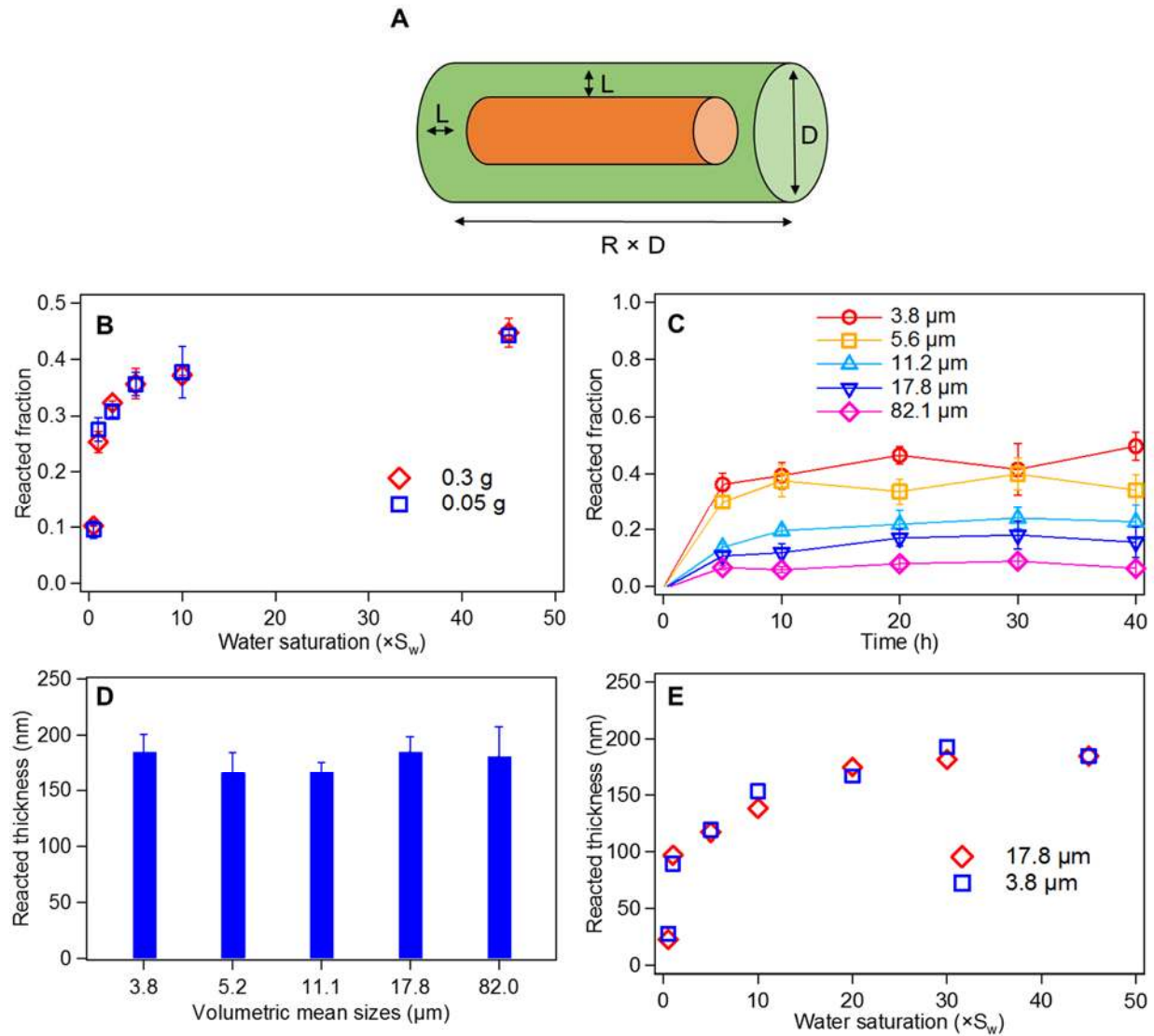
Figure 5.2. (A) Diagram of the shrinking core model used to calculate reacted thickness. The orange part is the unreacted core of wollastonite. The green part represents the wollastonite consumed during the reaction with water-bearing scCO$_2$. *L* is the reacted thickness, *D* is the diameter of the particle, and *R* is the aspect ratio of cylindrical shape particle. **(B)** Reacted fraction of wollastonite particles with a volumetric mean diameter of 3.8 μm after 40 hours at 45×S$_w$, 60 °C, and 100 bar CO$_2$. Samples containing 0.3 g and 0.05 g of particles showed the same reacted fraction. **(C)** Reacted fraction of wollastonite particles with volumetric mean diameters of 3.8, 5.2, 11.8, 17.8, and 81.0 μm reacted for 5, 10, 20, 30, and 40 hours with 45×S$_w$ at 60 °C and 100 bar CO$_2$. Error bars are the differences among three replicates. **(D)** The thickness of the reacted wollastonite layer calculated based on the reacted fraction. The thickness of the reacted surface layer is similar for different particle sizes, 177 ± 11 nm. **(E)** Reacted thicknesses of wollastonite particles with volumetric mean diameters of 3.8 and 17.8 μm at different water saturation percentages.

122

Next, the potential influence of CO_2 diffusion through interparticle spaces was investigated. Experiments using 0.3 g and 0.05 g particles (i.e., different packing heights and thus different path lengths) showed the same reacted fraction (Figure 5.2B). The top part and bottom part of the sample also showed the same reacted fraction (Figure 5-S4). This finding indicates that water-bearing $scCO_2$ easily reached the bottom of the tube, even though particles were packed inside the tubes, and each particle experienced exactly the same reaction condition. This observation also suggests that the ratio between mineral and water-bearing $scCO_2$ fluid will not affect the extent of reaction in the range of the experimental conditions. In our system, the small amount of water adsorbed on the mineral surface cannot change the water saturation percentage in CO_2 fluid, because $45 \times S_w$ was added. If a certain amount of water originally dissolved in CO_2 was adsorbed on the mineral surface, the loss of water in CO_2 fluid could be compensated quickly by the $45 \times S_w$ added. However, it is worthwhile to note that in field sites, low water saturation conditions can exist. The adsorption of water on the mineral surface may change the water saturation percentage in CO_2 and therefore affect the carbonation of silicates.

5.3.2 Reacted fractions of wollastonite decreased with larger particle sizes

The reacted fractions of wollastonite were measured after 5, 10, 20, 30, and 40 hours reaction at 60 °C and 100 bar with $45 \times S_w$. The reacted fractions did not keep increasing with time, but fluctuated in certain error ranges (Figure 5.2C). This observation shows that the reaction extent reached a plateau. To explain this trend, several limiting factors of mineral carbonation were considered.

First, a recent study using wollastonite suggested that the plateau results from the limited availability of water.[62] In our system, $45 \times S_w$ was added. Thus, the plateau is not due to limited water availability during the reaction. As we have shown above, no significant amount of structural

water existed in the reaction products, so the reaction did not consume large amounts of water. The water acted more likely as a catalyst for the overall reaction. After the reaction, there were significant amounts of water left in the aqueous phase, though the amount was not quantified.
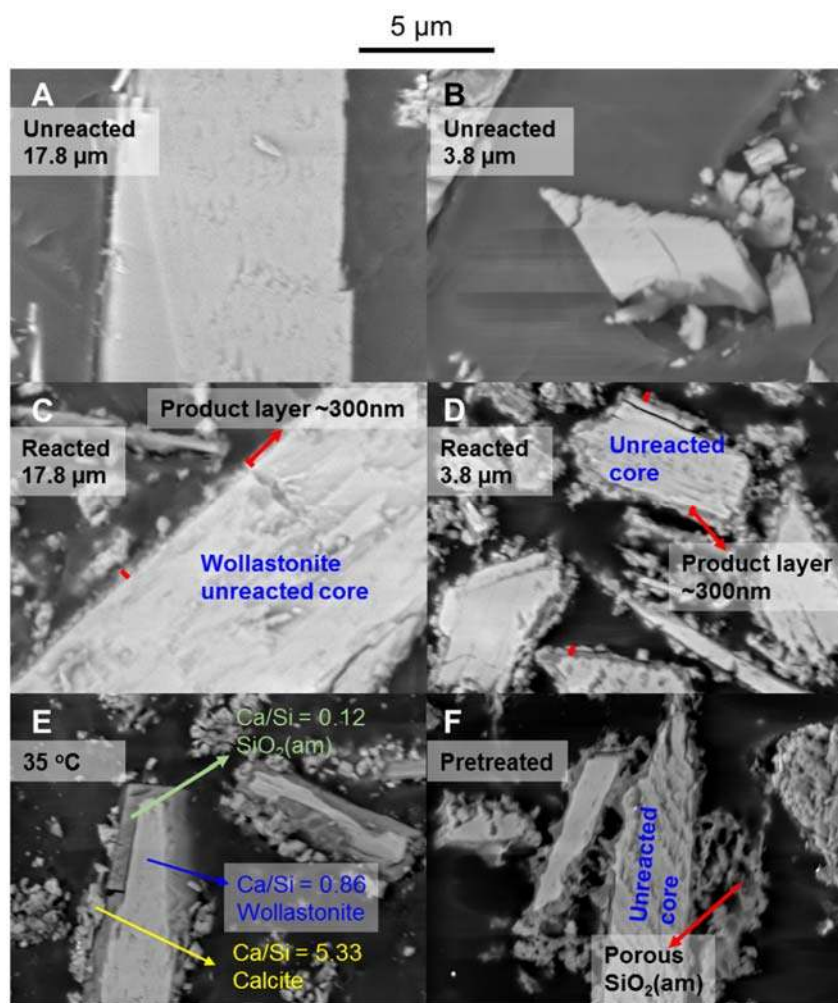
Figure 5.3. SEM images of wollastonite particle cross-sections. **(A)** Unreacted wollastonite particles with a volumetric mean diameter of 17.8 μm. **(B)** Unreacted wollastonite particles with a volumetric mean diameter of 3.8 μm. **(C)** Wollastonite particles with a volumetric mean diameter of 17.8 μm reacted for 40 hours with $45 \times S_w$, at 60 °C and 100 bar CO_2. **(D)** Wollastonite particles with a volumetric mean diameter of 3.8 μm reacted for 40 hours with $45 \times S_w$, at 60 °C and 100 bar CO_2. The thickness of product layer is similar to that of the 17.8 μm size particles. The red bars are 300 nm. **(E)** Wollastonite particles with a volumetric mean diameter of 17.8 μm reacted for 40 hours with $45 \times S_w$, at 35 °C and 100 bar CO_2. The unreacted wollastonite, with Ca/Si = 0.86 as determined by EDS, is surrounded by a darker layer, with Ca/Si = 0.12, which was attributed to amorphous silica. Outside the amorphous silica layer, discrete calcite, Ca/Si = 5.33, can be observed. **(F)** Wollastonite particles with a volumetric mean diameter of 17.8 μm pretreated with nitric acid.

124

Second, besides the availability of water, other controlling mechanisms for mineral carbonation have also been suggested. For example, a recent study of CaO carbonation in dry CO_2 found that the reacted fraction is independent of particle sizes and concluded that carbonation of CaO is not limited by reaction at the surface, but happens throughout the entire particle.[167] We show, however, that the reacted fraction of wollastonite decreased significantly with larger particle sizes (Figure 5.2B). From the SEM images (Figures 5.3 C and D), larger particles have much larger unreacted core than smaller particles, instead of keeping a constant reacted fraction. This finding confirms that carbonation of wollastonite in water-bearing CO_2 is substantially different from carbonation of CaO in CO_2. The wollastonite carbonation is limited to the surface.

Other studies also suggested that hydrolysis of the mineral can be the controlling step.[57, 166] Water adsorbs on the mineral surface and forms a thin film. Hydrolysis of silicates within the water film releases cations, such as Ca^{2+} and Mg^{2+}, which form carbonate later with the CO_2 dissolved in the water films. We hypothesize that this mechanism is applicable to our system: The extent of reaction is limited by the slow kinetics of wollastonite hydrolysis. This hypothesis is consistent with our observations of the reacted fraction: Smaller particles have larger surface area, which enhanced the kinetics of wollastonite hydrolysis, and thus led to a larger reacted fraction.

5.3.3 The reacted thickness is constant for various particle sizes

If the dissolution rate of the mineral phase is the limiting factor, it should be possible to observe differences in the thickness of the reacted wollastonite layer, because particles with different sizes may have different combinations of crystal surfaces, which can have different dissolution rates. To compare the thicknesses of the reacted layer on different particle sizes, we applied equation (5.4) and calculated the reacted thicknesses. Interestingly, the reacted thickness was constant for different particle sizes (Figure 5.2C). Because five different size ranges have been

used, the constant thickness from these samples is not a coincidence. We admit that the model used to calculate the thickness has simplifications: Ideal cylindrical shapes of particles are assumed, and the heterogeneity in shape and surface roughness of actual particles have been omitted. However, the thickness obtained with this model is a statistically averaged result, and thus it is not significantly affected by heterogeneity in shape and surface roughness. More specifically, the size used in the calculations is a volumetric equivalent, and hence already considers the heterogeneity in shape and surface roughness.

Because the reacted layers from different size samples have a constant thickness, the thickness of the product layer should also be constant: the particles share the same chemical phase and should produce the same products. This conclusion is proven by the similar thickness of the product layer observed in Figures 5.3 C and D. Thus, we suggest that the thickness of the reacted layers should be used to represent the extent of reaction, rather than reacted fraction of samples, or the weight fraction of CO_2 and carbonate in the samples after reaction. Because the thickness of the reacted layer is independent of particle size, such a replacement of the term can make the results obtained with different particle sizes directly comparable.

We also found that after converting the reacted fraction into the reacted thickness, the reacted thickness of different particle sizes showed the same dependency on the water saturation percentage (Figure 5.2D). Therefore, besides $45 \times S_w$ used above, at various water saturation conditions, the reacted thickness is independent of particle size. If the reacted fraction or other size-dependent indexes are used to represent reaction extent, smaller particles tend to have larger apparent dependency on the water saturation percentage (Figure 5.1D). However, using the reacted thickness, the reaction extents of various particle sizes have the same actual dependency on the water saturation percentage.

Furthermore, the constant reacted layer thickness suggests that particle size has no significant effects on the reaction extent if normalized by its surface area. These results show that the anisotropic reactivities of different crystal faces may not be significant. Another possibility is that the reactivity of wollastonite does not affect the reaction extent in water-bearing $scCO_2$–silicate reaction after 20 hours. The reaction is not controlled by the kinetics of mineral hydrolysis, but by the diffusion of water-bearing $scCO_2$ across the surface product layer. We observed that the product layer containing amorphous silica and calcite covered the surface of the wollastonite and thus could act as a diffusion barrier to water-bearing $scCO_2$. This mechanism explained why the reaction reached a plateau, which cannot be explained by mineral hydrolysis alone. The constant thickness of the product layer is strong evidence to support this mechanism. Although the reactivities of different crystal surfaces and different surface sites varied, various surfaces and particles tend to form a product layer with the same thickness. In addition to the conditions affecting the diffusivity of water-bearing $scCO_2$, such as temperature and pressure, the thickness and the permeability of the product layer are controlling factors for silicate carbonation in water-bearing $scCO_2$.

Earlier we have described that the reaction reached a plateau after 20 hours (Figure 5.2C). For all particle sizes, the pseudo-equilibrium reacted thickness was 177 ± 11 nm with $45 \times S_w$, 60 °C, and 100 bar CO_2. These results can be directly applied to bulk rocks at field sites. Provided a long enough reaction time, other silicates may follow the same mechanism, although their kinetics of hydrolysis can be much slower than for wollastonite. It could take longer than 20–40 hours before the reaction becomes diffusion-controlled. So within the time scale of days or weeks in laboratory experiments, other silicates may not reach plateau. Thus, wollastonite can be a good model for investigating the long-term state of silicate carbonation in water-bearing $scCO_2$.

127

5.3.4 Amorphous silica acts as a diffusion barrier for water-bearing scCO$_2$

Furthermore, based on our understanding of the reacted layer, we can provide an insight into the identity of the diffusion barrier of wollastonite reaction with water-bearing scCO$_2$. A recent study on wollastonite carbonation in water-bearing scCO$_2$ claimed that the calcite formed on the surface of wollastonite acted as diffusion barrier, because the amorphous silica looked highly porous.[54] Another study argued that the amorphous silica layer should be the diffusion barrier, because in their SEM images, the calcite particles were discontinuous and did not substantially cover the surface of the wollastonite particles.[59] Both studies cited references reporting wollastonite dissolution in the bulk water phase to support their points. However, whether the amorphous silica layer formed during silicate dissolution in the bulk solution acts as a diffusion barrier is still controversial.[173, 174] Previous studies found that the structure and degree of polymerization of silica layers formed in aqueous solutions are affected by the substrate and the solution chemistry, thus can be either passivating or nonpassivating.[175-178] Schott et al. found that for wollastonite, the amorphous silica layer is not a diffusion barrier for aqueous species.[173] Even if we know the answer in the presence of the bulk solution, there is still no evidence to show that the amorphous silica layer formed in exposure to water-bearing scCO$_2$ can be analogous to the amorphous silica layer formed in bulk solution.

Based on this study, we suggest that the amorphous silica layer should be the diffusion barrier for water-bearing scCO$_2$. The sample reacted at 35 $^\circ$C was used to clearly show the relative distribution of calcite and amorphous silica (Figure 5.3E), and it has a much thicker product layer than the 60 $^\circ$C samples that allowed us to do more accurate EDS analysis. We assumed the the distribution of calcite and amorphous silica was the same at 35 and 60 $^\circ$C. From the SEM results (Figure 5.3E), we learned that the calcite presents as discrete particles or aggregates, which did

not fully cover the surface of wollastonite. Thus, it is less likely that calcite can be the diffusion barrier. However, the amorphous silica layer substantially covered the surface of the unaltered core of wollastonite. This observation is consistent with the findings in the study of Miller et al..[59] In contrast, Daval et al. observed alternating layers of amorphous silica and calcite on wollastonite surfaces.[30] We suggest that the 60 ºC and 100 bar conditions used in our study are similar to the 50–70 ºC and 90–160 bar used in Miller et al.'s study,[59] and lower than the 90 ºC and 250 bar used in Daval et al.'s work.[30] In addition, Daval et al. conducted water-saturated CO_2 experiments together with bulk aqueous phase experiment in one reactor.[30] An unlimited amount of water was in their system and could potentially migrate to the wollastonite surface, which may explain the different observations in their work and in this study. In addition, analysis using the BET method indicated that the particles after reaction have a smaller specific surface area of 1.02 ± 0.08 m^2/g, compared to 1.57 ± 0.13 m^2/g for the unreacted sample. The decrease in surface area suggests that the average particle size may become larger and the amorphous silica layer may not be highly porous. Therefore, we concluded that the amorphous silica layer forms a diffusion barrier in our experimental systems.
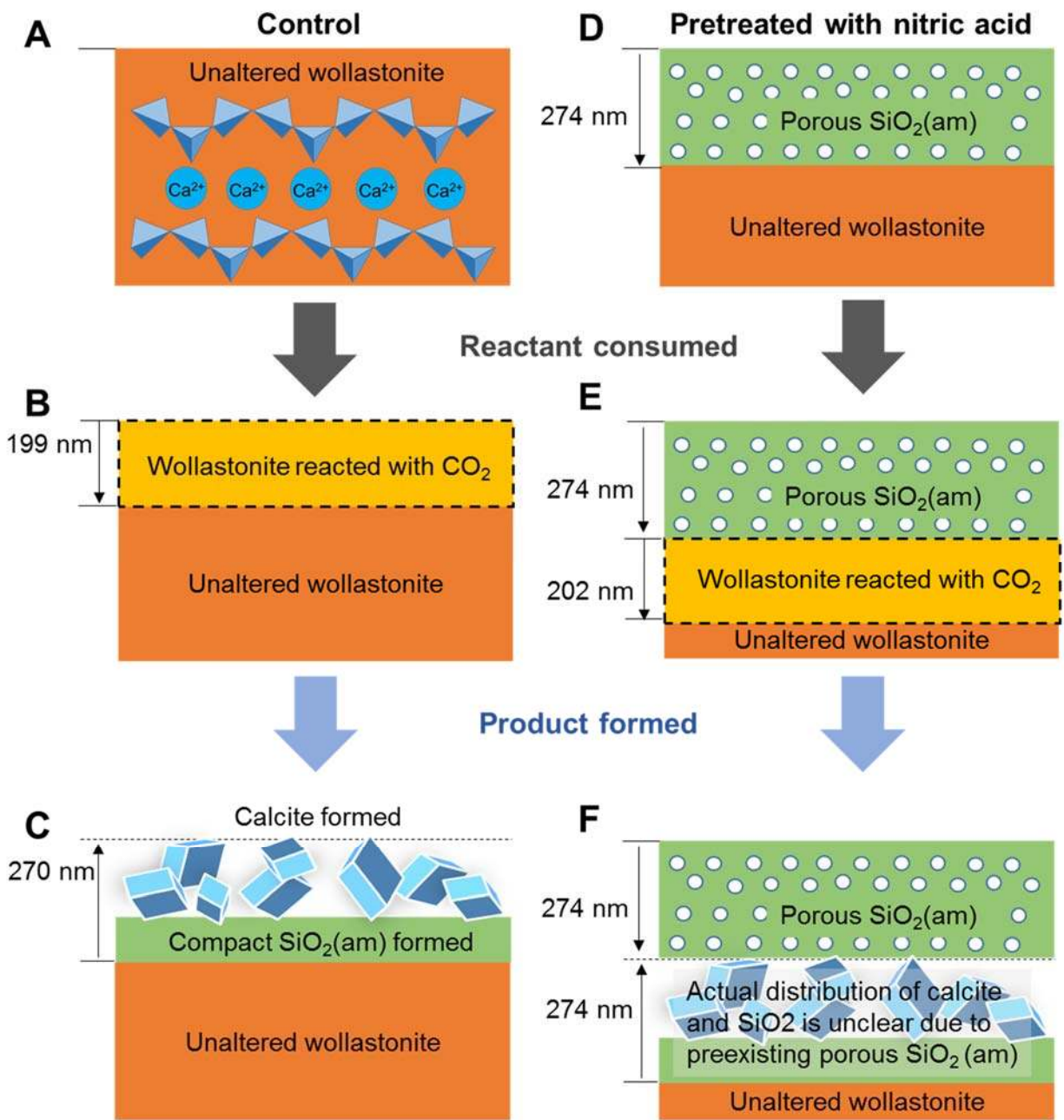
Figure 5.4. Schematic diagram of surface layers on a control and a sample pretreated with nitric acid. **(A-C)** Wollastonite particles reacted for 40 hours with $45 \times S_w$, at 60 °C and 100 bar CO_2. According to the measured reacted fraction, a 199 nm thick layer of wollastonite on the surface was reacted (dotted layer) (B). 270 nm product layer formed by calcite and amorphous silica (C). **(D-F)** Sample pretreated in nitric acid has a 274 nm highly porous amorphous silica layer on its surface (D), based on calculations using ICP results. A 202 nm thick layer of wollastonite was reacted after 40 hours with $45 \times S_w$, at 60 °C and 100 bar CO_2 (E). Compared to the 199 nm layer of the control sample, the same amount of wollastonite reacted, indicating that the porous amorphous silica layer formed in the aqueous phase cannot act as diffusion barrier for water-bearing scCO$_2$.

130

To demonstrate the differences between the amorphous silica layer formed in the bulk aqueous phase and that formed in water-bearing scCO$_2$ (Figure 5.4), we conducted the following experiments. As a control sample, wollastonite particles with a volumetric mean diameter of 17.8 μm were reacted for 40 hours with water-bearing scCO$_2$ with 45×S$_w$ at 60 °C and 100 bar. Based on TGA results, 17% of the raw wollastonite was consumed in the reaction with water-bearing scCO$_2$, which corresponds to a layer of wollastonite with a thickness of 199 nm, based on Equation 5.4. The products were calcite and amorphous silica, which formed a layer on the unaltered wollastonite core. According to the stoichiometry of the reaction (Equation 5.2), the thickness of the product layer was calculated to be 270 nm (Figure 5.4C), based on the reported densities of quartz, wollastonite, and calcite, i.e., 2.65, 2.90, and 2.71 g/cm^3, respectively.[179] We used the density of quartz for the vitreous amorphous silica, because the apparent density of vitreous amorphous silica depends on its porosity, which can vary significantly for different samples. The thickness of the product layer obtained is not the actual thickness, and is used only to compare the amount of surface layer on different samples. The details on the calculation of product layer thickness are shown in S1 in the Supporting Information.

In contrast, another sample with the same particle size was pre-reacted with nitric acid solution (initial pH = 1) to generate amorphous silica layer on the surface of the wollastonite. Based on the Ca and Si concentrations measured by ICP-OES, the thickness of this amorphous silica layer was calculated to be 274 nm (Figure 5.4D), assuming that the density of amorphous silica is 2.65 g/cm^3. Such a thickness is comparable with the thickness of the product layer formed on the control sample after reaction in water-bearing scCO$_2$. Therefore, if amorphous silica formed in the aqueous phase could act as diffusion barrier, the sample pretreated with nitric acid should not further react with water-bearing scCO$_2$ due to diffusion-limited reaction. However, when

pretreated wollastonite was reacted with water-bearing $scCO_2$ under the same conditions as the control sample, 21% of the sample had reacted, and the thickness of the reacted wollastonite layer was calculated to be 202 nm (Figure 5.4E). Such a small enhancement in the reacted fraction (17% to 21%) is due to the shrinkage of the particle during the reaction with nitric acid, and is consistent with the calculation using our shrinking core model (Equation 5.4). The similar reacted thicknesses (199 nm and 202 nm) show that the amorphous silica formed during the aqueous phase dissolution of wollastonite does not act as a diffusion barrier for water-bearing $scCO_2$ at all, while the amorphous silica layer formed in water-bearing $scCO_2$ can be a diffusion barrier. The specific surface areas of samples pretreated with nitric acid after reaction with nitric acid and after additional reaction with water-bearing $scCO_2$ were 14.16 ± 0.80 and 13.87 ± 1.20 m^2/g, respectively. These values are much larger than 1.572 ± 0.126 m^2/g for the original wollastonite sample. This observation indicates that the amorphous silica layer formed in the aqueous phase is highly porous (Figure 5.3F) compared to that formed in water-bearing $scCO_2$ (Figure 5.3C), which is further confirmed by SEM images. It shows that the amorphous silica layer formed in water-bearing $scCO_2$ and those formed in aqueous phase may have substantially different porosities, which is likely due to the different chemistries in the thin water film. The low porosity amorphous silica layer formed during water-bearing $scCO_2$–mineral interaction can act as diffusion barrier for water-bearing $scCO_2$.

5.4 Environmental Implications

We found that the amorphous silica layers formed in water-bearing $scCO_2$ and those formed in aqueous solutions have different morphologies. The altered amorphous silica layers formed in aqueous solutions have 10 to 100 times larger BET surface areas than those formed in water-bearing $scCO_2$. These results help to understand the differences between silicate reactions

in water-bearing $scCO_2$ and in aqueous solutions. They also provide insights into the role of water on the silicate carbonation in water-bearing $scCO_2$. In addition, our observations suggest that the carbonation of wollastonite in water-bearing $scCO_2$ was limited by the diffusion barrier of the amorphous silica layer. The thickness of the reacted wollastonite layer was determined to be 177 ± 11 nm with $45 \times S_w$ at 60 ºC and 100 bar CO_2. This thickness was found to be independent of the particle sizes used. Therefore, the reacted thickness should be used to represent the extent of reaction, instead of any other parameter that changes with particle size. These findings allow us to compare the results of previous studies using different particle sizes directly after normalization by surface area. Moreover, the work can be a good first step to fill the knowledge gap between small size particles used in the laboratory and the bulk rock in real GCS systems. Because we have shown that the equilibrium reacted thickness does not change with particle size, the thickness measured using small particles can be applicable to larger sizes of rocks.

Other Mg- or Fe-containing silicates also produce corresponding carbonate and amorphous silica during their reactions with water-bearing $scCO_2$. We suggest that the low porosity of amorphous silica layers formed in water-bearing $scCO_2$ is due to an insufficient amount of water compared to aqueous solutions. Thus, it is likely that the amorphous silica layers formed on other minerals in water-bearing $scCO_2$ are also diffusion barriers. However, there is a caveat that the substrate mineral may affect the structure of silica layers. The results obtained using wollastonite can be potentially applicable to other silicates. In addition, the plateau we observed in this study is not the real equilibrium. Provided a long enough reaction time, the crystallization of amorphous silica in water-bearing $scCO_2$ can possibly change the permeability of the amorphous silica layer. This process can determine the reaction extent on a geologic time scale.

The carbonation of silicates can lead to a change of wettability, as the silicates are usually more hydrophilic than carbonate.[180] It can also result in volume change, because the densities of reaction products are different from the original silicates. The carbonation can also contribute to CO_2 mineralization, which is the most permanent way to trap CO_2. With these considerations, the reacted thickness can be the most important factor in understanding water-bearing $scCO_2$ –mineral reactions. In short, the new insights provided in this work can help us predict both the stability of silicate in water-bearing $scCO_2$ and the impact of water-bearing $scCO_2$–silicate reactions on subsurface $scCO_2$ injections. Furthermore, the water-bearing $scCO_2$–silicates reaction can potentially be applicable to CO_2 capture and *ex situ* mineralization. The results of this work can benefit understanding all of these environmental processes.

Acknowledgments

Supporting Information for Chapter 5

Contents: Experimental details

Nine figures

Two tables

Table 5-S1. X-ray fluorescence (XRF) analysis of wollastonite used in this study (in weight %).

	Wollastonite		Number of ions on the basis of 3 oxygen
SiO_2	51.0	Si	0.991
CaO	45.7	Ca	0.951
Al_2O_3	0.60	Al	0.014
TiO_2	0.05	Ti	0.001
Fe_2O_3	0.67	Fe	0.010
MnO	0.15	Mn	0.002
MgO	0.80	Mg	0.023
Na_2O	0.20	Na	0.008
K_2O	0.03	K	0.001
P_2O_5	0.03	P	0.000
Loss on ignition	0.80		

S5.1. Calculation of product layer thickness

The thickness of the product layer is calculated based on this equation:

$$L_p = L_r \times \frac{\rho_w}{M_w} \times \left(\frac{M_c}{\rho_c} + \frac{M_s}{\rho_s}\right)$$
(5-S1)

where the L_p is the thickness of the product layer, L_r is the reacted thickness, and ρ_w, ρ_c, and ρ_s are the densities of wollastonite, calcite, and SiO_2(am), respectively. M_w, M_c, and M_s are the molecular weights of wollastonite, calcite, and SiO_2(am), respectively.

This equation is based on the stoichiometric ratio of wollastonite: calcite: amorphous silica is 1: 1: 1. For example, in Figure 5.4, the control sample has a 199 nm reacted thickness, and the thickness of the product layer is 270 nm. For comparison, on the pretreated sample, we made an amorphous silica layer with a similar thickness (274 nm vs. 270 nm) by aqueous phase dissolution. After reaction with water-bearing CO_2, a similar thickness of wollastonite in the pretreated sample (202 nm vs. 199 nm) was reacted and formed calcite and amorphous silica, which was coincidentally

274 nm. The thickness of the product layer is used only to compare the amount of product formed. The actual thickness would be different because of different porosities.
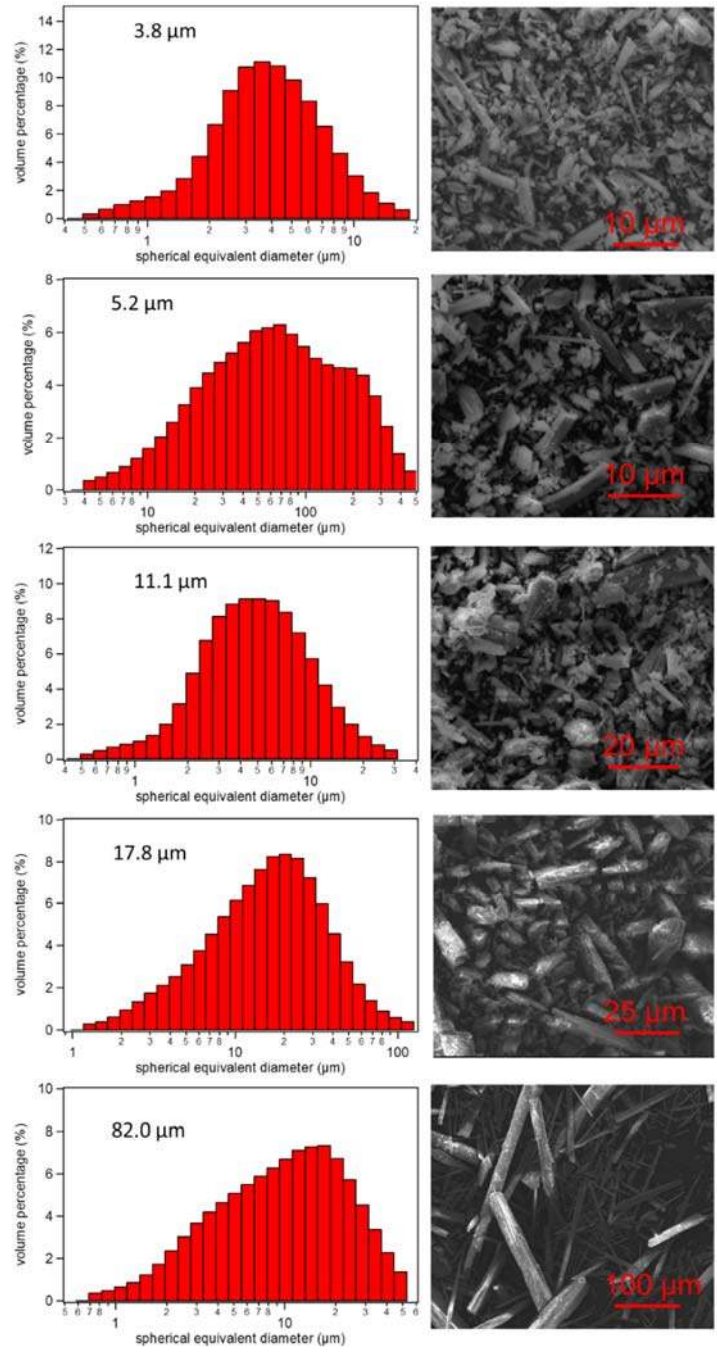
Figure 5-S1. Size distributions measured by laser diffraction and SEM images for the five size fractions used in this study. Commercially obtained wollastonite particles were provided by NYCO Company (Willsboro, NY). Please note that the size distributions show the spherical equivalent diameter. The volumetric mean sizes are 3.8, 5.2, 11.1, 17.8, and 82.0 µm. The sizes show in the SEM images may appear larger than the spherical equivalent size due to the cylindrical shape, but are consistent with the trend.
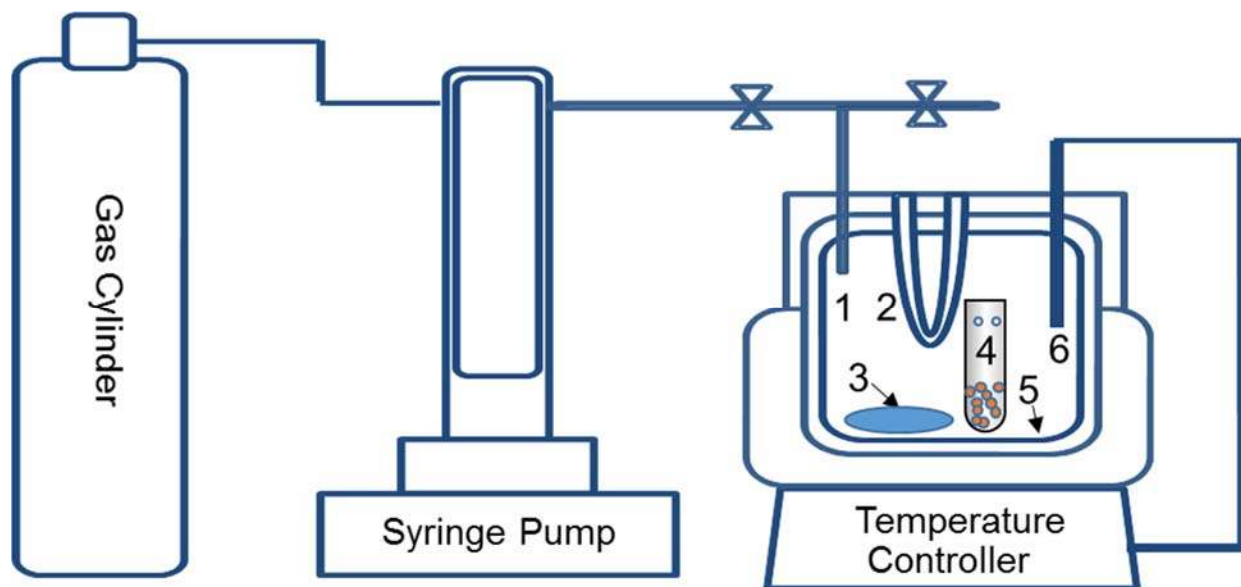
Figure 5-S2. Experimental setup. 1, Gas inlet and outlet tube; 2, Cooling loop; 3, Water; 4, Teflon tube; 5, Teflon liner; 6, Thermocouple.
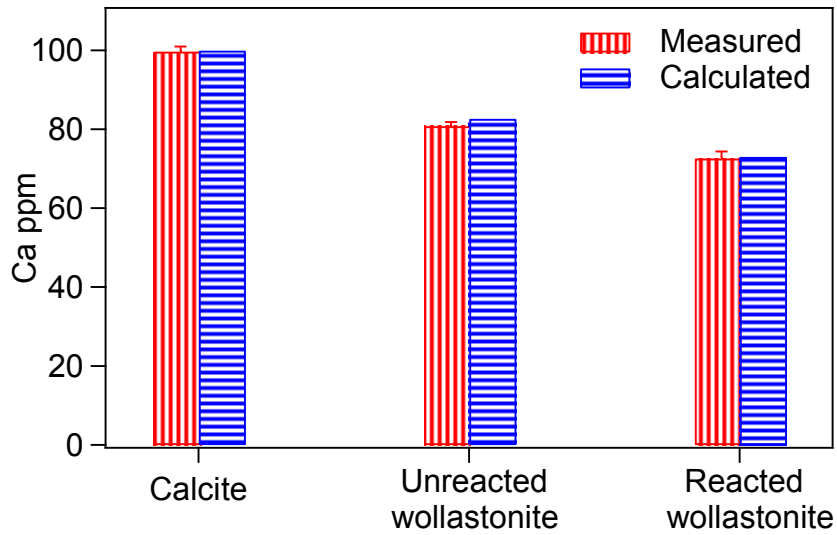
Figure 5-S3. Ca concentrations measured by ICP-OES compared to the prediction based on XRF results. 0.5 g calcium carbonate (Mallinckrodt Chemicals.), unreacted wollastonite (3.8 μm), and selected reacted sample (3.8 μm) were dissolved separately in 10 mL 67-70% nitric acid (BDH). The solutions were diluted 240 times before being analyzed. The similar concentrations indicate that the particles were completely dissolved.
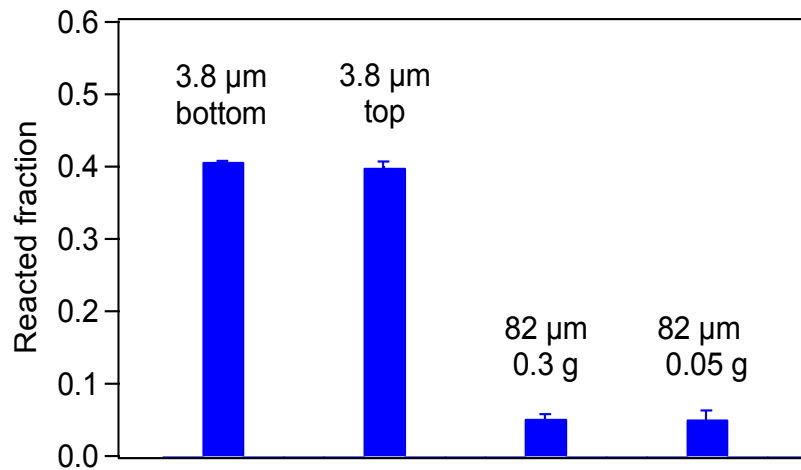
Figure 5-S4. Reacted fraction of wollastonite particles with mean diameter of 3.8 and 82 μm after 20 hours at $45 \times S_w$, 60 °C, and 100 bar CO_2. The top and bottom regions of the sample showed the same reacted fraction. Samples containing 0.3 g and 0.05 g of particles showed the same reacted fraction.
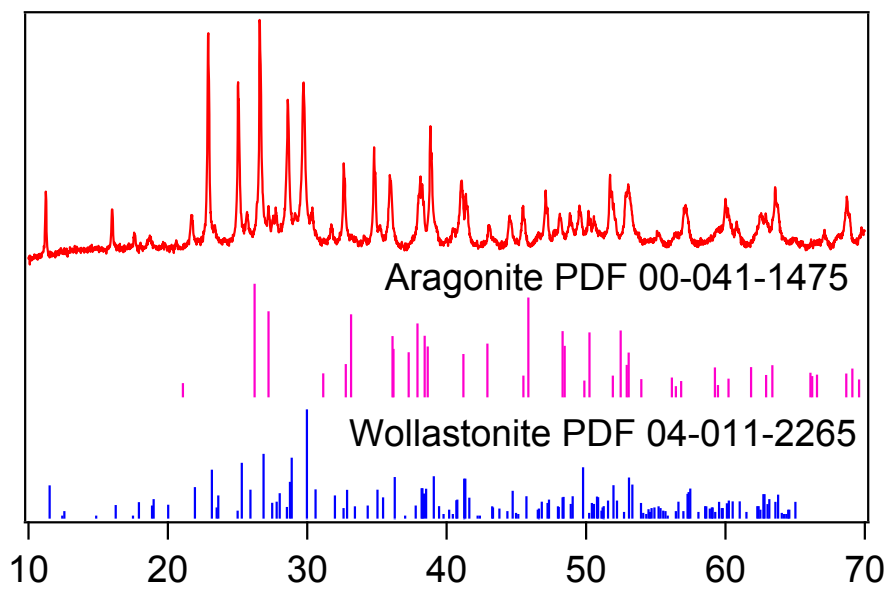
Figure 5-S5. XRD pattern of unreacted wollastonite particles with mean size of 3.8 μm.
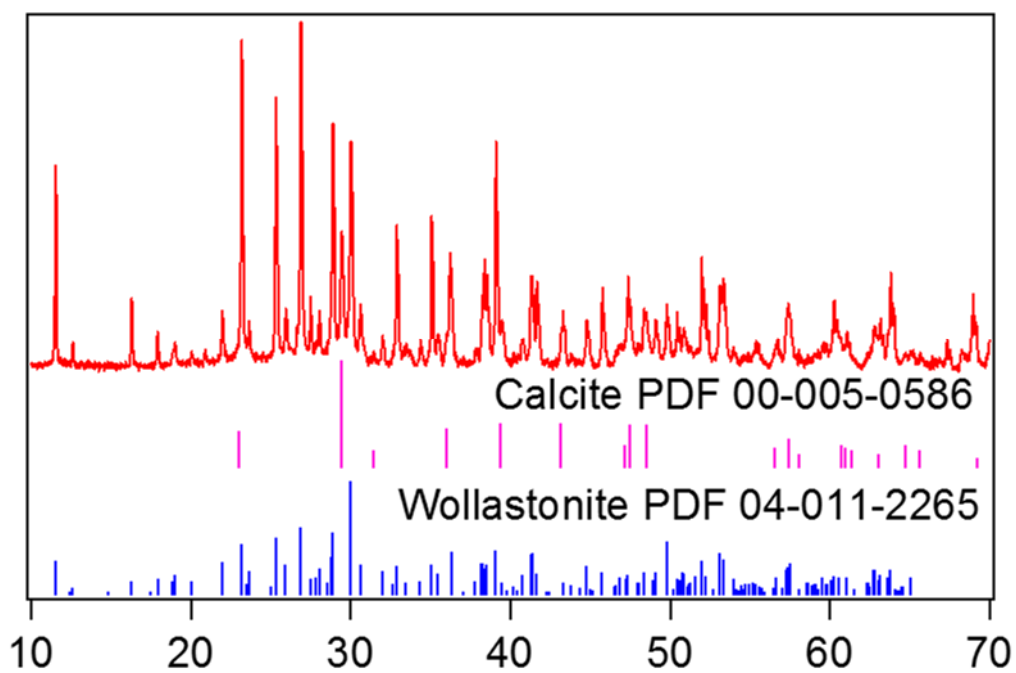
Figure 5-S6. XRD pattern of wollastonite particles with mean size of 17.8 μm, reacted for 40 hours at 45×S_w, 60 °C, and 100 bar.
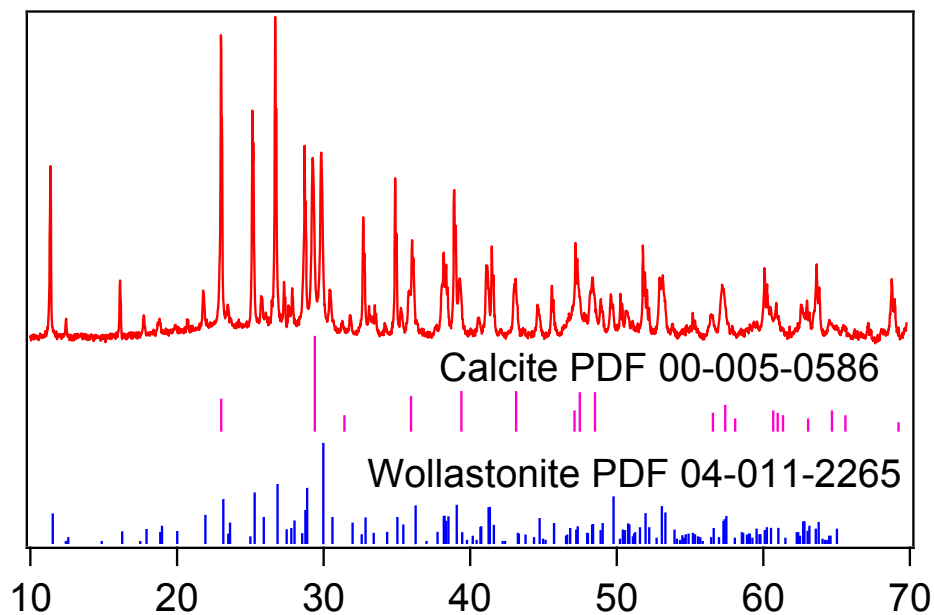
Figure 5-S7. XRD pattern of wollastonite particles with mean size of 11.2 μm, reacted for 40 hours at 45×S$_w$, 60 ºC, and 100 bar.
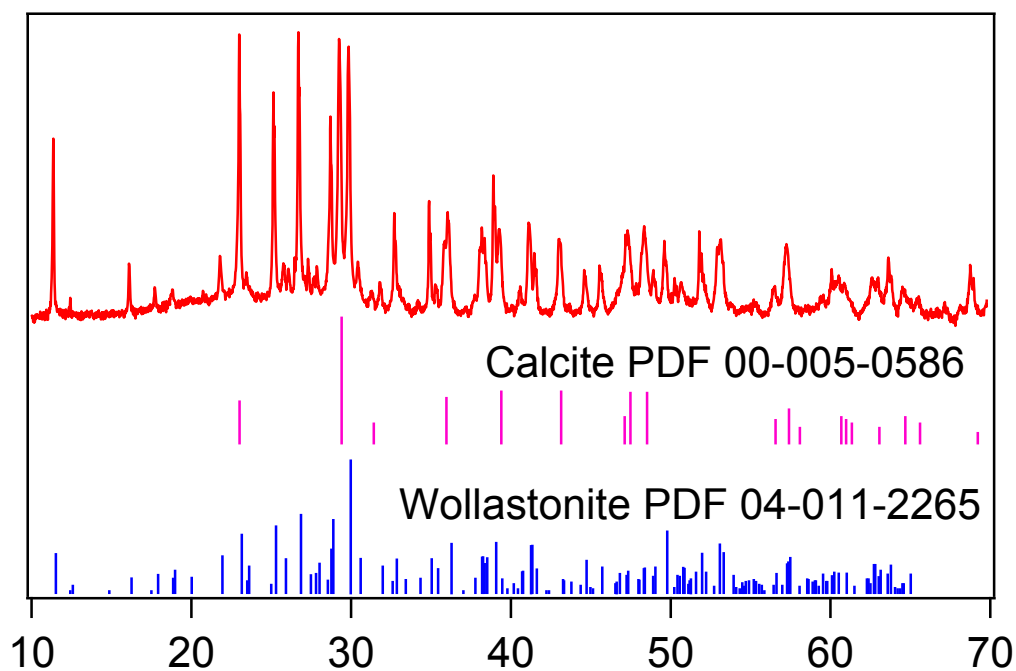
Figure 5-S8. XRD pattern of wollastonite particles with mean size of 5.6 μm, reacted for 40 hours at 45×S$_w$, 60 ºC, and 100 bar.
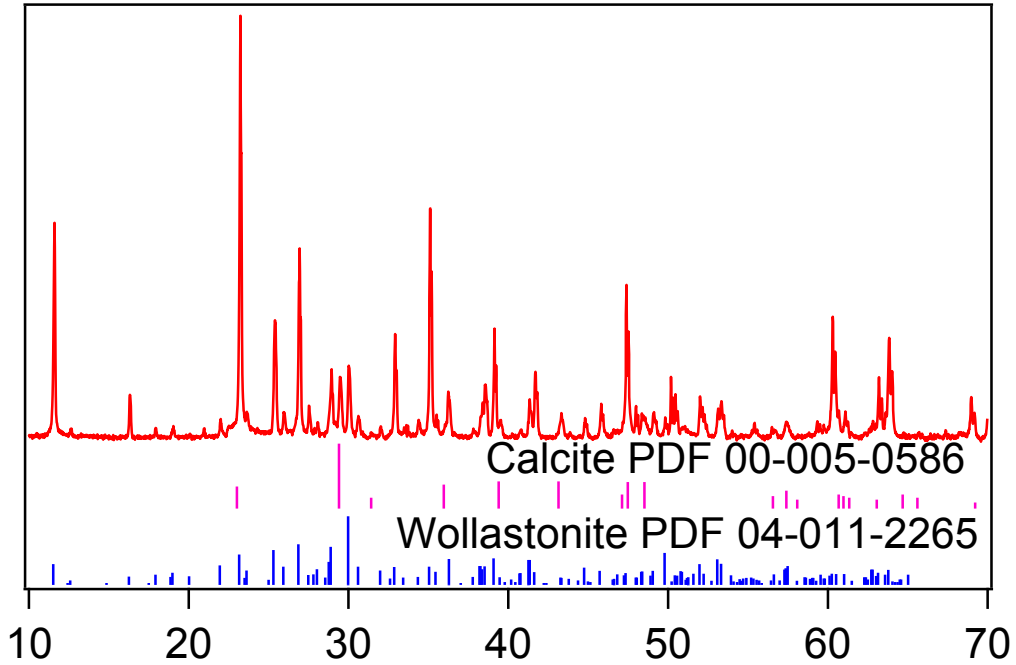
Figure 5-S9. XRD pattern of wollastonite particles with mean size of 82.1 μm, reacted for 40 hours at $45 \times S_w$, 60 °C, and 100 bar.

Table 5-S2. Experimental conditions and results.

Experiment number #	T (°C)	Duration (h)	S_w (100%)	Mass (g)	Size (μm)	BET surface area (m²/g)	Mass loss (%)	Reacted fraction (%)	Reacted thickness (nm)
1	60	20	0.5	0.3	3.8	4.46±0.01	4.14±0.47	10.1±1.15	27.8
2	60	20	1	0.3	3.8	4.46±0.01	8.57±0.69	23.3±1.85	89.6
3	60	20	5	0.3	3.8	4.46±0.01	12.3±0.70	35.6±2.12	119
4	60	20	10	0.3	3.8	4.46±0.01	13.7±0.19	40.3±0.57	153
5	60	20	20	0.3	3.8	4.46±0.01	14.4±0.56	42.8±1.62	167
6	60	20	30	0.3	3.8	4.46±0.01	15.6±2.22	47.2±6.56	193
7	60	20	45	0.3	3.8	4.46±0.01	15.3±1.21	45.9±3.78	185
8	60	20	0.5	0.3	17.8	1.45±0.01	1.64±0.18	3.17±0.56	22.6
9	60	20	1	0.3	17.8	1.45±0.01	4.04±0.15	9.81±0.42	97

10	60	20	5	0.3	17.8	1.45±0.01	4.63±0.10	11.5±0.29	117
11	60	20	10	0.3	17.8	1.45±0.01	5.18±0.55	13.1±1.58	138
12	60	20	20	0.3	17.8	1.45±0.01	5.73±0.20	14.7±0.56	175
13	60	20	30	0.3	17.8	1.45±0.01	6.37±0.49	16.6±1.52	185
14	60	20	45	0.3	17.8	1.45±0.01	6.04±0.55	15.6±1.57	182
15	60	20	2.5	0.3	3.8	4.46±0.01	11.39±0.62	32.4±1.85	N.D.
16	60	20	0.5	0.05	3.8	4.46±0.01	3.95±0.50	9.56±1.57	N.D.
17	60	20	1	0.05	3.8	4.46±0.01	9.93±0.78	27.6±2.10	N.D.
18	60	20	2.5	0.05	3.8	4.46±0.01	10.9±0.34	30.8±0.93	N.D.
19	60	20	5	0.05	3.8	4.46±0.01	12.3±0.74	35.6±2.01	N.D.
20	60	20	10	0.05	3.8	4.46±0.01	13.0±1.67	37.7±4.56	N.D.
21	60	20	45	0.05	3.8	4.46±0.01	14.8±0.03	44.2±0.09	N.D.
22	60	20	45	0.05	82.0	0.54±0.01	2.37±0.42	5.15±1.18	N.D.
23	60	5	45	0.3	3.8	4.46±0.01	12.5±1.33	36.2±3.99	N.D.
24	60	10	45	0.3	3.8	4.46±0.01	13.4±1.57	39.3±4.74	N.D.
25	60	30	45	0.3	3.8	4.46±0.01	14.0±3.04	41.5±9.19	176
26	60	40	45	0.3	3.8	4.46±0.01	16.3±1.66	49.6±5.06	226
27	60	5	45	0.3	5.6	3.61±0.01	10.7±0.81	30.0±2.28	N.D.
28	60	10	45	0.3	5.6	3.61±0.01	12.9±1.70	37.5±5.66	N.D.
29	60	20	45	0.3	5.6	3.61±0.01	11.8±1.46	33.7±4.39	168
30	60	30	45	0.3	5.6	3.61±0.01	13.6±1.85	39.9±5.57	211
31	60	40	45	0.3	5.6	3.61±0.01	11.9±1.77	34.2±5.35	171
32	60	5	45	0.3	11.1	1.945±0.01	5.42±0.49	13.8±1.38	N.D.
33	60	10	45	0.3	11.1	1.945±0.01	7.40±0.70	19.7±1.85	N.D.

34	60	20	45	0.3	11.1	1.945± 0.01	8.12± 1.82	21.9±4. 86	171
35	60	30	45	0.3	11.1	1.945± 0.01	8.83± 1.41	24.1±3. 77	193
36	60	40	45	0.3	11.1	1.945± 0.01	8.41± 2.30	22.8±6. 15	180
37	60	5	45	0.3	17.8	1.45±0 .01	4.35± 0.56	10.7±1. 40	N.D.
38	60	10	45	0.3	17.8	1.45±0 .01	4.77± 1.26	11.9±3. 22	N.D.
39	60	30	45	0.3	17.8	1.45±0 .01	6.87± 1.84	18.1±4. 84	214
40	60	40	45	0.3	17.8	1.45±0 .01	6.54± 1.12	17.1±2. 93	202
41	60	5	45	0.3	82.0	0.54±0 .01	2.92± 0.30	6.69±0. 70	N.D.
42	60	10	45	0.3	82.0	0.54±0 .01	2.63± 0.46	5.89±1. 08	N.D.
43	60	20	45	0.3	82.0	0.54±0 .01	3.40± 0.77	8.01±1. 87	194
44	60	30	45	0.3	82.0	0.54±0 .01	3.71± 0.98	8.90±2. 42	220
45	60	40	45	0.3	82.0	0.54±0 .01	2.81± 1.03	6.38±2. 43	173
46	35	180	45	0.3	17.8	1.45±0 .01	14.9± 1.13	44.5±3. 54	N.D.
47	60	20	45	0.3	17.8	1.57±0 .13	6.47± 0.58	16.9±1. 52	199
48	60	20	45	0.3	17.8	14.16± 0.80	8.31± 1.76	22.5±4. 97	202

N.D. = not determined

Chapter 6: Wollastonite Carbonation in Water-bearing Supercritical CO₂: Effects of Water Saturation Conditions, Temperature, and Pressure

Abstract

The carbonation of silicates in water-bearing supercritical CO_2 (scCO_2) can affect the performance of subsurface CO_2 injection. This study investigated the effects of water, temperature, and pressure on the carbonation of wollastonite ($CaSiO_3$) in water-bearing scCO_2 at 35–93 $^{\circ}$C, 25–125 bar, and from dry conditions to 140 times more water than needed for saturation ($140 \times S_w$). The extent of reaction increased with more water, higher pressure, and interestingly, lower temperature. In addition, for the first time, we report on water-bearing scCO_2–silicate reactions for samples with varying prior histories of water saturation conditions, temperature, and pressure. For a sample initially reacted at 100% water saturation ($1 \times S_w$) and then with $45 \times S_w$, the final reaction extent was smaller than the sample reacted only with $45 \times S_w$. Similarly, for a sample initially reacted at 60 $^{\circ}$C and then at 35 $^{\circ}$C, the reaction extent was smaller than for a sample reacted only at 35 $^{\circ}$C. In contrast, for a sample initially reacted at 50 bar and then at 100 bar, the reaction extent was the same as for a sample reacted only at 100 bar. These findings help us understand the extent to which water-bearing scCO_2–silicates reactions depend on environmental conditions and the reactions' impacts on subsurface CO_2 injection.

6.1 Introduction

In Chapter 5, we elucidated the effects of particle sizes on wollastonite carbonation in water-bearing $scCO_2$. In this chapter, we discuss the effects of reaction conditions, including water, temperature, and pressure. The information on the effects of water saturation conditions, temperature, and pressure on the carbonation of wollastonite in water-bearing $scCO_2$ is still limited. Miller et al. used experimental conditions, such as 50 °C and 90 bar, 55 °C and 120 bar, and 70 °C and 160 bar, and found that the extent of reaction increased as temperature and pressure became higher[59]. However, it is difficult to deconvolute the effects of temperature and pressure, as they were increased at the same time. Also, the amount of water was limited to < 5 times more water than needed for saturation in $scCO_2$ (< $5 \times S_w$, where S_w represents 100% water saturation in $scCO_2$), and the effects of higher water saturation conditions remained unknown[59]. Whitfield and Mitchell reported that carbonation of wollastonite was faster at higher temperature and there was no effect of pressure on it. However, in their study, liquid phase bulk water was added directly to the mineral and the amount is not specified[62]. Consequently, the reactions may have happened in the aqueous phase, rather than in water-bearing $scCO_2$. Still studies using other silicates, such as forsterite (Mg_2SiO_4), fayalite (Fe_2SiO_4), and antigorite ((Mg, Fe)$_3Si_2O_5(OH)_4$), investigated the effects of water, temperature, and pressure on the extent of reaction and phase and morphology of reaction products[55, 56, 60, 164, 166, 181]. However, carbonation reactions of these minerals in water-bearing $scCO_2$ have relatively slow kinetics and cannot reach equilibrium in a short time period. Consequently, the long term effects of water, temperature, and pressure on silicate carbonation in water-bearing $scCO_2$ are still unclear.

Moreover, the effects of varying water saturation conditions, temperatures, and pressures on silicate carbonation in water-bearing $scCO_2$ are also unknown. It is crucial to think about the

fact that while most studies on silicate carbonation in water-bearing $scCO_2$ fixed the water saturation percentage, temperature, and pressure at certain values, the minerals in field sites can experience a series of conditions. For example, the injection of CO_2 will first produce a dehydration front, then create a high water saturation percentage regime by the diffusion of water in $scCO_2$ fluid[28]. The temperature near the wellbore can temporarily decreased during CO_2 injection, and then recover in long run[182]. Pressure is also affected by the injection of CO_2, and can be changed by CO_2 leakage. The information obtained using fixed conditions may not be accurate enough to capture reactions undergoing dynamic conditions and can create discrepancies in predicting reactions under varying conditions. In Chapter 5, we found that the extent of reaction is limited by the surface coverage of the amorphous silica layer formed on the surface of wollastonite[183]. Similar situations could happen for other silicates after the reaction reaches a plateau. The surface coverage of the product layer formed at the initial conditions may influence subsequent reactions when conditions change. Elucidating the effects of varying conditions will allow us to more accurately predict water-bearing $scCO_2$–silicates reactions in field sites.

To address these knowledge gaps, this study investigated the carbonation of wollastonite in water-bearing CO_2 at 35, 60, and 93 $^{\circ}C$, 25–125 bar, and 0–$140 \times S_w$. In addition, for the first time, the effects of varying water saturation condition, temperature, and pressure have been studied. Although this study is single mineral study, it provides useful insights for better understanding multiple mineral systems. The new information obtained helps understand water-bearing $scCO_2$–silicate reactions under various subsurface conditions.

6.2　Materials and Methods

6.2.1　Minerals

Natural wollastonite particles were obtained from NYCO Minerals, Inc. (Willsboro, NY). Two different size ranges, with volumetric mean diameters of 3.8 and 17.8 μm, were used. The size distributions of these two size ranges are available in Figure 6-S1 in the Supplementary Content. The structure was identified to be wollasonite-1A using X-ray diffraction (XRD)[171]. Our X-ray fluorescence measurement (Table 6-S1) showed that the Ca/Si ratio was 0.959.

6.2.2　Carbonation in water-bearing scCO₂ at simulated GCS conditions

Carbonation experiments were conducted in a 300 mL HastelloyC-276 vessel (Parr Instruments, Moline, IL) modified from the reactor used in our previous studies[79, 80, 95, 105, 120, 121]. The CO_2 was injected using a syringe pump (Teledyne, ISCO). The temperature was maintained using a temperature controller (Parr Instruments, Moline, IL). Typical GCS conditions, 60 °C and 100 bar were used. When investigating effects of temperature and pressure, the conditions were varied between 35, 60, and 93 °C, and 25–125 bar CO_2. These conditions are within the range of the conditions in GCS sites (31–110 °C, 73.8–600 bar)[10]. For example, the typical conditions are 35 °C and 100 bar at the Sleipner site[64], 65 °C and 150 bar in the Frio formation[34], and 63 °C and 140 bar at the Weyburn field site[184].

To investigate water-bearing scCO₂ reactions, minerals and liquid phase water were separated. Water was added in the PTFE liner of the vessel. Mineral particles were added in PTFE tubes. The tubes were capped, but had small holes allowing contact between the wollastonite and water-bearing scCO₂. After CO_2 was injected into the vessel, water was dissolved in scCO₂. The water-bearing scCO₂ entered the tube and reacted with the mineral. A schematic diagram of the

reaction system setup is available in Figure 6-S2 in the Supplementary Content. The solubility of water in $scCO_2$ can be affected by the salinity of the water. In field sites, salinity is largely different from site to site, varying between 0.5 g/L and 400 g/L[42, 185]. Therefore, for simplicity, in this work, ultra-purified water was used, which serves a good starting point. The solubility of water in CO_2 was predicted using Spycher's model[172]. In addition, in Chapter 5, we found that the stacking of particles in the PTFE tubes did not affect the reaction, which was checked by comparing the extents of reaction using 0.3 g and 0.05 g particles[183].

6.2.3 Determination of reacted fractions and reacted thicknesses

The fractions of wollastonite that reacted with water-bearing $scCO_2$ were determined based on thermogravimetric analysis (TGA, Q5000IR, TA Instruments) results. Samples were heated to 900 °C, with a ramp of 20 °C/min under N_2 flow (25 ml/min). Wollastonite and amorphous silica were stable below 900 °C, but $CaCO_3$ completely decomposed into CaO and CO_2[59]. Chapter 5 showed that the amount of structural water was not significant[183]. So the mass loss between 150 and 780 °C during TGA was attributed to CO_2 resulting from $CaCO_3$ decomposition (Figure 6.1A), and used to derive the reacted fraction of original wollastonite, based on equation 5.1 developed in Chapter 5. Based on the reacted fraction, the thickness of the reacted layer on the surface of particles can be calculated by normalization to geometry surface area. The thickness of the reacted layer was calculated using equation 5.3 and 5.4 developed in Chapter 5.

This method assumed an ideal cylindrical shape for each particle. This assumption is reasonable because the results obtained are statistically averaged thickness. Although information on the heterogeneity of particles, including the shape, reactivity, and surface roughness, is not fully captured, in Chapter 5 we found that the reacted thickness can more accurately represent the extent of reaction than reacted fraction does. Reacted fraction is size-dependent, and thus is not

149

comparable among studies using different particle sizes. In contrast, the reacted thickness is independent of particle size, and provides directly comparable information on the extent of reaction. For this reason, in this study, the reacted thickness was used to show the extent of reaction. Specific reacted fraction results are available in the Supplementary Content (Figure 6-S3-S5).

6.3 Results and Discussion

6.3.1 Effects of water saturation conditions on wollastonite carbonation in water-bearing scCO$_2$

The reaction extents increased linearly with water saturation percentages between 30% and 80% at 60 °C and 100 bar.

As shown in Figure 6.1A, the sample reacted with dry scCO$_2$ showed < 1% mass loss during TGA analysis. This very small loss is consistent with conclusions of previous studies that dry scCO$_2$ cannot react with silicates[29, 57, 59, 166, 181]. Recently, the role of water in water-bearing scCO$_2$–silicate interactions was emphasized[26, 56, 57, 59, 181], because water vapor was found to form a water film on the mineral surface[166], enhance the kinetics and extents of reaction, and change the phase of the reaction product[55, 59, 166, 181]. As shown in Figure 6.1B, in our study, calcite was the dominant crystalline phase identified as the product of reaction. No significant amounts of aragonite and vaterite were observed. The formation of amorphous CaCO$_3$ is possible, but the *ex situ* analysis may cause phase transformation to more stable phases. Nevertheless, the potential phase transformation of CaCO$_3$ does not affect the determination of reaction extent.
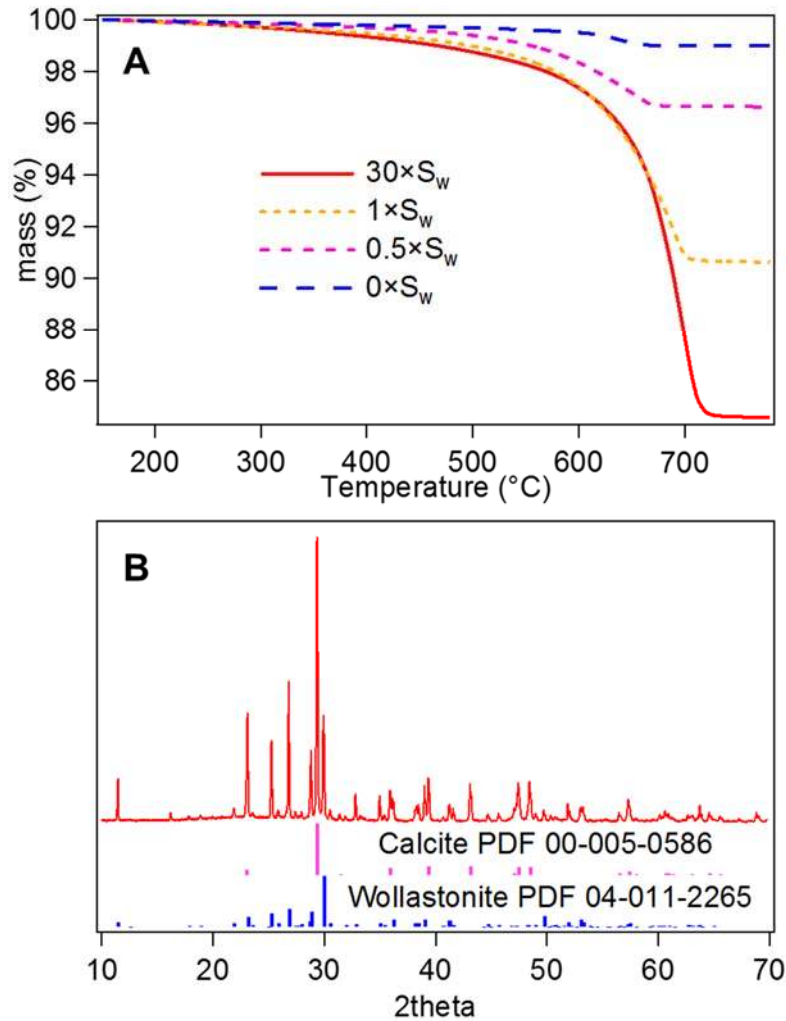
Figure 6.1. (A) TGA analysis of wollastonite particles with a volumetric mean size of 3.8 μm. Mass losses of 15.5%, 9.4%, 3.4%, and 1.0% were observed for samples reacted for 40 hours at 60 $^{\circ}$C and 100 bar CO_2 with 30×Sw, 1×Sw, 0.5×Sw, and no water added, respectively. **(B)** XRD pattern of wollastonite particles with a volumetric mean size of 17.8 µm reacted for 180 hours under 45×Sw, 35 $^{\circ}$C, and 100 bar CO_2. The presence of calcite was identified.

Considering the importance of water in reactions, we measured the dependency of reaction

extent on the water saturation percentage, as shown in Figure 6.2A. Wollastonite particles with a

volumetric mean size of 3.8 μm were reacted at 60 $^{\circ}$C and 100 bar CO_2 with different amounts of

water added. Small particles were used to better show the large reacted fraction. Each sample was

reacted for 40 hours, so that the reaction could reach a plateau. We found that the minimum water

saturation percentage required to have a detectable reaction was 30%. Between 30% and 80%, the

151

reacted thickness increased linearly with the water saturation percentage. These results indicate that the formation of a water film on the wollastonite surface requires a minimum amount of water, measured to be 30% water saturation. This conclusion is consistent with previous studies which suggested the formation of water film is possible even below 100% water saturation[56, 186].
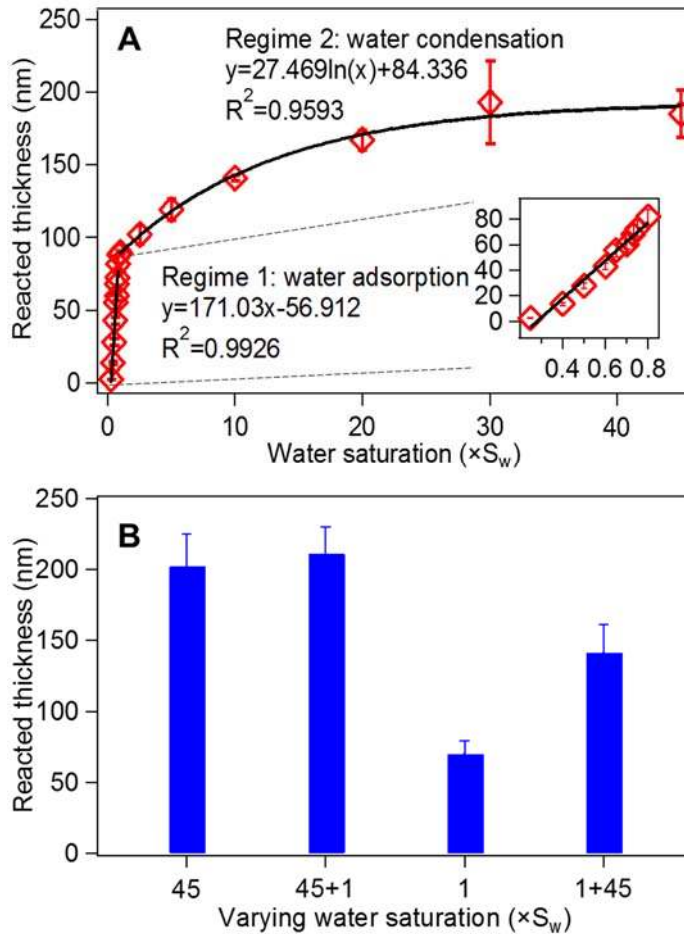
Figure 6.2. (A) Reacted thickness of wollastonite particles with volumetric mean size of 3.8 μm reacted for 40 hours with different water saturation percentages, at 60 °C and 100 bar CO_2. At least 30% water saturation is needed for reaction. The reacted thickness increased linearly between 30 to 80% water saturation, kept increasing even after 100% water saturation, and became less sensitive to water saturation beyond 20×Sw. **(B)** The reacted thickness of wollastonite particles with volumetric mean size of 3.8 μm reacted for 40 hours at varying water saturation conditions, 60 °C, and 100 bar CO_2. The reacted thicknesses were similar for the control sample reacted only with 45×Sw, and the sample reacted at 1×Sw after initial reaction with 45×Sw (shown as **45×Sw + 1×Sw**). The sample reacted with 45×Sw after initial reaction at 1×Sw (shown as **1×Sw + 45×Sw**) had larger reacted thickness than the sample reacted only at 1×Sw (shown as **1×Sw**), but smaller than the sample reacted only with 45×Sw.

152

The reaction extents further increased with excess water beyond 100% saturation (S_w).

Beyond 80% water saturation, the reacted thickness became less sensitive to the increasing water saturation percentage, as shown in Figure 6.2A. This result is likely due to the saturation of water adsorption sites on the mineral surface. However, the reacted thickness kept increasing with water saturation percentage even after 100% saturation (i.e., S_w) was reached. All the excess water existed in the liquid phase and did not directly contact with mineral particles. It is very interesting that reaction extent can be affected by the amount of liquid phase water, which is not in contact with the mineral particles. We suggest that the increasing reaction extent resulted from water vapor condensation from water-bearing $scCO_2$. After S_w was reached, water vapor in $scCO_2$ could condense into the liquid phase. The condensation of water vapor can happen at the surface of the liquid phase water added in the reactor. The same process may also happen at the water film on the mineral surface. In this way, even though the liquid phase water was separated from wollastonite particles in our reactor, the increasing amount of water beyond S_w could still increase the amount of water on the mineral surface. The underlying driving force for the partition of water to the mineral surface could be the hydrophilicity of the mineral surface and its reaction with water-bearing $scCO_2$. The water adsorbed on the mineral surface is electrostatically attracted by the mineral surface and the metal cations dissolved from the mineral surface. The lower activity of water bound on the mineral surface compared to that of the liquid phase water can promote the partitioning of water from the liquid phase to the mineral surface. In addition, as the reaction proceeds, more water would be attracted by the produced carbonate and amorphous silica. Therefore, more water would transport from water-bearing $scCO_2$ to the mineral surface. If more liquid phase water is in contact with $scCO_2$, the loss of water from water-bearing $scCO_2$ can be compensated faster by the liquid water originally put in the reactor. In addition, another potential

contribution to the water adsorption and condensation is from the water–water interactions in water-bearing scCO$_2$. According to modeling by Glezakou et al., the water molecules in water-bearing scCO$_2$ tend to attract one another and exist as clusters at high saturation percentages[187]. These water–water interactions could possibly contribute to the condensation of water vapor into the water film on mineral surfaces.

The increasing extent of reaction beyond S$_w$ has also been observed in several other studies[26, 56, 57, 59, 181]. Unfortunately, however, the implications of these observations have not been emphasized. In this study, we have shown that a further increase of water saturation over S$_w$ can lead to an almost two times higher reacted thickness, as shown in Figure 6.2A. In field sites, while 0–100% water saturation conditions can exist, conditions with an excess amount of water can also happen. In that case, condensation similar to that seen in our system could also happen in field sites. Thus, a better understanding of the transport of water in scCO$_2$ fluid is important for predicting the impact of water-bearing scCO$_2$–silicate interactions on the stability of geologic formations.

An initial reaction at a low water saturation condition partially inhibits subsequent reactions at high water saturation condition.

Before the transport of water vapor and CO$_2$ reaches an equilibrium in field sites, it is possible that minerals in field sites can initially react with water-bearing scCO$_2$ in one water saturation condition and then later be exposed to another. Although we know the reaction extent at certain water saturation conditions, the prediction of the actual reaction extent could also be difficult, because we do not know a full history of the water saturation conditions and the effects of previously exposed water saturation conditions. To elucidate how the reaction would be affected

by varying water saturation conditions, two situations have been investigated at 60 °C and 100 bar: For **Sample A**, samples were initially reacted with 45 times more water than needed for saturation (For simplicity, $45 \times S_w$) for 20 hours, and then the same samples were reacted at $1 \times S_w$ for another 20 hours. For **Sample B**, samples were initially reacted at $1 \times S_w$ for 20 hours, and then those samples were reacted with $45 \times S_w$ for another 20 hours. So only the sequences of water saturation were different. Figure 6.2B shows that the sample initially reacted with $45 \times S_w$ did not further react when the saturation was changed to $1 \times S_w$. Because the product layer produced with $45 \times S_w$ is thicker than that formed at $1 \times S_w$, the thicker product layer may prevent any further reaction in a less reactive condition ($1 \times S_w$). In contrast, when Sample B was initially reacted at $1 \times S_w$ first, and then reacted again with $45 \times S_w$, the reaction occurred continuously but the final reacted thickness was smaller than the sample reacted only with $45 \times S_w$ for 40 hours or for Sample A. This observation suggests that an initial reaction at low water saturation conditions would partially inhibit the subsequent reaction.

The findings provide new insights into mineral reactions under varying environmental conditions. Although a mineral is equilibrated at a high water saturation condition, if the mineral has previous experience with a lower water saturation condition before the high water saturation condition, the actual extent of reaction can be lower than predictions based on fixed conditions. The example of wollastonite described in this study is relatively simple, because the kinetics of wollastonite carbonation are fast so that the reaction reached pseudo-equilibrium in several hours. For other silicates in field sites with slower reaction kinetics, the water saturation conditions may vary before the reactions reach equilibria. In that case, predicting the effect of varying environmental conditions is even more complicated. The relationship between water transport and the kinetics of the water-bearing $scCO_2$–mineral reaction can affect the extent of reactions.

Water saturation conditions affect the permeability of the surface product layer.

While the extent of the water-bearing $scCO_2$–mineral reaction is known to be related to the amount of water adsorbed on the mineral surface[26, 56, 57, 59, 181], the underlying mechanism is still unclear. In studies using other minerals, such as forsterite, the extent of reaction is largely affected by the reaction kinetics[57, 166]. Because water is an important catalyst and reactant[55, 59, 166, 181], reaction kinetics can be faster at higher water saturation conditions. For wollastonite, we found that the extent of reaction was determined by the reaction conditions (temperature, pressure, and water saturation) and the thickness and porosity/permeability of the surface product layer[183]. Furthermore, the product layer formed at a lower water saturation percentage could be a stronger diffusion barrier to water-bearing $scCO_2$. In other words, a greater availability of water is not the only contribution of higher water saturation conditions. An indirect effect can be affecting the porosity and permeability of the reaction product layer. A few pieces of evidence support this postulation: For Sample A, a product layer was first produced at $1 \times S_w$, and then another product layer was produced by further reaction with $45 \times S_w$. The total thickness was smaller than for the control sample reacted at a fixed condition, $45 \times S_w$. This finding indicates that the product layer produced at $1 \times S_w$ can inhibit the access of water-bearing $scCO_2$ to the mineral surface more efficiently than the product layer produced at $45 \times S_w$. This result can also explain why the layer thickness is smaller at lower water saturation percentages. In addition, it confirms that the water saturation conditions can affect the access of water-bearing $scCO_2$ to the mineral surface, which should be achieved by changing the porosity and permeability of the reaction product layer. In Chapter 5 we found that the amorphous silica layer formed in the liquid phase is much more porous than that formed in the thin water film in water-bearing $scCO_2$[183]. This observation is consistent with the current finding that more abundant water will lead to more porous reaction product layer.

156

6.3.2 Effects of temperature on wollastonite carbonation in water-bearing scCO₂
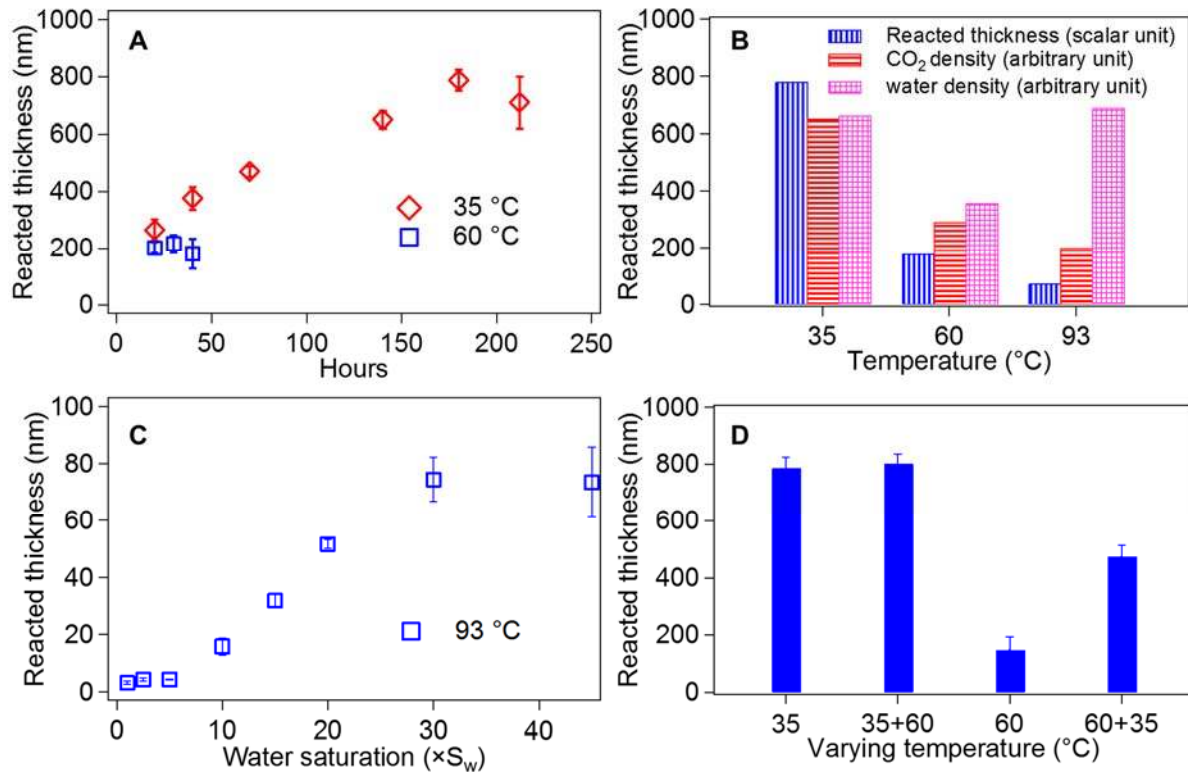
Figure 6.3. (A) Reacted thickness of wollastonite particles with volumetric mean size of 17.8 μm with 45×Sw at 35 °C (red diamond) and 60 °C (blue square), and 100 bar CO_2. The reacted thicknesses reached plateaus after 140 hours and 20 hours, respectively. **(B)** Reacted thicknesses of wollastonite particles after reaction with 45×Sw at 35, 60, and 93 °C, and 100 bar CO_2. The scales of the density of CO_2 and water are not shown. The reacted thickness showed the same trend as the density of CO_2, but was different from the trend of water density. **(C)** The reacted thickness of wollastonite particles with volumetric mean size of 3.8 μm reacted for 40 hours at different water saturation percentages, 93 °C, and 100 bar CO_2. The reacted thickness reached plateau beyond 30×Sw. **(D)** The reacted thicknesses of wollastonite particles with volumetric mean size of 17.8 μm reacted for 180 hours at varying temperatures, 45×Sw and 100 bar CO_2. The reacted thicknesses were similar for the control sample reacted only at 35 °C and the sample reacted at 60 °C after initial reaction at 35 °C. The sample reacted at 35 °C after initial reaction at 60 °C had larger reacted thickness than the sample reacted only at 60 °C, but smaller than the sample reacted only at 35 °C.

Besides water saturation conditions, temperature can strongly affect the carbonation of

wollastonite. While reacted thickness reached a plateau after 20 hours at 60 °C, Figure 6.3A shows

that, for the 35 °C experiments, the reaction did not reach plateau until 140 hours. In addition, the

reacted thickness decreased with increasing temperature, as shown in Figure 6.3B. This

observation is surprising because the kinetics of mineral surface reactions, such as the hydrolysis

of silicates, should be enhanced at higher temperature. But, as shown in Chapter 5, for wollastonite the reaction quickly reached a plateau, and was no longer controlled by the kinetics of the surface reaction of wollastonite[183]. Instead, the diffusion of water-bearing $scCO_2$ across the surface product layer limited the reaction. Thus, the smaller reaction extent at higher temperature could have several causes: First, the availability of $scCO_2$ for the reaction is limited at higher temperature. Figure 6.3B shows that the reacted thickness follows the same trend as the density of CO_2 calculated using Peace Software (Peace Software, Inc.), a program for calculating gas properties. In addition, the solubility of CO_2 in the water film on the mineral surface would be lower at high temperature, because the solubility of gases in water is usually lower at high temperature. Second, at high temperature, there is less water adsorption on mineral surfaces. From 35 °C to 60 °C, as shown in Figure 6.3B, the density of water (based on the density of CO_2 and the mole fraction of water vapor in CO_2, see Table 6-S2) decreased, and thus the availability of water vapor in $scCO_2$ is smaller. At 93 °C, although the density of water in water-bearing $scCO_2$ increased due to increasing mole fraction of water in CO_2 (Table 6-S2), the adsorption of water on wollastonite became more difficult. A recent study reported an activation energy of -148 kJ/mol for water adsorption on calico-olivine (Ca_2SiO_4)[188]. Although no study on wollastonite is available, we expect that water adsorption on wollastonite surface can similarly become more difficult at high temperature. We have investigated how the temperature affected the dependency of the reacted thickness of wollastonite on water saturation. Figure 6.3C shows that, at 93 °C, the reacted thickness became much smaller at low water saturation percentages, compared to the situation at 60 °C, shown in Figure 6.2A. At 93 °C, the reacted thickness increased significantly between 5 to $30 \times S_w$. A plateau was reached after $30 \times S_w$, which had appeared at $20 \times S_w$ in 60 °C experiments. These results suggest that the reaction needs more water at higher temperature, which can result

158

from less water adsorption on the mineral surface. Third, higher temperature also induces faster kinetics of reaction product formation. Thus, at higher temperature, the surface product layer formed and covered the wollastonite surface easily, and this layer can act as a transport barrier. These three reasons can potentially explain the longer time needed to reach a plateau at low temperature.

The fourth reason is the effect of temperature on the permeability of the surface product layer. We investigated the effects of varying temperature histories at 100 bar with $45 \times S_w$ (Figure 6.3D). **Sample C** was initially reacted at 35 $^{\circ}$C for 180 hours, long enough for the reaction to reach plateau. Then, when we tried to react sample C again at 60 $^{\circ}$C, it cannot further react, because 60 $^{\circ}$C is a less reactive condition for wollastonite carbonation than 35 $^{\circ}$C. However, **sample D**, initially reacted at 60 $^{\circ}$C for 40 hours, which was long enough for reaction to reach plateau, could further react at 35 $^{\circ}$C. The final reacted thickness of sample D was smaller than for the sample reacted only at 35 $^{\circ}$C for 180 hours. Similar to the varying water saturation situations, this finding indicates that the product layer produced at a lower temperature can be a weaker diffusion barrier for water-bearing $scCO_2$. One of the potential explanation is that water adsorption on mineral surfaces is easier at lower temperature. As we mentioned above, the product layer produced with more water will be weaker diffusion barrier. The weaker diffusion barrier at lower temperature can explain the higher reaction extent and the continuing reaction for a longer time before reaching a plateau.

For broader implications of this finding, the effects of varying temperature history showed that the reaction extent measured at a fixed temperature may not accurately capture the information needed to predict the reaction in field sites. For example, minerals near the wellbore can experience a lower temperature due to the cooling effects of CO_2 injection compared to other locations. Hence,

159

predictions based on the reservoir temperatures before injection will possibly underestimate the extent of reaction. The temperature change due to CO_2 injection could be important for predicting water-bearing $scCO_2$–silicate interactions.

6.3.3 Effects of pressure history on wollastonite carbonation in water-bearing scCO₂
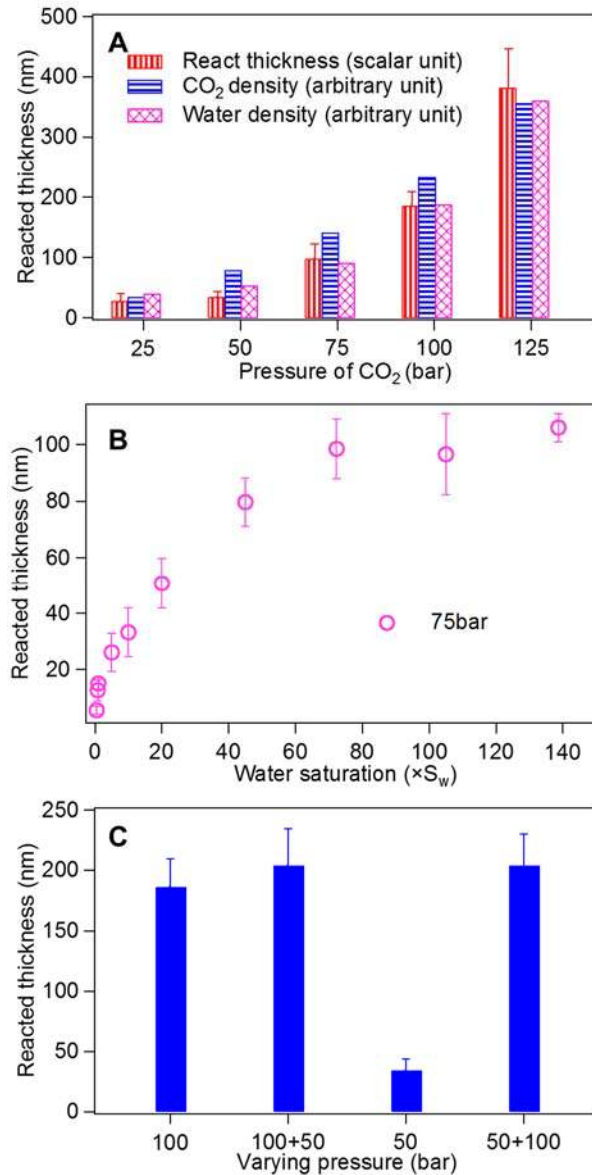
Figure 6.4. (A) Reacted thicknesses of wollastonite particles with volumetric mean size of 3.8 μm for 40 hours with 140×Sw, 60 °C, and different pressures of CO_2. The scales of the density of CO_2 and water at different pressure are not shown. The reacted thickness showed the same trend as the density of CO_2 and water. **(B)** Reacted thicknesses of wollastonite particles with volumetric mean size of 3.8 μm for 40 hours at different water saturation percentages, 60 °C, and 75 bar CO_2. The reacted thicknesses reached a plateau beyond 75×Sw. **(C)** The reacted thicknesses of wollastonite particles with volumetric mean size of 3.8 μm for 40 hours at varying pressures, 60 °C, and 140×Sw. The reacted thicknesses are similar for the control sample reacted only at 100 bar and the sample reacted at 50 bar after initial reaction at 100 bar. The sample reacted at 100 bar after initial reaction at 50 bar had larger reacted thickness than the sample reacted only at 50 bar, and was similar to the sample reacted only at 100 bar.

161

Besides water saturation conditions and temperature, pressure is another important factor affecting wollastonite carbonation in water-bearing $scCO_2$. Figure 6.4A shows that the extent of reaction increased significantly with increasing pressure. This observation is different from the finding of a previous study reporting that the kinetics of wollastonite carbonation are independent of pressure[62]. The different observation could easily result from the fact that water was added directly to the mineral in the previous study. In contrast, in our study, liquid phase water was physically separated from the minerals, and only water vapor could directly contact with sample surfaces. Among other recent studies of water-bearing $scCO_2$–silicate reactions, several added water directly to the mineral, so that liquid phase water directly contacted with the minerals[56, 62]. The reasoning is that in field sites, minerals are naturally contacted with water before CO_2 injection. However, in this case, aqueous phase dissolution reactions in CO_2-rich water could happen, and the results cannot be comparable with water-bearing $scCO_2$–silicate reactions. Because a certain amount of minerals may not naturally be in contact with water before CO_2 injection, or in the case of new fractured surfaces, the separated settings used in our work can also mimic the particular situations in field sites.

The higher reaction extent with higher pressure can be explained by several reasons: First, Figure 6.4A shows that the reacted thickness showed a similar trend to the density of CO_2. With a higher pressure, CO_2 has a stronger ability to diffuse across the product layer and reach deeper wollastonite surfaces. Second, as shown in Figure 6.4A, pressure can also change the density of water in water-bearing $scCO_2$. This result can be related to the changes in the dependency of the reacted thickness on the water saturation percentage at different pressures. We found that the trend of water dependency at 75 bar, as shown in Figure 6.4B, is similar to that for 100 bar, shown in Figure 6.2A. The reacted thickness increased quickly at low water saturation percentages, and then

slowly increased to a plateau. However, Figure 6.4B shows that at 75 bar, the plateau is reached after $75 \times S_w$, compared to $20 \times S_w$ for 100 bar, as shown in Figure 6.2A. This observation indicates that a lower pressure reaction needs more water, which results from the smaller water density. A third possible explanation is the different hydrophilicity of mineral surfaces under different pressures of CO_2. A previous study reported variation of wettability on mineral surfaces by different pressures of CO_2 fluid[189]. Unfortunately, similar results for wollastonite are not available. However, it is necessary to point out the wettability change under different CO_2 pressures could affect the water-bearing $scCO_2$–silicate reactions, and, reciprocally, the reactions can alter the wettability as well.

The effects of varying pressure history were also investigated at 60 ºC with $140 \times S_w$. The $140 \times Sw$ was chosen so that the reaction extent would not be sensitive to the water saturation percentage, as shown in Figure 6.4B. Figure 6.4C shows that, **sample E,** initially reacted at 100 bar for 20 hours, cannot further react at 50 bar, because 50 bar is a less reactive condition than 100 bar. However, **sample F,** initially reacted at 50 bar for 20 hours, can further react at 100 bar. Different from varying water saturation and temperature, the final reacted thickness was the same for the sample reacted only at 100 bar for 40 hours. This observation suggests that product layers produced at different pressures have the same permeability to water-bearing $scCO_2$.

Although pressure cannot significantly affect the permeability of the product layer, the importance of varying pressure should not be neglected. To inject CO_2 into a reservoir, pressure higher than the reservoir pressure must be applied. The prediction of water-bearing $scCO_2$–silicate reactions based on the original reservoir pressure may not be accurate.

163

6.4 Conclusions

Supercritical CO_2–water–rock interactions play a significant role in evaluating the feasibility of GCS[13]. Compared to the water–rock interactions in CO_2-rich brine, the information on water-bearing $scCO_2$–mineral reactions is limited. This study investigated the effects of fixed and varying water saturation conditions, temperatures, and pressures, on the carbonation of wollastonite in water-bearing $scCO_2$. The results provide useful insights for understanding water-bearing $scCO_2$–mineral reactions. In this study, we found a further increase of reaction extent beyond $1 \times S_w$. This result is likely due to the condensation of water vapor on the mineral surface with excess amounts of water beyond $1 \times S_w$ in water-bearing $scCO_2$. Understanding the transport of water in the $scCO_2$ phase and the role of the mineral surface in this process is necessary for studying water-bearing $scCO_2$–silicate interactions in the future.

We also showed that the extent of reaction decreases with increasing temperature. This finding indicates that after the reaction reached plateau, water-bearing $scCO_2$–silicate reactions were controlled by the diffusion of water-bearing $scCO_2$ across the surface product layer, rather than controlled by the kinetics of mineral surface reactions. These surprising results provide insights into water-bearing $scCO_2$–silicate interactions. The impact of water-bearing $scCO_2$–mineral interactions on the reservoir rocks could be particularly significant in geologic formations with lower temperatures.

Furthermore, for the first time, we reported the effects of varying water saturations, temperatures, and pressures on the water-bearing $scCO_2$–silicate reaction. The outcomes show that the varying conditions in field sites can have significant impacts on water-bearing $scCO_2$–silicate reactions. Results obtained only under fixed conditions are not adequate for understanding the

impacts of water-bearing scCO$_2$–silicate reactions on the stability of silicates in field sites. The accurate prediction of a real situation requires a better understanding of the water transport in scCO$_2$ fluid, the cooling effect of CO$_2$ injection, and the pressure change due to CO$_2$ injection.

Other silicates also react with water-bearing scCO$_2$ and form carbonate and amorphous silicate, which cover the mineral surface. Although these minerals have slow reaction kinetics with water-bearing scCO$_2$ and may not reach a diffusion-controlled regime within the days or weeks scale of most studies, it is likely that the reaction will eventually reach plateau. Although there is caveat that these minerals may have different reactions, it is possible that the mechanisms similar to those found in this study could apply.

The changes in wettability and potential pore closure induced by water-bearing scCO$_2$–silicate reactions (dissolution and re-precipitation) can significantly affect the permeability of reservoir rocks. The permeability of the geologic formation strongly affects many processes, such as geologic CO$_2$ sequestration, scCO$_2$–enhanced oil recovery, and scCO$_2$–hydraulic fracturing. These engineering processes have great impacts on our environmental safety and quality, and the results of this study can benefit studies on subsurface CO$_2$ injection and its environmental sustainability.

Acknowledgments

Supporting Information for Chapter 6

Contents: Experimental details

Five figures

Two tables

Table 6-S1. X-ray fluorescence (XRF) analysis of wollastonite used in this study (in weight %).[190]

	Wollastonite		Number of ions on the basis of 3 oxygen
SiO_2	51.0	Si	0.991
CaO	45.7	Ca	0.951
Al_2O_3	0.60	Al	0.014
TiO_2	0.05	Ti	0.001
Fe_2O_3	0.67	Fe	0.010
MnO	0.15	Mn	0.002
MgO	0.80	Mg	0.023
Na_2O	0.20	Na	0.008
K_2O	0.03	K	0.001
P_2O_5	0.03	P	0.000
Loss on ignition	0.80		

Table 6-S2. The densities of CO_2 and water shown in Figures 3 and 4 in main text.

Temperature (ºC)	Pressure (bar)	CO_2 density (g/mL)	Mole fraction of water (%)	Water vapor density (mg/mL)
35	100	0.653	0.407	1.087
60	100	0.293	0.490	0.587
93	100	0.201	1.374	1.130
60	25	0.044	0.620	0.112
60	50	0.098	0.360	0.147
60	75	0.174	0.345	0.250
60	125	0.447	0.540	0.983
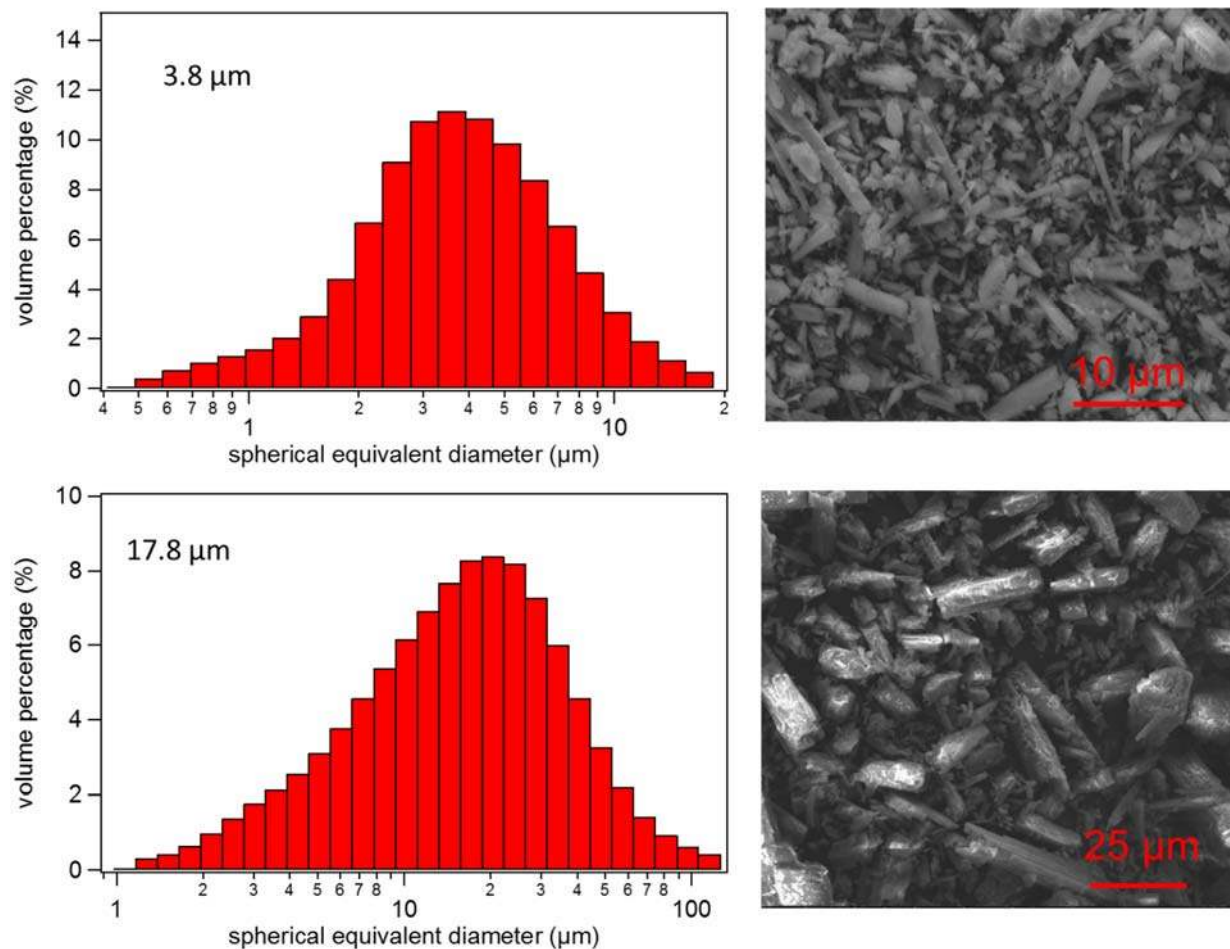
Figure 6-S1. Size distribution and SEM images of the two size fractions used in this study. The volumetric mean sizes are 3.8 and 17.8 µm.[190] The results were provided by NYCO Company and measured using laser diffraction. The SEM images shows consistently different particle sizes. Because 3.8 and 17.8 µm are spherical equivalent diameter, the particles in images can appear to be larger in size.
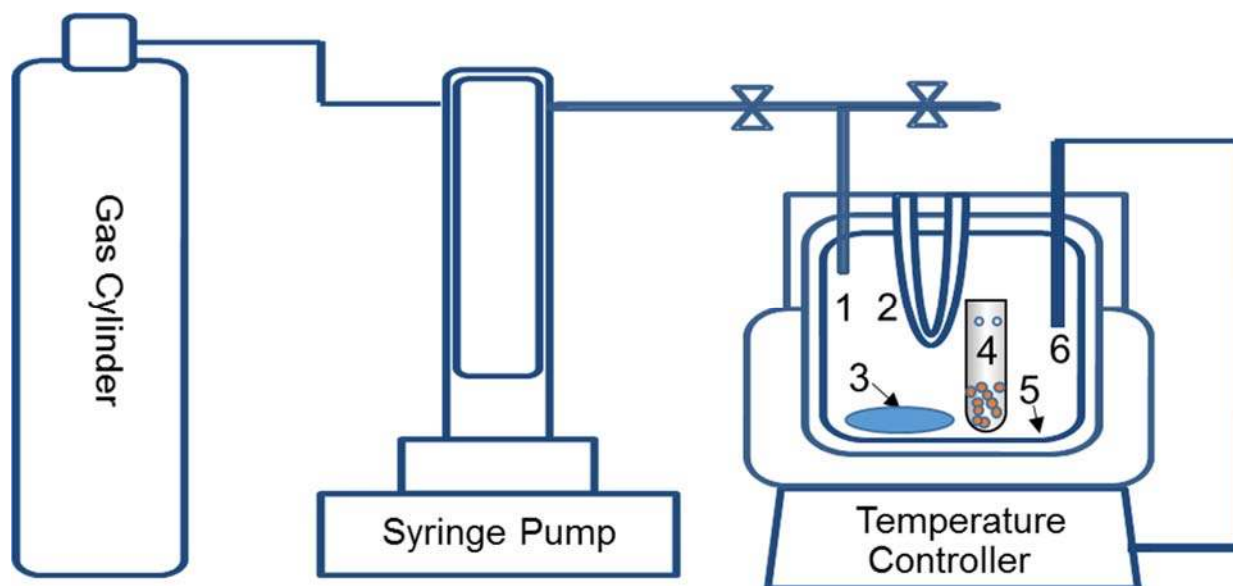
Figure 6-S2. Experimental setup. 1, Gas inlet and outlet tube; 2, Cooling loop; 3, Water; 4, Teflon tube; 5, Teflon liner; 6, Thermocouple.[190]
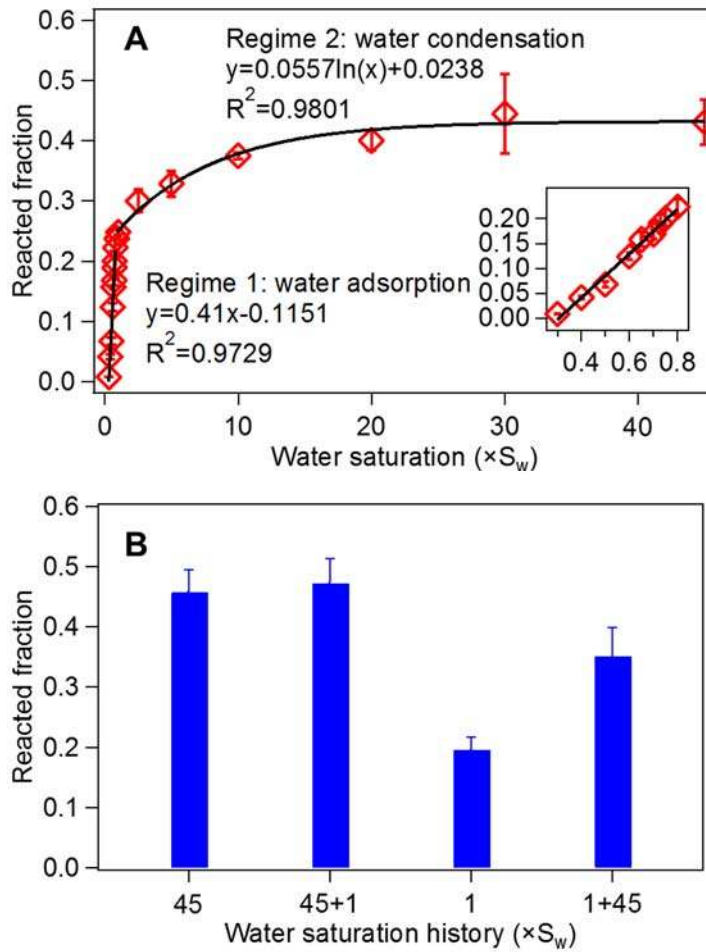
Figure 6-S3. Reacted fraction data used to calculate the reacted thickness in Figure 6.2 in the main text. **(A)** Reacted fraction of wollastonite particles with a volumetric mean size of 3.8 μm reacted for 40 hours at different water saturation percentages, 60 °C, and 100 bar CO_2. **(B)** The reacted fraction of wollastonite particles with a volumetric mean size of 3.8 μm reacted for 40 hours at varying water saturation conditions, 60 °C, and 100 bar CO_2.
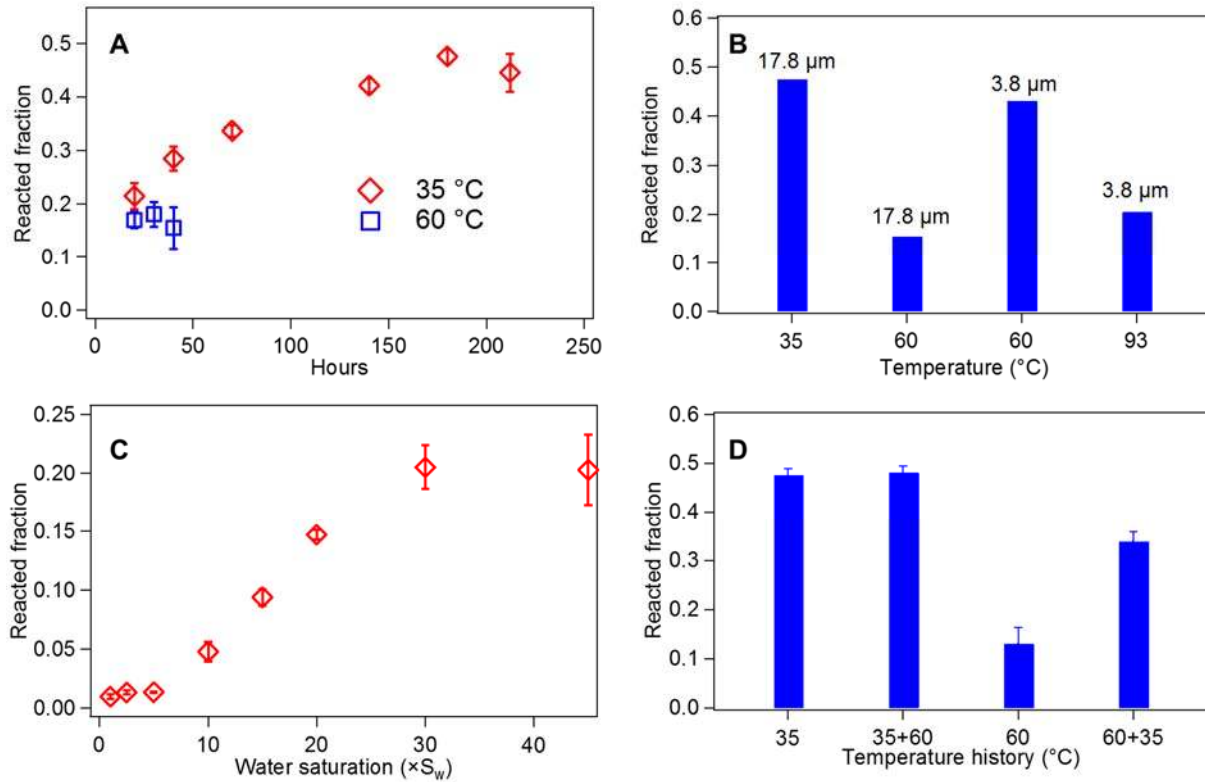
Figure 6-S4. Reacted fraction data used to calculate the reacted thickness in Figure 6.3 in the main text. **(A)** Reacted fraction of wollastonite particles with a volumetric mean size of 17.8 μm with $45 \times S_w$ at 35 °C (red diamond) and 60 °C (blue square), and 100 bar CO_2. **(B)** Reacted fraction of wollastonite particles after reaction with $45 \times S_w$ at 35, 60, and 93 °C and 100 bar CO_2. At 35 °C, 17.8 μm particles were used, because 3.8 μm particles were almost completely reacted. At 93 °C, 3.8 μm particles had to be used to obtain significant reacted fraction. At 60 °C, both 17.8 and 3.8 μm particles were used, and the reacted thicknesses were the same, which means the reacted thickness obtained using different particle sizes were comparable. This conclusion is shown in Chapter 5. **(C)** The reacted fraction of wollastonite particles with a volumetric mean size of 3.8 μm reacted for 40 hours at different water saturation percentages, 93 °C, and 100 bar CO_2. **(D)** The reacted fraction of wollastonite particles with a volumetric mean size of 17.8 μm reacted for 180 hours at varying temperature, $45 \times S_w$, and 100 bar CO_2.

170
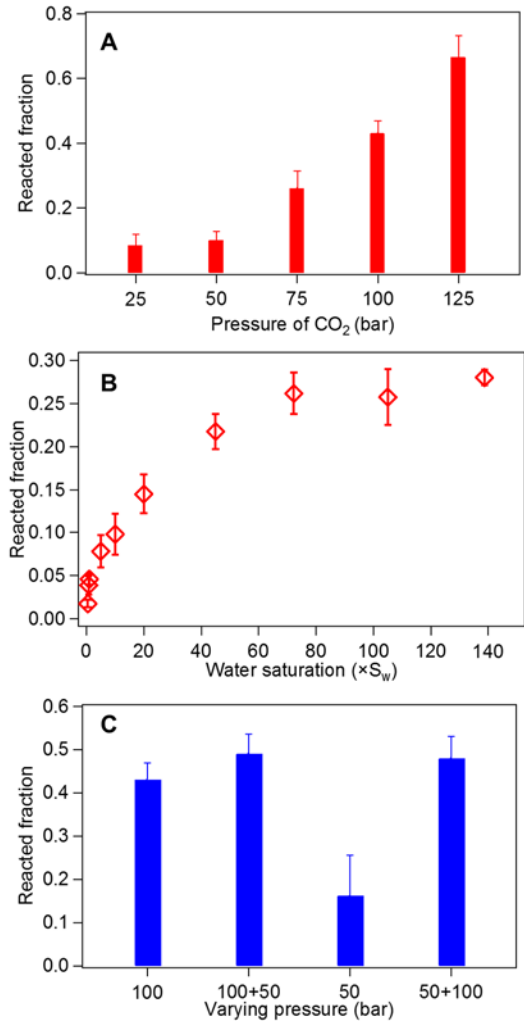
Figure 6-S5. Reacted fraction data used to calculate the reacted thickness in Figure 6.4 in the main text. **(A)** Reacted fraction of wollastonite particles with a volumetric mean size of 3.8 μm after 40 hours' reaction with $140 \times S_w$, at 60 °C and different pressure of CO_2. **(B)** Reacted fraction of wollastonite particles with a volumetric mean size of 3.8 μm reacted for 40 hours at different water saturation percentages, 60 °C, and 75 bar CO_2. **(C)** The reacted fraction of wollastonite particles with a volumetric mean size of 3.8 μm reacted for 40 hours at varying pressures, 60 °C, and $140 \times S_w$.

Chapter 7: Conclusions and Future Directions

7.1 Conclusions

To evaluate the feasibility and performance of GCS processes, it is critical to understand the compatibility between injected CO_2 and the mineralogy in storage sites. Currently, there are large uncertainties in the dissolution kinetics of aluminosilicates under GCS conditions. In addition, our knowledge on the silicate carbonation in water-bearing $scCO_2$ is still limited. This dissertation contributes to a better understanding of the reactions at CO_2–water–rock interfaces by investigating the dissolution of plagioclase and biotite in CO_2-acidified liquid phase water and the carbonation of wollastonite in water-bearing $scCO_2$. Particularly, by investigating the roles of sulfate anion and oxalate in the dissolution and subsequent precipitation at CO_2–water–rock interfaces, the CO_2–SO_2 co-sequestration and the GCS combined EOR have been considered.

Task 1 reported the effects of cations (e.g., Na, Ca, Al, and K) on the dissolution of plagioclase and biotite. **Task 2** elucidated the influence of anions (i.e., sulfate and oxalate) on the plagioclase dissolution and subsequent precipitations. **Task 3** investigated the effects of particle sizes of mineral grains, water, temperature, and pressure on the carbonation of wollastonite in water-bearing $scCO_2$.

In **Task 1**, Na inhibited the dissolution of plagioclase dissolution and the inhibition effects were particularly significant at > 0.1 M concentrations. Diffusion across the hydration layer on mineral surface did not affect the kinetics of dissolution in high salinity conditions. Ca also has a similar effect to Na at the same activities, and their effects did not suppress each other when Na and Ca coexisted. For biotite, Na enhanced dissolution by ion-exchange with interlayer K, which

172

caused swelling of interlayer spaces. This enhancing effect was coupled with an inhibition effect by competition for the adsorption of protons, which is similar to the Na inhibition on plagioclase dissolution. K is preferred as interlayer cations than Na in the biotite structure. K in aqueous phase can significantly suppress the Na-K ion-exchange in interlayer space and inhibit the dissolution of biotite. When biotite was pretreated with Na to replace the interlayer K with Na, the Na-biotite released Na rapidly, dissolved faster than original K-biotite, and formed vermiculite. Na in aqueous phase can inhibit the dissolution of Na-biotite and the formation of vermiculite. K in aqueous phase can reverse the ion-exchange and recover the original K-biotite. These findings demonstrated that the effects of cations can be as important as other factors, such as pH and temperature. Our results provide helpful information to predict the cation effect on the dissolution of aluminosilicates.

In **Task 2**, sulfate formed monodentate surface complexation with Al sites on plagioclase surface, which enhanced the dissolution. In the absence of sulfate, the Al dissolved from plagioclase precipitated as boehmite. Sulfate formed aqueous complexes with Al cations and suppress the boehmite formation. These observations help us understand the impacts of SO_2 co-sequestration. In addition, oxalate can suppress the sulfate effect when co-existed. These outcomes contribute to understanding the role of organic ligands in the dissolution of aluminosilicates.

In **Task 3**, wollastonite reacted with water-bearing $scCO_2$ and formed calcite and amorphous silica. The reaction occurs on the surface of wollastonite. The thickness of the reacted layer was similar for different size particles. The amorphous silica layer formed in water-bearing $scCO_2$ was much less porous than that formed in aqueous phase, and act as diffusion barrier for water-bearing $scCO_2$, which control the reaction extent. Higher extents of the reaction were observed at higher water saturation percentages, higher pressure, and lower temperature. Smaller

water saturation percentage and higher temperature produced less permeable amorphous silica layer, which can hinder further reactions when the water saturation percentage increased or temperature decreased. In contrast, the initial reaction at lower pressure did not affect further reactions at higher pressure. These results provide new insights for understanding silicate carbonation in water-bearing scCO$_2$.

This dissertation mainly focuses on the chemistry in GCS. The model minerals, plagioclase, biotite, and wollastonite, were chosen based on their reactivity and their relevance to GCS systems. We would like to point out that the results obtained using these minerals can also provide insights for other more abundant minerals in GCS field sites. For example, K-feldspar, which is a more abundant feldspar member, shares similar dissolution mechanisms with plagioclase. In addition, in our previous studies, we have elucidated how the dissolution kinetics of feldspars depend on their crystal structure.[79, 95, 105] Thus, the cation and anion effects observed in the current studies should be similar on the dissolution of K-feldspar. Furthermore, proton-promoted and ligand-promoted dissolution are common for aluminosilicates. Therefore, the competing adsorption between proton and cations, and the competing surface adsorption between organic and inorganic anions observed in this dissertation, should also affect the dissolution of other silicates.

7.2 Future Directions

In addition to the chemistry aspect in GCS, connecting with the geological preperties is important for further applications. Thus, a necessary step in future studies is to expand the investigation to more abundant but complex minerals. For example, using biotite, we have shown that interlayer ion-exchange reactions can strongly impact the dissolution of layered silicates. In

the future, more abundant micas, such as muscovite, and other phyllosilicates, such as smectite, should also be considered.

This dissertation investigated the molecular scale interactions of cations and anions with aluminosilicates surfaces and the nanoscale reactions between water-bearing CO_2 and silicates. There is a need to extend these studies to larger scale to know how these interfacial reactions can affect the pore scale and macroscale properties. An interesting future topic is to examine how geochemical reactions at CO_2–water–mineral interfaces change mechanical properties and hydrological properties, such as the porosity and permeability of rocks and cements. In addition, to scale up current studies, we should consider the interactions among different mineralogy in multi-mineral systems, and also the influence of pore structure in the geologic setting on the dissolution and precipitation processes.

This dissertation elucidated the impacts of dissolved SO_2 on the dissolution and precipitation of silicates by examining the effects of sulfate anions on the dissolution of plagioclase. The next step to further understand the impact of gas phase SO_2 co-sequestration could be investigating the effects of SO_2 and potential O_2 gas impurities on the carbonation of silicates in water-bearing $scCO_2$. The SO_2 impurities in CO_2 would tend to dissolve in the thin water film on mineral surfaces. Considering the high reactivity of SO_2, a greater extent of silicate hydrolysis and more carbonate and perhaps sulfate precipitations are expected. The reactions in water-bearing $scCO_2$ can be more important when SO_2 gas is co-injected with CO_2.

The dissertation also examined the influence of organic ligands on the aqueous phase reaction. In the future, the impact of organic compounds on the silicate carbonation should also be considered. For example, a previous study found that carboxylic acid ligands can dissolve into

175

water-bearing scCO$_2$ and enhance silicate carbonation.[58] Future studies can consider the less soluble organic compounds, because scCO$_2$ is better solvent to these organics than water.

In addition, we used wollastonite to elucidate the size effect and the equilibrium state of silicate carbonation, because wollastonite is the only natural mineral with enough reactivity within the short reaction time. The results obtained using wollastonite help understand the reaction mechanisms. However, to better predict understand the reaction in more abundant minerals, we will need to apply modeling approaches, which require a better understanding of the chemistry in thin water films on mineral surfaces. For example, an interesting future topic is to examine whether the formation of water films is necessary for reaction in water-bearing scCO$_2$, or if the reaction can directly happen with water molecules in the gas phase.

Considering the differences between reactions in the aqueous phase and non-aqueous phase, a critical future question is how we can improve CO$_2$ injectivity while minimize certain type of reactions. Before we figure out the strategy of CO$_2$ injection, further studies comparing the reactions of minerals in the aqueous phase and the non-aqueous phase water will be needed.

Finally, future studies should not be limited to the background of GCS and EOR. Other energy-related subsurface engineering processes with similar conditions, including unconventional oil and gas production and geothermal system, should be considered. For example, in enhanced oil recovery and unconventional gas production, many chemical additives are injected into the subsurface environment. These organic compounds are used as surfactants, scaling inhibitors, clay stabilizers, etc. Potentially, these organic compounds can cause different reactions at CO$_2$–water–rock interfaces and cause uncertainties in these industrial processes. Therefore,

future studies should consider the effects of chemical additives on the dissolution of silicate and aluminosilicates.

In sum, this dissertation has provided insights on the impacts of several important aqueous species, including Na, K, and Ca cations, and sulfate and carboxylic acid ligands, on the dissolution of plagioclase and biotite in CO_2-acidified liquid phase water. This work also includes a fundamental and systematical investigation on the effects of particle size, water, temperature, and pressure on silicate carbonation in water-bearing $scCO_2$. The outcomes can contribute to a comprehensive understanding of chemical reactions at CO_2–water–rock interfaces. Future directions of this work have been recommended to further improve our knowledge of the interactions among CO_2, water, and rock, which help predict the safety and efficiency of GCS processes.

References

1. Orr, F. M., Jr. Onshore Geologic Storage of CO_2. *Science.* **2009,** *325* (5948), 1656-1658.

2. Orr, F. M., Jr. CO_2 capture and storage: are we ready? *Energ. Environ. Sci.* **2009,** *2* (5), 449-458.

3. Bachu, S. Sequestration of CO_2 in geological media: criteria and approach for site selection in response to climate change. *Energ. Convers. Manage.* **2000,** *41* (9), 953-970.

4. Bruant, R. G., Jr.; Celia, M. A.; Guswa, A. J.; Peters, C. A. Peer Reviewed: Safe Storage of CO2 in Deep Saline Aquifers. *Environ. Sci. Technol.* **2002,** *36* (11), 240A-245A.

5. IPCC. *Special Report on Carbon Dioxide Capture and Storage*; Cambridge, 2005.

6. Jun, Y.-S.; Giammar, D. E.; Werth, C. J. Impacts of Geochemical Reactions on Geologic Carbon Sequestration. *Environmental Science & Technology* **2012,** *47* (1), 3-8.

7. Bickle, M. J. Geological carbon storage. *Nature Geoscience* **2009,** *2*, 815-818.

8. DePaolo, D. J.; Cole, D. R. Geochemistry of Geologic Carbon Sequestration: An Overview. *Rev. Mineral. Geochem.* **2013,** *77* (1), 1-14.

9. Bradshaw, J.; Cook, P. Geological Sequestration of Carbon Dioxide. *Environmental Geosciences* **2001,** *8* (3), 149-151.

10. Xu, T.; Kharaka, Y. K.; Doughty, C.; Freifeld, B. M.; Daley, T. M. Reactive transport modeling to study changes in water chemistry induced by CO_2 injection at the Frio-I Brine Pilot. *Chem. Geol.* **2010,** *271* (34), 153-164.

11. Andreani, M.; Gouze, P.; Luquot, L.; Jouanna, P. Changes in seal capacity of fractured claystone caprocks induced by dissolved and gaseous CO_2 seepage. *Geophysical Research Letters* **2008,** *35* (14), L14404.

12. Jun, Y.-S.; Zhang, L.; Min, Y.; Li, Q. Nanoscale Chemical Processes Affecting Storage Capacities and Seals during Geologic CO_2 Sequestration. *Acc. Chem. Res.* **2017**.

13. Gaus, I. Role and impact of CO_2-rock interactions during CO_2 storage in sedimentary rocks. *Int. J. Greenh. Gas. Con.* **2009,** *4* (1), 73-89.

14. Jun, Y.-S.; Giammar, D. E.; Werth, C. J. Impacts of Geochemical Reactions on Geologic Carbon Sequestration. *Environ. Sci. Technol.* **2013,** *47* (1), 3-8.

15. Gherardi, F.; Xu, T.; Pruess, K. Numerical modeling of self-limiting and self-enhancing caprock alteration induced by CO_2 storage in a depleted gas reservoir. *Chem. Geol.* **2007,** *244* (1–2), 103-129.

16. Zerai, B.; Saylor, B. Z.; Matisoff, G. Computer simulation of CO_2 trapped through mineral precipitation in the Rose Run Sandstone, Ohio. *Appl. Geochem.* **2006,** *21* (2), 223-240.

17. Cantucci, B.; Montegrossi, G.; Vaselli, O.; Tassi, F.; Quattrocchi, F.; Perkins, E. H. Geochemical modeling of CO_2 storage in deep reservoirs: The Weyburn Project (Canada) case study. *Chem. Geol.* **2009,** *265* (1–2), 181-197.

18. Eggleton, R. Weathering of basalt: Changes in rock chemistry and mineralogy. *Clays Clay Miner.* **1987,** *35* (3), 161-169.

19. Waters, A. C. Stratigraphic and lithologic variations in the Columbia River basalt. *Am. J. Sci.* **1961,** *259* (8), 583-611.

20. Hu, Y.; Ray, J. R.; Jun, Y.-S. Biotite-Brine Interactions under Acidic Hydrothermal Conditions: Fibrous Illite, Goethite, and Kaolinite Formation and Biotite Surface Cracking. *Environ. Sci. Technol.* **2011,** *45* (14), 6175-6180.

21. McGrail, B. P.; Schaef, H. T.; Glezakou, V. A.; Dang, L. X.; Owen, A. T. Water reactivity in the liquid and supercritical CO_2 phase: Has half the story been neglected? *Energy Procedia.* **2009,** *1* (1), 3415-3419.

22. Schaef, H. T.; Windisch Jr, C. F.; McGrail, B. P.; Martin, P. F.; Rosso, K. M. Brucite [Mg(OH2)] carbonation in wet supercritical CO_2: An in situ high pressure X-ray diffraction study. *Geochimica et Cosmochimica Acta 75* (23), 7458-7471.

23. Todd Schaef, H.; McGrail, B. P.; Loring, J. L.; Bowden, M. E.; Arey, B. W.; Rosso, K. M. Forsterite [Mg_2SiO_4)] Carbonation in Wet Supercritical CO_2: An in Situ High-Pressure X-ray Diffraction Study. *Environmental Science & Technology 47* (1), 174-181.

24. Kwak, J. H.; Hu, J. Z.; Turcu, R. V. F.; Rosso, K. M.; Ilton, E. S.; Wang, C.; Sears, J. A.; Engelhard, M. H.; Felmy, A. R.; Hoyt, D. W. The role of H_2O in the carbonation of forsterite in supercritical CO_2. *International Journal of Greenhouse Gas Control 5* (4), 1081-1092.

25. Loring, J. S.; Thompson, C. J.; Wang, Z.; Joly, A. G.; Sklarew, D. S.; Schaef, H. T.; Ilton, E. S.; Rosso, K. M.; Felmy, A. R. In Situ Infrared Spectroscopic Study of Forsterite Carbonation in Wet Supercritical CO_2. *Environmental Science & Technology 45* (14), 6204-6210.

26. Loring, J. S.; Thompson, C. J.; Zhang, C.; Wang, Z.; Schaef, H. T.; Rosso, K. M. In Situ Infrared Spectroscopic Study of Brucite Carbonation in Dry to Water-Saturated Supercritical Carbon Dioxide. *J. Phys. Chem. A* **2012,** *116* (19), 4768-4777.

27. Miller, Q. R. S.; Thompson, C. J.; Loring, J. S.; Windisch, C. F.; Bowden, M. E.; Hoyt, D. W.; Hu, J. Z.; Arey, B. W.; Rosso, K. M.; Schaef, H. T. Insights into silicate carbonation processes in water-bearing supercritical CO_2 fluids. *International Journal of Greenhouse Gas Control 15* (0), 104-118.

28. Lin, H.; Fujii, T.; Takisawa, R.; Takahashi, T.; Hashida, T. Experimental evaluation of interactions in supercritical CO_2/water/rock minerals system under geologic CO_2 sequestration conditions. *J. Mater. Sci.* **2008,** *43* (7), 2307-2315.

29. Shao, H.; Ray, J. R.; Jun, Y.-S. Effects of Salinity and the Extent of Water on Supercritical CO_2-Induced Phlogopite Dissolution and Secondary Mineral Formation. *Environ. Sci. Technol.* **2011,** *45* (4), 1737-1743.

30. Daval, D.; Martinez, I.; Guigner, J.-M.; Hellmann, R.; Corvisier, J.; Findling, N.; Dominici, C.; Goffe, B.; Guyot, F. Mechanism of wollastonite carbonation deduced from micro- to nanometer length scale observations. *Am. Mineral.* **2009,** *94* (11-12), 1707-1726.

31. Programme, I. G. G. R. D. *Effects of Impurities on Geological Storage of CO_2*; 2011.

32. Ogunberu, A. L.; Ayub, M. The Role of Wettability in Petroleum Recovery. *Pet. Sci. Technol.* **2005,** *23* (2), 169-188.

33. Dooley, K. M.; Cain, A. W.; Carl Knopf, F. Supercritical fluid extraction of acetic acid, alcohols and other amphiphiles from acid-water mixtures. *J. Supercrit. Fluids.* **1997,** *11* (1–2), 81-89.

34. Kharaka, Y. K.; Thordsen, J. J.; Hovorka, S. D.; Seay Nance, H.; Cole, D. R.; Phelps, T. J.; Knauss, K. G. Potential environmental issues of CO_2 storage in deep saline aquifers: Geochemical results from the Frio-I Brine Pilot test, Texas, USA. *Appl. Geochem.* **2009,** *24* (6), 1106-1112.

35. Shiraki, R.; Dunn, T. L. Experimental study on water-rock interactions during CO_2 flooding in the Tensleep Formation, Wyoming, USA. *Appl. Geochem.* **2000,** *15* (3), 265-279.

36. Wigand, M.; Carey, J. W.; Schutt, H.; Spangenberg, E.; Erzinger, J. Geochemical effects of CO_2 sequestration in sandstones under simulated in situ conditions of deep saline aquifers. *Appl. Geochem.* **2008,** *23* (9), 2735-2745.

37. Bourg, I. C.; Beckingham, L. E.; DePaolo, D. J. The Nanoscale Basis of CO_2 Trapping for Geologic Storage. *Environ. Sci. Technol.* **2015,** *49* (17), 10265-10284.

38. Blum, A. E.; Stillings, L. L. Feldspar dissolution kinetics. *Rev. Mineral. Geochem.* **1995,** *31* (1), 291-351.

39. Brantley, S. K., James; White, Art, *Kinetics of Water-Rock Interaction*. Springer: 2008.

40. Brantley, S. L.; Chen, Y. Chemical weathering rates of pyroxenes and amphiboles. *Rev. Mineral. Geochem.* **1995,** *31* (1), 119-172.

41. Brantley, S. L.; Stillings, L. Feldspar dissolution at 25 degrees C and low pH. *Am. J. Sci.* **1996,** *296* (2), 101-127.

42. Kharaka, Y. K. *Deep fluids in the continents:1. Sedimentary basins.*; 2007.

43. Koenen, M.; Tambach, T. J.; Neele, F. P. Geochemical effects of impurities in CO_2 on a sandstone reservoir. *Energy Procedia.* **2011,** *4* (0), 5343-5349.

44. Knauss, K. G.; Johnson, J. W.; Steefel, C. I. Evaluation of the impact of CO_2, co-contaminant gas, aqueous fluid and reservoir rock interactions on the geologic sequestration of CO_2. *Chem. Geol.* **2005,** *217* (3), 339-350.

45. Palandri, J. L.; Rosenbauer, R. J.; Kharaka, Y. K. Ferric iron in sediments as a novel CO_2 mineral trap: CO_2-SO_2 reaction with hematite. *Appl. Geochem.* **2005,** *20* (11), 2038-2048.

46. Xu, T.; Apps, J. A.; Pruess, K.; Yamamoto, H. Numerical modeling of injection and mineral trapping of CO_2 with H_2S and SO_2 in a sandstone formation. *Chem. Geol.* **2007,** *242* (3), 319-346.

47. Crandell, L. E.; Ellis, B. R.; Peters, C. A. Dissolution Potential of SO_2 Co-Injected with CO_2 in Geologic Sequestration. *Environ. Sci. Technol.* **2009,** *44* (1), 349-355.

48. Ellis, B. R.; Crandell, L. E.; Peters, C. A. Limitations for brine acidification due to SO_2 co-injection in geologic carbon sequestration. *Int. J. Greenh. Gas. Con.* **2009,** *4* (3), 575-582.

49. Dietzel, M.; Bohme, G. The dissolution rates of gibbsite in the presence of chloride, nitrate, silica, sulfate, and citrate in open and closed systems at 20 ºC. *Geochim. Cosmochim. Acta.* **2005,** *69* (5), 1199-1211.

50. Packter, A.; Dhillon, H. S. The heterogeneous reaction of Gibbsite powder with aqueous inorganic acid solutions; kinetics and mechanism. *J. Chem. Soc. A.* **1969,** *0* (0), 2588-2592.

51. Ridley, M. K.; Wesolowski, D. J.; Palmer, D. A.; Benezeth, P.; Kettler, R. M. Effect of Sulfate on the Release Rate of Al^{3+} from Gibbsite in Low-Temperature Acidic Waters. *Environ. Sci. Technol.* **1997,** *31* (7), 1922-1925.

52. Mogollon, J. L.; Prez-Diaz, A.; Lo Monaco, S. The effects of ion identity and ionic strength on the dissolution rate of a gibbsitic bauxite. *Geochim. Cosmochim. Acta.* **2000,** *64* (5), 781-795.

53. Ganor, J.; Reznik, I. J.; Rosenberg, Y. O. Organics in Water-Rock Interactions. *Rev. Mineral. Geochem.* **2009,** *70* (1), 259-369.

54. Daval, D.; Martinez, I.; Corvisier, J.; Findling, N.; Goffe, B.; Guyot, F. Carbonation of Ca-bearing silicates, the case of wollastonite: Experimental investigations and kinetic modeling. *Chem. Geol.* **2009,** *265* (1), 63-78.

55. Felmy, A. R.; Qafoku, O.; Arey, B. W.; Hu, J. Z.; Hu, M.; Todd Schaef, H.; Ilton, E. S.; Hess, N. J.; Pearce, C. I.; Feng, J.; Rosso, K. M. Reaction of water-saturated supercritical CO_2 with forsterite: Evidence for magnesite formation at low temperatures. *Geochim. Cosmochim. Acta.* **2012,** *91* (0), 271-282.

56. Kwak, J. H.; Hu, J. Z.; Turcu, R. V. F.; Rosso, K. M.; Ilton, E. S.; Wang, C.; Sears, J. A.; Engelhard, M. H.; Felmy, A. R.; Hoyt, D. W. The role of H_2O in the carbonation of forsterite in supercritical CO_2. *Int. J. Greenh. Gas. Con.* **2011,** *5* (4), 1081-1092.

57. Loring, J. S.; Thompson, C. J.; Wang, Z.; Joly, A. G.; Sklarew, D. S.; Schaef, H. T.; Ilton, E. S.; Rosso, K. M.; Felmy, A. R. In Situ Infrared Spectroscopic Study of Forsterite Carbonation in Wet Supercritical CO_2. *Environ. Sci. Technol.* **2011,** *45* (14), 6204-6210.

58. Miller, Q. R. S.; Kaszuba, J. P.; Schaef, H. T.; Bowden, M. E.; McGrail, B. P. Impacts of Organic Ligands on Forsterite Reactivity in Supercritical CO_2 Fluids. *Environ. Sci. Technol.* **2015,** *49* (7), 4724-4734.

59. Miller, Q. R. S.; Thompson, C. J.; Loring, J. S.; Windisch, C. F.; Bowden, M. E.; Hoyt, D. W.; Hu, J. Z.; Arey, B. W.; Rosso, K. M.; Schaef, H. T. Insights into silicate carbonation processes in water-bearing supercritical CO_2 fluids. *Int. J. Greenh. Gas. Con.* **2013,** *15* (0), 104-118.

60. Qafoku, O.; Kovarik, L.; Kukkadapu, R. K.; Ilton, E. S.; Arey, B. W.; Tucek, J.; Felmy, A. R. Fayalite dissolution and siderite formation in water-saturated supercritical CO_2. *Chem. Geol.* **2012,** *332-333* (0), 124-135.

61. Todd Schaef, H.; McGrail, B. P.; Loring, J. L.; Bowden, M. E.; Arey, B. W.; Rosso, K. M. Forsterite [Mg_2SiO_4)] Carbonation in Wet Supercritical CO_2: An in Situ High-Pressure X-ray Diffraction Study. *Environ. Sci. Technol.* **2012,** *47* (1), 174-181.

62. Whitfield, P. S.; Mitchell, L. D. In situ laboratory X-ray powder diffraction study of wollastonite carbonation using a high-pressure stage. *Appl. Geochem.* **2009,** *24* (9), 1635-1639.

63. Xu, T.; Apps, J. A.; Pruess, K. Mineral sequestration of carbon dioxide in a sandstone–shale system. *Chem. Geol.* **2005,** *217* (3–4), 295-318.

64. Gaus, I.; Azaroual, M.; Czernichowski-Lauriol, I. Reactive transport modelling of the impact of CO_2 injection on the clayey cap rock at Sleipner (North Sea). *Chem. Geol.* **2005,** *217* (3–4), 319-337.

65. Hangx, S. J. T.; Spiers, C. J. Reaction of plagioclase feldspars with CO_2 under hydrothermal conditions. *Chem. Geol.* **2009,** *265* (1), 88-98.

66. Sorai, M.; Ohsumi, T.; Ishikawa, M.; Tsukamoto, K. Feldspar dissolution rates measured using phase-shift interferometry: Implications to CO_2 underground sequestration. *Appl. Geochem.* **2007,** *22* (12), 2795-2809.

67. Zhang, L.; Kim, Y.; Jung, H.; Wan, J.; Jun, Y.-S. Effects of Salinity-Induced Chemical Reactions on Biotite Wettability Changes under Geologic CO_2 Sequestration Conditions. *Environmental Science & Technology Letters* **2016,** *3* (3), 92-97.

68. Hu, Y.; Ray, J. R.; Jun, Y.-S. Na^+, Ca^{2+}, and Mg^{2+} in Brines Affect Supercritical CO_2-Brine-Biotite Interactions: Ion Exchange, Biotite Dissolution, and Illite Precipitation. *Environ. Sci. Technol.* **2012,** *47* (1), 191-197.

69. Stillings, L. L.; Brantley, S. L. Feldspar dissolution at 25°C and pH 3: Reaction stoichiometry and the effect of cations. *Geochim. Cosmochim. Acta.* **1995,** *59* (8), 1483-1496.

70. Sposito, G., *The Chemistry of Soils*. Oxford University Press: 1989.

71. Oelkers, E. H.; Schott, J. Experimental study of anorthite dissolution and the relative mechanism of feldspar hydrolysis. *Geochim. Cosmochim. Acta.* **1995,** *59* (24), 5039-5053.

72. Muir, I. J.; Nesbitt, H. W. Effects of aqueous cations on the dissolution of labradorite feldspar. *Geochim. Cosmochim. Acta.* **1991,** *55* (11), 3181-3189.

73. Nesbitt, H. W.; MacRae, N. D.; Shotyk, W. Congruent and Incongruent Dissolution of Labradorite in Dilute, Acidic, Salt Solutions. *The Journal of Geology* **1991,** *99* (3), 429-442.

74. Ruiz-Agudo, E.; Kowacz, M.; Putnis, C. V.; Putnis, A. The role of background electrolytes on the kinetics and mechanism of calcite dissolution. *Geochim. Cosmochim. Acta.* **2010,** *74* (4), 1256-1267.

75. Ruiz-Agudo, E.; Urosevic, M.; Putnis, C. V.; Rodríguez-Navarro, C.; Cardell, C.; Putnis, A. Ion-specific effects on the kinetics of mineral dissolution. *Chem. Geol.* **2011,** *281* (3–4), 364-371.

76. Xu, M.; Sullivan, K.; VanNess, G.; Knauss, K. G.; Higgins, S. R. Dissolution Kinetics and Mechanisms at Dolomite–Water Interfaces: Effects of Electrolyte Specific Ionic Strength. *Environ. Sci. Technol.* **2013,** *47* (1), 110-118.

77. Dove, P. M.; Crerar, D. A. Kinetics of quartz dissolution in electrolyte solutions using a hydrothermal mixed flow reactor. *Geochim. Cosmochim. Acta.* **1990,** *54* (4), 955-969.

78. Sorai, M.; Sasaki, M. Dissolution kinetics of anorthite in a supercritical CO_2-water system. *Am. Mineral.* **2010,** *95* (5-6), 853-862.

79. Yang, Y.; Min, Y.; Lococo, J.; Jun, Y.-S. Effects of Al/Si ordering on feldspar dissolution: Part I. Crystallographic control on the stoichiometry of dissolution reaction. *Geochim. Cosmochim. Acta.* **2014,** *126* (0), 574-594.

80. Min, Y.; Kubicki, J. D.; Jun, Y.-S. Plagioclase Dissolution during CO_2–SO_2 Cosequestration: Effects of Sulfate. *Environ. Sci. Technol.* **2015,** *49* (3), 1946-1954.

81. D. White, G. B., T. Davis, Z. Hajnal, K. Hirsche, I. Hutcheon, E. Majer, B. Rostron, S. Whittaker. Greenhouse gas sequestration in abandoned oil reservoirs: the international energy agency weyburn pilot project. *GSA today.* **2003,** *14* (7), 40.

82. Carroll, S. A.; Knauss, K. G. Dependence of labradorite dissolution kinetics on $CO_2(aq)$, $Al(aq)$, and temperature. *Chem. Geol.* **2005,** *217* (3), 213-225.

83. Duan, Z.; Sun, R. An improved model calculating CO_2 solubility in pure water and aqueous NaCl solutions from 273 to 533 K and from 0 to 2000 bar. *Chem. Geol.* **2003,** *193* (3), 257-271.

84. Zhang, L.; Luttge, A. Theoretical approach to evaluating plagioclase dissolution mechanisms. *Geochim. Cosmochim. Acta.* **2009,** *73* (10), 2832-2849.

85. Chen, Y.; Brantley, S. L. Temperature- and pH-dependence of albite dissolution rate at acid pH. *Chem. Geol.* **1997,** *135* (3), 275-290.

86. Oelkers, E. H.; Schott, J.; Devidal, J.-L. The effect of aluminum, pH, and chemical affinity on the rates of aluminosilicate dissolution reactions. *Geochim. Cosmochim. Acta.* **1994,** *58* (9), 2011-2024.

87. Oelkers, E. H. General kinetic description of multioxide silicate mineral and glass dissolution. *Geochim. Cosmochim. Acta.* **2001,** *65* (21), 3703-3719.

88. Lasaga, A. C., *Kinetic Theory in the Earth Sciences*. Princeton University Press: Princeton, 1998.

89. Rydberg, J., *Solvent Extraction Principles and Practice, Revised and Expanded*. Taylor & Francis: 2004.

90. Ganor, J.; Lasaga, A. C. Simple mechanistic models for inhibition of a dissolution reaction. *Geochim. Cosmochim. Acta.* **1998,** *62* (8), 1295-1306.

91. Oxburgh, R.; Drever, J. I.; Sun, Y.-T. Mechanism of plagioclase dissolution in acid solution at 25 ºC. *Geochim. Cosmochim. Acta.* **1994,** *58* (2), 661-669.

92. Fleer, V. N., *The Dissolution Kinetics of Anorthite and Synthetic Strontium Feldspar in Aqueous Solutions at Temperatures Below 100 Degrees C: With Applications to the Geological Disposal of Radioactive Nuclear Wastes*. University Microfilms: 1985.

93. Brady, P. V.; Walther, J. V. Controls on silicate dissolution rates in neutral and basic pH solutions at 25°C. *Geochim. Cosmochim. Acta.* **1989,** *53* (11), 2823-2830.

94. Holdren, G. R.; Speyer, P. M. pH dependent changes in the rates and stoichiometry of dissolution of an alkali feldspar at room temperature. *Am. J. Sci.* **1985,** *285* (10), 994-1026.

95. Yang, Y.; Min, Y.; Jun, Y.-S. Effects of Al/Si ordering on feldspar dissolution: Part II. The pH dependence of plagioclases' dissolution rates. *Geochim. Cosmochim. Acta.* **2014,** *126* (0), 595-613.

96. Harbaugh, J. W.; George V. Chilingar, H. J. B.; Rhodes, W. F., Chapter 7 Carbonate Oil Reservoir Rocks. In *Developments in Sedimentology*, Elsevier: 1967; Vol. Volume 9, Part A, pp 349-398.

97. Finneran, D. W.; Morse, J. W. Calcite dissolution kinetics in saline waters. *Chem. Geol.* **2009,** *268* (1–2), 137-146.

98. Zavitsas, A. A. Properties of Water Solutions of Electrolytes and Nonelectrolytes. *J. Phys. Chem. B* **2001,** *105* (32), 7805-7817.

99. Zavitsas, A. A. Aqueous Solutions of Calcium Ions: Hydration Numbers and the Effect of Temperature. *J. Phys. Chem. B* **2005,** *109* (43), 20636-20640.

100. Song, J.; Zhang, D. Comprehensive Review of Caprock-Sealing Mechanisms for Geologic Carbon Sequestration. *Environ. Sci. Technol.* **2012,** *47* (1), 9-22.

101. Moore, J.; Adams, M.; Allis, R.; Lutz, S.; Rauzi, S. Mineralogical and geochemical consequences of the long-term presence of CO_2 in natural reservoirs: An example from the Springerville-St. Johns Field, Arizona, and New Mexico, U.S.A. *Chem. Geol.* **2005,** *217* (3-4), 365-385.

102. Kate, J. M.; Gokhale, C. S. A simple method to estimate complete pore size distribution of rocks. *Eng. Geol.* **2006,** *84* (1–2), 48-69.

103. Lasaga, A. C. Chemical kinetics of water-rock interactions. *J. Geophys. Res. Sol. Ea.* **1984,** *89* (B6), 4009-4025.

104. Steefel, C. I.; Lasaga, A. C. A coupled model for transport of multiple chemical species and kinetic precipitation/dissolution reactions with application to reactive flow in single phase hydrothermal systems. *Am. J. Sci.* **1994,** *294* (5), 529-592.

105. Yang, Y.; Min, Y.; Jun, Y.-S. A mechanistic understanding of plagioclase dissolution based on Al occupancy and T-O bond length: from geologic carbon sequestration to ambient conditions. *Phys. Chem. Chem. Phys.* **2013,** *15* (42), 18491-18501.

106. Jordan, G.; Higgins, S. R.; Eggleston, C. M.; Swapp, S. M.; Janney, D. E.; Knauss, K. G. Acidic dissolution of plagioclase: in-situ observations by hydrothermal atomic force microscopy - A study by direct-lattice resolution electron microscopy. *Geochim. Cosmochim. Acta.* **1999,** *63* (19), 3183-3191.

107. Taylor, A. S.; Blum, J. D.; Lasaga, A. C. The dependence of labradorite dissolution and Sr isotope release rates on solution saturation state. *Geochim. Cosmochim. Acta.* **2000,** *64* (14), 2389-2400.

108. Griffith, C. A.; Dzombak, D. A.; Lowry, G. V. Physical and chemical characteristics of potential seal strata in regions considered for demonstrating geological saline CO_2 sequestration. *Environ Earth Sci* **2011,** *64* (4), 925-948.

109. Cole, D. R.; Chialvo, A. A.; Rother, G.; Vlcek, L.; Cummings, P. T. Supercritical fluid behavior at nanoscale interfaces: Implications for CO_2 sequestration in geologic formations. *Philosophical Magazine* **2010,** *90* (17-18), 2339-2363.

110. Shao, H.; Ray, J. R.; Jun, Y.-S. Dissolution and Precipitation of Clay Minerals under Geologic CO_2 Sequestration Conditions: CO_2-brine-phlogopite Interactions. *Environ. Sci. Technol.* **2010,** *44* (15), 5999-6005.

111. Sakuma, H. C. J. B. Adhesion energy between mica surfaces: Implications for the frictional coefficient under dry and wet conditions. *J. Geophys. Res. Sol. Ea.* **2013,** *118* (12), 6066-6075.

112. Turpault, M. P.; Trotignon, L. The dissolution of biotite single crystals in dilute HNO_3 at 24 ºC: Evidence of an anisotropic corrosion process of micas in acidic solutions. *Geochim. Cosmochim. Acta.* **1994,** *58* (13), 2761-2775.

113. Shao, H.; Ray, J. R.; Jun, Y.-S. Effects of organic ligands on supercritical CO_2-induced phlogopite dissolution and secondary mineral formation. *Chem. Geol.* **2011,** *290* (3), 121-132.

114. Hu, Y.; Jun, Y.-S. Biotite Dissolution in Brine at Varied Temperatures and CO_2 Pressures: Its Activation Energy and Potential CO_2 Intercalation. *Langmuir.* **2012,** *28* (41), 14633-14641.

115. Gilkes, R. J.; Young, R. C. Artificial Weathering of Oxidized Biotite: IV. The Inhibitory Effect of Potassium on Dissolution Rate. *Soil Science Society of America Journal* **1974,** *38* (3), 529-532.

116. Malmstrom, M.; Banwart, S. Biotite dissolution at 25 ºC: The pH dependence of dissolution rate and stoichiometry. *Geochim. Cosmochim. Acta.* **1997,** *61* (14), 2779-2799.

117. Scott, A. D.; Smith, S. J., SUSCEPTIBILITY OF INTERLAYER POTASSIUM IN MICAS TO EXCHANGE WITH SODIUM. *Clays Clay Miner.*, Pergamon: 1966; pp 69-81.

118. Newman, A. C. D. CATION EXCHANGE PROPERTIES OF MICAS. *Journal of Soil Science* **1969,** *20* (2), 357-372.

119. Newman, A. C. D.; Brown, G. Chemical Changes during the Alternation of Micas. *Clay Minerals* **1966,** *6*, 297.

120. Yang, Y.; Min, Y.; Jun, Y.-S. Structure-Dependent Interactions between Alkali Feldspars and Organic Compounds: Implications for Reactions in Geologic Carbon Sequestration. *Environ. Sci. Technol.* **2012,** *47* (1), 150-158.

121. Min, Y.; Jun, Y.-S. Anorthite Dissolution under Conditions Relevant to Subsurface CO_2 Injection: Effects of Na^+, Ca^{2+}, and Al^{3+}. *Environ. Sci. Technol.* **2016,** *50* (20), 11377-11385.

122. Bray, A. W.; Oelkers, E. H.; Bonneville, S.; Wolff-Boenisch, D.; Potts, N. J.; Fones, G.; Benning, L. G. The effect of pH, grain size, and organic ligands on biotite weathering rates. *Geochim. Cosmochim. Acta.* **2015,** *164*, 127-145.

123. Reed, M. G. Formation Permeability Damage by Mica Alteration and Carbonate Dissolution. *Journal of petroleum technology* **1977,** *29* (sep), 1056-1060.

124. Stringfellow, W. T.; Domen, J. K.; Camarillo, M. K.; Sandelin, W. L.; Borglin, S. Physical, chemical, and biological characteristics of compounds used in hydraulic fracturing. *J. Hazard. Mater.* **2014,** *275* (0), 37-54.

125. Suter, J. L.; Coveney, P. V.; Anderson, R. L.; Greenwell, H. C.; Cliffe, S. Rule based design of clay-swelling inhibitors. *Energ. Environ. Sci.* **2011,** *4* (11), 4572-4586.

126. Fletcher, R. C.; Buss, H. L.; Brantley, S. L. A spheroidal weathering model coupling porewater chemistry to soil thicknesses during steady-state denudation. *Earth. Planet. Sci. Lett.* **2006,** *244* (1), 444-457.

127. Goodfellow, B. W.; Hilley, G. E.; Webb, S. M.; Sklar, L. S.; Moon, S.; Olson, C. A. C. J. F. The chemical, mechanical, and hydrological evolution of weathering granitoid. *Journal of Geophysical Research: Earth Surface* **2016,** *121* (8), 1410-1435.

128. Chialvo, A. A.; Vlcek, L.; Cole, D. R. Acid Gases in CO_2-rich Subsurface Geologic Environments. *Rev. Mineral. Geochem.* **2013,** *77* (1), 361-398.

129. Nogueira, M.; Mamora, D. D. Effect of Flue-Gas Impurities on the Process of Injection and Storage of CO_2 in Depleted Gas Reservoirs. *J. Energ. Resour.* **2008,** *130* (1), 013301-013301.

130. Dawson, G. K. W.; Pearce, J. K.; Biddle, D.; Golding, S. D. Experimental mineral dissolution in Berea Sandstone reacted with CO_2 or SO_2–CO_2 in NaCl brine under CO_2 sequestration conditions. *Chem. Geol.* **2014**, in press.

131. Pearce, J. K.; Kirste, D. M.; Dawson, G. K. W.; Farquhar, S. M.; Biddle, D.; Golding, S. D.; Rudolph, V. SO_2 Impurity Impacts on Experimental and Simulated CO_2-Water-Reservoir Rock Reactions at Carbon Storage Conditions. *Chem. Geol.* **2014**, in press.

132. Gunter, W. D.; Perkins, E. H.; Hutcheon, I. Aquifer disposal of acid gases: modelling of water-rock reactions for trapping of acid wastes. *Appl. Geochem.* **2000,** *15* (8), 1085-1095.

133. Palandri, J. L.; Kharaka, Y. K. Ferric iron-bearing sediments as a mineral trap for CO_2 sequestration: Iron reduction using sulfur-bearing waste gas. *Chem. Geol.* **2005,** *217* (3), 351-364.

134. Ridley, M. K.; Wesolowski, D. J.; Palmer, D. A.; Kettler, R. M. Association quotients of aluminum sulphate complexes in NaCl media from 50 to 125°C: Results of a potentiometric and solubility study. *Geochim. Cosmochim. Acta.* **1999,** *63* (3–4), 459-472.

135. Biber, M. V.; dos Santos Afonso, M.; Stumm, W. The coordination chemistry of weathering: IV. Inhibition of the dissolution of oxide minerals. *Geochim. Cosmochim. Acta.* **1994,** *58* (9), 1999-2010.

136. Bondietti, G.; Sinniger, J.; Stumm, W. The reactivity of Fe(III) (hydr)oxides: Effects of ligands in inhibiting the dissolution. *Colloids Surf., A.* **1993,** *79* (23), 157-167.

137. Stumm, W., *Aquatic Chemistry: Chemical Equilibria and Rates in Natural Waters*. Wiley: NY, 1996.

138. Ali, M. A.; Dzombak, D. A. Competitive Sorption of Simple Organic Acids and Sulfate on Goethite. *Environ. Sci. Technol.* **1996,** *30* (4), 1061-1071.

139. Yang, Y.; Ronzio, C.; Jun, Y.-S. The effects of initial acetate concentration on CO_2-brine-anorthite interactions under geologic CO_2 sequestration conditions. *Energ. Environ. Sci.* **2011,** *4* (11), 4596-4606.

140. Parfitt, R. L.; Smart, R. S. C. Infrared spectra from binuclear bridging complexes of sulphate adsorbed on goethite (a-FeOOH). *J. Chem. Soc. Faraday Trans.* **1977,** *73* (0), 796-802.

141. Wijnja, H.; Schulthess, C. P. Vibrational Spectroscopy Study of Selenate and Sulfate Adsorption Mechanisms on Fe and Al (Hydr)oxide Surfaces. *J. Colloid Interface Sci.* **2000,** *229* (1), 286-297.

142. Hug, S. J. In Situ Fourier Transform Infrared Measurements of Sulfate Adsorption on Hematite in Aqueous Solutions. *J. Colloid Interface Sci.* **1997,** *188* (2), 415-422.

143. Peak, D.; Ford, R. G.; Sparks, D. L. An in Situ ATR-FTIR Investigation of Sulfate Bonding Mechanisms on Goethite. *J. Colloid Interface Sci.* **1999,** *218* (1), 289-299.

144. M. J. Frisch, G. W. T., H. B. Schlegel, G. E. Scuseria, M. A. Robb, J. R. Cheeseman, G. Scalmani, V. Barone, B. Mennucci, G. A. Petersson, H. Nakatsuji, M. Caricato, X. Li, H. P. Hratchian, A. F. Izmaylov, J. Bloino, G. Zheng, J. L. Sonnenberg, M. Hada, M. Ehara, K. Toyota, R. Fukuda, J. Hasegawa, M. Ishida, T. Nakajima, Y. Honda, O. Kitao, H. Nakai, T. Vreven, J. A. Montgomery, Jr., J. E. Peralta, F. Ogliaro, M. Bearpark, J. J. Heyd, E. Brothers, ; K. N. Kudin, V.

N. S., T. Keith, R. Kobayashi, J. Normand, K. Raghavachari, A. Rendell, J. C. Burant, S. S. Iyengar, J. Tomasi, M. Cossi, N. Rega, J. M. Millam, M. Klene, J. E. Knox, J. B. Cross, V. Bakken, C. Adamo, J. Jaramillo, R. Gomperts, R. E. Stratmann, O. Yazyev, A. J. Austin, R. Cammi, C. Pomelli, J. W. Ochterski, R. L. Martin, K. Morokuma, V. G. Zakrzewski, G. A. Voth, P. Salvador, J. J. Dannenberg, S. Dapprich, A. D. Daniels, O. Farkas, J. B. Foresman, J. V. Ortiz, J. Cioslowski, and D. J. Fox *Gaussian 09, Revision B.01*, Gaussian, Inc.: Wallingford CT, 2010.

145. Becke, A. D. Density‐functional thermochemistry. III. The role of exact exchange. *J. Chem. Phys.* **1993,** *98* (7), 5648-5652.

146. Lee, C.; Yang, W.; Parr, R. G. Development of the Colle-Salvetti correlation-energy formula into a functional of the electron density. *Phys. Rev. B: Condens. Matter.* **1988,** *37* (2), 785-789.

147. Hehre, W. J.; Ditchfield, R.; Pople, J. A. Self—Consistent Molecular Orbital Methods. XII. Further Extensions of Gaussian—Type Basis Sets for Use in Molecular Orbital Studies of Organic Molecules. *J. Chem. Phys.* **1972,** *56* (5), 2257-2261.

148. Criscenti, L. J.; Brantley, S. L.; Mueller, K. T.; Tsomaia, N.; Kubicki, J. D. Theoretical and 27Al CPMAS NMR investigation of aluminum coordination changes during aluminosilicate dissolution. *Geochim. Cosmochim. Acta.* **2005,** *69* (9), 2205-2220.

149. Scott, A. P.; Radom, L. Harmonic Vibrational Frequencies: An Evaluation of Hartree−Fock, Møller−Plesset, Quadratic Configuration Interaction, Density Functional Theory, and Semiempirical Scale Factors. *J. Phys. Chem.* **1996,** *100* (41), 16502-16513.

150. Kubicki, J. D. Interpretation of Vibrational Spectra Using Molecular Orbital Theory Calculations. *Rev. Mineral. Geochem.* **2001,** *42* (1), 459-483.

151. Bloom, P. R.; Erich, M. S. Effect of Solution Composition on the Rate and Mechanism of Gibbsite Dissolution in Acid Solutions1. *Soil Sci. Soc. Am. J.* **1987,** *51* (5), 1131-1136.

152. Aagaard, P.; Helgeson, H. C. Thermodynamic and kinetic constraints on reaction rates among minerals and aqueous solutions; I, Theoretical considerations. *Am. J. Sci.* **1982,** *282* (3), 237-285.

153. Lowenstein, W. The distribution of aluminum in the tetrahedra of silicates and aluminates *Am. Mineral.* **1954,** *39*, 92-97.

154. Kubicki, J. D.; Paul, K. W.; Kabalan, L.; Zhu, Q.; Mrozik, M. K.; Aryanpour, M.; Pierre-Louis, A.-M.; Strongin, D. R. ATR–FTIR and Density Functional Theory Study of the Structures,

Energetics, and Vibrational Spectra of Phosphate Adsorbed onto Goethite. *Langmuir.* **2012,** *28* (41), 14573-14587.

155. Furrer, G.; Stumm, W. The coordination chemistry of weathering: I. Dissolution kinetics of a-Al$_2$O$_3$ and BeO. *Geochim. Cosmochim. Acta.* **1986,** *50* (9), 1847-1860.

156. Wyckoff, R. W. G., *Crystal Structures.* Interscience Publishers: New York, 1963; p 294.

157. Jun, Y.-S.; Lee, B.; Waychunas, G. A. In Situ Observations of Nanoparticle Early Development Kinetics at Mineral−Water Interfaces. *Environ. Sci. Technol.* **2010,** *44* (21), 8182-8189.

158. Munz, I. A.; Brandvoll; Haug, T. A.; Iden, K.; Smeets, R.; Kihle, J.; Johansen, H. Mechanisms and rates of plagioclase carbonation reactions. *Geochim. Cosmochim. Acta.* **2012,** *77* (0), 27-51.

159. Murakami, T. Formation of secondary minerals and its effect on anorthite dissolution. *Am. Mineral.* **1998,** *83*, 1209.

160. Fu, Q.; Lu, P.; Konishi, H.; Dilmore, R.; Xu, H.; Seyfried Jr, W. E.; Zhu, C. Coupled alkali-feldspar dissolution and secondary mineral precipitation in batch systems: 1. New experiments at 200 ºC and 300 bars. *Chem. Geol.* **2009,** *258* (3), 125-135.

161. Kim, Y.; Wan, J.; Kneafsey, T. J.; Tokunaga, T. K. Dewetting of Silica Surfaces upon Reactions with Supercritical CO$_2$ and Brine: Pore-Scale Studies in Micromodels. *Environ. Sci. Technol.* **2012,** *46* (7), 4228-4235.

162. Schrödle, S.; Rudolph, W. W.; Hefter, G.; Buchner, R. Ion association and hydration in 3:2 electrolyte solutions by dielectric spectroscopy: Aluminum sulfate. *Geochim. Cosmochim. Acta.* **2007,** *71* (22), 5287-5300.

163. J. Hlavay, K. J., S. Elek and J. Inczedy. Characterization of the Particle Size and the Crystallinity of Certain Minerals by IR Spectrophotometry and Other Instrumental Methods—II. Investigations on Quartz and Feldspar. *Clays Clay Miner.* **1978,** *26*, 139-143.

164. Qafoku, O.; Hu, J.; Hess, N. J.; Hu, M. Y.; Ilton, E. S.; Feng, J.; Arey, B. W.; Felmy, A. R. Formation of submicron magnesite during reaction of natural forsterite in H$_2$O-saturated supercritical CO$_2$. *Geochim. Cosmochim. Acta.* **2014,** *134* (0), 197-209.

165. Wang, X.; Alvarado, V.; Swoboda-Colberg, N.; Kaszuba, J. P. Reactivity of dolomite in water-saturated supercritical carbon dioxide: Significance for carbon capture and storage and for enhanced oil and gas recovery. *Energ. Convers. Manage.* **2013,** *65* (0), 564-573.

166. Thompson, C. J.; Loring, J. S.; Rosso, K. M.; Wang, Z. Comparative reactivity study of forsterite and antigorite in wet supercritical CO_2 by in situ infrared spectroscopy. *Int. J. Greenh. Gas. Con.* **2013,** *18* (0), 246-255.

167. Grasa, G. S.; Abanades, J. C.; Alonso, M.; González, B. Reactivity of highly cycled particles of CaO in a carbonation/calcination loop. *Chem. Eng. J.* **2008,** *137* (3), 561-567.

168. Peters, S.; Blum, J.; Driscoll, C.; Likens, G. Dissolution of wollastonite during the experimental manipulation of Hubbard Brook Watershed 1. *Biogeochemistry* **2004,** *67* (3), 309-329.

169. Pokrovsky, O. S.; Shirokova, L. S.; Bénézeth, P.; Schott, J.; Golubev, S. V. Effect of organic ligands and heterotrophic bacteria on wollastonite dissolution kinetics. *Am. J. Sci.* **2009,** *309* (8), 731-772.

170. Kelemen, P. B.; Matter, J.; Streit, E. E.; Rudge, J. F.; Curry, W. B.; Blusztajn, J. Rates and Mechanisms of Mineral Carbonation in Peridotite: Natural Processes and Recipes for Enhanced, in situ CO_2 Capture and Storage. *Annual Review of Earth and Planetary Sciences* **2011,** *39* (1), 545-576.

171. Deer, W. A.; Howie, R. A.; Zussman, J., *An Introduction to the Rock-Forming Minerals.* Mineralogical Society of Great Britain and Ireland: 2013; p 495.

172. Spycher, N.; Pruess, K.; Ennis-King, J. CO_2-H_2O mixtures in the geological sequestration of CO_2. I. Assessment and calculation of mutual solubilities from 12 to 100°C and up to 600 bar. *Geochim. Cosmochim. Acta.* **2003,** *67* (16), 3015-3031.

173. Schott, J.; Pokrovsky, O. S.; Spalla, O.; Devreux, F.; Gloter, A.; Mielczarski, J. A. Formation, growth and transformation of leached layers during silicate minerals dissolution: The example of wollastonite. *Geochim. Cosmochim. Acta.* **2012,** *98*, 259-281.

174. Hellmann, R.; Wirth, R.; Daval, D.; Barnes, J.-P.; Penisson, J.-M.; Tisserand, D.; Epicier, T.; Florin, B.; Hervig, R. L. Unifying natural and laboratory chemical weathering with interfacial dissolution–reprecipitation: A study based on the nanometer-scale chemistry of fluid–silicate interfaces. *Chem. Geol.* **2012,** *294–295* (0), 203-216.

175. Daval, D.; Sissmann, O.; Corvisier, J.; Garcia, B.; Martinez, I.; Guyot, F.; Hellmann, R., The effect of silica coatings on the weathering rates of wollastonite ($CaSiO_3$) and forsterite (Mg_2SiO_4): an apparent paradox? In *Water Rock Interaction- WRI-13 Proceedings of the 13Th international conference on Water Rock Interaction WRI-13 - Guanajuato, Mexico,16-20 August 2010*, P. Birkle, I.S. Torres-Alvarado, eds.: 2010; pp 713-720.

176. Saldi Giuseppe, D.; Daval, D.; Guo, H.; Guyot, F.; Bernard, S.; Le Guillou, C.; Davis James, A.; Knauss Kevin, G. Mineralogical evolution of Fe-Si-rich layers at the olivine-water interface during carbonation reactions. *Am. Mineral.* **2015,** *100*, 2655.

177. Saldi, G. D.; Daval, D.; Morvan, G.; Knauss, K. G. The role of Fe and redox conditions in olivine carbonation rates: An experimental study of the rate limiting reactions at 90 and 150 $^\circ$C in open and closed systems. *Geochim. Cosmochim. Acta.* **2013,** *118*, 157-183.

178. Sissmann, O.; Daval, D.; Brunet, F.; Guyot, F.; Verlaguet, A.; Pinquier, Y.; Findling, N.; Martinez, I. The deleterious effect of secondary phases on olivine carbonation yield: Insight from time-resolved aqueous-fluid sampling and FIB-TEM characterization. *Chem. Geol.* **2013,** *357*, 186-202.

179. Anthony, J. W., *Handbook of mineralogy*. Mineral Data Publ.: 1990.

180. Treiber, L. E.; Owens, W. W. A Laboratory Evaluation of the Wettability of Fifty Oil-Producing Reservoirs. *Soc. Petrol. Eng. J.* **1972,** *12* (06), 531-540.

181. Schaef, H. T.; McGrail, B. P.; Loring, J. L.; Bowden, M. E.; Arey, B. W.; Rosso, K. M. Forsterite [Mg_2SiO_4)] Carbonation in Wet Supercritical CO_2: An in Situ High-Pressure X-ray Diffraction Study. *Environ. Sci. Technol.* **2012,** *47* (1), 174-181.

182. Oldenburg, C. M. Joule-Thomson cooling due to CO_2 injection into natural gas reservoirs. *Energ. Convers. Manage.* **2007,** *48* (6), 1808-1815.

183. Min, Y.; Voltolini, M.; Kneafsey, T.; Jun, Y.-S. Wollastonite Carbonation in Water-bearing CO_2: Effects of Particle Sizes. **In review**.

184. White, D.; Burrowes, G.; Davis, T.; Hajnal, Z.; Hirsche, K.; Hutcheon, I.; Majer, E.; Rostron, B.; Whittaker, S. Greenhouse gas sequestration in abandoned oil reservoirs: The International Energy Agency Weyburn pilot project. *GSA today.* **2004,** *14* (7), 4-11.

185. Keller, S. J.; Survey, I. G., *Analyses of subsurface brines of Indiana*. State of Indiana, Dept. of Natural Resources, Geological Survey: 1983.

186. Kerisit, S.; Weare, J. H.; Felmy, A. R. Structure and dynamics of forsterite–scCO$_2$/H$_2$O interfaces as a function of water content. *Geochim. Cosmochim. Acta.* **2012,** *84*, 137-151.

187. Glezakou, V.-A.; Rousseau, R.; Dang, L. X.; McGrail, B. P. Structure, dynamics and vibrational spectrum of supercritical CO$_2$/H$_2$O mixtures from ab initio molecular dynamics as a function of water cluster formation. *Phys. Chem. Chem. Phys.* **2010,** *12* (31), 8759-8771.

188. Kerisit, S.; Bylaska, E. J.; Felmy, A. R. Water and carbon dioxide adsorption at olivine surfaces. *Chem. Geol.* **2013,** *359*, 81-89.

189. Saraji, S.; Goual, L.; Piri, M.; Plancher, H. Wettability of Supercritical Carbon Dioxide/Water/Quartz Systems: Simultaneous Measurement of Contact Angle and Interfacial Tension at Reservoir Conditions. *Langmuir.* **2013,** *29* (23), 6856-6866.

190. Min, Y.; Li, Q.; Voltolini, M.; Kneafsey, T.; Jun, Y.-S. Wollastonite Carbonation in Water-bearing Supercritical CO$_2$: Effects of Particle Size. **In review**.

Appendix A: Curriculum Vitae

YUJIA MIN

Washington University in St. Louis
Department of Energy, Environmental and Chemical Engineering
One Brookings Drive, Campus Box 1180, St. Louis, MO 63130
PHONE: 314-312-9658
E-MAIL: minyujia@wustl.edu

EDUCATION

Washington University in St. Louis

Ph.D., Energy, Environmental & Chemical Engineering   Expected Summer 2017

Dissertation title: "Effects of SO_2 and Organic Compounds on Silicate and Aluminosilicate Dissolution and Carbonate Precipitation during Geologic CO_2 Sequestration**"**

Advisor: Dr. Young-Shin Jun

M.S., Energy, Environmental & Chemical Engineering   2015

Peking University, China

B.S., Environmental Science   2011

RESEARCH EXPERIENCE

Washington University in St. Louis   2011-current

Research Assistant, Environmental NanoChemistry Laboratory

- Participated in experimental investigation of organic compounds' effects on alkali feldspar dissolution

- Conducted experiments to determine dissolution rates, pH dependency, and stoichiometry of plagioclase dissolution

- Performed research to measure Al occupancy and T–O bond length of plagioclases

- Participated in modelling the relationship between crystallography and dissolution of plagioclases

- Provided insights into the proper amount of SO_2 co-injection with CO_2 by investigating adsorption of sulfate on plagioclase and its effects on plagioclase dissolution

- Extended our knowledge of how high concentrations of cations affect plagioclase and biotite dissolution

- Investigated effects of particle sizes, water, temperature, and pressure on silicate

carbonation in water-bearing supercritical CO_2

- Prepared allocated proposal (ID: 40639) for the advanced photon source at Argonne National Laborotary

- Prepared accepted proposal (ID: 46212) for the Center for Nanoscale Materials at Argonne National Laborotary

- Participated in preparing proposal for DOE project DE-FE0025193

- Set up bench-scale high temperature and high pressure reaction system for flue gas purification

Peking University, China   2010-2011

   Undergraduate researcher

- Participated in experimental investigation of emission factors and size distribution of particulate matter and emission of polycyclic aromatic hydrocarbons from indoor solid fuel combustion

PUBLICATIONS

Articles in review

1. **Min, Y.**, Li, Q., Voltolini, M., Kneafsey, T., Jun, Y.-S., Wollastonite Carbonation in Water-bearing supercritical CO_2: Effects of Particle Sizes.

2. **Min, Y.**, Jun, Y.-S., Wollastonite Carbonation in Water-bearing supercritical CO_2: Effects of Water Saturation Conditions, Temperature, and Pressure.

3. Jung, H., Chadha, T. S., **Min, Y.**, Biswas, P., and Jun, Y.-S., Photochemically-assisted Synthesis of Birnessite Nanosheets and Their Structure Alteration in the Presence of Pyrophosphate.

4. Jiang, Q., Ghim, D., Tadepalli, S., Liu, K., Kwon, H., Luan, J., **Min, Y.**, Jun, Y.-S. and Singamaneni, S., Biofouling-resistant Ultrafiltration Membrane by Harnessing Sunlight.

Articles published in peer-reviewed journals

1. Jun, Y.-S., Zhang, L., **Min, Y.**, and Li, Q., Chemical Processes Affecting Storage Capacities and Seals during Geologic CO_2 Sequestration. *Accounts of Chemical Research*, 50, 1521-1529, **2017**.

2. **Min, Y.**, Jun, Y.-S., Plagioclase Dissolution under Conditions Relevant to Subsurface CO_2 Injection: Effects of Na^+, Ca^{2+}, and Al^{3+}. *Environmental Science and Technology*, 50, 11377–11385, **2016**.

3. **Min, Y.**, Kubicki, J.D., Jun, Y.-S., Plagioclase Dissolution during CO_2–SO_2 Co-sequestration: Effects of Sulfate. *Environmental Science and Technology*, 49, 1946-1954, **2015**.

4. Yang, Y., **Min, Y.**, Jun, Y.-S., Effects of Al/Si ordering on feldspar dissolution: Part II. The pH dependence of plagioclases' dissolution rates. *Geochimica et Cosmochimica Acta*, 126,

595-613, **2014**.

5. Yang, Y., **Min, Y.**, Lococo, J., Jun, Y.-S., Effects of Al/Si ordering on feldspar dissolution: Part I. Crystallographic control on the stoichiometry of dissolution reaction. *Geochimica et Cosmochimica Acta*, 126, 574-594, **2014**.

6. Yang, Y., **Min, Y.**, Jun, Y.-S., A mechanistic understanding of plagioclase dissolution based on Al occupancy and T–O bond length: from geologic carbon sequestration to ambient conditions. *Physical Chemistry Chemical Physics*, 15, 18491-18051, **2013**.

7. Yang, Y., **Min, Y.**, Jun, Y.-S., Structure-Dependent Interactions between Alkali Feldspars and Organic Compounds: Implications for Reactions in Geologic Carbon Sequestration. *Environmental Science and Technology*, 47, 150-158, **2013**.

8. Shen, G., Wei, S., Wang, W., Zhang, Y., **Min, Y.**, Wang, B., Wang, R., Li, W., Shen, H., Huang, Y., Yang, Y., Wang, W., Wang, X., Wang, X., Tao, S., Emission factors, size distributions, and emission inventories of carbonaceous particulate matter from residential wood combustion in rural China. *Environmental Science and Technology*, 46, 4207-14, **2012**.

9. Shen, G., Tao, S., Wang, W., Yang, Y., Ding, J., Xue, M., **Min, Y.**, Zhu, C., Shen, H., Li, W., Wang, B., Wang, R., Wang, W., Wang, X. Russell, A.G., Emission of Oxygenated Polycyclic Aromatic Hydrocarbons from Indoor Solid Fuel Combustion. *Environmental Science and Technology*, 45, 3459-3465, **2011**.

10. Shen, G., Wang, W., Yang, Y., Ding, J., Xue, M., **Min, Y.**, Zhu, C., Shen, H., Li, W., Wang, B., Wang, R., Wang, X., Tao, S., Russell, A.G., Emissions of PAHs from Indoor Crop Residue Burning in a Typical Rural Stove: Emission Factors, Size Distributions, and Gas-Particle Partitioning. *Environmental Science and Technology*, 45, 1206-1212, **2011**.

11. Shen, G., Wang, W., Yang, Y., Zhu, C., **Min, Y.**,Xue, M., Ding, J., Li, W., Wang, B., Shen, H., Wang, R., Wang, X., Tao, S., Emission factors and particulate matter size distribution of polycyclic aromatic hydrocarbons from residential coal combustions in rural Northern China. *Atmospheric Environment*, 44, 39, 5237-5243, **2010**.

12. Shen, G., Yang, Y., Wang, W., Tao, S., Zhu, C., **Min, Y.**, Xue, M., Ding, J., Wang, B., Wang, R., Shen, H., Li, W., Wang, X., Russell, A.G., Emission factors of particulate matter and black carbon for crop residues and coals burned in typical household stoves in China. *Environmental Science and Technology*, 44, 18, 7157-7162, **2010**.

PRESENTATIONS

Min, Y., Jun, Y.-S., "Effects of Na^+ and Ca^{2+} on plagioclase dissolution under high salinity conditions: Implications for subsurface CO_2 injection." Oral, session on "2017 Geochemistry Division Medal: Symposium in Honor of Dr. Susan Brantley." The 253th America Chemical Society National Meeting, San Francisco, CA, April 2-6, **2017.**

Min, Y., Jun, Y.-S., "Interfacial interactions between cations and biotite under conditions relevant to subsurface CO_2 injection." Oral, session on "Pore-Scale Geochemical Processes & the

Implications to CO2 Geologic Storage." The 253th America Chemical Society National Meeting, San Francisco, CA, April 2-6, **2017.**

Min, Y., Jun, Y.-S., "Silicate carbonation in water-bearing supercritical CO_2: New hints for connecting laboratory results to field sites." Oral, session on "Advances in Geologic Carbon Sequestration." The Geological Society of America North-Central Section 50th Annual Meeting, Champaign, IL, April 18-19, **2016.**

Min, Y., Jun, Y.-S., "Interfacial Interactions between Cations and Plagioclase under Conditions Relevant to Subsurface CO_2 Injection." Oral, session on "Environmental Interfaces: Complex Surface Reactions." The 251th America Chemical Society National Meeting, San Diego, March 13-17, **2016.**

Min, Y., Kubicki, J.D., Jun, Y.-S., "Effects of Carboxylic Acid Ligands on Plagioclase Dissolution During Geologic CO_2 Sequestration." Oral, session on "Understanding the Geochemical Interactions of Organic Compounds in the Subsurface." The 249th America Chemical Society National Meeting, Denver, March 22-26, **2015.**

Min, Y., Jun, Y.-S., "Sulfate Adsorption on Plagioclase and Its Effects on Plagioclase Dissolution: Implications for CO_2-SO_2 Co-sequestration" Oral, 20th Mid-America Environmental Engineering Conference (MAEEC), Missouri University of Science and Technology, Rolla, MO, November 15, **2014.**

AWARD

Student travel award   April 2016

The Geological Society of America

Best student paper award   March 2016

America Chemical Society: Division of Geochemistry

Student travel award   January 2016

America Chemical Society: Division of Geochemistry

TEACHING EXPERIENCE

Graduate teaching assistant

Course Number	Course Name	Students	Semester
ChE 368	Transport Phenomena II: Mass Transfer	27	Fall 2012
ChE 408/508	Environmental Engineering Laboratory	8	Spring 2013
EECE 448/548	Environmental Organic Chemistry	17	Fall 2013

COMPUTER SKILLS

Geochemist's Workbench, IGOR Pro, MATLAB, Generalized Structure and Analysis Software,

BRUKER-AXS TOPAS

COMMUNITY AND OUTREACH SERVICE

Graduate instructor, "Moving and Shaking: An Introduction to Engineering" for students in grades 6-8 (kindergarten through middle school), supported by St. Louis Area Gifted Resource Council, October-November, 2012, 2013, and 2016, St. Louis, MO, USA.

PROFESSIONAL AFFILIATIONS

Member of American Chemical Society

Member of Geological Society of America